Copyright

by

Christopher Michael Dundas

2020

The Dissertation Committee for Christopher Michael Dundas Certifies that this is the approved version of the following Dissertation:

Harnessing Bacterial Electroactivity with Materials Science and Synthetic Biology

Committee:

Benjamin Keitz, Supervisor

Hal Alper

George Georgiou

Charles Werth

Harnessing Bacterial Electroactivity with Materials Science and Synthetic Biology

by

Christopher Michael Dundas

Dissertation

Presented to the Faculty of the Graduate School of

The University of Texas at Austin

in Partial Fulfillment

of the Requirements

for the Degree of

Doctor of Philosophy

The University of Texas at Austin

August 2020

Dedication

To my brothers, my parents, and my wife.

Acknowledgements

I would like to sincerely thank all of the people who have made my doctoral journey possible. My PhD experience has had its ups and downs, but the steadfast support of my friends, family, and mentors has transformed me into the scientist and engineer that I am today. First and foremost, I need to thank Keith for his constant encouragement and guidance. I took a chance joining the lab of a new PI, and he took a chance on me, but I know that I could not have chosen a better mentor. Whether I was messaging Keith at midnight with some crazy research idea or we were both emotionally coping from the latest Game of Thrones episode, Keith was always there to support me. In his group, he let my voice be heard, fostered my scientific creativity, and encouraged me to pursue my own ideas. In sum, he let it be known that it was not *his* lab, but that it was *our* lab. Since the first day that I walked into CPE, I have been greeted by a plaque of our department's namesake, John J. McKetta, that has his quote, "a student you befriend is a friend forever". Having been a student of Keith Keitz, I know that the mentor I have befriended will be a friend forever.

I would also like to thank my committee members Hal Alper, George Georgiou, and Charlie Werth. During my doctoral studies, they have supported my work, offered sage advice, and contributed to making me a better researcher. Their guidance has honed the focus of my projects and taught me how to ask the right questions. I would also like to thank Jeff Gralnick for lending his expert opinion, laboratory resources, and friendly advice/support over the years.

Next, I thank the friends I have made in the Keitz group, CPE, and at UT. Angela, Mike, Katie, and Austin took the chance with me in joining a new lab and have been great coworkers and comrades as we navigated our studies. They have listened to my frustrations, encouraged me inside and outside the lab, and been my family away from home. I will fondly remember the many office laughs, restaurant runs, and crazy fun-filled nights in Austin that we have shared. I also sincerely thank the many undergraduates who I have had the pleasure of mentoring, including Aditya, Riley, Hazel, Rebecca, Seci, and Avery. All of them were wonderful collaborators and I have been proud to watch their academic and career successes.

A special thanks needs to be dedicated to my family – they are the primary reason I was able to enter graduate school. The love and support of Mom, Dad, Cameron, and Nicholas has followed me throughout my pre-college, undergraduate, and graduate school years. Cameron and Nicholas, you have been the best brothers anyone can ask for and were always there to encourage me when things got tough. Dad, I thank you for fostering my passion for science and problem-solving. You taught me that it is possible to achieve my dreams through hard work, and by emulating you I have become a better person. Mom, you made me the writer I am today and instilled in me a life-long love of education and self-betterment. You have always been my fiercest advocate, and I can never thank you enough for your unwavering help. Collectively, my family has propelled me to where I am today, and I sincerely thank them all for their past, present, and future aid.

Lastly, I give sincere appreciation and thanks to my research collaborator and the love of my life, Katie. When I entered graduate school, I didn't realize that I would leave being married to one of the most brilliant and compassionate people that I have ever met. With Katie, I have shared my passion for science, good food, and good times. Katie opened

me up to new joys too, which includes a newfound love of plants and pets. To that end, I also thank Islay and Pepper! Moreover, Katie has been there with me at my lowest, and has always been my champion who can raise my spirit. Katie, my relationship with you has been the best collaboration I will likely ever have in my life – I love you and I thank you for your constant support.

Harnessing Bacterial Electroactivity with Materials Science and Synthetic Biology

Christopher Michael Dundas, PhD

The University of Texas at Austin, 2020

Supervisor: Benjamin Keitz

Biotechnology has been transformed by increased cellular control over molecular products and processes. The fields of metabolic engineering and synthetic biology have standardized methods for biosynthesizing chemicals and progressed development of novel vaccines, genetic therapies, and transgenic organisms. Despite these significant advances, cellular programmability has largely stopped short of controlling the non-biological world – forward bioengineering of abiotic and inorganic processes, such as bio-electronic interfaces and material syntheses, remains a substantial challenge. To realize the benefits of engineered biology with such technologies, chassis organisms and extracellular pathways that connect genetics with inorganic transformations are required. In this work, we develop the electroactive bacterium *Shewanella oneidensis* and its extracellular electron transfer pathways as a genetically tunable platform to control redox-driven reactions.

To engineer *S. oneidensis* electroactivity for redox chemistry, we accomplish two overarching objectives. For the first objective, we establish genotype-phenotype relationships between *S. oneidensis* and material syntheses/transformations that tune material properties and functioning. In Chapter 2, we determine that *S. oneidensis* activates metal catalysts involved in atom-transfer radical polymerization and that polymerization rate depends on carbon metabolism and expression of key electron transfer proteins. In Chapter 3, we show that *S. oneidensis* reductively precipitates palladium nanoparticles onto the cell surface and that expression of outer membrane cytochromes and availability of

redox-active metabolites alters particle size and cellular localization. In Chapter 4, we demonstrate that *S. oneidensis* respires onto synthetic mineral analogs (metal-organic frameworks) *via* outer membrane cytochromes and that these bio-functionalized materials enable chromium remediation. For the second objective, we develop genetic tools to program extracellular electron flux and material formation by *S. oneidensis*. In Chapter 5, we use transcription/translation regulators and high throughput redox analysis to build plasmid-based logic gates in *S. oneidensis* that express single extracellular electron transfer proteins and exhibit inducible electroactivity responses, similar to fluorescent protein circuits. In Chapter 6, we leverage one of these *S. oneidensis* circuits to control radical crosslinking of a semi-synthetic hydrogel and predictably modulate gel stiffness *via* inducer molecule concentration. Taken together, this work provides new knowledge of *S. oneidensis*-controlled material transformations and presents a workflow to program extracellular electron transfer using synthetic biology.

Table of Contents

List of Tables xviii

List of Figures xx

Chapter 1: Background and Motivations 1

1.1 Introduction 1

1.2 Extracellular electron transfer (EET) Connects Genetics and Metabolism with Redox Transformations 3

1.3 *Shewanella oneidensis*: A Model Organism to Study and Apply EET 4

1.3.1 General Information on *Shewanella oneidensis* 4

1.3.2 Route of Electrons through the CymA/MtrCAB Pathway 5

1.3.3 Mechanisms of Electron Transfer onto Terminal Acceptors 7

1.4. Applications and Limitations of *S. oneidensis* EET 8

1.4.1 Power Generation 8

1.4.2 Nanomaterials Synthesis 9

1.4.3 Bioremediation and Bioelectrosynthesis 10

1.5 Genetic Control of *S. oneidensis* EET Activity 12

1.5.1 Background and Motivations 12

1.5.2 CymA/MtrCAB Expression 13

1.5.3 Metabolic Engineering of EET 14

1.5.3 Limitations and Challenges with Current Genetic Tools 14

1.6 Dissertation Objectives and Overview 15

Chapter 2: *Shewanella oneidensis* as a living electrode for controlled radical polymerization 18

2.1 Chapter Summary 18

2.2 Introduction 18

2.3 Results 22

2.3.1 Exogenous Metals and *S. oneidensis* Enable Atom-Transfer Radical Polymerization (ATRP). 22

2.3.2 Identification of Cu as a Viable ATRP Catalyst. 23

2.3.3 Use of TPMA Ligand Accelerates Polymerization Rate and Improves Control of Polymer Properties. 24

2.3.4 Viable Bacteria Enable ATRP, Not Secreted or Released Reducing Factors. 25

2.3.5 Carbon Source Affects Polymerization Kinetics. 27

2.3.6 MtrC Expression is Critical for ATRP Activity. 28

2.4 Discussion and Conclusions 30

2.5 Materials and Methods 33

2.5.1 Chemical and Reagents 33

2.5.2 Analysis and Measurement 33

2.5.3 Bacterial Strains and Culture 34

2.5.4 General Polymerization Conditions 35

2.5.5 Polymerization of Diblock Copolymer 35

2.5.6 SEM Analysis of Bacterial Before/After Polymerization 36

2.5.7 Polymerization Controls 36

2.5.8 Copper Treatment of CF4 Loaded Bacteria. 36

2.5.9 Copper Detection by CF4 in Bacterial Supernatant 37

2.5.10 Bacterial Growth/Viability Assessment 37

2.5.11 Construction of pShew-mtrC and plasmid complemented strains 38

2.5.12 Functional expression of MtrC by pShew-mtrC 39

2.5.13 Monomer conversion analysis by NMR 40

2.5.14 Statistical Analysis 40

Chapter 3: Extracellular electron transfer by *Shewanella oneidensis* controls palladium nanoparticle phenotype 41

3.1 Chapter Summary 41

3.2 Introduction 41

3.3 Results and Discussion 44

3.3.1 Optimizing *S. oneidensis* Control Over Nanoparticle Biosynthesis and Cellular Viability 44

3.3.2 Loss of Outer Membrane Cytochromes Decreases Pd Nanoparticle Size and Alters Cellular Localization 46

3.3.3 Loss of Outer Membrane Cytochromes Attenuates Pd(II) Reduction 50

3.3.4 MtrC Expression Controls Extracellular Pd Nanoparticle Formation 53

3.3.5 Flavins Decrease Outer Membrane-Nanoparticle Size 56

3.4 Conclusions 60

3.5 Materials and Methods 61

3.5.1 Chemicals and Reagents 61

3.5.2 Bacterial Strains and Culture 62

3.5.3 Nanoparticle Biosynthesis 63

3.5.4 Transmission Electron Microscopy 64

3.5.5 Nanoparticle Size and Number Analysis 65

3.5.6 Pd(II) Quantification 65

3.5.7 Powder X-Ray Diffraction 66

3.5.8 Flow Cytometry Analysis 67

3.5.9 Statistical Analysis 67

Chapter 4: Microbial reduction of metal-organic frameworks enables synergistic chromium removal 68

4.1 Chapter Summary 68

4.2 Introduction 69

4.3 Results 71

4.3.1 Stability of metal-organic frameworks in abiotic culture conditions 71

4.3.2 Metal-organic frameworks support microbial growth and reduction 72

4.3.3 Genetic and metabolic effects on metal-organic framework reduction 75

4.3.4 Stability of metal-organic frameworks in the presence of *S. oneidensis* 77

4.3.5 Cr(VI) adsorption by microbially-reduced metal-organic frameworks 79

4.3.6 Repeated cycles of Cr(VI) removal with *S. oneidensis*-reduced MIL-100 83

4.4 Discussion and Conclusions 86

4.5 Materials and Methods 90

4.5.1 Synthesis of metal-organic frameworks and iron oxides 90

4.5.2 Strains and culture conditions 90

4.5.3 Growth of MR-1 on metal-organic frameworks and iron oxides 91

4.5.4 Reduction of metal-organic frameworks and ferrihydrite 92

4.5.5 Cr(VI) adsorption to MR-1 reduced metal-organic frameworks and ferrihydrite 93

4.5.6 Cr(VI) cycling 94

4.5.7 Powder X-Ray Diffraction 94

4.5.8 Surface Area Measurements 95

4.5.9 Electron Microscopy 95

4.5.10 Leaching and Framework Stability Analysis 95

4.5.11 Nucleic Acid and Extracellular Protein Staining 96

4.5.12 Reduction of MIL-100 by *E. coli* 97

4.5.13 ICP-MS analysis 97

4.5.14 MR-1 reduction of Cr(VI) 97

4.5.15 Cr(VI) reduction by $FeCl_2$ 98

4.5.16 Cr(VI) reduction by MR-1 reduced Fe(III)-citrate 98

4.5.17 Chemicals and reagents 98

4.5.18 Statistical Analysis 99

Chapter 5: Tuning extracellular electron transfer by *Shewanella oneidensis* using transcriptional logic gates 101

5.1 Chapter Summary 101

5.2 Introduction 102

5.3 Results 104

5.3.1 High Throughput and Real-Time Quantification of Microbial Fe(III) Reduction 104

5.3.2 A Monod-type Model Connects Steady-State Gene Expression to Fe(III) Reduction 107

5.3.3 RBS Strength Tunes Dynamic Range of Inducible Fe(III) Reduction 108

5.3.4 Inducible Fe(III) Reduction Occurs in the Absence of Ferrozine 115

5.3.5 Reduction Rate Response Functions from Steady-State EET Gene Expression 115

5.3.6 A Polynomial Model Describes Dynamic Gene Expression and Fe(III) Reduction 117

5.3.7 Dynamic Expression of EET Genes Predictably Controls Reduction Rate 118

5.3.8 NOT Gate Circuits Turn Off Fe(III) Reduction in the Presence of IPTG 120

5.4 Discussion and Conclusions 123

5.5 Materials and Methods 128

5.5.1 DNA and Strain Construction 128

5.5.2 RBS Library Design 129

5.5.3 Measurement of Fe(III) Reduction Kinetics by *S. oneidensis* 130

5.5.4 Derivation of Monod-type Model for Fe(III) Reduction 132

General relationship between cell growth and Fe(III) Reduction 132

Comment on assumption of constant μ 134

Relationship between fitted rate constant and EET gene expression 135

5.5.5 Derivation of Polynomial Model for Fe(III) Reduction 137

Dynamic protein expression model 137

Connection of dynamic protein expression with Fe(III) reduction ... 138

5.5.6 Reduction Kinetics and Rate Constant Response Function Fitting ... 139

Chapter 6: Genetic control of radical cross-linking in a semisynthetic hydrogel 140

6.1 Chapter Summary 140

6.2 Introduction 141

6.3 Results 145

6.3.1 Extracellular Electron Transfer from Live *S. oneidensis* Controls Aerobic Radical Crosslinking 145

6.3.2 *S. oneidensis* Remains Viable and Metabolically Active in the Network 149

6.3.3 Bacterial Genetics Govern Crosslink Density 153

6.3.4 Transcriptional Regulation of Extracellular Electron Transfer Yields Tunable Crosslinking Activity 154

6.3.5 Modeling Gene Expression Enables Predictable Material Properties 157

6.4 Discussion and Conclusions 158

6.5 Materials and Methods 161

6.5.1 Chemicals and Reagents 161

6.5.2 Methacrylated Hyaluronic Acid Synthesis and Purification 162

6.5.3 Bacteria Strains and Culture 162

6.5.4 MeHA Hydrogel Crosslinking using *S. oneidensis* 163

6.5.5 Rheological Analysis 164

6.5.6 Microscopy and Cell Tracking 164

6.5.7 Plasmid Construction 165

6.5.8 Verification of MtrC Inducible Expression and Functional Activity 167

6.5.9 Models of Inducible Gene Expression and Storage Moduli 168

Hill Function Model 168

Derivation of Linear Relationship Between REU and G' 168

6.5.10 Quantification and Modeling of Inducible Constructs 169

Chapter 7: Conclusions and Future Work 171

7.1 Introduction 171

7.2 Chapter 2 Summary and Outlook 171
7.3 Chapter 3 Summary and Outlook 172
7.4 Chapter 4 Summary and Outlook 174
7.5 Chapter 5 Summary and Outlook 175
7.6 Chapter 6 Summary and Outlook 176
7.7 Proposed Research and Final Comments 177
Appendices 182
Appendix A: Supplementary Data for Chapter 2 182
Supplementary Tables for Chapter 2 182
Supplementary Figures for Chapter 2 185
Appendix B: Supplementary Data for Chapter 3 209
Supplementary Tables for Chapter 3 209
Supplementary Figures for Chapter 3 210
Appendix C: Supplementary Data for Chapter 4 230
Supplementary Tables for Chapter 4 230
Supplementary Figures for Chapter 4 233
Appendix D: Supplementary Data for Chapter 5 247
Supplementary Tables for Chapter 5 247
Supplementary Figures for Chapter 5 255
Appendix E: Supplementary Data for Chapter 6 274
Supplementary Tables for Chapter 6 274
Supplementary Figures for Chapter 6 278
References 297

List of Tables

Table A.1: Metals present in *Shewanella* basal medium Wolfe's mineral solution. Adapted from ATCC recipe. 182

Table A.2: MR-1 mediated controlled polymerization of $OEOMA_{500}$ in SBM buffer at 30 °C. (*exclusion limit)..... 182

Table A.3: Bacterial strains and plasmids used in this study. 183

Table A.4: Primers used in this study. 184

Table A.5: Comparison of first-order rate constants under different polymerization conditions. 184

Table B.1: Bacterial Strains and Plasmids Used in this Study. 209

Table C.1: Cr(VI) cycles. 230

Table C.2: Cr(VI) removal by both biotic and abiotic agents. 232

Table C.3: Metal-organic framework surface areas. 232

Table D.1: Bacterial strains and plasmids used in this study. 248

Table D.2: Strain/Plasmid Information for RBS Library. 249

Table D.3: Genetic parts/sequences used to construct the plasmids in this study. Underline indicates added insulator sequence. 253

Table D.4: Nonlinear fit parameters for main text Figures 5.4-5.6. 254

Table E.1: Bacterial strains and plasmids used in this study. 274

Table E.2: Ingredients in *Shewanella* Basal Medium. Growth media was supplemented with casamino acids and Wolfe's mineral solution, whereas crosslinking media was only supplemented with casamino acids. 275

Table E.3: Ingredients in Wolfe's mineral solution, adapted from ATCC recipe. 275

Table E.4: Genetic parts/sequences used to construct the plasmids in this study. 277
Table E.5: Nonlinear fit parameters for products of *sfgfp* expression (fluorescence) and *mtrC* expression (storage modulus) 278

List of Figures

Figure 1.1: General model of extracellular electron transfer (EET) as a bacterial respiration mechanism. 4

Figure 1.2: Model of CymA/MtrCAB pathway in *Shewanella oneidensis* MR-1. 7

Figure 2.1: *S. oneidensis* enabled atom-transfer radical polymerization (ATRP) and initial polymerization kinetics. 21

Figure 2.2: Kinetics and properties of polymers formed with *S. oneidensis* MR-1. 25

Figure 2.3: Polymerization activity is controlled by electroactive metabolism. 28

Figure 2.4: Electron transfer proteins impact polymerization kinetics. 30

Figure 3.1: Formation of extracellular Pd nanoparticles requires outer membrane cytochromes. 47

Figure 3.2: Loss of outer membrane cytochromes decreases Pd nanoparticle size. 49

Figure 3.3: Loss of outer membrane cytochromes attenuates Pd(II) reduction rate. 52

Figure 3.4: MtrC expression controls extracellular localization of Pd nanoparticles. 54

Figure 3.5: Plasmid-based MtrC expression rescues large particle phenotype in *S. oneidensis* Δ*mtrC*Δ*omcA*. 54

Figure 3.6: MtrC expression rescues Pd(II) reduction rate. 55

Figure 3.7: Flavin supplementation decreases size of extracellular Pd nanoparticles. 57

Figure 3.8: Flavin supplementation decreases Pd nanoparticle size and increases particle count per cell. 58

Figure 3.9: Flavin supplementation affects Pd(II) reduction rate by *S. oneidensis*. 59

Figure 4.1: *S. oneidensis* MR-1 metal reduction pathway and metal-organic framework structure. 70

Figure 4.2: Growth of *S. oneidensis* MR-1 and reduction of metal-organic frameworks. 73
Figure 4.3: Genetic and metabolic effects on reduction. 76
Figure 4.4: Stability of metal-organic frameworks in the presence of *S. oneidensis*. 79
Figure 4.5: Cr(VI) removal in reduced metal-organic frameworks 81
Figure 4.6: Cr(VI) cycling with reduced metal-organic frameworks. 84
Figure 5.1: CymA/MtrCAB extracellular electron pathway in *S. oneidensis* MR-1 103
Figure 5.2: Measurement and modeling of Fe(III) reduction kinetics by *S. oneidensis* .. 106
Figure 5.3: Dynamic range optimization for inducible EET circuits. 111
Figure 5.4: Buffer gate response functions under steady-state EET gene expression. 114
Figure 5.5: Buffer gate response functions under dynamic EET gene expression and from aerobic pregrowth. 119
Figure 5.6: NOT gate response functions under steady-state EET gene expression. 122
Figure 6.1: Extracellular electron transfer from *S. oneidensis* controls radical crosslinking of a semi-synthetic hydrogel. 144
Figure 6.2: Living hydrogel materials crosslinked by *S. oneidensis* MR-1 can be chemically or biologically tuned. 147
Figure 6.3: Cell motility, synthesis rate, and crosslink density within living hydrogels are governed by *S. oneidensis* genetics and EET machinery. 152
Figure 6.4: Modeling gene expression allows quantitative prediction of living hydrogel properties. 156
Figure A.1: Kinetics of monomer conversion using MR-1 in SBM with (solid points) and without (hollow points) added metal. Data show mean ± S.D. of three independent experiments. 185

Figure A.2: Conversion of $(OEOMA)_{500}$ using other metals as catalysts and EDTA as ligand. Metals were evaluated at their concentrations listed in Table A.1. 186

Figure A.3: Fluorescence intensity change of CF4 with increasing concentrations of $Cu^{I}(CH_3CN)_4BF_4$. 186

Figure A.4: Calibration curve for CF4 fluorescence intensity as a function of increasing concentrations of $Cu^{I}(CH_3CN)_4BF_4$. Line of best fit: y = 77.8 + 42.8X, R^2 = 0.929. 187

Figure A.5: Fluorescence intensity change in MR-1 supernatant following incubation with $CuSO_4$•$5H_2O$ (2 μM) and CF4 or CTRL-CF4. 188

Figure A.6: Fluorescence intensity change in *E. coli* (MG1655) supernatant following incubation with $CuSO_4$•$5H_2O$ (2 μM) and CF4 or CTRL-CF4. 188

Figure A.7. No detectable increase in cytoplasmic Cu(I) following incubation with exogeneous Cu(II). 189

Figure A.8: Representative gating scheme for flow cytometric analyses on a BD LSRII Fortessa SOPR Flow Cytometer. 190

Figure A.9: Number average molecular weight and PDI versus conversion using MR-1, Cu(II/I)-EDTA as catalyst, and $OEOMA_{500}$ as monomer. Data points were collected over a 24-hour time period. 190

Figure A.10: Gel permeation chromatographs of poly($OEOMA_{500}$) synthesized via MR-1, Cu(II/I)-EDTA as catalyst and $OEOMA_{500}$ as monomer after 24 hours. GPC mobile phase was DMF. (Note: [M] = $OEOMA_{500}$, [I] = HEBIB, [C] = Cu(II/I)-EDTA, molar concentration.) 191

Figure A.11: Gel permeation chromatographs of poly($OEOMA_{500}$) synthesized via MR-1, Cu(II/I)-TPMA as catalyst and $OEOMA_{500}$ as monomer at different time points. GPC mobile phase was PBS buffer. 192

Figure A.12: Effect of different Cu(II/I)-TPMA concentrations on polymerization kinetics. 192

Figure A.13: Linear polymerization kinetics using MR-1, Cu(II/I)-TPMA, and $OEOMA_{900}$ as monomer. Line of best fit: $y = 0.15 + 0.92X$, $R^2 = 0.988$. . 193

Figure A.14: ^1H NMR spectra for the polymerization of Poly$(OEOMA_{500})_m$-*b*-$(NIPAM)_n$ (blue) and its respective homo-polymers, poly$(OEOMA_{500})_m$ (green) and poly$(NIPAM)_n$ (Red). 194

Figure A.15: Molecular weight distribution of poly($OEOMA_{500}$) and block copolymer $(OEOMA_{500})_x$-*b*-$(NIPAM)_y$. 195

Figure A.16: Reducing factors such as glutathione contribute to polymerization in a dose-dependent manner. 195

Figure A.17: Monomer conversion is dependent on cell metabolism and membrane integrity. 196

Figure A.18: Growth curves for MR-1 under aerobic conditions when incubated with **a**, $CuBr_2$-EDTA (5 μM). **b**, $OEOMA_{500}$ (100 mM). **c**, anaerobic polymerization conditions including Cu-EDTA (2 μM), $OEOMA_{500}$ (100 mM), and HEBIB (100 μM). Data show mean ± S.D. of three independent experiments. 197

Figure A.19: MR-1 is viable following polymerization. 197

Figure A.20: Bacterial viability assessment post-polymerization shows mostly live cells for both MR-1 and *E. coli*. 198

Figure A.21: Scanning electron micrograph (SEM) of MR-1 before polymerization, scale bar = 2 μm. 199
Figure A.22: Scanning electron micrograph (SEM) of MR-1 after polymerization, scale bar = 2 μm. 199
Figure A.23: Metabolic activity is required for monomer conversion. 200
Figure A.24: Accompanying for Figure 2.3b. 201
Figure A.25: Accompanying for Figure 2.4b. 202
Figure A.26: Accompanying for Figure 2.4c. 203
Figure A.27: Iron reduction of different *S. oneidensis* strains. 204
Figure A.28: IPTG inducibility of MtrC and iron reduction in Δ*mtrC*Δ*omcA* strains. ... 205
Figure A.29: Example of ^{1}H NMR spectra for determination of monomer conversion during the polymerization of $OEOMA_{500}$ ([M]/[I]=1000/1, HEBIB, *Shewanella* basal medium with Wolfe's mineral solution). Residual water peak has been removed for clarity. 206
Figure A.30: ^{1}H NMR spectra for the polymerization of $OEOMA_{900}$. Residual water peak has been removed for clarity. (Note: T indicates different reaction time.) 207
Figure A.31: ^{1}H NMR spectra for the polymerization of NIPAM ([M]/[I]/[Cu/TPMA]=1000/1/0.02, MR-1 initial OD = 0.02, SBM lacking trace mineral mix and supplemented with casamino acids). Residual water peak has been removed for clarity. (Note: T indicates different reaction time. * proton peaks due to the impurities from cell culture medium.) 207

Figure A.32: ^{1}H NMR spectra for the polymerization of OEOMA500 using MR-1 and E. coli, respectively ([M]/[I]/[Cu/TPMA]=1000/1/0.02, Initial OD600 = 0.02, SBM lacking trace mineral mix and supplemented with casamino acids, 2 hours). Residual water peak has been removed for clarity.....208
Figure B.1: Effect of lactate on Pd(II) reduction by *S. oneidensis*.....210
Figure B.2: Effect of casamino acids on Pd nanoparticle formation by *S. oneidensis*....211
Figure B.3: Effect of Pd(II) concentration on *S. oneidensis* MR-1 viability.....212
Figure B.4: Bacterial viability affects reduction of 100 μM Pd(II).....213
Figure B.5: Representative gating scheme for flow cytometric analyses of *S. oneidensis*. 213
Figure B.6: Flow cytometry side scatter signal for Pd-free MR-1 and MR-1/Δ*mtrC*Δ*omcA* after 2 hours of reaction with 100 μM Pd(II).....214
Figure B.7: Simultaneous quantification of palladization and cell death for *S. oneidensis* MR-1 and Δ*mtrC*Δ*omcA* using flow cytometry. 215
Figure B.8: Color change of *S. oneidensis* cell pellet after Pd(II) reduction.....216
Figure B.9: Effect of *S. oneidensis* genotype on Pd nanoparticle formation.....217
Figure B.10: Effect of *S. oneidensis* genotype on Pd nanoparticle localization.....218
Figure B.11: Effect of *S. oneidensis* genotype on Pd nanoparticle powder x-Ray diffraction patterns. Data was normalized to the most intense peak height. 219
Figure B.12: Effect of 100 μM Pd(II) on (a) *S. oneidensis* MR-1 and (b) *E. coli* MG1655 after 4 hours. Scale bars represent 500 nm. 219
Figure B.13: Effect of *S. oneidensis* genotype on viability during Pd(II) reduction.....220

Figure B.14: Pd(II) reduction by *S. oneidensis* MR-1 and *E. coli* MG1655 after 4 hours. 221
Figure B.15: Pd(II) reduction kinetics fitting for knockout and complemented knockout *S. oneidensis* strains. 222
Figure B.16: HEPES buffer age affects Pd(II) reduction rate by *S. oneidensis* MR-1 223
Figure B.17: Effect of outer membrane cytochrome complementation on Pd nanoparticle formation. 224
Figure B.18: Effect of MtrC expression on Pd nanoparticle localization by *S. oneidensis*. 224
Figure B.19: Effect of increasing riboflavin concentration on Pd nanoparticle formation by *S. oneidensis* MR-1. 225
Figure B.20: Effect of supplemented riboflavin and flavin mononucleotide on Pd nanoparticle formation by *S. oneidensis* MR-1. 225
Figure B.21: Effect of increasing sodium fumarate concentration on Pd nanoparticle formation by *S. oneidensis* MR-1. 226
Figure B.22: Effect of Increasing Fe(III)-Citrate Concentration on Pd Nanoparticle Formation by *S. oneidensis* MR-1. 227
Figure B.23: Effect of flavin supplementation on *S. oneidenis* viability during Pd(II) reduction. 228
Figure B.24: Effect of flavins on abiotic Pd nanoparticle formation. 229
Figure C.1: Stability of metal-organic frameworks. 233
Figure C.2: Concomitant Fe(III) reduction with CFU counts. 234
Figure C.3: Growth on MIL-88A. 235
Figure C.4: Morphology of metal-organic frameworks and ferrihydrite. 236

Figure C.5: Nucleic acid and biofilm matrix protein quantification. 236
Figure C.6: Normalized Fe(III) reduction rates after 48 h. 237
Figure C.7: Metabolite quantification. 238
Figure C.8: *E. coli* reduction of MIL-100. 239
Figure C.9: Normalized Fe(III) reduction rate with exogenous riboflavin. 240
Figure C.10: Total Cr removal. 241
Figure C.11: Cr(VI) reduction by *S. oneidensis* and Fe(II). 241
Figure C.12: Cr(VI) cycling. 242
Figure C.13: Cr(VI) removal for long-term cycling. 243
Figure C.14: Fe(II) reduction of Cr(VI). 244
Figure C.15: Cycled metal-organic framework morphology. 245
Figure C.16: Bacterial viability post-cycling. 246
Figure D.1: Anaerobically sealed 96-well plate within a plate reader after an 18-hour microbial Fe(III) reduction experiment. 255
Figure D.2: Inducible *mtrC* construct exhibits Monod-type behavior for fitted rate constant with varying initial Fe(III) concentration. 256
Figure D.3: Raw kinetic data for RBS libraries. 257
Figure D.4: Concomitant Fe(III) reduction (left) and CFU counts (right) for RBS-optimized *mtrC* (*S. oneidensis* Δ*mtrC*Δ*omcA*Δ*mtrF*+pCD24r1), *mtrA* (*S. oneidensis* Δ*mtrA*+pCD25r0), and *cymA* (*S. oneidensis* Δ*cymA*+pCD26r4) constructs. 258
Figure D.5: Early timescale Fe(III) reduction by the *mtrC* construct (*S. oneidensis* Δ*mtrC*Δ*omcA*Δ*mtrF*+pCD24r1). 259

Figure D.6: Fe(III) reduction by each Buffer gate strain background carrying the empty Buffer gate plasmid (pCD8). 260
Figure D.7: Heme staining of IPTG-induced EET gene expression constructs. 261
Figure D.7: Heme staining of IPTG-induced EET gene expression constructs. 262
Figure D.8: Buffer gate response functions under dynamic expression for *cymA*, *mtrA*, and *mtrC* constructs using Monod and polynomial parameters. 263
Figure D.8: Buffer gate response functions under dynamic expression for *cymA*, *mtrA*, and *mtrC* constructs using Monod and polynomial parameters. 264
Figure D.9: NOT gate empty vector controls with MR-1 and knockout strains. 265
Figure D.10: Dynamic NOT gate activity for *mtrC* construct with 0 and 40 mM sodium fumarate. 266
Figure D.11: Gene circuit maps for the empty, *sfgfp*, *cymA*, *mtrA*, and *mtrC* Buffer gate plasmids. 267
Figure D.11: Gene circuit maps for the empty, *sfgfp*, *cymA*, *mtrA*, and *mtrC* Buffer gate plasmids. 268
Figure D.12: Gene circuit maps for the empty, *cymA*, and *mtrC* NOT gate plasmids. ... 269
Figure D.13: Raw kinetic data and replicates for main text Figure 5.4..... 270
Figure D.13: Raw kinetic data and replicates for main text Figure 5.4..... 271
Figure D.13: Raw kinetic data and replicates for main text Figure 5.4..... 272
Figure D.13: Raw kinetic data and replicates for main text Figure 5.4..... 273
Figure E.1: ^{1}H-NMR spectrum of 65% methacrylated hyaluronic acid macromer dissolved in D_2O after synthesis, dialysis, and lyophilization..... 278

Figure E.2: Strain and frequency sweeps of MeHA hydrogels crosslinked by *S. oneidensis* MR-1 at standard conditions (OD_{600} = 0.2 cells, 3 wt.% MeHA65, 10 μM Cu-TPMA, 500 μM HEBIB, 20 mM lactate, 40 mM fumarate) to determine storage modulus (G', closed circles) and loss modulus (G'', open circles) for *n* = 3 biological replicates. 279

Figure E.3: Storage modulus (G', filled circles) and loss modulus (G'', open circles) of hydrogels crosslinked by *S. oneidensis* MR-1 at standard conditions in either aerobic or anaerobic environments. 280

Figure E.4: *In situ* rheology showing G' (filled circles) and G'' (open circles) of MeHA65 gels synthesized using 500 μM lithium phenyl-2,4,6-trimethylbenzoylphosphinate (LAP) as a photoinitiator with 365 nm light at 10 mW/cm^2 laser intensity. 281

Data are reported as the mean ± SD of *n* = 3 gels. 281

Figure E.5: *In situ* rheology showing G' and G'' of non-functionalized HA solutions containing all crosslinking components and either MR-1 (left) or *E. coli* MG1655 (right). 281

Figure E.6: Methacrylate functional group conversion as determined by ^{1}H-NMR spectroscopy after enzymatically degrading MeHA hydrogels with hyaluronidase. 282

Figure E.7: Rheological frequency sweeps for end-point measurements in Fig. 6.2. G' (filled circles) and G'' (open circles) for *n* = 3 biological replicates. 283

Figure E.8: *In situ* G' measurement of MeHA65 gels synthesized using varying concentrations of poly(ethylene glycol) bis(2-bromoisobutyrate) ($M_{n,avg}$ = 700 g/mol, PEGBBiB). HEBiB, the initiator for standard gelation conditions, is included for comparison. 284
Figure E.9: Storage modulus for MeHA hydrogels crosslinked at standard conditions for 2 hours with varying degrees of methacrylate functionalization of the HA backbone. 284
Figure E.10: Viability analysis 5 days after crosslinking as determined by the BacLight Live/Dead stain. Cells are almost completely viable (green) as opposed to non-viable (red). 285
Figure E.11: Cells can be recovered after crosslinking to synthesize new gels. 285
Figure E.12: Bacteria do not appreciably escape the gels after synthesis. OD_{600} measurements of swelling media (left) after washing gels 3x in PBS and allowing to swell in 1 mL PBS for varying lengths of time. 286
Figure E.13: Fluorescence microscopy images of 1000 μM IPTG induced MR-1 and Δ*mtrC*Δ*omcA*Δ*mtrF* strains show swimming and convective movement over 5 seconds. 287
Figure E.13: Fluorescence microscopy images of 1000 μM IPTG induced MR-1 and Δ*mtrC*Δ*omcA*Δ*mtrF* strains show swimming and convective movement over 5 seconds. 288
Figure E.14: Average cell displacement within a non-functionalized 3 wt.% HA solution as measured by microscopy over 10 s time-lapses at 0 and 2 hours. 288

Figure E.15: sfGFP fluorescence demonstrates metabolic activity for extended time periods after crosslinking. 289
Figure E.15: sfGFP fluorescence demonstrates metabolic activity for extended time periods after crosslinking. 290
Figure E.16: Rheological frequency sweeps for end-point measurements in Fig. 6.3. G' (filled circles) and G'' (open circles) for individual replicates. 291
Figure E.17: Gene circuit maps for both the *sfgfp* (top, pCD7sfGFP) and *mtrC* (bottom, pCD24r1) expression vectors. 292
Figure E.18: Plasmid maps for all plasmids used in this study. Terminator sequences are depicted as red, *lacI* and $P_{tacsymO}$ as blue, *sfgfp* as green, and *mtrC* as orange. 293
Figure E.19: Heme-stained SDS-PAGE gel of uninduced (0 μM IPTG) and induced (1000 μM IPTG) *S. oneidensis* strains. 294
Figure E.20: Reduction of Fe(III)-citrate over 2 hours by *S. oneidensis* Δ*mtrC*Δ*omcA*Δ*mtrF* carrying either pCD24r1 (+*mtrC*) or pCD8 (+empty). 295
Figure E.21: Dynamic range of storage modulus response function changes with time. 296

Chapter 1: Background and Motivations

1.1 Introduction

Biotechnological innovation has accelerated with the development of improved methods for controlling cellular activities. Through targeted genetic changes that alter the expression and activity of enzymes and other functional proteins, microorganisms have been modified to generate a diverse array of chemical products, including pharmaceuticals[1–4], fuels[5–8], and other industrially relevant compounds[9–11]. More recently, these techniques have been applied to direct complex behavior of single and multicellular organisms in medical and agricultural settings[12–15]. Progress in the fields of metabolic engineering and synthetic biology have been essential for these advances. Through development of precise genome modification tools[16–18], synthetic gene regulations[19–21], non-natural biomolecules[22–25], and abstraction of biological networks into modular components[26], the programmability of living systems has substantially increased. Collectively, these disciplines and techniques encompass a diversity of bioengineering workflows that can be leveraged to address technological and societal problems using DNA, proteins, and cells.

Despite these advances, the use of engineered biology has been predominantly restricted to processes and products with clear biological origin or that are organic in nature[27,28]. Common chassis organisms, such as *Escherichia coli* and *Saccharomyces cerevisiae*, are generally limited to manipulating compounds composed of carbon, hydrogen, oxygen, nitrogen, phosphorous, and sulfur[29,30] – a small fraction of chemical elements on the periodic table. Consequently, technologies involving transition-metal elements and inorganic compounds, such as electronics and structural materials, typically do not integrate living components as a part of their fabrication or functioning[31,32]. Moreover, the reaction space available to engineered biological systems is, at present, smaller than what is controllable by synthetic chemistry methods (i.e., designer nanomaterial synthesis and chemical bond formation)[33,34]. These and many other non-biological fields could benefit from genetically-encoded sensing, computation, and

actuation at the molecular level. Engineered biotic-abiotic interfaces could endow next-generation technologies (e.g., environmental remodeling/terraforming, solar energy capture/storage)[35–38] with biological programmability, responsiveness, dynamism, and potentially evolvability. Since significant knowledge gaps have kept bioengineering as a relatively separate discipline, there is an unmet need to develop tunable genotype-phenotype relationships that can precisely control inorganic or traditionally "abiotic" reactions.

While there are several examples of engineered biomolecules and microorganisms that participate in abiotic or inorganic reactions[32,39–41], there is a lack of universality to how they can be applied. Many of these systems rely upon specific reduction/oxidation (redox) reactions carried out by expressed proteins[42] or binding of functional biomolecules to target inorganic surfaces[43,44]. Although these examples provide genotype-phenotype linkages that can be manipulated, each technology is limited to controlling a small set of inorganic reactions and products. Additionally, most of these methods lack direct connection to other well-studied and controllable cellular processes, such as growth and carbon metabolism[45–47]. Despite the relative paucity of manmade examples, nature is brimming with inorganic transformations that are controlled by genetics and metabolism. From the length scale of bones and seashells[48,49] to the nanosized biogeochemical transformations of bacteria and archaea[50], there is a wealth of naturally occurring pathways that may be co-opted to bioengineer inorganic and abiotic technologies. However, domestication of these pathways and microorganisms has been a significant bottleneck to their implementation[51,52]. This dissertation proposes that a specialized respiratory pathway of electroactive bacteria, known as extracellular electron transfer (EET), may provide a tractable and universal modality to genetically control inorganic/abiotic technologies and potentially any biocompatible process that is underpinned by redox chemistry.

1.2 Extracellular electron transfer (EET) Connects Genetics and Metabolism with Redox Transformations

Respiration is a metabolic process that is critical to life on earth[53,54]. In brief, respiratory pathways enable cells to conserve chemical energy through transfer of electrons from donor molecules (e.g., sugars, organic acids, hydrogen) onto exogenous terminal electron acceptors. Key to enabling this metabolism are electron transfer pathways comprised of redox-active proteins (e.g., cytochromes, iron-sulfur proteins) and metabolites (e.g., quinones, $NADH/^{+}$)[55]. While much of life, including humans, rely upon molecular oxygen as an environmentally abundant and thermodynamically favorable electron sink, many microorganisms are found in ecological niches with little or no oxygen. In the absence of fermentation processes (which rely on internal electron acceptor metabolites), these anaerobic microbes contain pathways that transfer respiratory electrons onto alternative environmental acceptors, including organic (e.g., fumarate, DMSO) and inorganic (e.g., oxidized metals, nitrate, sulfate) species[56,57]. Since redox interactions underpin many inorganic and abiotic technologies, anaerobic respiratory pathways offer a wealth of biological mechanisms that can be mined for biotechnology purposes.

The metal reduction capabilities of certain anaerobic respiration pathways are particularly noteworthy, as metal reduction is ubiquitous in electronics and electrochemistry[58,59]. Several technologically relevant metals can serve as biological electron acceptors, including Fe, Mn, Cr, Co, U, Ag, Au, Pd, Pt[39,60,61]. Remarkably, many microbes possess anaerobic pathways that transfer electrons onto insoluble metal acceptors located outside of the cell, such as iron and manganese oxides[62,63]. Soluble and insoluble metal reduction occurs via two general mechanisms: (1) diffusion-reaction of cell-generated soluble redox shuttles and (2) direct electron transfer by redox-active proteins[64]. Although linkage of metal reduction to respiratory energy conservation is not obligatory depending on the specific pathway/microbe[65,66], the phenomena is collectively termed "extracellular electron transfer (EET)" (Figure 1.1). Additionally, microbes that exchange electrons with external substrates are described as "electroactive". Electroactive microbes are found within many ecosystems, including aquatic/oceanic sediments[62,63,67], plant

rhizospheres[68,69], and more recently within human oral/gut microbiota[70,71]. Moreover, microbial electroactivity is a major driver of global biogeochemical processes, such as environmental cycling of iron and manganese[72–74]. Given their diverse metal substrate range, connection to cellular growth/metabolism, and genetic underpinnings, EET pathways are attractive for interfacing bioengineering with inorganic and abiotic applications.

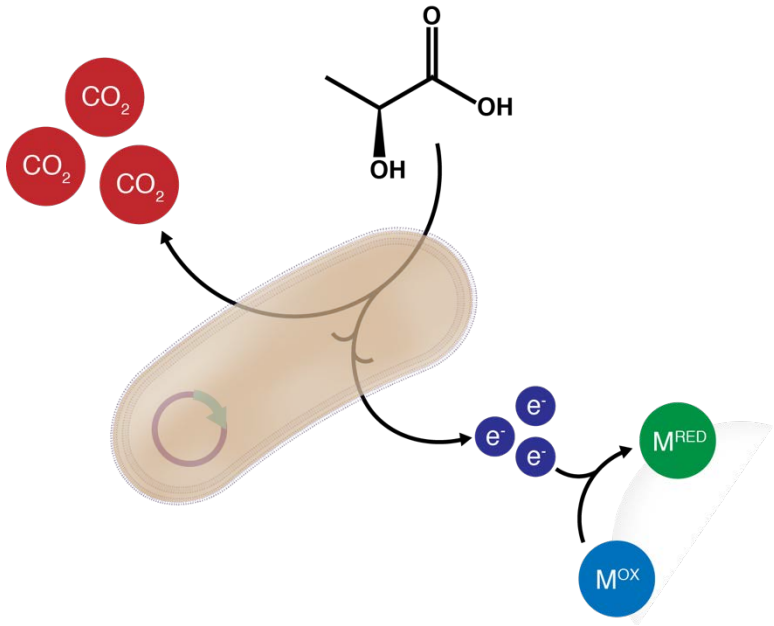

Figure 1.1: General model of extracellular electron transfer (EET) as a bacterial respiration mechanism.

Electrons obtained from carbon source oxidation (example shown is lactate) are transferred to oxidized metal species (M^{OX}), which converts them to a reduced state (M^{RED}).

1.3 *Shewanella oneidensis*: A Model Organism to Study and Apply EET

1.3.1 General Information on *Shewanella oneidensis*

Shewanella oneidensis MR-1 is arguably the most prominent model electroactive microbe, as the identities and functioning of its EET proteins/metabolites are well-studied[61,75]. *S. oneidensis* MR-1 is a gram-negative bacterium isolated from Lake Oneida, NY and was the first isolated strain to exhibit coupling of carbon oxidation and growth to

reduction of Mn(IV) oxides[62]. Many features of *S. oneidensis* MR-1 make it ideal for laboratory study and biotechnology applications, such as its ability to grow aerobically and anaerobically, its ease of culture in minimal and rich media, and its rapid doubling time (about 45 minutes when grown aerobically in LB broth)[60,76]. Notably, we can genetically modify the bacterium using techniques employed for the more domesticated workhorse, *E. coli*. This includes electroporation-based transformation, maintenance of multi-copy plasmids, and homologous recombination-based protocols for deleting/inserting DNA in the genome[77–80]. Together, these traits have enabled facile dissection and application of EET pathways in *S. oneidensis*.

Since its isolation over thirty year ago, a mechanistic model of electron transfer in *S. oneidensis* MR-1 has emerged, which connects movement of electrons from cytoplasmic carbon metabolism, across the inner and outer membrane layers, the periplasm, and into the extracellular space[81–88]. While *S. oneidensis* respires onto many organic and inorganic electron acceptors and accomplishes this using different sets of respiratory proteins/metabolites, one relatively small pathway (hereafter referred to as CymA/MtrCAB) is utilized for EET to several soluble and insoluble metals, including Fe and Mn[89]. Since this pathway connects genetics and metabolism with extracellular processes, understanding the flow of electrons through this pathway and the details of electron transfer can inform biotechnology applications that leverage *S. oneidensis* and EET[90,91].

1.3.2 Route of Electrons through the CymA/MtrCAB Pathway

Based on a present understanding, the CymA/MtrCAB model for electron transfer will be now be described (Figure 1.2). First, electrons are directly or indirectly (e.g., via NADH) transferred into the quinone pool by carbon-catabolizing enzymes[92–97]. *S. oneidensis* MR-1 cannot metabolize many sugars but can use simple organic acids (e.g., lactate, pyruvate) as carbon sources[98]. Subsequently, reduced quinones (quinols) are oxidized by a tetraheme *c*-type cytochrome that is periplasmically-facing and localized to the inner membrane, termed CymA[82,99,100]. For CymA and other multiheme *c*-type

cytochromes in *S. oneidensis*, intra- and inter-protein electron transfer occurs via 'electron hopping' between heme-coordinated Fe ions[101–103]. CymA largely acts as a respiratory hub in *Shewanella* and related species, since it is able to direct quinone-derived electrons into several respiratory pathways (e.g., nitrate, fumarate, DMSO)[82,104]. Next, electrons from CymA are transferred onto periplasmic carriers, including fumarate reductase (FccA) and small tetraheme cytochrome (STC)[105,106], and eventually end up on the periplasmic decaheme *c*-type cytochrome, MtrA[107]. MtrA is one of three proteins that comprise an outer membrane-spanning complex, MtrCAB, which is central to EET-based reduction of insoluble metals located outside of the cell[86,88,103,108]. MtrC is also a decaheme *c*-type cytochrome that is extracellularly localized on the outer membrane[83,109,110]. MtrB is an outer membrane β-barrel protein that acts as a sheath for MtrA and MtrC, thereby enabling the two proteins to exchange electrons with each other[84,88,103,108]. For many soluble and insoluble substrates, MtrC is the terminal reductase of *S. oneidensis* that deposits electrons into the extracellular space[111].

It should be noted that *S. oneidensis* expresses a paralog of the MtrCAB conduit, termed MtrDEF[86]. In this outer membrane-spanning protein complex, MtrD is a periplasmic decaheme *c*-type cytochrome (paralog of MtrA), MtrE is an outer membrane β-barrel protein (paralog of MtrB), and MtrF is an extracellular decaheme *c*-type cytochrome (paralog of MtrC). Although electron flow through this conduit is similar to MtrCAB and the individual proteins can exhibit functional overlap with their MtrCAB counterparts, the MtrDEF conduit is generally less involved in EET when MtrCAB is present[111]. Additionally, another extracellular decaheme *c*-type cytochrome, OmcA, associates with MtrC and can participate in EET reactions[108,109,112,113]. As will be further discussed in Chapters 5 and 6, *S. oneidensis* strains lacking MtrF and OmcA exhibit lower levels of background EET activity, but MtrC remains the master controller of electron flux.

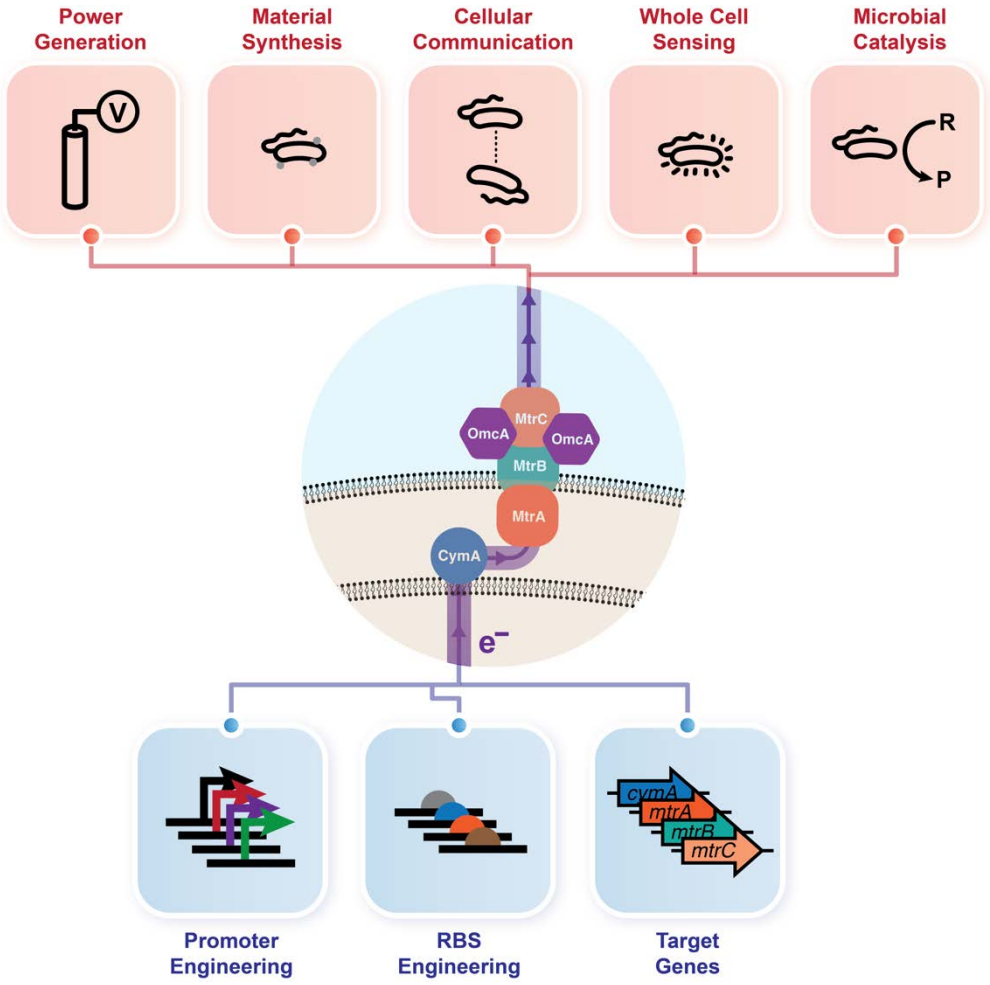

Figure 1.2: Model of CymA/MtrCAB pathway in *Shewanella oneidensis* MR-1.

Extracellular electron transfer flux through this pathway (purple arrow) enables genetic control (blue boxes) over inorganic/abiotic phenotypes (orange boxes).

1.3.3 Mechanisms of Electron Transfer onto Terminal Acceptors

Electron transfer from MtrC onto terminal acceptors occurs through a combination of direct and molecular shuttling-based mechanisms[114]. Direct electron transfer involves tunneling of electrons from MtrC hemes onto acceptor substrates, without any intermediate redox carriers[115,116]. Alternatively, shuttling mechanisms involve MtrC-mediated reduction of soluble cell-secreted redox-active molecules: riboflavin (RF) and flavin mononucleotide (FMN)[117]. Cytochrome-reduced flavins diffuse away from the cell, deposit electrons onto

the acceptor substrate, and can be recycled by returning to the cell to receive further electrons. A third hybrid mechanism involves flavins acting as redox-active cofactors that bind to MtrC and other outer membrane cytochromes[118,119]. In this mechanism, reduced flavins are capable of acting as radical-carrying semiquinones, which is hypothesized to increase the thermodynamic favorability of electron transfer. Between these two mechanisms, direct reduction appears to play a larger role in reduction of soluble substrates, such as chelated Fe(III)[117]. In contrast, flavin-based mechanisms dominate during reduction of insoluble substrates, such as metal oxides and electrodes, and have been measured as contributing 75-80% of EET flux[117,118,120]. Though the exact nature of these mechanisms is still a topic of debate in the EET research community, combinations of these processes are speculated to be occurring simultaneously.

Knowledge of the protein-to-protein route of electron flow and mechanisms of electron transfer provides handles to alter EET activity in *S. oneidensis*. Strains carrying genetic knockouts, overexpression, and mutagenesis with the CymA/MtrCAB proteins have been the primary means to study EET and understand genotype-phenotype relationships[121]. As will be discussed in the subsequent sections, these same manipulations can be used to engineer EET activity and optimize cellular performance in target applications.

1.4. Applications and Limitations of *S. oneidensis* EET

1.4.1 Power Generation

EET by *S. oneidensis* and other electroactive microbes has been applied in several redox-based technologies, most notably power generation[58]. Early electrochemical analyses of *Shewanella* spp. determined that anodically poised electrodes could support bacterial growth when supplied as the sole electron acceptor[122,123]. This motivated the development of microbial fuel cell (MFC) setups, where *S. oneidensis*-based oxidation of carbon sources (i.e., fuel) is coupled to EET-driven electricity generation[124,125]. Although current output from these systems is relatively low (milliampere range), the ability to

convert wastewater pollutants or biomass substrates to electricity has garnered much attention as a platform for sustainable energy. Additionally, the current output of these devices is appropriate for sensors or other microelectronic devices and has been applied to monitor environmental settings[67,126–129]. Consequently, engineering *S. oneidensis*-based bioelectrochemical systems for increased power generation[130,131], wider substrate utilization[132,133], and genetic responsiveness[134–136] is an active area of research.

MFC optimization efforts typically seek to develop bacterial strains with improved EET flux or examine different materials for the anode/cathode. Electroactive bacteria are able to colonize electrodes and transfer electrons through direct and shuttling mechanisms[137,138]. Accordingly, *S. oneidensis* strains have been engineered to enhance biofilm growth and anode colonization[139,140], increase EET flux through the CymA/MtrCAB pathway[131,141], and increase secretion of electrode-reducing flavins[130]. On the material side, materials with varying electrochemical properties have been tested to increase microbial colonization and electron transfer kinetics. Carbon-based anodes, such as graphite, are inexpensive and frequently employed to culture electroactive microbes[59]. Choice of carbon-based materials can alter microbially-accessible surface area on electrodes (e.g., carbon cloth) and increase current output[142]. Anode materials composed of different elements (e.g., gold) or metal oxides may also increase power generation[143–145]. However, for each biology and material chemistry optimization, tradeoffs occur due to bidirectional influence between EET processes/cell growth and functioning of the anode material[139,146]. This feedback makes rational design of MFC performance challenging. To address this and further improve bioelectrochemical systems, genetic factors and material platforms that increase the tunability of biotic-abiotic interface need to be identified.

1.4.2 Nanomaterials Synthesis

Nanomaterials contain structural length scales within 1 to 100 nanometers and often possess distinct mechanical, optical, and chemical properties[147]. To expand the utility of nanotechnology in sensors, medical devices/therapies, electronics, and manufacturing, there has been significant interest in coupling biological programmability and

responsiveness with the synthesis/functioning of inorganic nanomaterials[148–152]. Functional metal nanoparticles (e.g., catalysts) can be synthesized through the transfer of electrons to metal ions, and microbial electroactivity has been leveraged to direct this synthesis[39]. Examples of nanoparticles formed by *S. oneidensis* EET include Au, Ag, Pd, Pt, and Cu[153–159]. These nanoparticles can catalyze environmentally- and industrially-relevant reactions, such as carbon-carbon bond formation and dehalogenations[156,160,161].

As with traditional nanoparticle synthesis, bacterial reduction rate and passivation of nanoparticles during their formation influences their final morphology[162] and, consequently, their catalytic capabilities[163,164]. In *S. oneidensis*, the identity of nanoparticle-forming reductases is not pinned down to any one protein or electron transfer pathway. With UO_2 particles, the MtrCAB conduit is involved[165], while other metal nanoparticles are influenced by intracellular reductases (e.g., CymA, fumarate reductase, hydrogenases)[166–168]. These and other studies have examined the effect of bacterial genetics on metal ion reduction rate[169,170], but it is not clear how genetic factors govern particle properties (e.g., morphology, crystallinity, size). Pinpointing the identity and effect of these genetic factors in *S. oneidensis* is critical for enabling designer formation of metal nanoparticles and potentially integrating genetic computation with more complex inorganic processes, such as biopatterning electronics[40].

1.4.3 Bioremediation and Bioelectrosynthesis

S. oneidensis EET activity can facilitate catalytic transformations that involve redox chemistry. Many environmental pollutants are redox-active, and their degradation or detoxification occurs through reductive mechanisms[171]. Accordingly, *S. oneidensis* and other electroactive bacteria have been employed in bioremediation schemes for compounds such as azo dyes[172–175], carcinogenic metal species[176–178], and organohalides[156,179,180]. EET-based reduction can transform these pollutants into inert byproducts or aid in their

separation/collection. As with nanoparticle synthesis, the contribution of the MtrCAB conduit largely depends on the target pollutant. For example, genetic knockout studies have demonstrated that pollutant degradation mechanisms and efficacy can be highly variable between dye compounds[173,181,182]. Sorbent or catalytically-active materials are also used in conjunction with *Shewanella* spp., since they can aid in otherwise recalcitrant bioremediation treatments via synergistic interactions with the bacteria[183,184]. However, many of these systems require harsh chemical regeneration steps and can be challenging to biologically optimize. Taken together, these performance limitations highlight our limited understanding of pollutant interactions with EET components and the *S. oneidensis*-abiotic material interface. Developing a more detailed molecular understanding could guide development of *S. oneidensis* strains optimized for pollutant degradation and inform the design of improved bio-material treatment platforms.

In addition to directly catalyzing chemical reactions, EET activity can be used to control intracellular metabolic transformations. Metabolic engineering seeks to rewire cellular metabolism, through knockout or overexpression of target proteins, with the goal of increasing cellular production of target compounds[27]. However, generation of certain metabolic products is thermodynamically unfavorable or requires significant rewiring of intracellular redox metabolite pools (e.g., $NADH/^{+}$)[185–187]. To this end, reversal of EET activity via *S. oneidensis* uptake of externally-derived electrons can drive these challenging metabolic reactions in a process termed bioelectrosynthesis[188]. The MtrCAB conduit is able to receive electrons from cathodically poised electrodes and inward-bound electrons can reduce intracellular metabolites, such as NAD^{+}, or bias the equilibrium of redox reactions[189–191]. While only a handful of chemical biosyntheses have been demonstrated using this method (e.g., succinate, 2,3-butanediol), the technology offers promise for directly connecting external electrical energy with biochemical production and cellular metabolism.

Collectively, these applications represent the major technology thrusts that leverage EET activity by *S. oneidensis*. However, at present, EET-based products (e.g., nanoparticles, produced metabolites) and processes (e.g., MFC operation, bioremediation

treatments) are primarily restricted to research projects. Only a few systems have been applied outside of research settings or commercialized[91]. Improvements in scalability, homogeneity, and yield will be necessary to increase the commercial feasibility of EET technologies[31,32]. A better understanding for how *S. oneidensis* EET genetic factors (i.e., genotype) govern application outputs (phenotype) should accelerate these developments.

1.5 Genetic Control of *S. oneidensis* EET Activity

1.5.1 Background and Motivations

Understanding genotype-phenotype relationships in EET-based applications could be accomplished through increased genetic control over EET activity by *S. oneidensis*. Novel strains with augmented EET flux, defined spatiotemporal dynamics in EET activity, and increased responsiveness to environmental/process stimuli, would allow for the magnitude and timing of EET to be dialed based on application needs. Developing this level of control may also enable EET to find use in new technologies and technical disciplines, where a lack of precision in EET flux has stifled its prior integration (e.g., patterned materials synthesis)[13,32,192,193].

To enable designer control over EET activity in *S. oneidensis*, there has been much interest in adapting tools from the fields of metabolic engineering and synthetic biology. In metabolic engineering, the flux of cellular metabolites is manipulated through model-guided knockout and expression of target proteins, which enables increased generation of desired metabolic products[27,194]. Growth of this discipline has led to greater understanding of fundamental biological processes[195,196] and enabled widespread rewiring of metabolisms for technological benefit[1–4]. In a similar vein, synthetic biology has sought to rewire cellular functioning by applying design-driven principles of mathematical modeling[197,198], electrical engineering[19,20], and computer science[26,199,200]. Microbes engineered by these modalities can carry out complex sensing[201–203], computation[21,204], and actuation functions[12,205,206], as well as give rise to emergent phenomena, such as spatiotemporal patterns and dynamics[202,207–209].

These techniques can control EET activity in *S. oneidensis* by altering the expression of proteins and metabolites that are part of the CymA/MtrCAB pathway. By changing expression levels of these factors, the flux of electrons through the pathway can be toggled[210]. Expression of target EET genes can also be tied to more complex genetic circuits, thereby enabling stimuli-responsiveness and computation via logical operations[211]. Major developments in controlling EET flux by *S. oneidenis* will now be briefly reviewed and current limitations/knowledge gaps will be highlighted.

1.5.2 CymA/MtrCAB Expression

Since the CymA/MtrCAB proteins of *S. oneidensis* are necessary for EET flux to many metals and extracellular substrates, they are frequent targets in genetic engineering efforts. In the *S. oneidensis* MR-1 genome, MtrCAB are encoded in a single operon that is natively regulated by anaerobic sensing machinery (i.e., cAMP Receptor Protein)[212]. Genomic deletion of single genes or the entire operon leads to strains with drastic loss of EET capabilities[86,111]. These knockout strains can be complemented with plasmids encoding the lost proteins to facilitate engineering control over EET activity. For example, circuits driven by small-molecule inducers, such as IPTG or AHL, have been used for plasmid-based expression of Mtr proteins[129,134,213,214]. Alternatively, the native promoter of the genomic *mtrCAB* operon can be replaced with inducible variants to alter pathway expression[129,136]. Recently, CRISPR/Cas9-based tools have become available for use in *S. oneidensis*, which has expedited genome engineering and enabled plasmid-based regulation of genomically-encoded proteins[79]. Specifically, CRISPRi constructs have been used to multiplex knock down of *mtrC*, *mtrA*, *mtrB*, and other ancillary EET proteins[215,216]. To a lesser extent, CymA has also been leveraged as an engineering target to control EET activity[141,166]. While its small size (CymA ~20 kDa) and inner membrane localization offer engineering benefits[108], its centrality to many respiratory processes and the presence of functional paralogs (e.g., NapC) has decreased CymA targeting over the more 'insulated' MtrCAB conduit[82,217]. Nonetheless, these systems validate that genetic control over CymA/MtrCAB expression is a practical means to alter EET activity.

1.5.3 Metabolic Engineering of EET

In addition to altering expression of electron-carrying proteins in *S. oneidensis*, key metabolites provide a handle to tune EET. In the early steps of cellular electron flux generation, breakdown of carbon sources yields reduction of inner membrane quinones[92–96]. Since *S. oneidensis* MR-1 metabolizes relatively few carbon sources, strain engineering has increased substrate diversity and enabled electrons to be derived from catabolized sugars, such as xylose and glucose[132,133,218–221]. Additionally, bioengineers have sought to boost cytoplasmic quinone reduction via NADH-mediated mechanisms. *S. oneidensis* strains possessing elevated $NADH/^{+}$ biosynthesis or processing exhibit higher EET flux[131,222,223]. Alternatively, pathways that produce EET flux-draining metabolites, such as molecular hydrogen, can be knocked down to increase electron flow through the MtrCAB conduit[216,224]. Soluble flavins can also increase EET activity under certain conditions, particularly when *S. oneidensis* are cultured with insoluble substrates. Accordingly, strains have been engineered to increase flavin levels through heterologous biosynthetic pathways[130,225]. These various metabolite-based strategies illustrate how EET flux by *S. oneidensis* can be metabolically engineered akin to other desired cellular products.

1.5.3 Limitations and Challenges with Current Genetic Tools

Despite the genetic systems that are available to control CymA/MtrCAB expression or manipulate EET metabolites, control over EET activity remains substantially limited relative to more modern synthetic biology systems. Whereas most EET engineering efforts seek to maximize current output[226], there are relatively few engineered EET circuits in *S. oneidensis* or other electroactive microbes that exhibit dynamics or spatiotemporal patterns in electron flux. Workflows that are commonplace in synthetic biology, such as generating inducer-output response functions[227], optimizing inducible dynamic range[228,229], and construction of modular transcriptional circuit layers[19,21], are largely unexamined in the context of EET. This lack of genetic control is, in part, due to limited understanding for how individual EET genes influence the magnitude and timing of EET activity.

Although sets of promoters and transcriptional regulators have been used to test the effect of key *S. oneidensis* EET genes, choice of parameterization for EET activity is not standardized and highly variable between studies[129,136,230]. Whereas the relative expression unit (REU) fluorescence measurement has become a convention when quantifying transcriptional inputs/outputs for fluorescent protein-based circuits[231], adoption of similar standards is not as simple given the dynamic nature of EET activity. The catalytic activity of EET proteins (i.e., electron transfer) is intimately tied to cell growth, and EET product concentrations (e.g., Fe(II) levels) are changing with time[232]. Accordingly, high throughput EET assays and improved mathematical models are needed to connect gene expression dynamics[202,209,233], cell growth[45,234], and EET activity[232] and obtain model-fitted rate constants from kinetic data. Adopting these standards will likely enable more systematic characterization of individual EET genes/circuits and permit forward engineering of microbial electroactivity. With this foundation, it may be possible to adapt previously designed genetic sensing/computation circuits from *E. coli* or other chassis organisms[211], and dynamically control the aforementioned applications using *S. oneidensis* EET.

1.6 Dissertation Objectives and Overview

Biological engineering is underpinned by human understanding and manipulation of genotype-phenotype relationships. Given the enormous potential of EET technologies for controlling redox reactions, there is significant motivation to (1) improve our understanding of EET genotype-phenotype relationships and (2) develop improved genetic methods for tuning EET flux in the chassis organism *S. oneidensis*. This dissertation seeks to meet these two objectives and will describe new processes, genetic tools, and material platforms that simplify and expand our ability to interface with *S. oneidensis* EET. Specifically, in Chapters 2-4 we report the discovery of novel EET genotype-phenotype relationships involving materials synthesis and transformation. In Chapter 5-6, we develop new genetic tools that can be used to control EET flux and program material formation. Across all chapters, our unifying hypothesis is that the *S. oneidensis* CymA/MtrCAB pathway acts as a master controller of EET activity (Figure 1.2).

In Chapter 2, a materials synthesis called atom transfer radical polymerization (ATRP) will be described, which leverages *S. oneidensis* EET flux to control formation of synthetic organic polymers. Whereas this polymerization reaction is commonplace in abiotic synthetic chemistry, we present the first demonstration that EET flux can place the reaction under strict cellular control. We examine genetic and metabolic factors of *S. oneidensis* EET that tune polymerization rate and highlight the potential for expanding the reaction space available to biological engineers.

In Chapter 3, we study the genetic and metabolic factors that govern palladium nanoparticle biosynthesis by *S. oneidensis* EET. Specifically, we examine how nanoparticle properties are affected by expression of the outer membrane cytochrome, MtrC, and soluble flavin molecules. Our results demonstrate that particle size and cellular localization can be controlled at the genetic level, which may guide synthesis of bio-Pd catalysts and materials using synthetic biology strategies.

In Chapter 4, an iron-containing material, called metal-organic frameworks, are tested as a new EET respiratory substrate for *S. oneidensis*. We show that this highly porous and chemically tunable material serves as a robust platform to culture the bacterium. Additionally, the bacteria-framework system is able to synergistically remediate chromium from solution. These results suggest that metal-organic frameworks may offer a more tunable biotic-abiotic interface for EET activity relative to common material substrates, such as metal oxides.

In Chapter 5, we develop a synthetic biology framework to control EET activity in *S. oneidensis* using transcriptional logic gates. To characterize engineered genetic circuits, we report a high throughput Fe(III) reduction assay and a kinetic model that relates gene expression to EET flux. A library of plasmid-expressed EET genes are also designed, where expression is regulated by computationally-predicted ribosome binding sites and inducible Buffer and NOT gate architectures. Response functions from plasmid-transformed strains demonstrate that EET activity is programmable at the transcription/translation level and suggest that more complex sensing/computation circuits could be adapted to control EET in *S. oneidensis.*

In Chapter 6, we build upon the ATRP chemistry developed in Chapter 2 and demonstrate that *S. oneidensis* EET can control formation of a macroscopic soft material – semisynthetic hydrogels. Notably, hydrogel cross-linking and material stiffness is controlled by the expression of *S. oneidensis* EET proteins. We demonstrate that one of the EET genetic circuits developed in Chapter 5 regulates gel formation/stiffness based on the presence of an inducing molecule. These results illustrate how EET flux by *S. oneidensis* can govern a materials synthesis and suggest that macroscopic material properties are programmable using genetic circuits.

In Chapter 7, we summarize the major conclusions of Chapters 2-6 and propose future research using *S. oneidensis* EET that builds off of our previous work. Taken together, this dissertation reports new concepts and tools for engineering *S. oneidensis* EET activity. The findings described herein may expand biological control over existing applications in bio- and nano-technology and propel EET into new fields that are governed by redox interactions.

Chapter 2: *Shewanella oneidensis* as a living electrode for controlled radical polymerization[1]

2.1 Chapter Summary

Metabolic engineering has facilitated the production of pharmaceuticals, fuels, and soft materials but is generally limited to optimizing well-defined metabolic pathways. We hypothesized that the reaction space available to metabolic engineering could be expanded by coupling extracellular electron transfer to the performance of an exogenous redox-active metal catalyst. Here we demonstrate that the electroactive bacterium *Shewanella oneidensis* can control the activity of a copper catalyst in atom transfer radical polymerization (ATRP) via extracellular electron transfer. Using *S. oneidensis*, we achieved precise control over the molecular weight and polydispersity of a bioorthogonal polymer while similar organisms, such as *E. coli*, showed no significant activity. We found that catalyst performance was a strong function of bacterial metabolism and specific electron transport proteins, both of which offer potential biological targets for future applications. Overall, our results suggest that manipulating extracellular electron transport pathways may be a general strategy for incorporating organometallic catalysis into the repertoire of metabolically-controlled transformations.

2.2 Introduction

Metabolic engineering has provided alternative production pathways for the synthesis of pharmaceuticals[2], fuels[8], and soft materials by redirecting carbon flux toward specific metabolites[235]. Despite significant progress, the reaction space available for metabolic engineering is still relatively limited when compared to synthetic chemistry[27]. One way to expand the scope of metabolic transformations is to leverage respiratory

[1]Adapted from Fan, G., Dundas, C.M., Graham, A.J., Lynd, N.A., Keitz, B.K. (2018) *Shewanella oneidensis* as a living electrode for controlled radical polymerization. *Proc. Natl. Acad. Sci. U.S.A. 115*(18), 4559-4564. Gang Fan and Christopher M. Dundas contributed equally to this work. Christopher M. Dundas designed the research, performed the experiments, analyzed the results, and wrote the chapter.

electron flux, which can be used for power generation, as in microbial fuel cells[130,236], or inverted to produce metabolites from exogenously-supplied electrons, as in bioelectrosynthesis[189,237]. The flexibility of these applications can be further extended by coupling metabolic transformations to processes that occur independently of the cell, such as nanoparticle photoexcitation or electrocatalytic hydrogen generation[152,238]. However, these advances are still generally limited to native metabolic intermediates and products.

In an effort to expand the power of microbial catalysis, we hypothesized that electron flux from metabolic activity could be adapted to control exogenous, bioorthogonal reactions via extracellular electron transfer to a redox-active metal catalyst. To test our hypothesis, we leveraged the electroactive bacterium *Shewanella oneidensis* MR-1. Similar to other electroactive bacteria[64,121], MR-1 is able to transport electron equivalents over micron distances and has specialized machinery for moving electrons in and out of the cell[239,240]. Under anaerobic conditions, MR-1 consumes lactate, or other small carbon sources, and deposits electrons into redox-active organics, metals, and materials. Given the relatively negative potential of its terminal outer membrane cytochromes (ca. –350 to +50 mV vs. SHE) [37,241], MR-1 is able to reduce a variety of soluble metals including U(VI), Cr(VI), Fe(III), V(III), and Mn (IV), as well as oxides such as hematite, ferrihydrite, and graphene oxide[242,243]. MR-1 can also respire onto electrodes poised at an appropriate potential[124]. Overall, the unique electron transport machinery and genetic tractability of MR-1 has made it a popular organism for use in microbial fuel cells[130,236], bioelectrosynthesis[189,237], and bioremediation[165,244].

To explore if extracellular electron transfer from MR-1 could control the performance of an exogenous metal catalyst, we examined atom-transfer radical polymerization (ATRP). In ATRP, a redox-active metal catalyst reacts with a halogenated initiator to generate a radical that propagates through the addition of monomers or reacts with the newly oxidized catalyst to produce a dormant polymer chain (Figure 2.1a)[245]. The concentration of active radicals and polymerization rate is controlled by the redox equilibrium of the metal catalyst, which can be influenced through the application of an external potential[246–249]. This suggests that an electroactive bacterium with appropriate

redox capabilities, such as MR-1, could control catalysis in a similar manner to an electrode via direct extracellular electron transfer to the metal catalyst[250]. Here we show that MR-1 can activate copper (Cu) catalysts for ATRP and that this mechanism is coupled to bacterial metabolism via specific electron transport proteins. Organisms lacking analogous extracellular electron transport machinery, such as *E. coli*, showed minimal polymerization activity under our conditions. Polymerizations in the presence of MR-1 exhibited rates comparable to other aqueous controlled radical polymerizations and provided narrowly dispersed polymers with controlled molecular weights. Ultimately, our results demonstrate that extracellular electron transport can control redox-based catalysis and suggest that targeting biological electron transport pathways may combine the genetic tunability of metabolic engineering with the mechanism-driven design of organometallic catalysis.

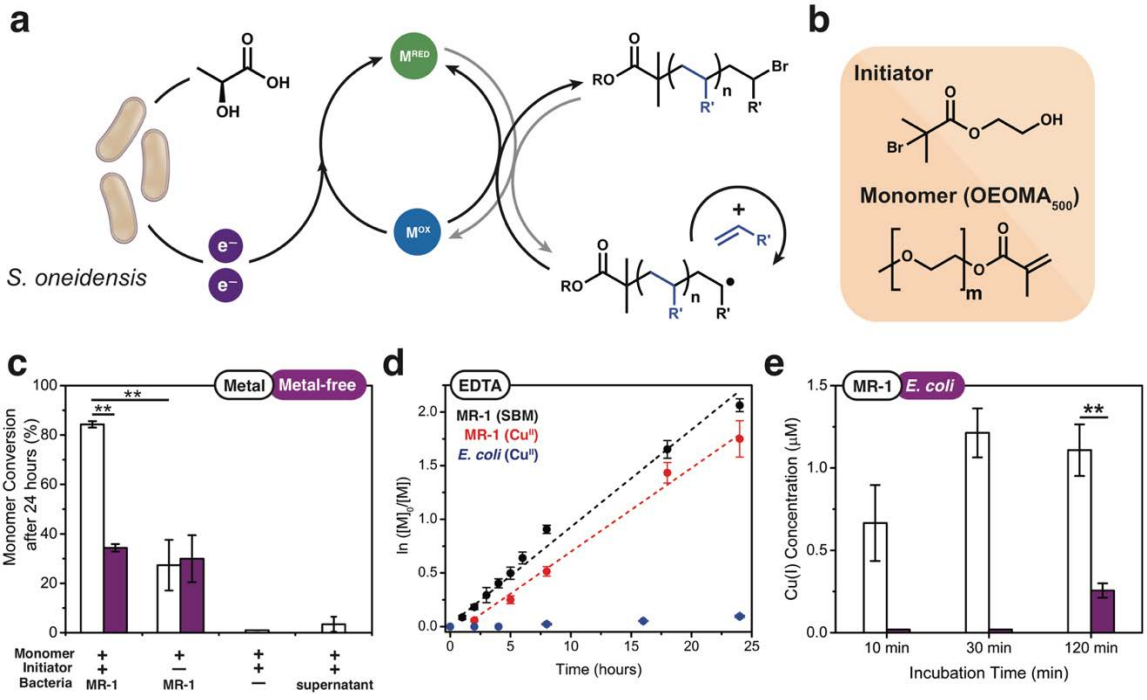

Figure 2.1: *S. oneidensis* enabled atom-transfer radical polymerization (ATRP) and initial polymerization kinetics.

(a) Electron equivalents generated from *S. oneidensis* MR-1 reduce a metal catalyst from an inactive state (M^{OX}) to an active state (M^{RED}). The active catalyst reacts with a halogenated initiator or polymer chain to produce a radical (grey arrow) that can polymerize olefins. The radical can also react with the now-deactivated catalyst (M^{OX}) to form a dormant chain (black arrow, right). (b) ATRP initiator (2-hydroxyethyl 2-bromoisobutyrate, HEBiB) and macromonomer ($OEOMA_{500}$) used in this study. (c) Monomer conversion after 24 hours under various conditions with (white) and without (purple) trace metal mix added to bacterial media. (d) Kinetics of monomer conversion in MR-1 or *E. coli* culture using Cu(II)-EDTA as catalyst (e) Extracellular Cu(II) reduction monitored with the Cu(I) specific fluorescent dye CF4. Data show mean ± S.D. of three independent experiments. **, $P < 0.01$.

2.3 RESULTS

2.3.1 Exogenous Metals and *S. oneidensis* Enable Atom-Transfer Radical Polymerization (ATRP).

An anaerobic reaction mixture containing poly(ethylene glycol) methyl ether methacrylate monomer with M_n = 500 g/mol ($OEOMA_{500}$) and a halogenated initiator was inoculated with stationary-phase MR-1 (anaerobically pregrown with lactate/fumarate) (Figure 2.1b). After 24 hours, the solution became viscous and almost complete conversion of monomer was measured using ^1H NMR spectroscopy. As expected, no polymerization activity was observed under aerobic conditions. Cell-free and MR-1 supernatant controls also showed minimal monomer conversion. Bacterial pregrowth and reaction mixture balance volume were comprised of *Shewanella* basal medium (SBM), which contains ethylenediaminetetraacetic acid (EDTA) and several redox-active metals that could be functioning as catalysts (Table A.1). Reaction mixtures omitting these metals displayed significantly attenuated polymerization activity (Figure 2.1c). Similarly, removal of initiator decreased monomer conversion after 24 hours of MR-1 culture, independently of metal presence. We measured background radical polymerization activity in all reactions containing metabolically-active cells. Contributors to this background polymerization could include bacterially-secreted flavins and outer membrane heme-containing proteins. Flavins can act as radical initiators while heme-containing proteins have previously been used as catalysts for ATRP[251,252]. However, the significant decrease in monomer conversion when exogenous metals were removed from solution suggests that it is primarily extracellular metal ions that act as catalysts. Following the kinetics of the polymerization, we discovered that metals, initiator, and MR-1 were all required to give well-controlled first-order kinetics in $OEOMA_{500}$ conversion, which is indicative of a constant radical concentration (Figure A.1). Foregoing any of these components resulted in decreased monomer conversion and non-first-order polymerization kinetics. Together, these results confirm that exogenous metals and MR-1 are required for the controlled polymerization kinetics that are characteristic of ATRP.

2.3.2 Identification of Cu as a Viable ATRP Catalyst.

Next, we identified the specific metal responsible for polymerization activity. Based on previous studies of ATRP(22), we hypothesized that polymerization activity could be primarily attributed to *Shewanella*-induced reduction of Cu(II) to Cu(I). Indeed, almost complete rescue of polymerization activity was observed when all exogenous metals were removed from the reaction culture except for $CuSO_4 \bullet 5H_2O$ and EDTA (Figure 2.1d). We also briefly explored the activity of other known polymerization catalysts present in SBM. For example, both Fe(III) and Co(III) can be reduced by MR-1 and can serve as catalysts for ATRP and cobalt-mediated radical polymerization respectively[253]. Co(III)-porphyrins can also catalyze the radical-based dehalogenation of C-Cl bonds in the presence of MR-1[250]. We found that both $FeSO_4$ and $Co(NO_3)_2$ yielded polymerization activity above metal-free controls (Figure A.2), but continued with Cu(II/I) since it is the most well-understood and established catalyst for ATRP. Notably, substituting *E. coli* MG1655 for MR-1 under otherwise identical conditions completely abolished polymerization activity with Cu(II/I) as the catalyst (Figure 2.1d). Additionally, we did not observe any significant polymerization activity under several alternative *E. coli* culture conditions. Overall, these results show that Cu(II/I) is an active catalyst for MR-1 enabled ATRP and suggest that the unique electron transport machinery of MR-1 is critical for polymerization activity.

ATRP activity in our system is contingent upon the MR-1 controlled reduction of Cu(II) to Cu(I). Thus, we measured the extracellular concentration of Cu(I) using the Cu(I) specific fluorescent probe Copper Fluor-4 (CF4)[254]. Cultures of MR-1 were incubated with $CuSO_4 \bullet 5H_2O$ and CF4, spun down, and the extracellular concentration of Cu(I) measured via plate reader. Immediate reduction of Cu(II) was observed in the presence of MR-1, whereas *E. coli* controls showed minimal reduction on the same time scale (Figure 2.1e). In eukaryotic systems, incubation with exogenous copper results in a measurable increase in free cytoplasmic Cu(I)[255]. In contrast, bacteria quickly detect and sequester free Cu(I)[256]. The effective concentration of free Cu(I) in bacterial cytoplasm is estimated to be in the attomolar (10^{-18} M) range and is difficult to detect[257]. Consistent with these reports, we

measured no significant increase in cytoplasmic Cu(I) (via flow cytometry) following incubation of MR-1 with $CuSO_4 \cdot 5H_2O$ and CF4 (Figure A.7). Together, these data confirm that MR-1 extracellularly reduces Cu(II) and explain the observed differences in polymerization activity between MR-1 and *E. coli*.

2.3.3 Use of TPMA Ligand Accelerates Polymerization Rate and Improves Control of Polymer Properties.

Having demonstrated robust monomer conversion, we measured the properties of polymers formed with MR-1, Cu(II), and EDTA. Polymerization kinetics were well-controlled under these conditions, but polymer molecular weights were higher than expected based on the monomer-to-initiator ratio. Similarly, we measured a non-linear dependence of molecular weight on monomer conversion (Figure A.9). Under aqueous conditions, Cu(I) is prone to decomposition in the absence of a suitable ligand, which can lead to kinetic anomalies and uncontrolled molecular weights[246]. Thus, we predicted that changing the ligand would yield improved control over polymer microstructure. We replaced EDTA with tris(2-pyridylmethyl)amine (TPMA), a well-known ligand for aqueous ATRP, and observed an immediate increase in polymerization rate. Complete conversion of $OEOMA_{500}$ occurred in ca. two hours while cell-free, supernatant, and *E. coli* experiments showed no significant conversion. A higher molecular weight macromonomer, $OEOMA_{900}$, showed similar polymerization kinetics in the presence of MR-1 and Cu(II/I)-TPMA (Figure A.13). Under optimized conditions, we achieved precise control over poly($OEOMA_{500}$) molecular weight and measured a linear relationship between polymer molecular weight and conversion, indicative of a living polymerization (Figure 2.2b). Repeated addition of $OEOMA_{500}$ to the microbial culture yielded first order-kinetics with rate constants consistent with the initial addition (Figure 2.2c). Moreover, we prepared diblock copolymers via sequential addition of $OEOMA_{500}$ and N-isopropylacrylamide (NIPAM) to the MR-1 culture (Figures A.14, A.15). Combined, these results demonstrate the living nature of the polymerization, highlight its synthetic utility, and definitively show that the reaction is metal-catalyzed. Our data are also consistent with

previous reports on aqueous ATRP describing the significant influence of catalyst stability on polymer conversion and microstructure.

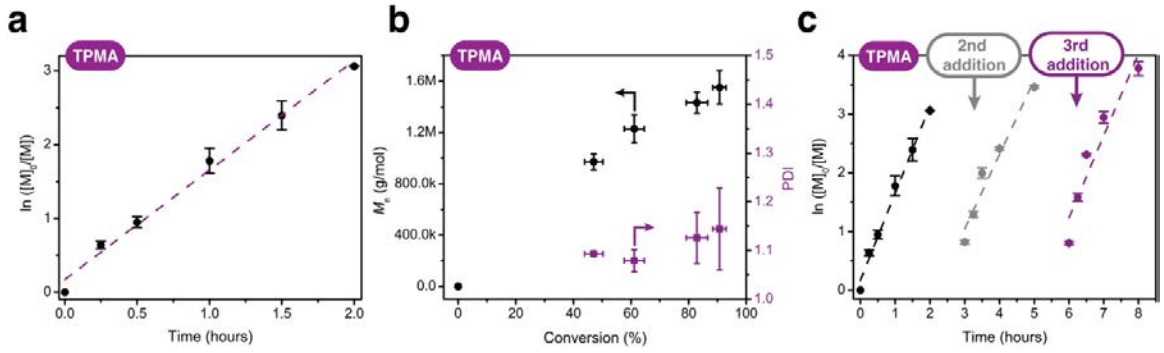

Figure 2.2: Kinetics and properties of polymers formed with *S. oneidensis* MR-1.

(a) First-order kinetics for conversion of monomer over time using Cu(II)-TPMA with *S. oneidensis* MR-1. (b) Molecular weight and polydispersity of poly($OEOMA_{500}$) as a function of monomer conversion. (c) Repeated addition of $OEOMA_{500}$ monomer showing first-order kinetics and living nature of polymerization. Data show mean ± S.D. of three independent experiments.

2.3.4 Viable Bacteria Enable ATRP, Not Secreted or Released Reducing Factors.

Having established that MR-1 facilitates ATRP, we next examined the biological factors that contribute to polymerization activity. Specifically, we investigated whether promiscuous cellular reductants or metabolic activity of viable bacteria was responsible for Cu(II) reduction and subsequent catalysis. The cytoplasm and periplasm of bacteria are reducing environments, easily capable of reducing Cu(II). Under stress conditions, cell lysis can release intracellular reductants and influence the overall redox potential of a microbial culture. Both *E. coli* and MR-1 can secrete reducing factors, such as glutathione and flavins, into the extracellular space[117,258–260]. Secretion or release of metal ions, like Fe(II), could also cause Cu(II) reduction. We hypothesize that these effects may explain polymerization activity that was previously observed with *E. coli* and *Pseudomonas aeruginosa*[247]. Indeed, polymerizations using glutathione as reductant showed dose-dependent polymerization activity, but polymerization rates were at least an order of magnitude slower relative to reactions containing MR-1 (Figure A.16). Lysed MR-1 and

E. coli also showed significant polymerization activity, consistent with the release of intracellular reducing factors. However, heat-killed cells from both species, which are metabolically inactive but retain membrane structure, showed no detectable polymerization activity (Figure A.17). Combined with the minimal activity of supernatant from active MR-1 cultures, these results demonstrate that secreted reducing factors are not a significant contributor to polymerization activity in our system.

To further rule out cell lysis and assess the influence of Cu(II/I) toxicity on polymerization activity, we evaluated MR-1 and *E. coli* viability under optimized polymerization conditions. Cu(II/I) is a potent microbial toxin, particularly under anaerobic conditions. Similar to Fe(III/II), Cu(II/I) can participate in Fenton chemistry and contribute to oxidative stress[261]. In addition, copper can readily replace iron in enzyme cofactors, such as those in fumarate reductase[262]. We speculated that Cu(II) supplementation may induce cell lysis, thereby contributing to polymerization activity. However, under aerobic conditions, we observed minimal inhibition of MR-1 growth when it was incubated with exogenous Cu(II) (5 μM) (Figure A.18). Switching to our standard reaction conditions, we measured no significant difference in MR-1 colony forming units (CFUs) following polymerization (Figure A.19). Similarly, bacterial viability measurements, assessed via fluorescence microscopy, showed minimal loss in cell viability for both MR-1 (74% viable) and *E. coli* (86% viable) under typical polymerization conditions and corroborated our CFU counts (Figure A.20). Moreover, scanning electron micrographs revealed that polymer was extracellular and closely associated with intact MR-1 (Figure A.22). Finally, we note that the Cu(II/I) concentrations (2 μM and below) used in our studies are significantly lower than levels reported to induce a microbial stress response in MR-1[263]. Together, these data suggest that the Cu(II/I) concentrations and monomer/initiator used for our polymerizations do not elicit a stress response that can explain polymerization activity.

2.3.5 Carbon Source Affects Polymerization Kinetics.

In order to investigate the extent of metabolic control over catalyst performance, we examined the effect of carbon source on polymerization activity. Carbon source affects electron flux through the central metabolism of MR-1 and should influence polymerization rate if they are coupled (Figure 2.3a). With TPMA as the ligand, we found that MR-1 fed with lactate, which generates 4 electron equivalents per molecule, yielded the fastest rate of polymerization (Figure 2.3b). In contrast, starved cells showed lower polymerization activity, as did cells fed with acetate, which can not be used as a carbon source by MR-1 under anaerobic conditions[264]. MR-1 supplied with pyruvate, which yields 2 electron equivalents per molecule, showed polymerization activity between lactate- and acetate-fed/starved cells. The residual activity observed in starved and acetate-fed cells is likely due to latent metabolic activity from growth in rich media or from residual electron density on the outer membrane cytochromes, both of which have been observed for MR-1 and *Geobacter sulfurededucens*[243,265]. The short time scale (< 2 hours) of reactions conducted using TPMA also makes it challenging to observe metabolic effects. Replacing TPMA with EDTA resulted in a larger difference between lactate-fed and starved cells, likely because the longer timescale of these polymerizations (24 hours) accentuated metabolic differences (Figure A.23). The EDTA experiments also suggest that continuous metabolic activity and associated Cu(II) reduction counters catalyst deactivation when a less supportive ligand is used[246]. In sum, these results demonstrate that polymerization rate is strongly coupled to metabolic activity and subsequent electron flux.

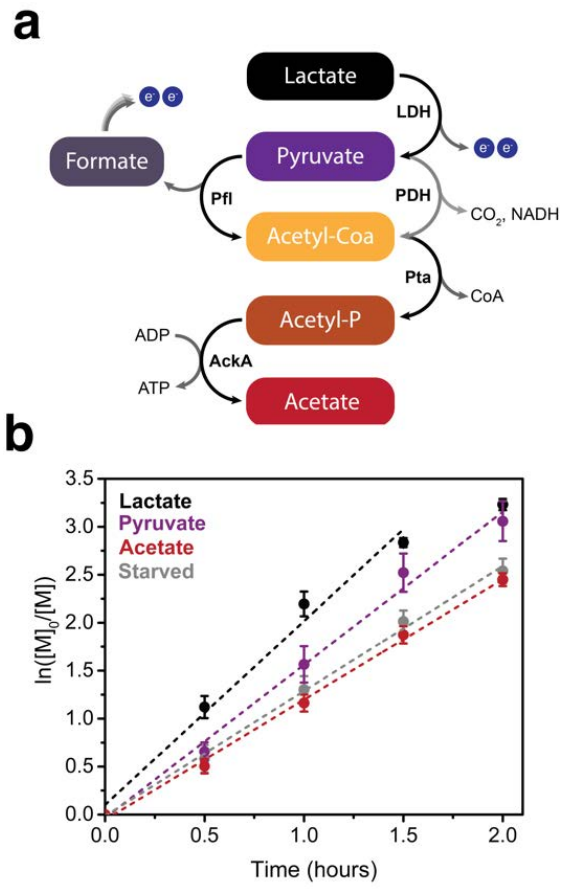

Figure 2.3: Polymerization activity is controlled by electroactive metabolism.

(a) Simplified carbon metabolism of *S. oneidensis*. (b) Polymerization kinetics for MR-1 supplied with different carbon sources using Cu(II)-TPMA as catalyst. Data show mean ± S.D. of three independent experiments. Statistical analysis for 2.3b is presented in Figure A.24.

2.3.6 MtrC Expression is Critical for ATRP Activity.

MR-1 uses specialized respiratory pathways to transport electron equivalents from the cytoplasm and periplasm to the extracellular space (Figure 2.4a)[239,266]. To understand how the components of these pathways influence ATRP activity, we measured the effect of knocking out select cytochromes and other redox-relevant proteins on polymerization kinetics. Molecular hydrogen and flavins are strong reductants generated by MR-1 that may participate in Cu(II) reduction[267,268]. However, knockouts of periplasmic

hydrogenases (Δ*hydA*Δ*hyaB*) and an inner membrane flavin exporter (Δ*bfe*) exhibited no difference in monomer conversion when compared to MR-1. In contrast, a mutant lacking outer membrane cytochromes (Δ*mtrC*Δ*omcA*) showed significantly attenuated polymerization rates (Figure 2.4b). MtrC is a key decaheme c-type cytochrome through which MR-1 interacts with metals and metal oxides; our results suggest that it is also important for Cu(II) reduction[240]. *E. coli* cytochromes are not homologous to MtrC and the organism largely lacks the cytochrome content of MR-1 (42 cytochrome genes in MR-1 vs. 5-7 in *E. coli*)[269]. This deficiency in extracellular electron transport machinery explains why *E. coli* showed minimal polymerization activity. Complete abolishment of activity was not observed for the Δ*mtrC*Δ*omcA* mutant because it is unlikely that Cu(II) reduction is completely tied to an exclusive cytochrome reduction pathway. MR-1 expresses several other electron transfer proteins that could mediate Cu(II) reduction and their transcription levels appear agnostic toward different soluble electron acceptors[242]. MR-1 also possesses outer membrane cytochromes other than MtrC (e.g. MtrF), which can compensate for its absence[86]. We attempted to inhibit all outer membrane cytochromes using KCN, but found that this also disrupted positive polymerization controls. Notably, normal polymerization activity was partially rescued after complementation with a plasmid encoding MtrC (Figure 2.4c). This finding is consistent with previous reports showing that MtrC alone is sufficient to rescue the majority of electron transfer activity and that OmcA is not required for the Mtr pathway to function[86]. More importantly, the complementation result suggests that polymerization activity can be controlled by manipulating MtrC expression. Altogether, our results highlight the unique role that outer membrane cytochromes play in extracellular electron transport and offer additional support for a specific and manipulable link between metabolic activity and catalyst performance.

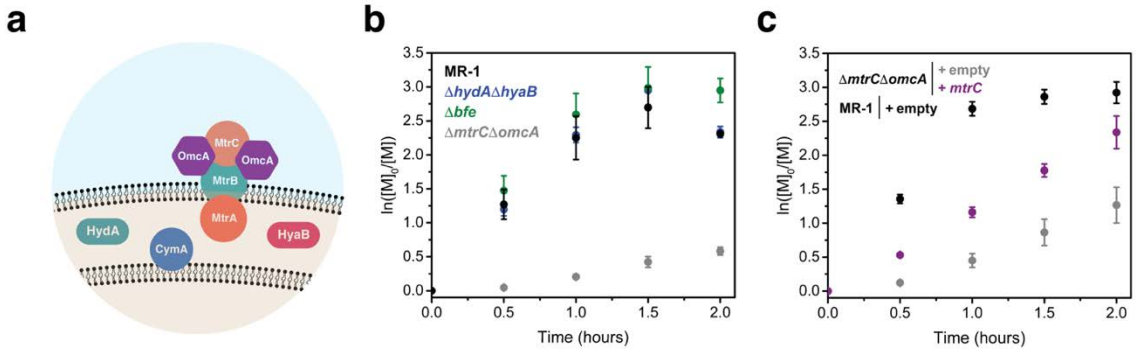

Figure 2.4: Electron transfer proteins impact polymerization kinetics.

(a) Key proteins involved in extracellular electron transport in *S. oneidensis* MR-1. (b) Effect of gene knockouts on polymerization activity using Cu(II)-TPMA. (c) Rescue of normal polymerization activity via complementation with a plasmid encoding MtrC, using Cu(II)-TPMA as a catalyst. Data show mean ± S.D. of three independent experiments. Statistical analysis for Figure 2.4b,c is presented in Figures A.25, A.26 respectively.

2.4 Discussion and Conclusions

In this study, we evaluated the ability of an electroactive bacteria to control an extracellular metal-catalyzed reaction. Most reports describing non-enzymatic metal catalysis in the presence of cells have focused on developing new reactions for bioorthogonal labeling or pro-drug activation[270,271]. These reactions are compatible with the cellular environment, but are generally not under metabolic control. In contrast, several metabolic engineering efforts have coupled abiotic catalytic cycles to cellular metabolism through the use of secondary metabolites such as hydrogen, formate, and other small molecules, or through bioelectrochemical cells[236–238,272]. Synthesizing aspects of these fields, we showed that respiratory electron flux can be directly harnessed to control the performance of a metal-catalyzed polymerization and that extracellular electron transfer proteins are a critical enabler of this process.

Radical polymerizations in the presence of MR-1 and Cu(II/I)-TPMA were very well-controlled. We initially chose $OEOMA_{500}$ as a monomer because it is common in aqueous radical polymerizations and allows for quantitative rate comparisons between polymerization methodologies. Under optimized conditions, the rate of polymerization was

first-order with a rate constant comparable to polymerizations conducted in the presence of an external electrode[273]. Specifically, MR-1 with Cu(II/I)-TPMA polymerized $OEOMA_{500}$ with a rate constant of 2.20 h^{-1} at 30 °C while electrochemical ATRP under similar conditions yielded a rate constant of ca. 1.52 h^{-1} at 25 °C [273]. We measured similar rate constants under several alternative conditions (Table A.5). Also similar to electrochemical ATRP, we found that very low concentrations of catalyst (0.2 μM) were sufficient for polymerization activity. In contrast, polymerizations conducted in the presence of a sacrificial reductant require higher catalyst concentrations[245]. Polymerizations in the presence of MR-1 yielded polymers with well-defined molecular weights and narrow molecular weight distributions. We also highlighted the synthetic utility of our polymerization by preparing diblock copolymers with controlled molecular weight using $OEOMA_{500}$ and NIPAM as monomers. Similar polymers have been used for self-assembly, drug delivery, and other applications[274]. Alternatively, polymers with well-defined microstructure could be used to coat bacterial cells, providing protection from toxins or initiating biofilm phenotypes[275,276]. Given our results, it is likely that a wide variety of applications relying on water-soluble polymers can leverage *S. oneidensis* controlled polymerization.

By probing the biology of *S. oneidensis* controlled ATRP, we demonstrated that electroactive metabolism and polymerization activity are highly coupled. The catabolic pathways controlling electron flux exerted significant influence on polymerization rate, which makes them promising targets for future engineering applications. For example, pathways for utilization of different carbon sources (e.g. glucose, glycerol, xylose) or increasing electron-equivalent flux to the inner membrane via NADH dehydrogenase overexpression could be integrated into *S. oneidensis* to modulate Cu(II) reduction[132,221,222]. Alternatively, controlling the expression of electron transfer proteins could be used to tune polymerization activity. Towards this goal, we identified MtrC as an important regulator of polymerization activity in *S. oneidensis*. Although *E. coli* does not natively possess cytochromes that are homologous to MtrC, the Mtr pathway can be heterologously expressed in it[277]; this offers a potential means to adapt our polymerization system into a

standard chassis organism. Other electroactive bacteria with outer membrane cytochromes, such as *G. sulfurreducens*, could also be used to control polymerization activity[55]. Overall, we found that MtrC serves as a master controller of polymerization activity and believe that it is a promising biological target for future optimization and synthetic biology applications involving extracellular metal catalysis.

In conclusion, we discovered that *S. oneidensis* MR-1 can effectively control polymerization activity in the absence of an electrode via extracellular electron transfer to a redox-active metal catalyst. Polymers formed in the presence of *S. oneidensis* and Cu(II/I) were narrowly dispersed with defined molecular weights indicative of a living polymerization. Furthermore, polymerization kinetics were strongly dependent on catalyst structure, metabolic activity, and specific electron transport proteins. Future work may focus on optimizing both the chemical (e.g. ligand design) and biological (e.g. cytochrome expression) components of our system. More importantly, the reduction potential of MR-1 combined with the wealth of chemical transformations enabled by redox-active transition metals suggests that our system can be readily expanded to reactions beyond polymerization. Overall, our results demonstrate that the metabolic activity of an electroactive bacterium can be coupled to the performance of a redox-active metal catalyst and indicate that engineering of bacterial electron transport pathways may provide a general template for adapting traditional metal-catalyzed reactions for use in metabolic engineering.

2.5 MATERIALS AND METHODS

2.5.1 Chemical and Reagents

Tetrakis(acetonitrile)copper(I) tetrafluoroborate ($Cu(CH_3CN)_4BF_4$, Sigma-Aldrich, 97%), N-isopropylacrylamide (NIPAM, Sigma-Aldrich, 97%), L-Glutathione reduced (GSH, Sigma-Aldrich, 98%), Cupric sulfate pentahydrate ($CuSO_4 \cdot 5H_2O$, VWR, ACS grade), Tris(2-pyridylmethyl)amine (TPMA, Sigma-Aldrich, 98%), Copper(II) bromide ($CuBr_2$, Sigma-Aldrich, 99%), 2-Hydroxyethyl 2-bromoisobutyrate (HEBIB, Sigma-Aldrich, 95%), Sodium fumarate ($Na_2C_4H_2O_4$, Alfa Aesar, 98%) and Sodium DL-lactate ($NaC_3H_5O_3$, TCI, 60% in water) were used as received. Poly(ethylene glycol) methyl ether methacrylate ($OEOMA_{500}$, Sigma-Aldrich, average M_n 500) was passed through a column filled with activated basic alumina (Al_2O_3, Sigma-Aldrich) to remove polymerization inhibitors immediately prior to use. $OEOMA_{900}$ (Sigma-Aldrich, average M_n 950) was dissolved in THF and passed through basic alumina. The solution was then precipitated with cold hexanes and dried under reduced pressure overnight prior to use. Methanol (MeOH, Fisher Chemical, HPLC grade), N,N-Dimethylformamide ($HCON(CH_3)_2$, Alfa Aesar, 99.7%, HPLC grade) and sodium azide (NaN_3, Sigma-Aldrich, 99%) were used as received for GPC characterization. Deuterium oxide (D_2O, Sigma-Aldrich, 99.9%) was used as received for NMR characterization. CF4 and CF4-CTRL imaging probes (1mM) were dissolved in DMSO and stored at –20 ºC. Ultrapure Water was generated from a Milli-Q Integral Water Purification System.

2.5.2 Analysis and Measurement

Polymer samples were analyzed by gel permeation chromatography (GPC) with a Superdex 200 Increase 10/300 GL (GE Healthcare Bio-Sciences AB, Particle size ~ 8.6 μm) column using 20% (v/v) methanol aqueous solution (0.05 M NaCl) as the eluent (25 °C), or Agilent PLgel 10 μm MIXED-B and 5 μm MIXED-C columns using DMF as the eluent (30 °C) and a 3-angle laser light scattering (MALLS) detector (Wyatt Technology, miniDAWN TREOSII). Molecular weights were determined using ASTRA software

(Version: 6.0) from Wyatt Technology. The dn/dc value for poly($OEOMA_{500}$) was obtained from the literature (0.115 mL/g)[278]. ^1H NMR spectra of monomer/polymer solutions were collected on an Agilent 400 MHz NMR spectrometer or a Bruker Avance III 500 spectrometer using D_2O as solvent.

2.5.3 Bacterial Strains and Culture

Strains and plasmids used in this study are listed in Table A.3. Anaerobic culture was performed with an incubator located inside a Coy Anaerobic Glovebox containing a humidified atmosphere of 3% hydrogen and balance nitrogen. The *Escherichia coli* strains used for cloning and conjugal transfer were maintained on lysogeny broth (LB) that was supplemented with 25 μg/mL kanamycin and 250 μM 2,6-diaminopimelic acid as necessary. During routine propagation, *Shewanella oneidensis* strains were maintained on LB agar plates containing 25 μg/mL kanamycin as necessary. For growth assays and polymerization reactions, *S. oneidensis* and *E. coli* strains were grown in *Shewanella* basal medium (SBM) supplemented with 0.05% casamino acids stock (10% w/v). SBM was supplemented with 5 mL/liter mineral mix when indicated. Cells were prepped for polymerization reactions as follows: Strains stored in 20% glycerol at –80 °C were freshly streaked onto LB agar plates and aerobically incubated for ~16 h at 30 °C (*S. oneidensis*) or 37 °C (*E. coli*). Plates were brought into the anaerobic glovebox and single colonies were used to inoculate SBM supplemented with 20 mM sodium lactate and 40 mM sodium fumarate. Inoculated cultures were then incubated for ~16 h at 30 °C (*S. oneidensis*) or 37 °C (*E. coli*). Stationary-phase cultures were washed by transferring cells to centrifuge tubes inside the anaerobic chamber and spinning at 6000 x g for 20 min. Supernatant was exchanged with fresh SBM supplemented with casamino acids and mineral mix (when indicated). Two washes were performed and on the final wash, cells were concentrated to a 200x stock (OD600 of 2.0). Cells were used to initiate polymerization immediately after concentration.

2.5.4 General Polymerization Conditions

All stock solutions and reaction mixtures were prepared in an anaerobic glovebox. Prior to polymerizations, stock solutions of HEBiB (100X stock, 2.9 µL in 287 µL SBM containing casamino acids) and Cu-EDTA (200X stock from 10 mg $CuSO_4$•$5H_2O$ in 1 L of 1.35 mM EDTA buffer) or Cu-TPMA (200X stock from 8.9 mg $CuBr_2$ and 11.6mg TPMA in 100mL DMF) were mixed. Afterwards, a 2 mL polymerization reaction mixture was prepared as follows. To a sterile polypropylene culture tube was added 60% w/w sodium lactate solution (5.7 µL), 1 M fumarate solution (80 µL), $OEOMA_{500}$ (92.6 µL, 200 µmol), HEBIB (2.9 µL of 100X stock), Cu-EDTA (10 µL of a 200X aqueous stock) or Cu-TMPA (10 µL of a 200X DMF stock), and a balance of SBM lacking trace mineral mix. Final concentrations were lactate (20 mM), fumarate (40 mM), $OEOMA_{500}$ (0.1 M), HEBiB (0.1mM), and Cu-EDTA (0.2 µM) or Cu-TPMA (2.0 µM). For reactions with different carbon sources, lactate was replaced with sodium pyruvate (20 mM) or sodium acetate (20 mM). Polymerization was initiated by adding 20 µL of 200X cell stock (OD600 = 2.0) to bring the final reaction volume to 2 mL and starting bacterial OD600 to 0.02. Final reaction mixtures were incubated at 30 °C (*S. oneidensis*) or 37 °C (*E. coli*). Time points were aliquoted, diluted with deuterium oxide or GPC solvents, exposed to air to quench the reaction, then flash frozen in liquid N_2. Aliquots were stored at –20 °C until analysis via NMR spectroscopy or GPC.

2.5.5 Polymerization of Diblock Copolymer

The polymerization of $OEOMA_{500}$ was initiated as the conditions illustrated above. After the complete depletion of $OEOMA_{500}$ (confirmed by NMR), a 2 mL mixture of NIPAM (22.6 mg, 0.1 M), 60% w/w sodium lactate solution (5.7 µL, 20 mM), 1 M fumarate solution (80 µL, 40 mM), Cu-TMPA (10 µL of a 200X DMF stock, 2 µM), and a balance of SBM lacking trace mineral mix were added to above reaction medium. The reaction was kept at 30 °C overnight. Aliquots were removed at fixed time points, diluted with deuterium oxide or GPC mobile phases, exposed to air to quench the reaction, then

flash frozen in liquid N_2. Aliquots were stored at –20 °C until analysis via NMR spectroscopy.

2.5.6 SEM Analysis of Bacterial Before/After Polymerization

Bacterial cells before/after polymerization were fixed in a 2% formaldehyde (0.85% NaCl) solution for 2 hours. The cell suspension was rinsed with fresh buffer (0.85% NaCl) and pelleted by centrifugation (6000 x g, 20min, 3X). Aqueous buffer solution was slowly exchanged with ethanol using a series of ethanol dilutions (20%, 40%, 60%, 80% and 100%) with pelleting in between (6000 x g, 20min). The ethanol solution of concentrated cell suspension was drop-cast onto glass, dried under ambient conditions, and sputter-coated with Pt before SEM analysis.

2.5.7 Polymerization Controls

MR-1 and *E. coli* polymerization controls (cell supernatant, heat-killed, and lysed cells) were performed using the standard reaction conditions described above. All cellular samples were grown anaerobically to stationary-phase. Cell supernatant was obtained after centrifugation for 20 min at 6000 x g. The supernatant was aspirated and passed through a 0.22 micron filter to sterilize after which 200 µL of saturated growth supernatant was added to each 2 mL polymerization reaction. Heat-killed cells were incubated in a block heater at 80 °C for 20 min, and cells were adjusted to a final OD of 0.02 in the reaction media. Lysed cells were obtained using a Branson Model 250 sonicator with a Model 102C Converter. Cells suspensions on ice were sonicated for 3 cycles of 5 s each. The solutions changed from opaque to clear, indicating cell lysis. The volume of cell lysate corresponding to a final OD of 0.02 of live cells in the reaction media was added to the polymerization mixture.

2.5.8 Copper Treatment of CF4 Loaded Bacteria.

S. oneidensis was suspended in 1 mL SBM (OD600 = 0.2). 5 µL of 200X Cu(II) stock solution (0.4 mM, $CuSO_4 \cdot 5H_2O$, Final Concentration = 2 µM) was added to the

above suspension and cells were incubated in the dark in an anaerobic chamber for 2 hours. The bacteria were pelleted (6000 x g, 20 min) and resuspended in SBM. After repeating five times, the cells were concentrated via resuspension in 200 µL SBM. 1 µL of the dye CF4 or CF4_CTRL (1 mM stock) was mixed with 4 µL SBM to make the pre-mixed dye solutions. 2 µL pre-mixed dye solutions was added to the concentrated cell suspension (Final dye concentration: 2 µM) and incubated in the dark for 15 min or 30 min. The bacteria were pelleted (6000 x g, 20 min) and resuspended in 0.85% NaCl buffer to a cell density of ~10^6 cells/mL for analysis by flow cytometry. Cells were analyzed on a BD LSRFortessa SORP Flow Cytometer using an excitation of 561 nm and emission of 610/20 nm.

2.5.9 Copper Detection by CF4 in Bacterial Supernatant

MR-1 was anaerobically cultured in 1 mL SBM (OD600 = 0.2). 2 µL CF4 or CF4-CTRL and/or 5 µL of 200X Cu(II) stock solution (0.4 mM, $CuSO_4 \bullet 5H_2O$, Final Concentration = 2 µM) were added to the cell suspension followed by incubating in the dark for 2 hours. Time points were obtained by pelleting a 200 µL cell suspension, aliquoting supernatant into a 96-well microplate, and measuring the fluorescence via plate reader (E_{ex} = 536 nm, E_{em} = 560-610 nm). Incubating with CF4 was necessary to prevent Cu(I) decomposition. TPMA was not included since it interfered with CF4-Cu(I) binding.

2.5.10 Bacterial Growth/Viability Assessment

Competitive growth assays were performed in sterile 24-well plates, and OD600 was monitored by plate reader. Bacterial viability was determined by CFU counting and staining with the LIVE/DEAD BacLight Viability Kit (Invitrogen). For CFU counting, serial dilutions from the Cu-TPMA polymerization reaction and a control culture containing 20 mM sodium lactate and 40 mM sodium fumarate were plated onto LB agar containing 20 mM sodium lactate and 40 mM sodium fumarate, and incubated anaerobically for 18 hours. The LIVE/DEAD BacLight Viability Kit was used according to manufacturer instructions. Briefly, cells were harvested after polymerization and washed

3x with 0.85% saline by centrifugation at 6000 x g for 20 min. Cells were concentrated to an OD600 of ~2.0 and incubated with the LIVE/DEAD BacLight Bacterial Viability dye mixture in the dark for 15 minutes. Excess, unbound dye was removed by repeated centrifugation and washing with 0.85% saline (total of 5 washes). 20 µL of cells were placed on glass slides, allowed to settle, and covered with a 0.17 mm coverslip. Excess moisture was wicked from the slide edges and the coverslips were sealed with nail polish. A Zeiss Axiovert 200M Fluorescent Microscope was used to image live and dead cells at room temperature. Images were captured using 475/40 nm excitation and 530/50 nm emission for green (live) fluorescence and 560/40 nm excitation and 630/75 nm emission for red (dead) fluorescence with a 40X oil objective. Cell counts to determine the viable population percentages were quantified by thresholding using Fiji 1.0 software from at least 3 different fields of view. Representative images were background subtracted using a rolling ball radius of 10 pixels in Fiji 1.0.

2.5.11 Construction of pShew-mtrC and plasmid complemented strains

pZ8-T_dcas9 was a gift from Timothy Lu (Addgene plasmid # 74062) and served as a base vector in our study[279]. The pZ8-1 backbone contains several attractive features for use in *S. oneidensis* including a kanamycin resistance marker, a p15A origin of replication[280], and expression of the LacI repressor that can confer IPTG inducibility to genes under control of the Ptac promoter. Although the pZ8-1 backbone contains no annotated origin of transfer, we found that the plasmid could be successfully conjugated into *S. oneidensis*. A similar result had been observed with another plasmid that contained the p15A origin[281].

A derivative of pZ8-T_dcas9 that lacks *dcas9* was engineered for improved stability in *S. oneidensis* by removal of a ClaI restriction site in the kanamycin resistance gene[282]. Primers pShewFWD1/pShewREV1 and pShewFWD2/pShewREV2 were used to PCR amplify the pZ8-T_dcas9 backbone around the *dcas9* gene and into two separate fragments. pShewREV1 and pShewFWD2 introduced a silent mutation in the kanamycin resistance gene, which removed the ClaI site without disrupting the encoded amino acid sequence.

These fragments were ligated together by Gibson Assembly, and the resultant plasmid was termed pShew. Sequencing results verified successful removal of *dcas9* and the ClaI site in pShew. *S. oneidensis* genomic DNA was purified using the PureLink Genomic DNA Mini Kit (Invitrogen) and served as a template to PCR amplify *mtrC* using primers Shew_genome_mtrC_Fwd/Shew_genome_mtrC_rev. pShew and the PCR amplified *mtrC* were digested with EcoRI and SalI enzymes, and ligated together to form pShew-mtrC. Sequencing showed successful ligation of this construct and that a single base pair deletion occurred in the *mtrC* stop codon, TAA, deleting the terminal A. A functional TAG stop codon was formed due to the adjacent downstream base pair containing a G (the start of the SalI cut site, GTCGAC). All plasmid constructs were electroporated into *E. coli* DH5α for cloning steps, plasmid amplification, and long-term storage at –80 °C. We found that low-concentration of kanamycin (25 μg/mL) was sufficient to select for pShew harboring *E. coli* strains. Higher concentrations reduced growth yield and lowered transformation efficiencies.

Final plasmid constructs were electroporated into *E. coli* WM3064 for conjugation with *S. oneidensis* strains. Conjugation was performed as previously described[77]. Plasmids from transformed strains were purified using the QIAprep Spin Miniprep Kit (Qiagen), and sequence verified to ensure plasmid stability. Strains were stored long-term in 20% glycerol at –80 °C.

2.5.12 Functional expression of MtrC by pShew-mtrC

SDS-PAGE/heme staining analysis of boiled cell lysate was unable to detect expression of MtrC (uninduced and induced with 0.01-1 mM IPTG) in *S. oneidensis* strains carrying pShew-mtrC, compared to strains with the empty vector. As SDS-PAGE may not be sensitive enough to detect low levels of MtrC expression, we directly assayed MtrC activity. Previous studies have shown that the deficiency of Fe(III) reduction by a Δ*mtrC*Δ*omcA* mutant could be rescued by complementation with an *mtrC* plasmid[85,86,111]. Thus, we tested whether pShew-mtrC could restore Fe(III) reduction in this mutant. SBM containing 20 mM sodium lactate, 5 mM Fe(III)-citrate, and no IPTG was inoculated with

MR-1 carrying pShew, Δ*mtrC*Δ*omcA* carrying pShew, or Δ*mtrC*Δ*omcA* carrying pShew-mtrC. Timepoints were aliquoted from the cultures and mixed with equal volume 1 N HCl to cease further reduction and capture Fe(III)/Fe(II) levels. Fe(II) concentrations were determined using the Ferrozine Assay as previously described[86]. Whereas Δ*mtrC*Δ*omcA* carrying pShew showed no Fe(III) reduction, Δ*mtrC*Δ*omcA* carrying pShew-mtrC showed a rescue of Fe(III) reduction comparable to MR-1 carrying the empty vector (Figure A.27). We found that with no addition of IPTG, leaky expression of *mtrC* is able to rescue the Fe(III) reduction phenotype. Addition of IPTG had minimal effect on increasing the rate of Fe(III) reduction (Figure A.28).

2.5.13 Monomer conversion analysis by NMR

The integral of Δ = 3.25-3.23 ppm (Peak a, Figure A.20) corresponds to the methyl signal of the unreacted $OEOMA_{500}$. The integrals of Peak a' (Δ = 3.27-3.25 ppm) corresponds to the methyl signal of Poly($OEOMA_{500}$). The conversion of the monomer to polymer was characterized by the disappearance of olefinic peaks b and c and emergence of methyl peak a'. Spectra were baseline corrected prior to integration using MestReNova 10.0.2. The residual water peak was also subtracted out for clarification.

2.5.14 Statistical Analysis

Unless otherwise noted, data is plotted and reported as the mean ± S.D of N = 3 replicates. Preliminary experiments indicated that this sample size would be sufficient to detect significant differences in mean values. Unless otherwise noted, P values were calculated using a two-tailed unpaired Students' t-test and OriginPro software.

Chapter 3: Extracellular electron transfer by *Shewanella oneidensis* controls palladium nanoparticle phenotype[2]

3.1 Chapter Summary

Biological production of inorganic materials is impeded by relatively few organisms possessing genetic and metabolic linkage to material properties. The physiology of electroactive bacteria is intimately tied to inorganic transformations, which makes genetically tractable and well-studied electrogens, such as *Shewanella oneidensis,* attractive hosts for material synthesis. Notably, this species is capable of reducing a variety of transition-metal ions into functional nanoparticles, but exact mechanisms of nanoparticle biosynthesis remain ill-defined. We report two key factors of extracellular electron transfer by *S. oneidensis*, the outer membrane cytochrome, MtrC, and soluble redox shuttles (flavins), that affect Pd nanoparticle formation. Changes in the expression and availability of these electron transfer components drastically modulated particle phenotype, including particle synthesis rate, structure, and cellular localization. These relationships may serve as the basis for biologically tailoring Pd nanoparticle catalysts and could potentially be used to direct the biogenesis of other metal nanomaterials.

3.2 Introduction

Control over cellular machinery has enabled the production of diverse compounds including pharmaceuticals, fuels, fine chemicals, and soft materials[3,27,148]. However, microbial engineering of metal and metal oxide products remains a significant challenge. Attributes such as electron transfer and nucleation are typically absent from organic biosyntheses, and their presence adds increased complexity to inorganic transformations.

[2]Adapted from Dundas, C.M., Graham, A.J., Romanovicz, D.K., Keitz, B.K. (2018) Extracellular Electron Transfer by *Shewanella oneidensis* Controls Palladium Nanoparticle Phenotype *ACS Synth. Biol. 7*(12), 2726-2736. Christopher M. Dundas conceived the project, performed the experiments, analyzed the results, and wrote the chapter.

As a result, the enzymatic and metabolic factors that drive material formation in biological systems have been challenging to study and manipulate[31]. Despite the paucity of bioengineered inorganic products, microbial transformation of inorganics occurs quite frequently in nature. Several organisms generate highly functional and ordered materials, including metal nanoparticles, silicas, calcium carbonates, and metal oxides[39,48,49]. In these systems, coordinated protein and metabolite networks exert control over material morphology, composition, and function. For instance, the magnetotactic bacterium, *Magnetospirillum gryphiswaldense*, uses several proteins that govern nucleation, electron transfer, and vesicle formation to generate size-controlled magnetite nanoparticles[283]. This example highlights the capability of living systems to tailor inorganic structure-function relationships and suggests that exploiting naturally-occurring pathways may provide a means for designer material biosynthesis.

Electroactive bacteria are attractive hosts for inorganic materials engineering, as a diversity of soluble and insoluble inorganic substrates can be incorporated into their metabolism[64]. Many electrogens can transfer respiratory electron flux onto several metal species, including Cu(II), U(VI), Ag(I), Au(III), and Pd(II), to generate functional nanoparticles[39]. However, it is generally unclear how electroactive physiology dictates the structural and functional properties of produced nanoparticles. One electroactive bacterium, *Shewanella oneidensis* MR-1, is poised to address this issue, as it directs metabolic electron flux onto metals using a well-characterized electron transport pathway[75]. The organism's genetic tractability has also facilitated understanding and control of this network, with knockout, complementation, and overexpression studies leading to identification of important redox-active metalloproteins and small-molecules[111]. Notably, this pathway can reduce substrates located outside the bacterial outer membrane in a process known as extracellular electron transfer (EET). Despite significant progress in applying this system towards bioremediation and microbial fuel cell engineering, elucidating the function of EET components in nanoparticle formation has proven challenging. Whereas the outer membrane cytochromes, MtrC and OmcA, are primary mediators of EET to iron oxides and electrodes[85,86], their activity in nanoparticle formation

appears largely dependent on culture conditions and the identity of metal reduced. For example, a knockout strain deficient in these proteins changed the cellular localization of produced UO_2 nanoparticles relative to those of MR-1[165], but had no measured effect on the kinetics of Pd or Cu nanoparticle formation[159,168]. Additional proteins have been identified as influencing nanoparticle formation rates, including hydrogenases and other periplasmic reductases[166,167], but little is known of their influence on particle properties. Furthermore, the importance of soluble redox shuttles (flavins) in EET by *Shewanella* has become increasingly apparent[117], but their impact on nanoparticle synthesis is wholly unexamined.

To better inform the design of material syntheses using *S. oneidensis*, we explored the role of key EET factors in the formation of Pd nanoparticles. Pd was chosen as it is one of the more well-studied nanoparticles generated by *S. oneidensis* and enabled us to draw comparisons with previous reports[156,157,168,284]. Bio-based stabilization of specific Pd crystal facets was previously demonstrated via peptide-directed synthesis[285], and we reasoned that *S. oneidensis* cells may exhibit similar control of particle nucleation and growth. In contrast to previous works, the EET machinery of *S. oneidensis* also affords the opportunity to genetically and metabolically instruct electron transfer to Pd(II) ions during nanoparticle synthesis. Thus, we tested the effect of *S. oneidensis* genotype and the role of redox-active small molecules in Pd nanoparticle formation. Here, we report two factors of *S. oneidensis* electron transport that strongly influence nanoparticle phenotype: the outer membrane cytochrome, MtrC, and soluble redox shuttles (flavins). After manipulating the bacterial concentration of these species, through control of gene expression and exogenous supplementation, respectively, we observed drastic effects on the synthesis rate and phenotype (i.e. size and cellular localization) of biogenic nanoparticles. Identification of these factors provides proof-of-principle for using genetic and metabolic manipulation to tune the properties of Pd and potentially other metal nanoparticles generated by *S. oneidensis*.

3.3 Results and Discussion

3.3.1 Optimizing *S. oneidensis* Control Over Nanoparticle Biosynthesis and Cellular Viability

To drive *S. oneidensis* control over Pd nanoparticle formation, we first identified nanoparticle synthesis conditions that minimized abiotic effects and exhibited unambiguous nanoparticle phenotypes. Specifically, we examined how reaction media formulation and method of anoxic culture influenced nanoparticles formed by *S. oneidensis* MR-1. The general procedure for Pd nanoparticle biosynthesis was as follows: MR-1 was anaerobically pregrown overnight to stationary-phase in *Shewanella* Basal Medium (SBM) containing lactate/fumarate, anaerobically washed with degassed SBM, and finally used to inoculate a Pd nanoparticle reaction mixture (final OD_{600} ~0.2). Whole mount transmission electron microscopy (TEM) enabled initial assessment of different conditions, as the bacteria became palladized upon exposure to Pd(II) and adherent nanoparticles could be visualized by electron micrographs.

Choice of electron donor can greatly affect bacterial nanoparticle formation, as many metabolically accessible electron donors (e.g. formate, hydrogen) also abiotically reduce palladium ions[286]. Indeed, we found that the hydrogenous atmosphere (3%) of a humidified anaerobic glovebox caused autocatalytic reduction of palladium in the absence of bacteria. Thus, we used butyl rubber-stoppered Hungate Tubes purged with argon to maintain anaerobicity for bacterial pregrowth and nanoparticle biosynthesis reactions. As lactate is relatively inert to palladium and generates metabolic electron flux in *Shewanella,* we used it as our primary electron donor. Reaction mixtures omitting lactate or any other electron donor showed no Pd(II) reduction (Figure B.1). We also assessed the influence of culture medium components that could cause abiotic reduction of Pd(II). Prior to bacterial inoculation of the reaction mixture, *S. oneidensis* was pregrown in SBM supplemented with casamino acids. When the nanoparticle reaction mixture was similarly supplemented, small Pd nanoparticles were formed on bacteria (<10 nm) (Figure B.2). In contrast, mixtures omitting casamino acids had a larger nanoparticle size distribution, with particles generally falling within one of two populations: small (<10 nm) and large (~50 nm) particles. We

speculated that the presence of free cysteines may cause abiotic reduction of Pd(II) and lead to fewer large particles formed on bacteria. Thus, to minimize abiotic effects we utilized reaction mixtures that lacked casamino acids.

The intracellular space is a reducing environment and leakage of promiscuous reductants (e.g. NADH, glutathione) through compromised membranes could also contribute to Pd(II) reduction[42,287]. To address this, we performed viability measurements to quantify the effect of increasing concentration of Pd(II) in the *S. oneidensis* reaction mixtures. Viability was quantified using the BacLight Live/Dead stain after exposure to 10, 100, and 1000 μM Pd(II) for two hours under our standard nanoparticle synthesis conditions. *S. oneidensis* viability exhibited a dose-dependent response for the concentration range tested, varying from ~80% to ~30% viable with increasing Pd(II) concentration (Figure B.3). We also examined how cell viability affects reduction rate when cells were mixed with 100 μM Pd(II) and given lactate as a carbon source. Viable MR-1 samples demonstrated initial adsorption and sustained reduction of Pd(II) over four hours (Figure B.4), similar to what has been observed by others[168]. In contrast, Pd(II) levels for heat-killed MR-1 and fully lysed MR-1 were lower at the initial time point and did not significantly vary over time. We interpreted this result as a confirmation that promiscuous cell reductants can reduce Pd(II), but that continuous reduction requires active metabolism.

As MR-1 palladization increases the 600 nm light scattering signal for single cells[288], we hypothesized that cellular nanoparticle formation could be assessed by flow cytometry side scattering. To further probe the relationship between palladization and *S. oneidensis* viability, we used flow cytometry to simultaneously measure side scattering and fluorescence from a dye (propidium iodide, PI) that indicates membrane permeability of palladized bacteria[157,289]. At both 100 and 1000 μM Pd(II), increases in side scatter were detected for palladized *S. oneidensis* strains, relative to a Pd-free control (Figure B.6). At the higher Pd(II) concentration, there was a corresponding increase in both side scatter and PI fluorescence, indicating the presence of a dead population that is highly palladized. However, the same increase in PI fluorescence was not detectable at the lower Pd(II) concentration (Figure B.7). This result corroborates our microscopic viability

measurements and indicate that the majority of palladized cells remain viable. Based on these results, we chose 100 μM Pd(II) as our primary concentration for nanoparticle synthesis reactions (except where noted) as to mitigate the effects of promiscuous reducing agents and cell death, while balancing sufficient nanoparticle yield for characterization and analysis.

3.3.2 Loss of Outer Membrane Cytochromes Decreases Pd Nanoparticle Size and Alters Cellular Localization

Pathways for both soluble and insoluble metal reduction are well-studied in *S. oneidensis*[75]. These EET pathways utilize a network of electron transfer proteins to direct metabolic electron flux from the cytoplasm, across the periplasm, and into the extracellular space (Figure 3.1a). As reduction of Pd(II) is necessary for nanoparticle formation, we examined the effect of strains lacking key components of this network. The outer membrane *c*-type cytochromes, MtrC and OmcA, are critical mediators of extracellular electron transfer to metal substrates and have shown some influence on affecting the localization of produced nanoparticles[165]. We hypothesized that they may also participate in Pd(II) reduction and that a knockout strain (Δ*mtrC*Δ*omcA*) would exhibit distinct nanoparticle properties. Additionally, periplasmic hydrogenases have demonstrated Pd(II) reduction activity in *S. oneidensis* and several other bacteria[168–170]. Thus, we also examined the characteristics of Pd nanoparticles formed by a hydrogenase deficient strain (Δ*hydA*Δ*hyaB*).

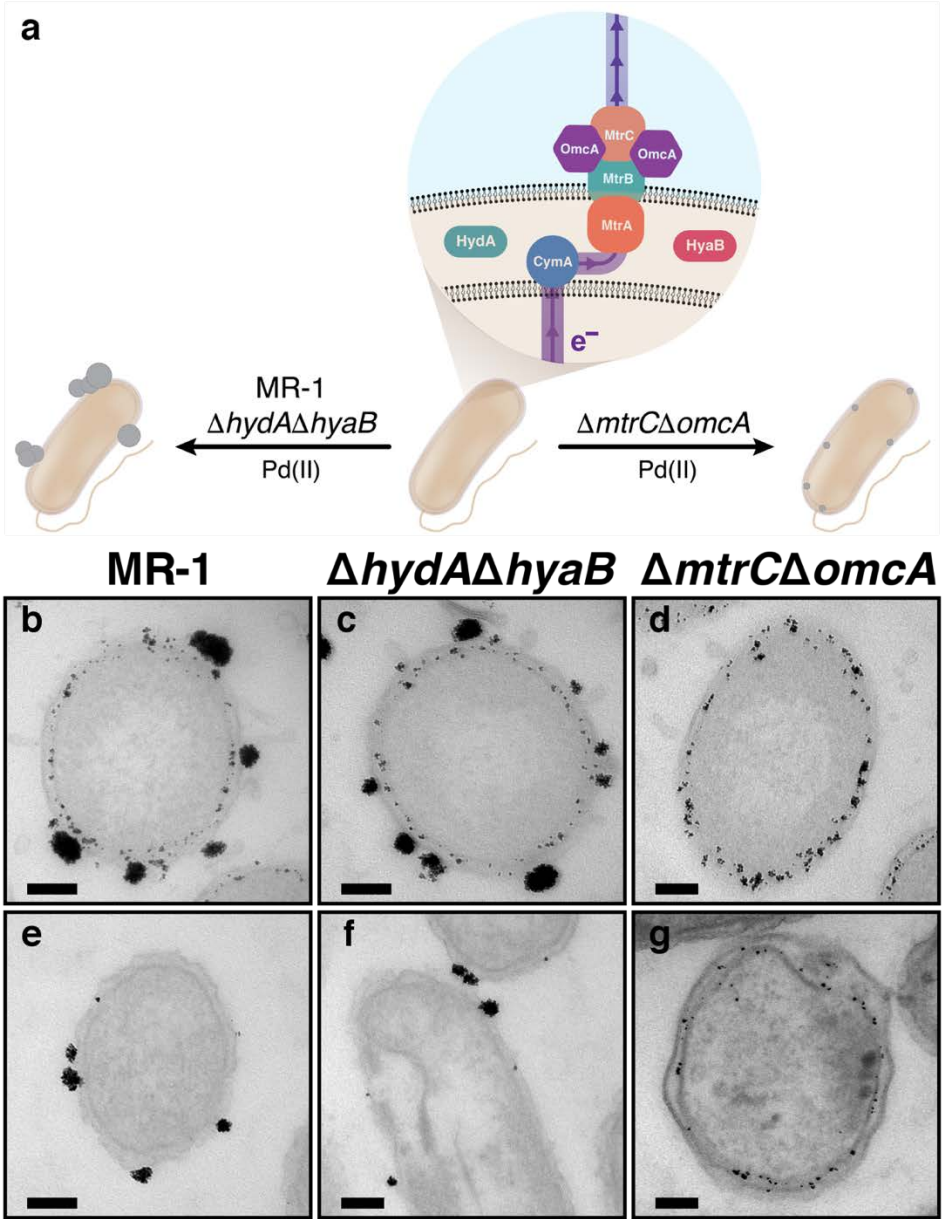

Figure 3.1: Formation of extracellular Pd nanoparticles requires outer membrane cytochromes.

(a) General diagram of electron transport in *S. oneidensis* and genotypic effects on Pd nanoparticle formation. Thin section transmission electron micrographs of *S. oneidensis* (b) MR-1, (c) Δ*hydA*Δ*hyaB*, and (d) Δ*mtrC*Δ*omcA* after 24 hour reactions containing 1000 µM Pd(II). *S. oneidensis* (e) MR-1, (f) Δ*hydA*Δ*hyaB*Δ, and (g) *mtrC*Δ*omcA* after 2 hour reactions containing 100 µM Pd(II). Scale bars represent 100 nm.

Noticeable differences between nanoparticle reaction mixtures containing different strains were observed shortly after bacterial inoculation. Reactions inoculated with MR-1 or the Δ*hydA*Δ*hyaB* strain turned a diffuse black color that is characteristic of reduced Pd[170], while those with the Δ*mtrC*Δ*omcA* mutant remained relatively colorless. Similarly, the cell pellets for the MR-1 and the Δ*hydA*Δ*hyaB* strains were dark black, while the Δ*mtrC*Δ*omcA* pellet appeared light grey (Figure B.8). Whole mount TEM showed that these differences arose based on the size of nanoparticles generated by each strain. The large particle population observed on MR-1 was not found on the Δ*mtrC*Δ*omcA* strain and only small nanoparticles were adherent to this cytochrome double knockout (Figure B.9). In contrast, nanoparticles on the Δ*hydA*Δ*hyaB* strain were identical to those on MR-1, exhibiting both large and small particle populations. As whole mount TEM cannot resolve the cellular location of particles, thin section TEM was performed. Thin sectioning of all three strains revealed that the two populations of particles not only differ in size, but also in cellular localization: smaller (<10 nm) particles localized to the periplasm and larger particle aggregates (~50 nm) adhered to the outer membrane and faced the extracellular space (Figure 3.1b-g, 3.2, B.10). Consistent with whole mount observations, MR-1 and the Δ*hydA*Δ*hyaB* strain contained both particle populations, while the Δ*mtrC*Δ*omcA* strain lacked extracellular particles. A similar change in UO_2 nanoparticle localization has previously been observed with this mutant[165]. Across all strains, no Pd particles were detected within the bacterial cytoplasm, indicating that reduction primarily occurred in the periplasm or extracellular space. When comparing bacteria palladized at 100 and 1000 μM Pd(II), increased overlap in the nanoparticle size distributions between strains was observed at the higher concentration of Pd(II) (Figure 3.2). However, nanoparticle localization and size was more binary at the lower Pd(II) concentration. At 100 μM Pd(II), particles exclusively nucleated extracellularly on the outer membrane (MR-1, Δ*hydA*Δ*hyaB*) or within the periplasm (Δ*mtrC*Δ*omcA*) (Figure 3.1e-g). Together, our data suggest that low Pd(II) concentrations accentuate genotypic differences, whereas decreased cell viability at high Pd(II) concentrations (Figures B.3-B.4) results in more promiscuous Pd(II) reduction.

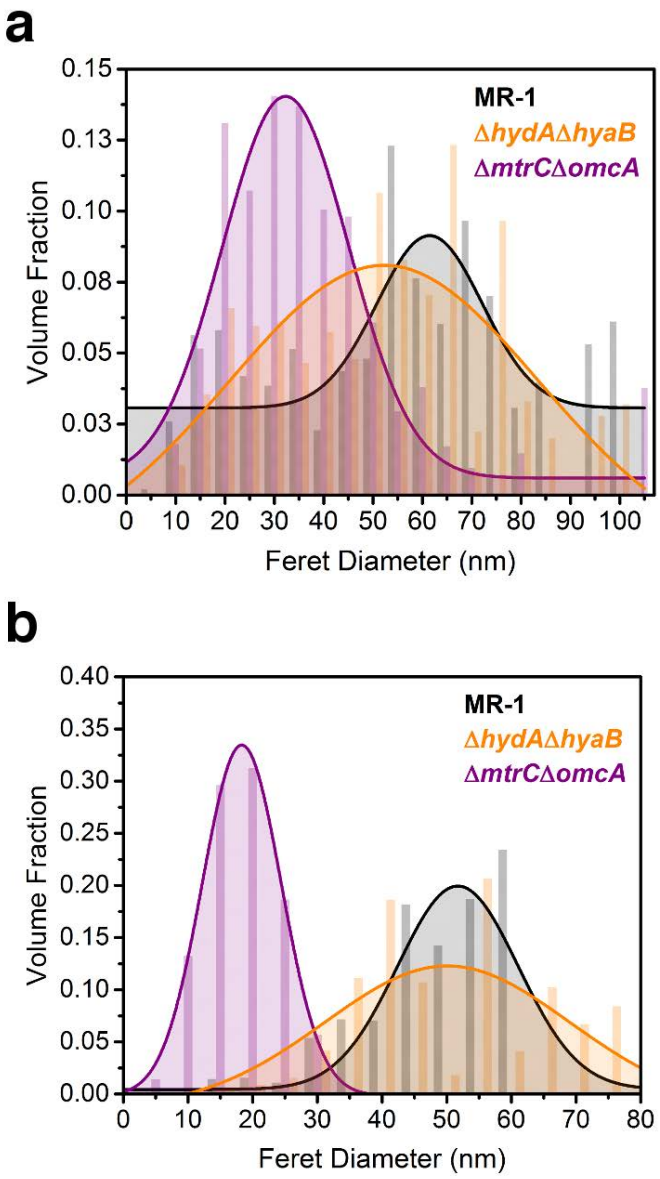

Figure 3.2: Loss of outer membrane cytochromes decreases Pd nanoparticle size.

Nanoparticle size distributions at (a) 1000 µM and (b) 100 µM Pd(II) were determined by analyzing thin section transmission electron micrographs (n = 5 images) for each strain.

In addition to TEM, powder x-ray diffraction (PXRD) was used to characterize the properties of bacterial Pd nanoparticles. PXRD patterns can reveal the chemical identity and relative size of analyzed nanomaterials. Differences between *S. oneidensis* strains were

detected by PXRD, and corroborated trends observed by TEM (Figure B.11). While nanoparticles formed by MR-1 and the Δ*hydA*Δ*hyaB* mutant had comparable patterns, broader peaks were observed for those from the Δ*mtrC*Δ*omcA* strain, indicating smaller grain size of Pd nanocrystallites as predicted by the Scherrer equation[290]. The observed peak locations were consistent with previous Pd-*Shewanella* studies and with abiotic Pd(0) patterns[156], verifying that peaks were a result of palladization. Additionally, our collected patterns suggest that cell-associated Pd nanocrystals possess rhombic dodecahedron or octahedron structures[291]. These results further demonstrate the importance of outer membrane cytochromes in controlling nanoparticle properties and show that PXRD can be used to distinguish genotypic differences.

The existence of the two particle populations illuminates how bacterial membranes and outer membrane cytochromes influence nanoparticle nucleation and growth. Cellular compartmentalization appears to physically constrain nanoparticle structure size, as evidenced by intracellular particles limited in size by periplasmic dimensions (<50 nm), while extracellular particles further aggregated (>50 nm) (Figure 3.2). Importantly, bacterial genotype controlled particle localization, since loss of outer membrane cytochromes MtrC and OmcA was coincident with loss of outer membrane particles (Figure 3.1d, 3.1g). Nanoparticle reaction mixtures that replaced *S. oneidensis* with a bacterium lacking cell-surface cytochromes (*Escherichia coli* MG1655) similarly exhibited no large extracellular particles formed on bacteria (Figure B.12). Additionally, post-palladization viability studies performed on MR-1 and the Δ*mtrC*Δ*omcA* strain showed that changes in cell viability do not account for the differences between particle phenotypes (Figure B.13). In sum, these results suggest that outer membrane cytochromes are sites of electron transfer to Pd(II) and may participate in Pd nanoparticle nucleation.

3.3.3 Loss of Outer Membrane Cytochromes Attenuates Pd(II) Reduction

Generally, the structures of biosynthesized metabolites are invariant to the rate at which they are produced. In contrast, metal ion reduction rates can exert significant influence over the size and morphology of produced nanoparticles[162]. To assess whether

reduction kinetics could explain differences in Pd particle size/localization between *S. oneidensis* strains, we quantified Pd(II) concentrations over the course of nanoparticle synthesis.

With all strains, extracellular Pd(II) concentrations were measured as low as 50 μM at the first time point (starting concentration was 100 μM), indicating rapid Pd(II) adsorption to cells upon bacterial inoculation (Figure 3.3). Reaction mixtures with *E. coli* MG1655 also showed Pd(II) adsorption to cells, but no Pd(II) reduction was detected on the same time scale (Figure B.14). Following the initial adsorption event, we measured a comparable first-order Pd(II) reduction rate[232] between MR-1 and the hydrogenase deficient mutant when lactate was utilized as an electron donor (Figure 3.3, B.15). Although kinetic differences between these strains have previously been measured when utilizing formate[168], less metabolic electron flux is directed to the quinone pool from formate catabolism[95]. This suggests that the outer membrane cytochromes are primarily responsible for Pd(II) reduction when electron flux can be directed through the Mtr pathway, which utilizes the quinone pool. Accordingly, the Δ*mtrC*Δ*omcA* strain showed attenuated Pd(II) reduction relative to MR-1. These results differed from a previous study, where a strain lacking these cytochromes had a rate of reduction rate that was identical to MR-1[168]. Although we measured a specific reduction rate by lactate-fed MR-1 over the initial three hours (69×10^{-12} μmol cell^{-1} h^{-1}) that was comparable to this report (20×10^{-12} μmol cell^{-1} h^{-1}), we consistently measured an order of magnitude difference in the fitted kinetic rate constants between MR-1 and the Δ*mtrC*Δ*omcA* strain (Figure 3.3). We attribute these conflicting observations to the significant effects that buffering capacity can exert on the kinetics of Pd(II) reduction by *S. oneidensis*. We note that our bacterial pregrowth and nanoparticle reaction mixtures utilized substantially more buffered media (100 mM HEPES) than this previous study (30 mM HEPES). Even under our conditions, Pd(II) reduction rate greatly decreased with increasing age of dissolved HEPES in pregrowth and reaction media (Figure B.16) and day-to-day variability was observed in the amounts of Pd(II) reduced. Cell growth can alter culture medium acidity, and the pH stability of strongly buffered media may counter physiological shifts such as cytochrome

downregulation or inactivity that otherwise occurs[292]. Alternatively, the loss of MtrC and OmcA increased the variability between biological replicates, which could arise from the increased role of promiscuous reductants as opposed to specific electron transport pathways. This may have further obscured kinetic differences between strains in previous studies. Despite this increased kinetic variability, TEM-observed particle properties seemed invariant to day-to-day reduction kinetics, as the Δ*mtrC*Δ*omcA* strain always exhibited the small particle phenotype (Figure 3.1d, 3.1g). Taken together, our results are consistent with previously purported nanoparticle formation mechanisms by *S. oneidensis*: Pd(II) adsorbs to cells, Pd(II) is reduced, and Pd nanoparticles nucleate[168]. Notably, our results highlight the importance of outer membrane cytochromes in the latter two steps.

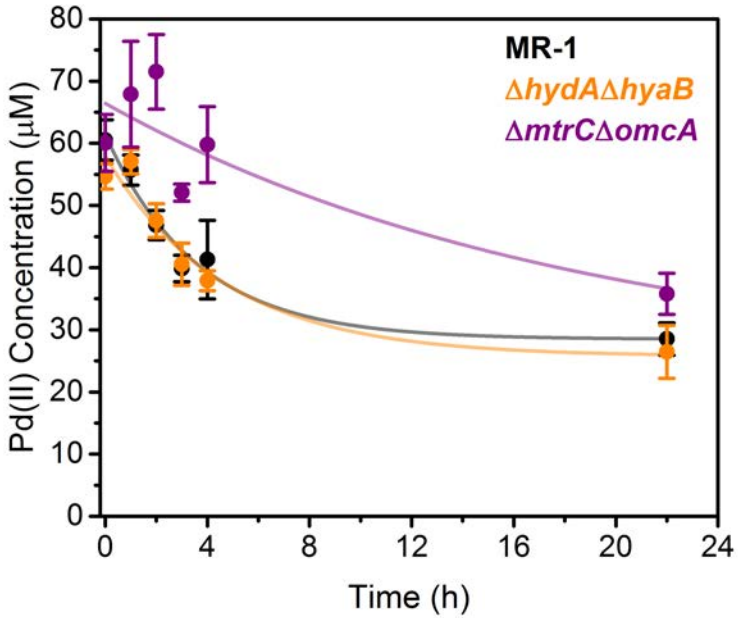

Figure 3.3: Loss of outer membrane cytochromes attenuates Pd(II) reduction rate.

Extracellular Pd(II) concentrations during nanoparticle synthesis was quantified for *S. oneidensis* MR-1, Δ*hydA*Δ*hyaB*, and Δ*mtrC*Δ*omcA*. Raw data for each strain was fitted to a first order exponential decay and depicted are the fitted curves overlaid onto the mean ± S.E from each experimental time point. First order rate constants ± fitting error were 0.28 ± 0.08 h^{-1} for MR-1, 0.22 ± 0.06 h^{-1} for Δ*hydA*Δ*hyaB*, and 0.05 ± 0.02 h^{-1} for Δ*mtrC*Δ*omcA*. n = 3.

3.3.4 MtrC Expression Controls Extracellular Pd Nanoparticle Formation

To better understand the role of MtrC and OmcA in Pd(II) reduction and nanoparticle formation, we complemented the Δ*mtrC*Δ*omcA* strain with one of three plasmids that was either an empty control vector or vectors carrying *mtrC* and *omcA* under constitutive control[293].

We first tested whether the presence of either MtrC or OmcA was sufficient to restore the extracellular particle phenotype observed with MR-1. Whole mount TEM showed that Δ*mtrC*Δ*omcA* strains carrying either an empty vector or an *omcA*-expressing vector were unable to form large nanoparticles that are characteristic of extracellular localization (Figure B.17). However, large particles were observed on the double knockout strain complemented with a plasmid carrying *mtrC*. Thin section TEM confirmed that large particles formed by this *mtrC*-complemented strain were extracellular and adherent to the bacterial outer membrane (Figure 3.4, B.18). The average nanoparticle size for the *mtrC*-complemented strain was significantly larger relative to the Δ*mtrC*Δ*omcA* strain with an empty plasmid (Figure 3.5). Interestingly, structures that appear similar to previously reported bacterial vesicles[294,295] were observed with the *mtrC*-complemented strain in addition to almost all other *S. oneidensis* strains tested in this study. However, their presence did not appear to influence nanoparticle formation. MR-1 carrying an empty plasmid also exhibited the extracellular particle phenotype, which validated that MtrC expression is critical for particle nucleation on the outer membrane and plasmid maintenance does not interfere with this process. These results are consistent with previous reports that describe MtrC functioning in the Mtr pathway[86]. In these studies, MtrC expression restored EET to Fe(III) species in outer membrane cytochrome deficient strains, while OmcA only partially contributed to EET. OmcA may act as a non-critical helper protein that requires MtrC to receive electrons for subsequent metal reduction. Our results suggest that this mechanism is also true for Pd(II) reduction.

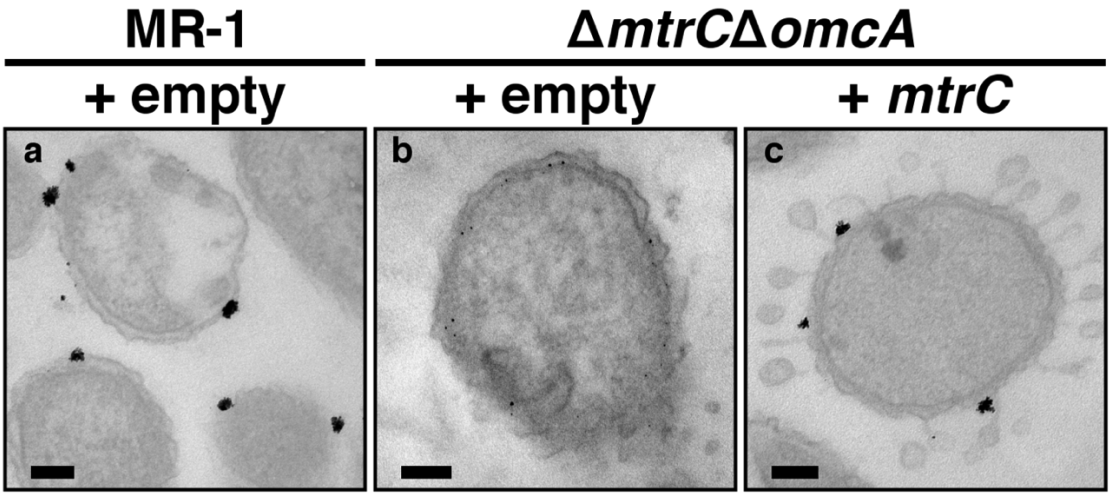

Figure 3.4: MtrC expression controls extracellular localization of Pd nanoparticles.

Thin section transmission electron micrographs of *S. oneidensis* (a) MR-1 with an empty vector and Δ*mtrC*Δ*omcA* with an (b) empty vector or (c) *mtrC* vector after 2 hours with 100 μM Pd(II). Scale bars represent 100 nm.

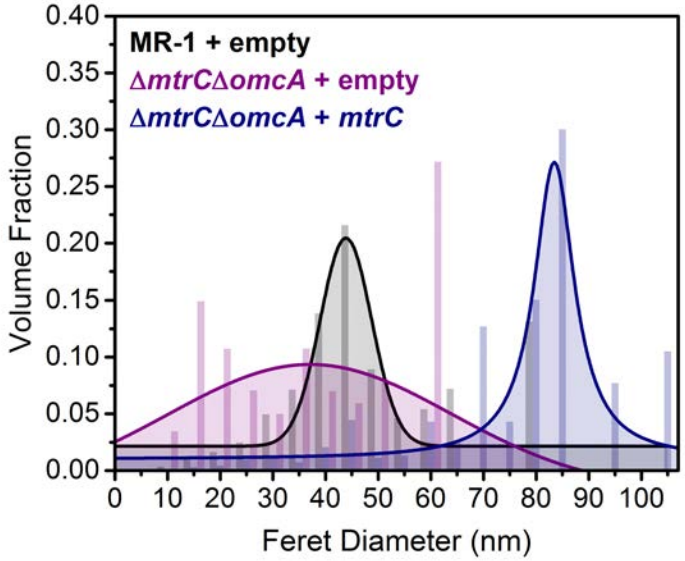

Figure 3.5: Plasmid-based MtrC expression rescues large particle phenotype in *S. oneidensis* Δ*mtrC*Δ*omcA*.

Nanoparticle size distributions for *S. oneidensis* MR-1 carrying an empty plasmid and *S. oneidensis* Δ*mtrC*Δ*omcA* carrying either an empty or *mtrC*-expressing plasmid after 2 hours with 100 μM Pd(II).

We next measured Pd(II) reduction kinetics with the *mtrC*-complemented mutant to assess whether wild-type Pd(II) reduction was rescued. Indeed, reduction was substantially faster with the *mtrC*-complemented mutant relative to the same mutant carrying an empty plasmid (Figure 3.6, B.15). Moreover, the *mtrC*-complemented mutant exhibited a faster Pd(II) reduction rate compared to MR-1 carrying an empty plasmid. This is likely due to different MtrC expression levels between our engineered strain and MR-1. Taken together with our microscopy and knockout results, our complementation studies confirm that MtrC is a critical enabler of Pd(II) reduction and contributes to extracellular nanoparticle nucleation. The complementation kinetics also suggest that manipulating expression levels of MtrC may be a viable means for tuning Pd(II) reduction rates or controlling Pd nanoparticle localization.

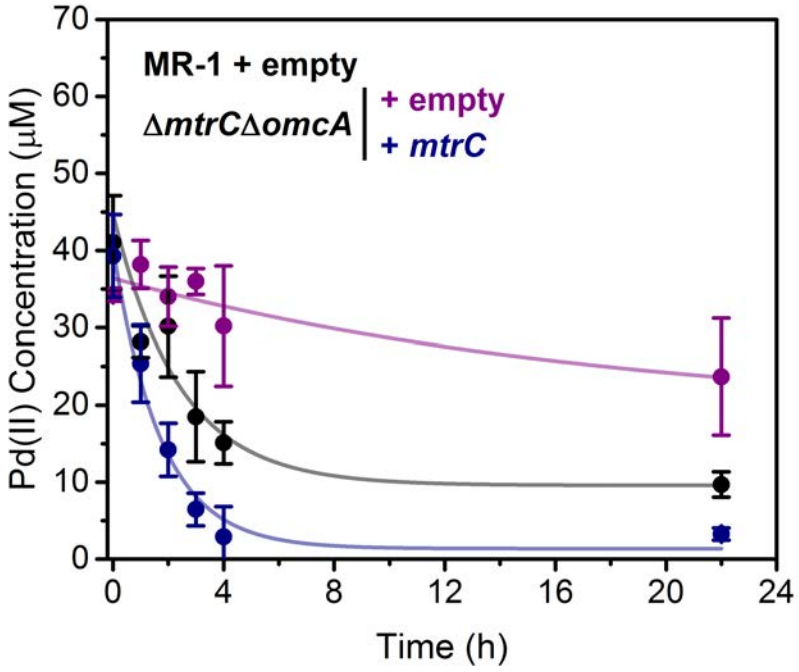

Figure 3.6: MtrC expression rescues Pd(II) reduction rate.

Extracellular Pd(II) concentrations during nanoparticle synthesis were quantified for plasmid-complemented *S. oneidensis* strains. Raw data for each strain was fitted to a first order exponential decay and depicted are the fitted curves overlaid onto the mean ± S.E from each experimental time point. First order rate constants ± fitting error were 0.42 ± 0.15 h-1 for MR-1 +empty, 0.06 ± 0.03 h-1 for Δ*mtrC*Δ*omcA* +empty, and 0.58 ± 0.15 h-1 for Δ*mtrC*Δ*omcA* +*mtrC*. n = 3.

3.3.5 Flavins Decrease Outer Membrane-Nanoparticle Size

Flavins are a family of redox-active small-molecules that function in *E. coli*, *Shewanella*, and other microorganisms[267]. In *Shewanella*, they have been implicated in a unique role of accelerating electron transfer to insoluble metal substrates[117]. Strains lacking a key periplasmic flavin exporter (Δ*bfe*) exhibit significantly attenuated electron transfer to iron oxides and electrodes[120]. It has been proposed that flavin binding to MtrC and other outer membrane cytochromes is critical for enabling direct-contact electron transfer to insoluble substrates[118]. Furthermore, flavins are known chelators that can bind to a variety of soluble and insoluble metal species[117,296]. These findings suggest that flavin concentration may also play a role in nanoparticle synthesis by influencing electron transfer and/or instructing metal binding.

We measured Pd nanoparticle properties in response to flavin supplementation of the nanoparticle reaction mixture. Nanoparticle size decreased in a dose-dependent manner with increasing riboflavin concentration (1, 10, 100 μM), when analyzed by whole mount TEM (Figure B.19). Similarly, supplementing reaction mixtures with flavin mononucleotide (100 μM) caused a small-particle phenotype (Figure B.20). Thin section TEM demonstrated that in the presence of exogenous flavins, Pd nanoparticles were localized to both the periplasm and outer membrane (Figure 3.7). However, extracellular particles were significantly smaller (<10 nm) and in greater number per cell compared to the non-supplemented reaction mixtures (Figure 3.8). This differs substantially from strains lacking *mtrC*, which generated smaller particles exclusively confined to the periplasm (Figure 3.1d, 3.1g). Riboflavin and flavin mononucleotide are thought to directly mediate electron transfer by binding to OmcA and MtrC[118], respectively, and an increase in cytochrome-binding may explain the greater number of Pd nanoparticles on the outer membrane. In contrast to flavins, supplementing other respiration substrates (sodium fumarate and Fe(III)-citrate) showed no effect on nanoparticle size (Figure B.21, B.22). Additionally, we measured no effect on cell viability when supplementing with flavins, which discounts the influence of stress response on affecting nanoparticle formation

(Figure B.23). These results support our hypothesis that, unlike other metabolites, flavins play a role in either electron transfer to Pd(II), particle nucleation/growth, or both.

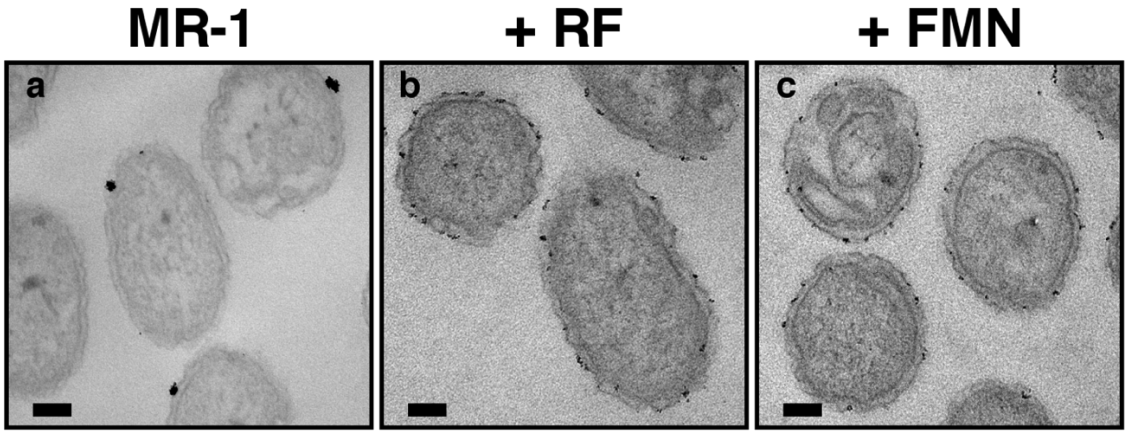

Figure 3.7: Flavin supplementation decreases size of extracellular Pd nanoparticles.

Thin section transmission electron micrographs of *S. oneidensis* (a) MR-1 and MR-1 with (b) 100 μM riboflavin (RF) or (c) 100 μM flavin mononucleotide (FMN) after 2 hours with 100 μM Pd(II). Scale bars represent 100 nm.

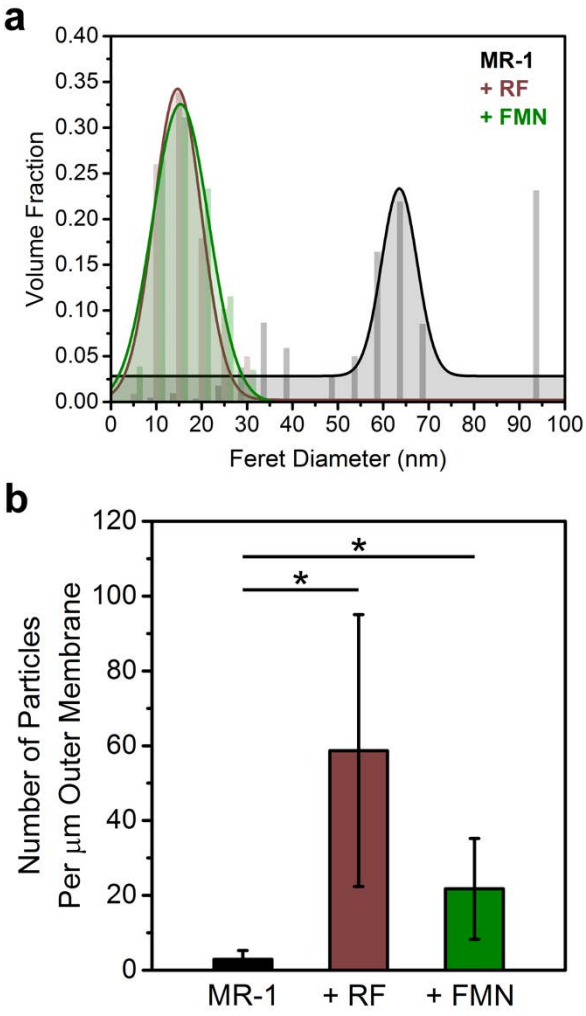

Figure 3.8: Flavin supplementation decreases Pd nanoparticle size and increases particle count per cell.

(a) Nanoparticle size distributions for unsupplemented *S. oneidensis* MR-1 and MR-1 supplemented with 100 μM riboflavin (RF) or 100 μM flavin mononucleotide (FMN). (b) Outer membrane-normalized particle counts for unsupplemented and flavin-supplemented MR-1. Histogram bars represent the mean ± S.D. of n = 5 micrographs per sample. *, $p < 0.05$.

To further investigate this mechanism, we measured Pd(II) reduction kinetics in the presence of 100 μM of exogenous riboflavin or flavin mononucleotide. Pd(II) reduction rates of MR-1 supplemented with flavins were slightly slower compared to samples omitting supplementation (Figure 3.9). While previous findings suggest that flavins are not

critical mediators of electron transfer to soluble metal acceptors[120,293], their function in precipitation of soluble Pd appears more nuanced and with competing factors at play. Attenuated Pd(II) reduction could be explained by flavins binding and sequestering soluble Pd(II). Flavins could also act as capping agents that passivate growing nanoparticle surfaces and hinder further Pd(II) reduction[297]. Indeed, the presence of riboflavin or flavin mononucleotide in an abiotic synthesis of Pd nanoparticles using $NaBH_4$ prevented significant particle aggregation relative to a flavin-free control (Figure B.24). Overall, our results demonstrate that flavins exert control over Pd nanoparticle size and may influence reduction rate without affecting their cellular localization.

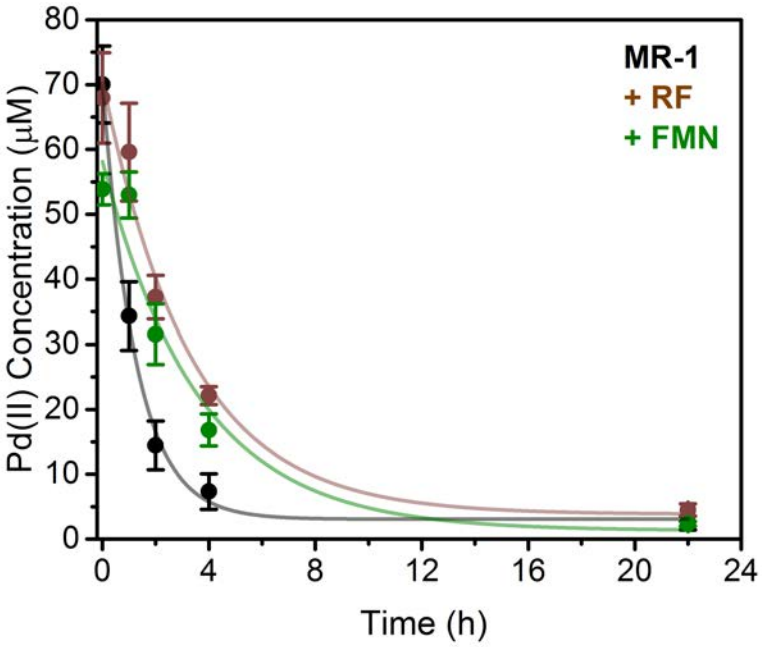

Figure 3.9: Flavin supplementation affects Pd(II) reduction rate by *S. oneidensis*.

Extracellular Pd(II) concentrations were quantified for unsupplemented *S. oneidensis* MR-1 and *S. oneidensis* MR-1 supplemented with 100 μM riboflavin (RF) or 100 μM flavin mononucleotide (FMN). Raw data for each strain was fitted to a first order exponential decay and depicted are the fitted curves overlaid onto the mean ± S.E from each experimental time point. First order rate constants ± fitting error were 0.81 ± 0.13 h^{-1} for unsupplemented MR-1, 0.31 ± 0.07 h^{-1} for MR-1 with RF, and 0.28 ± 0.06 h^{-1} for MR-1 with FMN. n = 3.

3.4 CONCLUSIONS

To summarize, we determined that the EET components, MtrC and flavins, can exert significant influence over Pd nanoparticle formation by *Shewanella oneidensis*. By adjusting their concentration in the bacterial environment, significant changes were actuated in Pd nanoparticle synthesis rate, size, and cellular localization.

Knockout and complementation experiments confirmed that the outer membrane cytochrome, MtrC, is a critical enabler of rapid Pd(II) reduction and extracellular nanoparticle nucleation. Notably, expression of MtrC via an engineered plasmid led to Pd(II) reduction rates that were faster than wild-type controls. Given this observation, coupled with the loss of extracellular particles on *mtrC* knockouts, we hypothesize that more fine-tuned expression of MtrC may correlate to different numbers and sizes of produced nanoparticles. This strategy may also be adapted to standard chassis organisms that express functional MtrC, such as engineered *E. coli* strains[298], or other electroactive bacteria possessing Pd(II)-reducing outer membrane cytochromes (e.g. *Geobacter sulfurreducens*)[299,300]. Alternatively, nanoparticle formation could be varied by directly engineering the MtrC polypeptide sequence, either through rational or evolutionary mutagenesis. Altering the redox-potential and catalytic activity of heme-containing proteins is well-precedented[301], and key mutations could be applied to identify/tune the Pd(II) reduction activity of MtrC hemes[110]. Additionally, a binding-site for iron oxide nanoparticles to the outer membrane cytochrome, MtrF, has recently been elucidated using protease footprinting[302], and similar methods could be used to identify and affect residues involved in particle nucleation by MtrC.

We observed a decrease in the size of Pd nanoparticles with increasing concentration of supplemented flavins to nanoparticle reaction mixtures. Reduction kinetics again appear to play a role in nanoparticles produced in the presence of flavins; however, unlike the effect of *mtrC* deletion, nanoparticles formed with flavins were extracellularly bound to the bacterial membrane. Given our understanding of flavin interaction with soluble metals and metal surfaces, it is likely that increased flavin concentration alters nanoparticle dimensions through binding and nucleation interactions.

Shewanella-secreted flavins have been measured as ~0.1-1.5 μM in culture supernatants[120,303], therefore our supplementations (100 μM) far exceeded physiologically generated concentrations. However, strains with additional flavin biosynthesis pathways have increased secreted concentrations to as high as ~25 μM[130]. Further pathway engineering would likely increase this concentration and potentially facilitate control over nanoparticle size. Flavin binding to outer membrane cytochromes likely also plays a role in the observed particle phenotypes[118], and we speculate that modulating flavin-cytochrome binding affinities through protein engineering could produce similar effects without exogenous supplementation[110]. Overall, our results shed further light on the role of flavins in *S. oneidensis*-metal chemistry and demonstrate another means of tunability for biological nanoparticle synthesis.

Biological generation of inorganic structures most commonly arises in nature through the actions of complex protein and metabolic networks. However, engineered systems have been described where relatively simple biological interactions (e.g., amyloid fibers[148], phage scaffolds[44]) can direct nanomaterial morphologies. We present an alternative strategy that uses single genetic or metabolic factors of viable *S. oneidensis* cells to control Pd nanoparticle phenotype. Our results, combined with the genetic tractability of *S. oneidensis*, suggest that it may serve as an intriguing model platform for studying nanoparticle biogenesis and engineering these particles for catalysis and sensing applications.

3.5 Materials and Methods

3.5.1 Chemicals and Reagents

Sodium tetrachloropalladate(II) trihydrate ($Na_2PdCl_4 \cdot 3H_2O$, Strem Chemicals), argon (Ar, Airgas), 4-(2-Pyridylazo)resorcinol ($C_{11}H_9N_3O_2$, Alfa Aesar), HEPES Free Acid Powder ($C_8H_{18}N_2O_4S$, Sigma-Aldrich), potassium phosphate dibasic (K_2HPO_4, Sigma-Aldrich), potassium phosphate monobasic (KH_2PO_4, VWR), sodium chloride (NaCl, VWR), ammonium sulfate $(NH_4)_2SO_4$, Fisher Scientific), magnesium(II) sulfate

heptahydrate ($MgSO_4 \cdot 7H_2O$, Sigma-Aldrich), EDTA acid disodium salt dihydrate ($C_{10}H_{14}N_2Na_2O_8 \cdot 2H_2O$, VWR), manganese(II) sulfate monohydrate ($MnSO_4 \cdot H2O$, VWR), ferrous sulfate heptahydrate ($FeSO_4 \cdot 7H_2O$, Alfa Aesar), cobalt(II) nitrate hexahydrate ($Co(NO_3)_2 \cdot 6H_2O$, Strem Chemicals), calcium chloride dihydrate ($CaCl_2 \cdot 2H_2O$, Sigma-Aldrich), zinc(II) sulfate monohydrate ($ZnSO_4 \cdot H_2O$, Strem Chemicals), cupric sulfate pentahydrate ($CuSO_4 \cdot 5H_2O$, VWR), aluminum potassium sulfate ($AlK(SO_4)_2$, Acros Organics), boric acid (H_3BO_3, VWR), sodium molybdate dihydrate ($Na_2MoO_4 \cdot 2H_2O$, Beantown Chemical), sodium selenite (Na_2SeO_3, Acros Organics), sodium tungstate dihydrate ($Na_2WO_4 \cdot 2H_2O$, Alfa Aesar), nickel(II) chloride hexahydrate ($NiCl_2 \cdot 6H_2O$, Alfa Aesar), D-(+)-glucose ($C_6H_{12}O_6$, Sigma-Aldrich), flavin adenine dinucleotide disodium salt hydrate ($C_{27}H_{31}N_9Na_2O_{15}P_2 \cdot xH_2O$, Sigma-Aldrich), riboflavin ($C_{17}H_{20}N_4O_6$, Alfa Aesar), kanamycin sulfate ($C_{18}H_{38}N_4O_{15}S$, Growcells) and casamino acids (VWR) were used as received. For thin section preparation, cacodylate buffer, glutaraldehyde (50%), paraformaldehyde (16%), potassium ferrocyanide, and osmium tetroxide, and epoxy resin solutions were obtained from Electron Microscopy Sciences. Sodium DL-lactate ($C_3H_5NaO_3$, VWR, 60% in water) was filtered using 0.2 µm PES filters. Sodium fumarate ($Na_2C_4H_2O_4$, VWR) was diluted in H_2O and then filtered using 0.2 µm PES filters. LB Lennox agar powder (VWR) was dissolved in H_2O and sterilized at 121°C and 100 kPa for 1 h. Kanamycin sulfate stock was dissolved in H_2O and filter sterilized using 0.2 µm PES filters. When preparing *Shewanella* Basal Medium, all components were added to H_2O and filter-sterilized using 0.2 µm PES filters.

3.5.2 Bacterial Strains and Culture

Bacterial strains, plasmids, and their sources are listed in Table B.1. Except where noted, liquid cultures and nanoparticle biosynthesis reactions occurred in autoclaved Hungate culture tubes capped with a butyl-rubber stopper and plastic screw-cap. Pregrowth for nanoparticle biosynthesis reactions was prepared as follows. Bacterial stocks stored in 20% glycerol at -80 °C were freshly streaked onto LB agar plates (containing 25 µg mL^{-1} kanamycin when appropriate) and incubated aerobically for ~18 hours at 30 °C (*S.*

oneidensis) or 37 °C (*E. coli*). Colonies were picked from these plates and used to inoculate Hungate tubes containing pregrowth medium that was comprised of *Shewanella* Basal Medium with 100 mM HEPES[304], 5 mL L^{-1} trace metal mix[139], 0.05% casamino acids, 20 mM sodium lactate (*S. oneidensis*) or 20 mM glucose (*E. coli*), and 40 mM sodium fumarate. After inoculation, tubes were incubated at 30 °C and shaken for ~18 hours at 250 rpm. Anoxic conditions were maintained by bubbling all solutions, flushing tube headspace, and overpressuring Hungate tubes (>15 psi) with argon. During transient exposure to atmosphere (during inoculation and between washes/centrifugations), solutions were strictly handled under a gassing cannula that jettisoned argon.

3.5.3 Nanoparticle Biosynthesis

To prepare 3 mL of a standard nanoparticle biosynthesis reaction, 4 mL of anaerobic pregrowth was started the previous day. Once pregrowth reached stationary-phase, the entire volume was transferred to a 15 mL conical tube and centrifuged at 3400 rcf for 1 h. The supernatant was removed, 1 mL of degassed SBM containing trace metal mix was used to resuspend the pellet, and this suspension was subsequently transferred to a sterile 1.5 mL microcentrifuge tube for centrifugation at 6000 rcf for 20 minutes. A second 1 mL SBM wash/centrifugation was performed and the bacterial suspension was concentrated to an OD_{600} of 3.0 in 200 µL, which was to be later used as reaction inoculum. 2.8 mL of reaction volume was prepared by mixing 8.55 µL of sodium lactate (60% w/w) and 30 µL of freshly prepared 10 mM $Na_2PdCl_4 \cdot 3H_2O$ (dissolved in autoclaved Milli-Q H_2O) to 2.76 mL of SBM containing trace metals. This mixture was bubbled with argon and then transferred to sealed Hungate tubes. Prior to inoculation, tube headspace was flushed with additional argon for 15 minutes. Using sterile syringe needles, the entire bacterial inoculum volume was injected into to the reaction mixture, setting the final OD_{600} to 0.2., and the first time point was simultaneously aliquoted. The headspace of reaction mixtures was briefly flushed with argon for 1 minute, and incubated inside a shaker at 30 °C and 250 rpm. All time point aliquots (~300 µL) were flash frozen in liquid N_2 and store at -20 °C for later analysis. Reactions with higher concentrations of Pd(II) or 0.05%

casamino acids were performed when indicated. For reactions inoculated with plasmid-complemented knockouts, kanamycin was supplemented to mixtures at a concentration of 25 μg mL^{-1}. To perform viability controls, heat-killed MR-1 were prepared by incubating twice-washed cells at 80 °C for 20 minutes. Lysed MR-1 were prepared by sonicating twice-washed cell pellets with a Qsonica 55 probe (Qsonica, LLC,Newtown, CT) for 90 seconds at 4 °C, maintaining between 10-15 W of output energy and alternating between ten-seconds "ON" and 5-seconds "OFF". For *E. coli*-inoculated reactions, sodium lactate was replaced with 20 mM glucose and reactions were incubated at 37 °C. As noted in the Results and Discussion, the age of HEPES in SBM pregrowth and reaction mixtures significantly affected Pd(II) reduction. Therefore, HEPES was dissolved in SBM for pregrowth and nanoparticle reaction mixtures and used within 2 weeks.

3.5.4 Transmission Electron Microscopy

Palladized bacteria were prepared as described above. Nanoparticle synthesis was stopped after 2 hours (100 μM Pd(II)) or 24 hours (1 mM Pd(II)), and cells were centrifuged/washed twice. In early experiments, cells were washed with SBM containing trace metals as to minimize osmotic shock, but we later found that autoclaved H_2O could be utilized with minimal change in cell shape and improved electron micrograph contrast. For whole mount TEM, washed cells were concentrated to an OD_{600} of ~2.7 and 5 μL was drop-cast onto glow-discharged 200 mesh carbon-coated copper TEM grids (Electron Microscopy Sciences). For thin section TEM, cells were fixed prior to sectioning and imaging. First, a 100 mL cation stock solution was prepared that contained $CaCl_2 \cdot 2H_2O$ (0.3 g) and $MgSO_4 \cdot 7H_2O$ (1 g). Next, aldehyde fixation solution was prepared by mixing 1 mL of cation stock with 5 mL of cacodylate buffer (0.2 M, pH 7.4), 0.8 mL of glutaraldehyde (50%), 1.25 mL of paraformaldehyde (16%), and 2 mL of H_2O. The washed cell pellet was resuspended in 1 mL of aldehyde fixation solution and incubated at room temperature for 4 hours. After, cells were washed three times in 0.1 M cacodylate buffer. An osmium tetroxide fixation solution was prepared immediately before use by mixing in a 1:1 ratio of 4% potassium ferrocyanide in 0.2 M cacodylate buffer (also prepared

immediately before use) and 4% osmium tetroxide. The cell pellet was resuspended in 1 mL osmium textroxide fixation solution and incubated for 4 hours on ice. Next, the pellet was resuspended in H_2O for 10 minutes, spun-down, and repeated until the supernatant was clear (~10 washes required). Subsequently, the pellet was dehydrated in 50, 70, 95%, and 100% (twice) ethanol, for 15 minutes at each dehydration. After the final 100% ethanol wash, the pellet was washed in acetone for 15 minutes, twice. Next, the pellet was infiltrated with 30% epoxy resin in 100% acetone, 66% resin in 100% acetone, and finally 100% resin (twice), for ~16 hours with each infiltration. Finally, the pellet was placed in fresh epoxy resin, cast into a sectioning-block mold, and heated at 65 ºC for 2 days. Sectioning was accomplished using a Leica UltraCut Microtome and sections were placed on copper TEM grids to for imaging. Whole mount and thin section TEM was performed using a FEI Tecnai Transmission Electron Microscope.

3.5.5 Nanoparticle Size and Number Analysis

Representative thin section TEM images (n = 5) for each sample were analyzed using Fiji 1.0. Image thresholding enabled counting and determination of the Feret diameter for isolated particles. Results were binned into histograms for each sample and fit to a Gaussian distribution using OriginPro 8.1. To analyze relative particle counts per cell, each visible outer membrane in an image was traced and the perimeter lengths were summed. The threshold-determined particle counts for a single image were normalized by the summed outer membrane length for that same image. This process was repeated for each of the 5 sample-representative TEM images, which allowed statistics to be obtained for comparing different samples.

3.5.6 Pd(II) Quantification

Extracellular Pd(II) concentrations were primarily quantified using the colorimetric 4-(2-pyridylazo)-resorcinol (PAR) assay[305], the general procedure is as follows. A 0.1% PAR stock solution was freshly prepared by dissolving 25 mg PAR in 1 mL 1% NaOH, and then adding this solution to 24 mL MilliQ H_2O. A stock solution of 100 mM EDTA

was also prepared and the pH was adjusted to 10.5 using NaOH. Frozen nanoparticle reaction mixture aliquots (~300 µL) were quickly thawed and centrifuged at 10,000 rcf for 5 minutes to pellet bacteria. Next, 100 µL of each reaction mixture supernatant was added to microcentrifuge tubes containing 500 µL of the 100 mM EDTA stock and 5 µL of the 0.1% PAR stock. This solution was heated at 80 ºC for 10 minutes, cooled at 4 ºC for 20 minutes, and absorbance at 515 nm was measured using a CLARIOStar platereader (BMG Labtech). Standard curves were prepared in SBM containing trace metals over a range of 0-125 µM Pd(II). Flavins exhibit absorbance overlapping that of PAR, which obscured Pd(II) quantification using this method. Therefore, inductively coupled plasma mass spectrometry (ICP-MS) was used to obtain reduction kinetics in the presence of flavins. To prepare samples for ICP-MS, aliquots were thawed, centrifuged at 10,000 rcf for 5 minutes, and the supernatant mixed in a 1:1 ratio with strong (~70%) nitric acid. Samples were further diluted 80-fold in weak (~2%) nitric acid to bring total dissolved solids to ppm levels and then analyzed using an Agilent 7500ce ICP-MS. Pd(II) concentration at each time point was then calculated based on the degree of sample dilution.

3.5.7 Powder X-Ray Diffraction

To analyze biogenic particles by PXRD, 10 mL of nanoparticle reaction mixtures using 1000 µM Pd(II) were prepared and inoculated with MR-1, Δ*mtrC*Δ*omcA*, or Δ*hydA*Δ*hyaB*. After ~18 hours, cells were washed by centrifuging at 3400 rcf for 40 minutes, removing supernatant, and adding equal volume of autoclaved MilliQ H_2O. Two more washes were performed, and after the supernatant was removed in the final wash, 1 mL of acetone was used to resuspend the pellet. This acetone-cell suspension was transferred to a microcentrifuge tube and centrifuged for 20 minutes at 6000 rcf. Acetone was again used to resuspend cells, and this suspension was vacufuged to aspirate the supernatant and pellet dried cell mass. X-ray diffraction (XRD) was performed on a Rigaku R-Axis Spider diffractometer with an image plate detector using Cu Kα radiation (λ=1.54 Å) and a graphite monochromator. XRD samples were prepared by mixing a small amount of dried cell mass with a droplet of mineral oil followed by mounting on a cryoloop.

3.5.8 Flow Cytometry Analysis

To quantify side scatter and viability of *S. oneidensis*, cultures were collected after 2 hr of Pd(II) reduction as described above and centrifuged (all spins 20 minutes at 6000 rcf). Cells were washed twice in 0.85% NaCl solution and incubated in 200 µL BacLight Live/Dead (Invitrogen) dye mixture (2.5 µL propidium iodide per mL NaCl solution) for 15 minutes. Cells were again washed twice in NaCl solution to remove unbound dye, and normalized to 10^6 cells/mL for flow cytometric analysis on a BD LSRFortessa Flow Cytometer (ICMB Core Facilities, University of Texas at Austin) using the PE-Texas Red filter (excitation of 488 nm and emission of 610/20 nm). Single cell events were gated for subsequent analyses (Figure B.5).

3.5.9 Statistical Analysis

Unless otherwise noted, data are reported as mean ± S.E. of n = 3 biological replicates, as this sample size was sufficiently large to detect significant differences in means. Significance was calculated using a two-tailed unpaired Student's t-test (α=0.05) and OriginPro Software (OriginLab, Northhampton, MA).

Chapter 4: Microbial reduction of metal-organic frameworks enables synergistic chromium removal[3]

4.1 Chapter Summary

Redox interactions between electroactive bacteria and inorganic materials underpin many emerging technologies, including bioelectrochemical cells and bioremediation. However, commonly utilized materials, such as metal oxides, suffer from a lack of tunability and can be challenging to characterize, leaving relatively limited choices for applications seeking to pair electroactive metabolism with insoluble substrates. Metal-organic frameworks are materials exhibiting well-defined structures, high crystallinity, large surface areas, and extensive chemical tunability, but their utility as microbial substrates has not been examined. Here, we report that metal-organic frameworks can support the growth of the metal-reducing bacterium *Shewanella oneidensis*. Specifically, we demonstrate that Fe(III)-containing frameworks, MIL-100 and Fe-BTC, can be reduced via the microbe's extracellular electron transfer pathways and that reduction rate is tied to framework structure. In a practical application, we show that cultures containing *S. oneidensis* and reduced metal-organic frameworks can remediate lethal concentrations of Cr(VI), and that pollutant removal exceeds the performance of either component in isolation or bio-reduced iron oxides. Repeated cycles of Cr(VI) dosing had little effect on bacterial viability or Cr(VI) adsorption capacity. This demonstrates that the framework confers protection to the bacteria, which continuously regenerate Cr(VI)-reactive Fe(II). Together, our results show that metal-organic frameworks can serve as microbial respiratory substrates and suggest that they may offer a promising alternative to metal oxides in applications seeking to combine the advantages of bacterial metabolism and synthetic materials.

[3]Adapted from Springthorpe, S.K., Dundas, C.M., Keitz, B.K. (2019) Microbial reduction of metal-organic frameworks enables synergistic chromium removal. *Nat. Commun. 10*, 5212. Christopher M. Dundas conceived, designed, and performed the experiments, contributed to data analysis, and contributed to writing the chapter.

4.2 INTRODUCTION

Redox-active minerals support the growth of microorganisms capable of extracellular electron transport in anaerobic environments[64]. These microbe-mineral interactions play a key role in biogeochemical processes, including the nitrogen and carbon cycles[306,307], as well as nascent technologies like microbial fuel cells[58] and bioremediation[237]. For many of these applications, iron oxides are commonly employed as low-cost and widely available substrates for microbial reduction. However, iron oxides are significantly limited in structural diversity and only a fraction can be prepared under laboratory conditions[308]. Moreover, even relatively accessible structures, such as ferrihydrite ($FeOOH{\cdot}0.4H_2O$), are recalcitrant to structural characterization[308]. As such, synthetic materials may offer opportunities to better leverage microbial metabolism and improve applications dependent upon both microbial physiology and material characteristics.

One emerging alternative to metal oxides are metal-organic frameworks. Relative to metal oxides, these materials generally exhibit higher surface areas, superior crystallinity, and can possess oxide-like redox-activity[309]. Metal-organic frameworks also facilitate the development of highly tunable structure-function relationships since properties such as pore size, linker identity, and metal node can be varied independently of one another[310]. As a result, they have received significant interest across several fields, including gas separations[311], catalysis[312], drug delivery[313], and environmental remediation[314]. Despite their advantages over metal oxides and potential presence in nature[315], metal-organic frameworks have not been examined as substrates for the growth of metal-reducing or -oxidizing microorganisms. Due to their high surface areas and redox-active nature, we hypothesized that metal-organic frameworks could support microbial growth and potentially augment biological/material applications that rely upon biologically-driven redox transformations.

Here, we tested whether select iron-based metal-organic frameworks can serve as respiratory electron acceptors for the metal-reducing bacterium *Shewanella oneidensis* MR-1 (Figure 4.1). We chose the frameworks Fe-BTC (BTC = 1,3,5-

benzenetricarboxylate), $Fe_3O(BTC)_2(OH)•nH_2O$ (MIL-100), and $Fe_3O[(C_2H_2(CO_2)_2]_3(OH)•nH_2O$ (MIL-88A) for our growth and reduction assays, as their nodes are a well-precedented *S. oneidensis* substrate (namely, Fe(III)), the frameworks are water-stable, and they span a range of morphologies. We established that bacterial growth and Fe(III) reduction can occur on metal-organic frameworks in the absence of material toxicity, and that reduction occurs using known *S. oneidensis* metabolic and protein (MtrCAB) pathways (Figure 4.1a). Two frameworks (MIL-100 and Fe-BTC) exhibited accelerated reduction rates relative to a model iron oxide (ferrihydrite), which we attribute to the higher surface areas of the metal-organic frameworks.

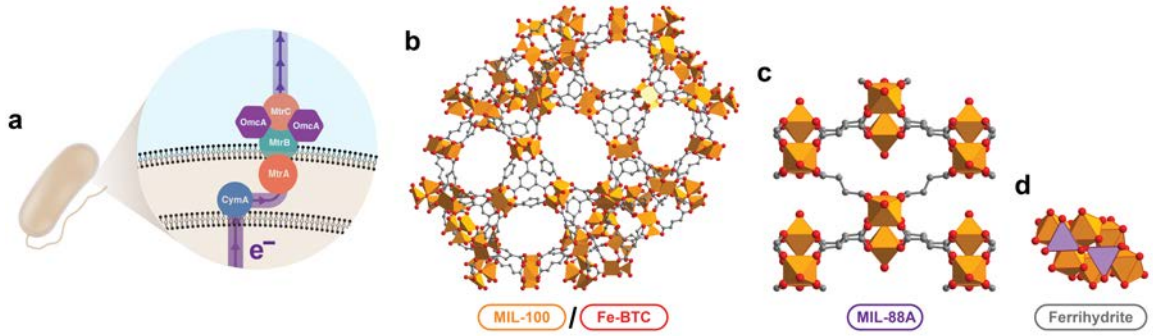

Figure 4.1: *S. oneidensis* MR-1 metal reduction pathway and metal-organic framework structure.

(a) The MtrCAB pathway by which *S. oneidensis* reduces both soluble and insoluble metal species[64]. (b-d) The crystal structure of MIL-100/Fe-BTC[316,317] (b), MIL-88A[318] (c), and ferrihydrite[319] (d). Fe-BTC does not have a known crystal structure (due to its amorphous nature), but it is analogous to MIL-100.

Applying this microbe-material pairing, we found that *S. oneidensis* and metal-organic frameworks synergistically facilitate bioremediation of Cr(VI), a known environmental and carcinogenic pollutant. Microbial reduction of framework-bound Fe(III), especially in MIL-100, generated high levels of redox-active Fe(II) that increased Cr(VI) reduction and its adsorption to frameworks. Notably, Cr(VI) removal rates and capacities drastically exceeded those of biotic metal oxides, abiotic frameworks, and *S. oneidensis* alone. When operated together, a cycling treatment scheme was enabled, whereby *S. oneidensis* continuously regenerated reactive Fe(II) that could treat multiple

Cr(VI) additions. Under our conditions, we found that MIL-100 protected the bacteria from lethal challenges of Cr(VI) and that tens of treatment cycles were possible. Overall, our results highlight the ability of metal-organic frameworks to support bacterial growth and reduction in a structure dependent manner and demonstrate how the advantages of these materials can be co-opted for pollutant adsorption when coupled to bacterial metabolism.

4.3 RESULTS

4.3.1 Stability of metal-organic frameworks in abiotic culture conditions

Prior to using the materials as microbial substrates, we examined the stability of metal-organic frameworks under abiotic culture conditions. We chose the Fe(III)-containing metal-organic frameworks MIL-100, Fe-BTC, and MIL-88A due to their reported aqueous stability, range of crystallinities, and range of surface areas[320,321]. To determine if the materials were stable in typical culture conditions, each metal-organic framework (initial Fe(III) concentration set to 15 mM) was suspended in *Shewanella* Basal Medium (SBM) containing 20 mM lactate and anaerobically stored at 30 °C for 48 h. Our SBM formulation was buffered with 100 mM HEPES and contained 0.05% casamino acids and 1X Wolfe's Mineral Solution (ATCC). After 48 h, powder X-ray diffraction (PXRD) patterns were collected and the leaching of potential microbial substrates, namely Fe(III) for all three metal-organic frameworks and fumarate in MIL-88A, was also monitored. MIL-100 and Fe-BTC maintained structural integrity, as indicated by agreement between the as synthesized and exposed patterns. On the other hand, MIL-88A exhibited a slight, but detectable, change in its PXRD pattern (Figure C.1a). Furthermore, none of the materials showed significant leaching of Fe(III) or fumarate (Figure C.1b-c). These results indicate that the metal-organic frameworks were stable under our culture conditions and could be used as insoluble substrates for *S. oneidensis.*

4.3.2 Metal-organic frameworks support microbial growth and reduction

We first examined whether *S. oneidensis* MR-1 could use iron-based metal-organic frameworks as respiratory substrates for cell growth. In addition to the frameworks, MIL-100, Fe-BTC, and MIL-88A, we utilized the *Shewanella* growth substrate ferrihydrite in order to draw comparisons with iron oxides. To monitor the growth of *S. oneidensis*, each material was suspended in SBM containing lactate as the carbon source and inoculated with anaerobically pregrown cells. Colony forming units (CFU) from plated dilutions of each material-bacteria suspension were used to measure cell concentration. With MIL-100, Fe-BTC, and ferrihydrite suspensions, we observed comparable increases in cell concentration after 12 hours that stayed constant up to 24 hours (Figure 4.2a). Concomitant Fe(III) reduction was also observed with these three materials (Figure C.2). In contrast, cell concentration in the MIL-88A suspension significantly decreased over a 24-hour period ($P = 0.028$, two-tailed t-test), while Fe(II) levels slightly increased. As a control, we measured cell concentration of *S. oneidensis* MR-1 in electron acceptor-free medium and found that, although CFU counts slightly increased over this same timescale, they were still an order of magnitude lower than suspensions containing MIL-100, Fe-BTC, and ferrihydrite (Figure C.3). Additionally, we incubated *Escherichia coli* MG1655 in lactate supplemented media with and without MIL-88A. In both cases, CFU counts increased to comparable levels, indicating MIL-88A does not impede *E. coli* growth. Thus, the decrease in viable CFU counts in *S. oneidensis*-MIL-88A suspensions is not due to inability of *S. oneidensis* to respire and suggests MIL-88A exhibits *Shewanella*-specific toxicity. We posited this toxicity might arise due to MIL-88A particle morphology. Indeed, scanning electron micrographs (SEM) revealed that MIL-88A formed small needle-like particles whereas MIL-100, Fe-BTC, and ferrihydrite generated large, morphologically similar particle aggregates (Figure C.4). Overall, the frameworks MIL-100 and Fe-BTC facilitated increases in cell growth that were associated with simultaneous Fe(III) reduction, similar to ferrihydrite.

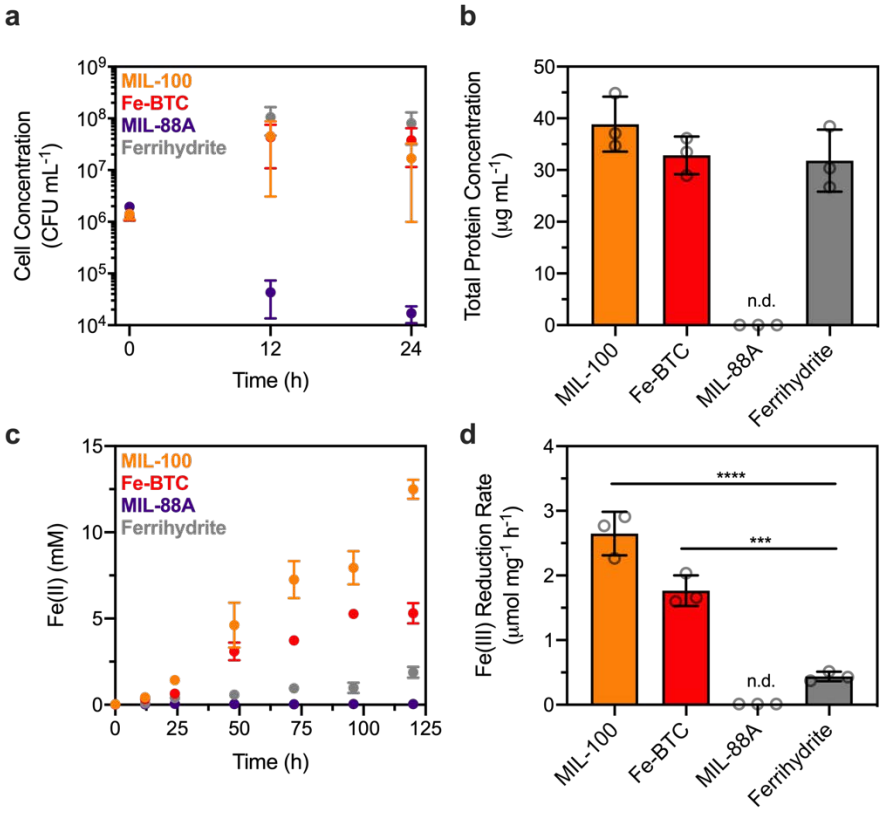

Figure 4.2: Growth of *S. oneidensis* MR-1 and reduction of metal-organic frameworks.

(a) CFU counts of *S. oneidensis* MR-1 (inoculating OD_{600}=0.002) grown on MIL-100, Fe-BTC, MIL-88A, and ferrihydrite over 24 h. Data show mean ± S.E. for three independent biological replicates. (b) Total protein concentration of *S. oneidensis* MR-1 (inoculating OD_{600}=0.002) grown on MIL-100, Fe-BTC, MIL-88A, and ferrihydrite after 120 h. Data shown are mean ± S.D. for three independent biological replicates. (c) Total Fe(II) concentrations in suspensions containing *S. oneidensis* MR-1 (inoculating OD_{600}=0.002) and either MIL-100, Fe-BTC, MIL-88A, or ferrihydrite over 120 h. Data shown are mean ± S.D. for three independent biological replicates. (d) Total protein normalized Fe(III) reduction rates for *S. oneidensis* (inoculating OD_{600}=0.002) MR-1 grown on either MIL-100, Fe-BTC, MIL-88A, or ferrihydrite as measured at 120 h. "n.d." indicates that the rate could not be determined due to lack of detectable biomass. Data shown are mean ± S.D. for three independent biological replicates. Figures (b)-(d) were collected in the same experiment. For Figure (d), statistical comparisons were made to ferrihydrite using a one-way ANOVA with Dunnett's post-test, ***P=0.001, ****P<0.0001.

As CFU counts on insoluble materials can violate the assumption that one bacterium results in one CFU, we sought to confirm cell growth via other biomass

measurements. Increases in cellular DNA were measured using the fluorescent dye, Syto™ 9 (ThermoFisher Scientific). The fluorescent dye SYPRO™ Ruby (ThermoFisher Scientific) was also used to monitor increases in extracellular biofilm matrix proteins. This non-specific dye is known to stain a large variety of proteins, including glycoproteins, phosphoproteins, lipoproteins, calcium binding proteins, and fibrillar proteins. Starting with a ten-fold higher starting concentration of *S. oneidensis* MR-1 compared to our CFU counts (to improve signal-to-noise), we in parallel measured Fe(II) levels, Syto™ 9 fluorescence, and SYPRO™ Ruby fluorescence over 48 h for MIL-100 and ferrihydrite suspensions. For each bacteria-material suspension, Syto™ 9 signal increased and rapidly plateaued to relatively similar extents after ~8 h (Figure C.5a). Likewise, the SYPRO™ Ruby signals for biotic material suspensions increased at comparable rates (Figure C.5b). Together, these fluorescence results corroborate the similar increases in CFU counts for *S. oneidensis* grown on MIL-100 and ferrihydrite.

Finally, we quantified total protein levels after material reduction using the Bradford assay. With the exception of MIL-88A, all material suspensions exhibited similar increases in protein content after 120 h and were measured as ca. 30-40 μg mL^{-1} (Figure 4.2b). This yield is comparable to previously reported stationary-phase protein levels for *S. oneidensis* MR-1[322]. Protein levels in the MIL-88A suspension were below the assay's limit of detection, which indicated a lack of appreciable biomass accumulation and further confirmed the measured decreases in CFU counts. Based on all our biomass/CFU results, in the absence of material toxicity, biomass accumulation appears relatively invariant to the framework used and comparable to growth with a model iron oxide (ferrihydrite). Our results are also in agreement with previous *Shewanella* growth studies on soluble/insoluble iron substrates, which showed that cell yields were similar regardless of electron acceptor used[323].

Simultaneous monitoring of Fe(II) levels over time and end-point biomass measurements for each material-bacteria suspension enabled the calculation of biomass-normalized Fe(III) reduction rates. Across all abiotic material suspensions, Fe(II) levels

remained low and did not increase in control experiments, indicating that increases in Fe(II) were due to cellular activity. In contrast, each biotic material suspension showed distinct extents of Fe(III) reduction over time (Figure 4.2c). After 120 h, both MIL-100 and Fe-BTC exhibited similar biomass-normalized rates of reduction that were significantly higher from that of ferrihydrite (Figure 4.2d). Comparable trends in reduction rate were observed from biomass and Fe(II) levels measured after 48 h (Figure C.6). At all timescales, the Fe(III) reduction rate for MIL-88A could not be determined due to the lack of appreciable Fe(II) and biomass. Encouraged by the drastic differences in raw Fe(II) kinetics and biomass-normalized Fe(III) reduction rates with each framework and ferrihydrite, we further examined the biological and material effects influencing framework reduction.

4.3.3 Genetic and metabolic effects on metal-organic framework reduction

Towards understanding the mechanism of metal-organic framework reduction by *S. oneidensis*, we assessed the importance of key genetic and metabolic factors that are well established for metal oxide reduction. We tested whether Fe(III) reduction is a result of active cellular metabolism by comparing Fe(II) levels across material suspensions containing either healthy or metabolically impaired *S. oneidensis* MR-1 cells. In agreement with our observed increases in CFU counts and biomass on MIL-100 and Fe-BTC, heat killed cells and cell lysate did not yield appreciable Fe(III) reduction on these materials (Figure 4.3a). These results imply that growth and metabolic activity are necessary for Fe(III) reduction in the tested frameworks. In our experiments, lactate was presumed to be the primary electron donor of our medium formulation. Indeed, higher levels of Fe(III) reduction occurred in the presence of 20 mM lactate relative to formulations where it was omitted (Figure 4.3b). However, even without lactate, Fe(II) levels were markedly higher in biotic samples over abiotic, suggesting other electron donors (e.g., chamber atmosphere H_2) were metabolically accessible. In lactate-supplemented medium, metabolite measurements revealed that lactate consumption generally followed the extent of Fe(III) reduction for *S. oneidensis* MR-1 cultures containing either MIL-100, Fe-BTC, or ferrihydrite (Figure C.7a). Additionally, metabolic intermediates associated with lactate

catabolism/anaerobic respiration were generated in both framework- and ferrihydrite-containing cultures (i.e., pyruvate and acetate)[94]. Collectively, these results indicate that *S. oneidensis* reduces Fe(III) in MIL-100, Fe-BTC, and iron oxides using similar metabolic pathways (Figure C.7b).

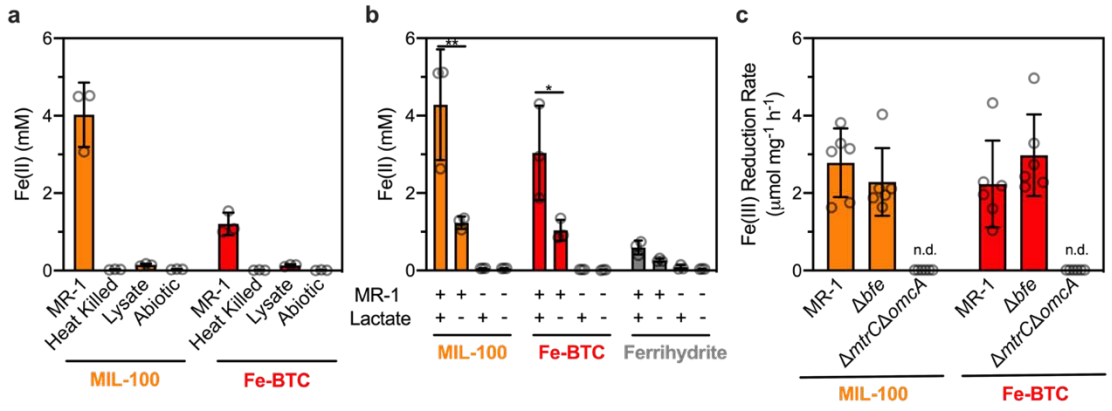

Figure 4.3: Genetic and metabolic effects on reduction.

(a) Fe(II) concentrations after 48 h in cultures containing either heat-killed, lysed , or whole cell inocula of *S. oneidensis* MR-1(inoculating OD_{600}=0.002). Data shown are mean ± S.D. for three independent biological replicates. (b) Fe(II) concentrations after 48 h for cultures of *S. oneidensis* MR-1 (inoculating OD_{600}=0.02) with 0 mM lactate or 20 mM lactate. "+" indicates the presence of either *S. oneidensis* MR-1 or lactate, while "-" indicates the absence of the components. Data shown are mean ± S.D. for three independent biological replicates. Three abiotic replicates are also shown. Statistical comparisons were made between lactate "+" and lactate "-" biotic samples using two-way ANOVA and Sidak's post-test. *P=0.0255, **P=0.0014. (c) Total protein normalized Fe(III) reduction rate of *S. oneidensis* MR-1 and knockout strains Δ*bfe* and Δ*mtrC*Δ*omcA* after 48 h. "n.d." indicates that the rate could not be determined due to lack of detectable biomass. Data shown are mean ± S.D. for six independent biological replicates.

We next attempted to identify the direct contributors to Fe(III) reduction by *S. oneidensis* and determine how they compare to previously reported iron oxide reduction pathways. In *S. oneidensis* MR-1, catabolic electron flux is linked to the respiration of extracellular metal oxides via the MtrCAB pathway[86]. Specifically, the outer-membrane cytochromes MtrC and OmcA enable the terminal extracellular electron transfer step onto both soluble and insoluble metal species[85]. Without these proteins, *S. oneidensis* shows

attenuated respiration onto iron and graphene oxides[324]. Consistent with these results, an outer-membrane cytochrome deficient strain, Δ*mtrC*Δ*omcA*, showed diminished Fe(III) reduction and biomass accumulation when cultured with MIL-100 or Fe-BTC, relative to MR-1 (Figure 4.3c). *E. coli* MG1655, which does not possess a homolog to MtrC or OmcA and lacks electroactivity, was also unable to reduce Fe(III) in these materials (Figure C.8). In addition to direct cytochrome-based reduction, *S. oneidensis* can use soluble redox shuttles (flavins) to indirectly transfer reducing equivalents from the cell to metal oxides, with exogenously supplied flavins accelerating the rate of Fe(III) reduction[117]. Flavins bound to extracellular cytochromes can also potentially mediate extracellular electron transfer[118]. To examine the role of flavins, we cultured a *S. oneidensis* mutant that exhibits diminished flavin secretion (Δ*bfe*) with MIL-100 and Fe-BTC. While this mutant was previously reported as having Fe(III) reduction defects when grown on ferrihydrite[120], we did not observe a statistically different biomass-normalized Fe(III) reduction rate when grown on metal-organic frameworks relative to the wild-type strain (MR-1) (Figure 4.3c). Similarly, we found that supplementation of 1 μM or 10 μM riboflavin to *S. oneidensis* MR-1 cultures containing MIL-100 or Fe-BTC led to slight but statistically non-significant increases in Fe(III) reduction rates relative to non-supplemented controls (Figure C.9), indicating *S. oneidensis* MR-1 may be accessing soluble iron[120]. Thus, our data confirms that *S. oneidensis*-based Fe(III) reduction in metal-organic frameworks follows similar metabolic and protein pathways as iron oxides, and is primarily mediated by extracellular cytochromes.

4.3.4 Stability of metal-organic frameworks in the presence of *S. oneidensis*

Next, we asked if Fe(III) reduction and metabolic activity from *S. oneidensis* negatively impacted solution stability of the frameworks. Microbial reduction of iron oxides increases dissolution of oxide-bound Fe[325] and we hypothesized that similar dissolution may occur with framework-bound Fe. Additionally, *S. oneidensis* may only be able to reduce soluble Fe(III), which creates a driving force for further leaching and framework destabilization. To probe both of these scenarios, we examined post-reduction

PXRD patterns of each material. As previously mentioned, MIL-100 and Fe-BTC maintained structural integrity while MIL-88A exhibited a slight, but detectable, change in structure under abiotic culture conditions. However, post-reduction PXRD patterns showed that MIL-88A eventually decomposed under biotic conditions after 48 h (Figure 4.4a). In contrast, characteristic MIL-100 and Fe-BTC peaks were discernable after exposure to the bacteria, indicating that these materials remain structurally intact and crystalline over the course of our experiments. Additionally, we qualitatively observed that MIL-100 and Fe-BTC changed from orange to grey/black following reduction by *S. oneidensis*, suggesting Fe(II) was contained in the framework (Figure 4.4b). Similar color changes have previously been noticed with Fe-BTC when the framework was exposed to chemically reducing conditions[326]. We quantitatively confirmed that Fe(II) was contained within each framework by measuring Fe(II) in pelleted/washed samples of biotic MIL-100 and Fe-BTC (Figure 4.4c). Nonetheless, ca. 50% of the total reduced Fe in framework suspensions was soluble Fe(II) after 48 h of microbial culture. Similar to observations with iron oxides that are partially solubilized upon microbial reduction, our results indicate that *S. oneidensis* can both directly reduce Fe(III) in MIL-100 and Fe-BTC and partially remove Fe(II/III) from the framework structure while maintaining framework stability[325].

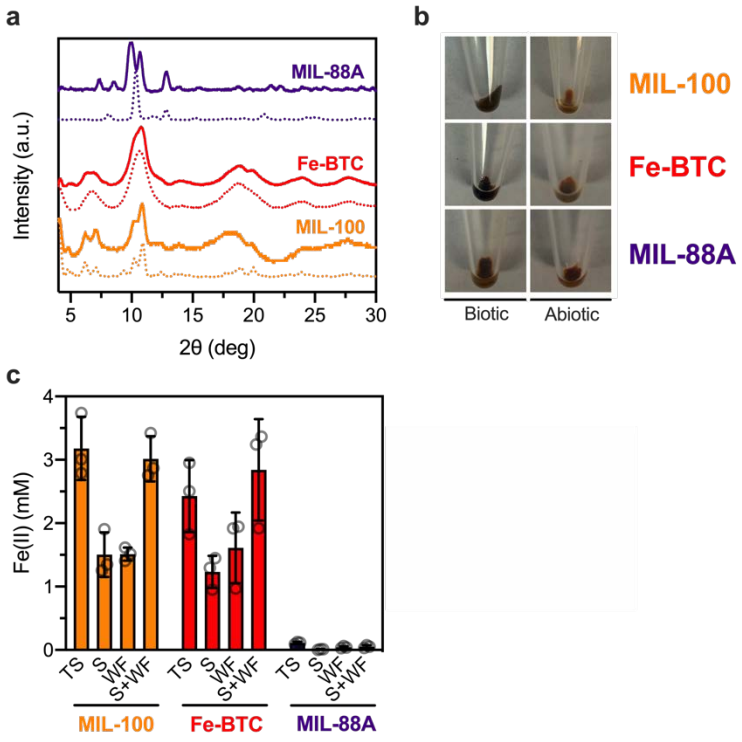

Figure 4.4: Stability of metal-organic frameworks in the presence of *S. oneidensis*.

(a) As-synthesized (dashed lines) and post-reduction (solid lines) PXRD patterns of MIL-100, Fe-BTC, and MIL-88A. (b) Images of biotic and abiotic treated MIL-100, Fe-BTC, and MIL-88A after 48 h. (c) Fe(II) concentrations as measured in the total suspension (TS), isolated supernatant (S), and isolated/washed framework (WF. The sums of the isolated supernatant and isolated/washed framework are also shown (S+WF). Data shown are mean ± S.D. for three independent biological replicates.

4.3.5 Cr(VI) adsorption by microbially-reduced metal-organic frameworks

Having determined that *S. oneidensis* electroactive metabolism can interface with structurally-intact metal-organic frameworks, we sought to harness this microbe-material pairing for environmental remediation. Detoxification and separation of environmental contaminants often leverages redox-based transformations, and many schemes are enabled by the release of reactive Fe from iron oxides. In these systems, generated Fe(II) can reductively precipitate oxidized organics and transition metals[327]. Likewise, electroactive bacteria can be used in bioreactors to directly reduce these pollutants[61]. As a result, metal-

reducing bacteria, acting in conjunction with iron oxides, have shown promise for the bioremediation of redox-controlled toxins[328].

Alternatively, high surface area inorganic adsorbents, including activated carbons and metal-organic frameworks, can be used for the remediation of environmental pollutants. For example, some metal-organic frameworks have been used for Cr(VI) adsorption, but generally show slow adsorption kinetics and limited capacities[329–331]. A more recent study found that Cr(VI) adsorption to a metal-organic framework could be dramatically improved by adding exogenous Fe(II)[332]. This result implies that, similar to the case with iron oxides, the presence of Fe(II) can enhance reductive adsorption of Cr(VI). Drawing influence from these various redox-driven and adsorptive treatments, we hypothesized that microbial reduction of Fe(III)-containing frameworks could exhibit a synergistic effect on Cr(VI) removal. Specifically, we predicted that the reduction of Cr(VI) to Cr(III) by *S. oneidensis* and microbially-generated Fe(II) would promote Cr adsorption into the framework (Figure 4.5a).

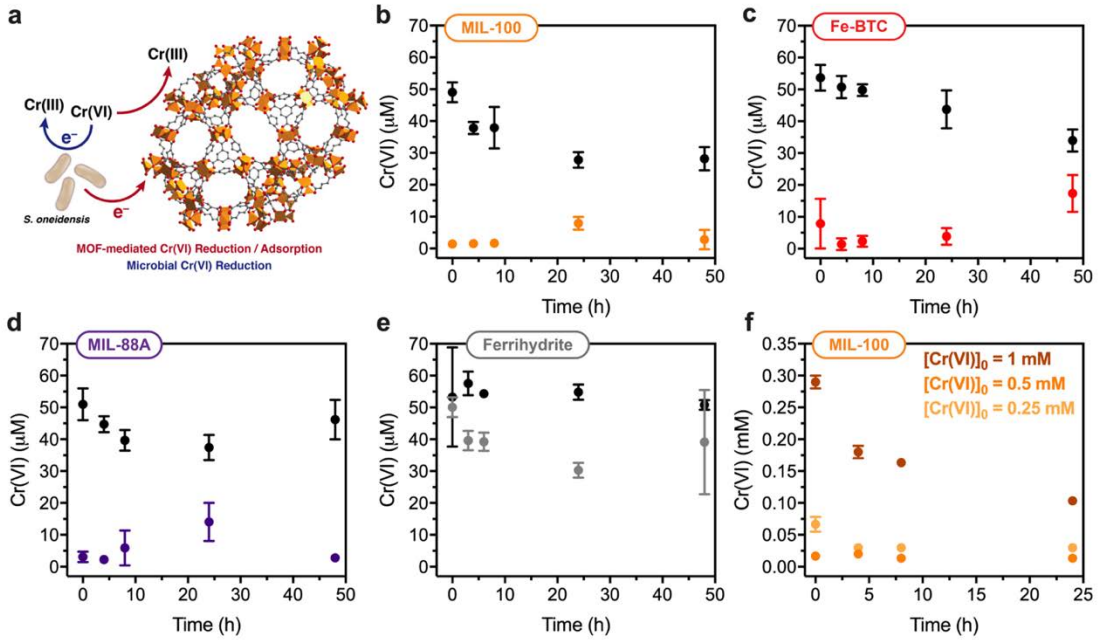

Figure 4.5: Cr(VI) removal in reduced metal-organic frameworks.

(a) Generalized scheme for Cr(VI) reduction by both *S. oneidensis* MR-1 and a reduced metal-organic framework. (b-e) Cr(VI) removal by *S. oneidensis* MR-1-reduced (b) MIL-100, (c) Fe-BTC, (d) MIL-88A, and (e) ferrihydrite when challenged with 70 μM Cr(VI). Abiotic samples for each material are shown in black. (f) Cr(VI) removal by *S. oneidensis* MR-1-reduced MIL-100 when challenged with 0.25 mM, 0.5 mM, and 1 mM Cr(VI).

In initial experiments, we grew *S. oneidensis* MR-1 on each metal-organic framework for 24 hours and then challenged the culture with a single dose of Cr(VI). At initial Cr(VI) concentrations of 70 μM, all frameworks showed immediate removal of soluble Cr(VI) below the detection limit of the diphenylcarbazide (DPC) assay (Figure 4.5b-d). Abiotic controls and biotic ferrihydrite (Figure 4.5e) showed minimal and slow Cr(VI) adsorption. In the case of MIL-100 and Fe-BTC, we found that Fe(III) reduction continued to take place after Cr(VI) addition, indicating that *S. oneidensis* was still viable under these conditions. Even though MIL-88A showed minimal Fe(III) reduction in the presence of *S. oneidensis* MR-1, the basal Fe(II) levels still reduced the relatively small initial dose of Cr(VI). These results are a preliminary indication that there is a synergistic

interaction between the frameworks and *S. oneidensis* that accelerates Cr(VI) reduction and adsorption.

To understand the range of Cr(VI) concentration that could be treated with our system, we challenged *S. oneidensis* MR-1 growing on MIL-100 with increasing concentrations of Cr(VI) up to 1 mM (Figure 4.5f). After dosing with 0.5 mM Cr(VI), *S. oneidensis* MR-1 and MIL-100 reduced all detectable Cr(VI) within minutes. Under these conditions, the total solution concentration of Cr, as measured by inductively coupled plasma – mass spectrometry (ICP-MS), fell below 10 ppm within minutes and reached ~1 ppm after 24 hours (Figure C.10). Furthermore, Fe(III) reduction continued to take place after Cr(VI) addition, suggesting that *S. oneidensis* can survive normally toxic Cr(VI) concentrations in the presence of MIL-100[178]. At 1 mM Cr(VI), *S. oneidensis* MR-1 on MIL-100 showed almost complete reduction, but over a much longer time period, indicating that this concentration is approaching the limit of toxicity for our system.

Since our system allows for both bio- and material-based mechanisms of Cr(VI) removal, we sought to disentangle the role of each in reduction/adsorption of the pollutant. As mentioned above, *S. oneidensis* can directly reduce Cr(VI) through the MtrCAB pathway. Alternatively, *S. oneidensis* may indirectly reduce Cr(VI), with bacterially-generated Fe(II) from MIL-100 acting as the mediator. Overall, we found that biotic samples in the absence of MIL-100 showed considerably slower Cr(VI) reduction kinetics and were more sensitive to the initial Cr(VI) dose (Figure C.11a). These results are consistent with previous reports indicating that 200 μM Cr(VI) is the upper limit for *S. oneidensis* MR-1 survivability[178]. We also measured Cr(VI) reduction/adsorption kinetics for *S. oneidensis* grown on ferrihydrite and found, even at low initial Cr(VI) concentrations, biotic and abiotic ferrihydrite samples exhibited slower adsorption kinetics and capacities relative to all frameworks tested (Figure 4.5). Additionally, after *S. oneidensis* had reduced appreciable amounts of Fe(III) in ferrihydrite, there was not a corresponding decrease in Cr(VI), as would have been expected if Fe(II) alone was responsible for Cr(VI) reduction. We further tested the influence of Fe(II) by adding soluble $FeCl_2 \cdot 4H_2O$ to abiotic/material-free Cr(VI) solutions. While we observed a dose dependent increase in Cr(VI) reduction

with addition of Fe(II), Cr(VI) reduction rates decreased relative to biotic/material samples and no precipitate was observed (Figure C.11b). Together, our results support a synergistic interaction between *S. oneidensis* MR-1 and MIL-100 that enhances Cr(VI) reduction/adsorption kinetics and capacity relative to material-free systems, abiotic frameworks, and *S. oneidensis* growing on iron oxides.

4.3.6 Repeated cycles of Cr(VI) removal with *S. oneidensis*-reduced MIL-100

The majority of materials for Cr(VI) adsorption require a regeneration step using pH adjustments after saturation[333]. Additionally, iron-based treatments require Fe(II) regeneration since Fe(III)-Cr aggregates form when Fe(II) reacts with Cr(VI). Based on our initial Cr(VI) adsorption experiments involving *S. oneidensis* and MIL-100, we predicted that viable cells could metabolically regenerate Fe(II) in the framework for continued Cr(VI) reduction and adsorption (Figure 4.6a). To determine and compare the recyclability of *S. oneidensis*-reduced materials, samples containing either MIL-100, ferrihydrite, or fumarate were reduced by *S. oneidensis* MR-1 for 24 h before being challenged with 10 cycles of $[Cr(VI)]_0$=0.50 mM, once every 24 hours. For all additions to *S. oneidensis* growing on MIL-100, soluble Cr(VI) was removed below the limit of detection within minutes (Figure 4.6b, Figure C.12). After 10 cycles of Cr(VI) addition, the total amount of Cr(VI) reduced by *S. oneidensis* and MIL-100 per mass of material was 78.7±0.1 mg g^{-1} (Table C.1), which represents a 125-fold increase over MIL-100 alone. When the maximum Cr(VI) capacity was assessed, we found that 320±1 mg g^{-1} was reduced after 41 cycles (Figure C.13), which compares favorably to other Cr(VI) adsorbents (Table C.2).

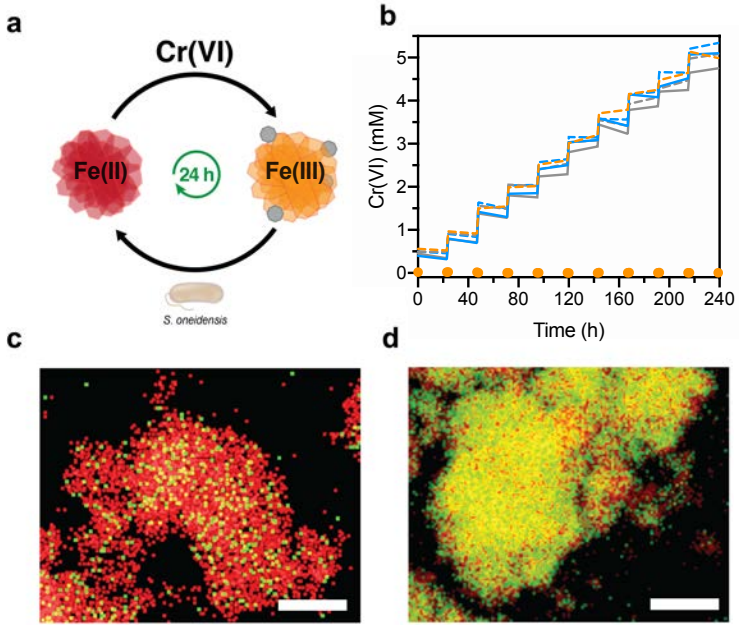

Figure 4.6: Cr(VI) cycling with reduced metal-organic frameworks.

(a) Generalized scheme for Cr(VI) cycling where *S. oneidensis* regenerates Fe(II) following Cr(VI) additions. (b) Cr(VI) removal in *S. oneidensis* MR-1-reduced MIL-100 (orange), ferrihydrite (grey) and fumarate (blue) when challenged with ten cycles of 0.5 mM Cr(VI). Abiotic samples are shown as dashed lines. (c-d) EDX element mapping of (c) abiotic cycled MIL-100 and (d) *S. oneidensis* MR-1-reduced and cycled MIL-100. Fe is shown in red and Cr is shown in green. Scale bars are 1 µm. Data show mean ± S.D. for three independent biological replicates.

In contrast, biotic and abiotic treatments with fumarate and ferrihydrite showed no appreciable Cr(VI) adsorption and the amount of Cr(VI) in solution increased after each new dose (Figure 4.6b). We also investigated whether a microbially-reduced soluble iron source could aid in removal of Cr(VI). Indeed, we found that *S. oneidensis* MR-1 grown on Fe(III)-citrate enabled instantaneous reduction after repeated cycles of 0.50 mM Cr(VI) addition (Figure C.14). However, similar to our abiotic experiment with supplemented Fe(II), no precipitate was formed upon Cr(VI) reduction (Figure C.11b). These results suggest that, under our pH operating conditions, Cr(III) can only be efficiently removed from solution in the presence of a sorbent material, such as MIL-100.

After Cr(VI) cycling, we characterized MIL-100 using scanning transmission electron microscopy (STEM) and transmission electron microscopy (TEM). Abiotic and biotic samples were morphologically similar (Figure C.15). In contrast, elemental mapping revealed that cycled abiotic MIL-100 was primarily composed of Fe with small amounts of Cr while cycled biotic MIL-100 contained substantially more Cr (Figure 4.6c-d). This result supports our solution-based measurements and confirms that metabolic reduction of MIL-100 significantly increases its overall capacity for Cr(VI) adsorption. Our cycling data suggests that *S. oneidensis* MR-1 growing on fumarate or ferrihydrite is quickly overwhelmed after repeated challenges with Cr(VI). Indeed, we observed no increase in OD_{600} in the fumarate samples following the first addition of Cr(VI), implying that cell growth was compromised (Figure C.16a). In contrast, we measured an increase in Fe(II) over the course of the cycling experiment when *S. oneidensis* was grown on MIL-100. As expected, Fe(II) concentrations decreased immediately after the addition of Cr(VI) but rebounded as viable cells continued to reduce Fe(III) (Figure C.16b). We did not measure a similar trend in Fe(III) reduction for *S. oneidensis* MR-1 grown on ferrihydrite that was repeatedly challenged with Cr(VI) (Figure C.16b). We also verified the observed trends in Fe(III) reduction during Cr(VI) cycling by directly assaying cell viability. Following the tenth Cr(VI) addition, we plated undiluted aliquots from the MIL-100, ferrihydrite, and fumarate samples onto LB agar. After overnight aerobic growth, the MIL-100 plates exhibited bacterial lawns, indicating viable bacteria remained after Cr(VI) cycling (Figure C.16c-d). In contrast, abiotic samples, biotic ferrihydrite samples, and biotic fumarate samples showed no growth on LB agar plates. Together, these results demonstrate that MIL-100 both effectively protects *S. oneidensis* from repeated challenges of cytotoxic Cr(VI) concentrations and synergistically enables Cr(VI) adsorption with rates and capacities that greatly exceed those of biotic metal oxide or abiotic metal-organic frameworks.

4.4 Discussion and Conclusions

We demonstrated that iron-containing metal-organic frameworks can serve as growth substrates for *S. oneidensis*. Biomass measurements and quantitation of Fe(II) levels revealed that these materials behave as respiratory electron sinks similarly to a model iron oxide (namely, ferrihydrite). Across various metrics, biomass yields were comparable for both nontoxic frameworks (MIL-100 and Fe-BTC) and ferrihydrite, despite large differences in the extent of Fe(III) reduction (Figure 4.2, Figure C.5). As others have observed similar results for lactate-fed *S. oneidensis* grown on a variety of electron acceptors[323], these results collectively indicate that metal respiration is not growth limiting under certain experimental conditions. While our lactate supplementation/omission and metabolite measurements demonstrated that electron flux primarily derives from lactate catabolism, significant residual Fe(III) reduction was measured in biotic lactate-free experiments compared to abiotic controls (Figure 4.3b). Since casamino acids were previously shown to be unimportant for metal oxide reduction[334], this suggests that *S. oneidensis* can metabolize dissolved H_2 from the anaerobic chamber atmosphere as an electron donor. Alternatively, residual reducing power (e.g. high NADH or reduced quinone pools) from the pre-growth inoculum could account for lactate-free Fe(III) reduction[243].

Notably, we observed that biomass normalized Fe(III) reduction rates were accelerated over ferrihydrite with the frameworks MIL-100 and Fe-BTC. Although the preparation conditions of ferrihydrite may affect absolute reduction rates, reduction of the frameworks appeared markedly different from the model iron oxide under our tested conditions. As mentioned, *S. oneidensis*-based reduction may increase solubilization of framework Fe[325]. In contrast to insoluble Fe(III), soluble Fe(III) exhibits faster reduction kinetics by *S. oneidensis*, which could contribute to faster reduction rates of frameworks relative to ferrihydrite. Since others have shown that flavins minimally influence soluble Fe(III) reduction by *S. oneidensis*[120], our *bfe* knockout and flavin supplementation observations further support this mechanism. Nonetheless, substantial levels of Fe(II) were retained within the structures of MIL-100 and Fe-BTC. Moreover, our use of the

extracellular cytochrome knockout (Δ*mtrC*Δ*omcA*) demonstrated that canonical iron oxide *S. oneidensis* extracellular electron transfer pathways (namely, MtrCAB) are required for framework reduction. These results, coupled with minimal changes to biomass yields between materials, suggest that differences in Fe(III) reduction rate are directed by material properties instead of changes to metabolism or the cellular route of electron transfer.

Although Fe(III) was present in all tested materials, particle structure and surface area widely differed between the frameworks and ferrihydrite. As has been shown with iron oxides, the extent of Fe(III) reduction by metal-reducing bacteria likely depends on the interplay between particle size, extent of aggregation, and surface area[335–337]. For example, interfacial contact between bacterial outer membrane cytochromes and iron oxides likely impacts reduction rates, with smaller particles unable to provide adequate contact for reduction[338]. Structurally, MIL-100 and Fe-BTC both possess the same organic ligand, but MIL-100 is more crystalline. While iron oxides with higher degrees of crystallinity are typically associated with slower Fe(III) reduction rates across the *Shewanella* genus[339,340], we observed that MIL-100 exhibited slightly faster Fe(III) reduction kinetics than the more amorphous Fe-BTC. SEM images showed that MIL-100 and Fe-BTC were highly aggregated, while MIL-88A was comprised of small, well-defined crystals approximately the same size as *S. oneidensis* MR-1 (Figure C.4). Although they are morphologically similar, MIL-100 and Fe-BTC differ in accessible surface area. MIL-100 had the largest Langmuir surface area (2188 m^2g^{-1}) followed by Fe-BTC (1512 m^2g^{-1}), ferrihydrite (311 m^2g^{-1}, [319]) and MIL-88A (130 m^2g^{-1}) (Table C.3). These surface areas closely track our measured Fe(III) reduction rates. Thus, increased surface area likely contributes to significantly faster reduction kinetics by cultures with MIL-100 and Fe-BTC over ferrihydrite. Overall, our results are consistent with previous studies of *S. oneidensis* growth on iron oxides and show that biotic metal-organic framework reduction is governed through a combination of material properties.

Material morphology can also negatively impact Fe(III) reduction and growth, as evidenced by the decline in cell viability for *S. oneidensis* cultures supplemented with MIL-88A. This result was surprising as MIL-88A is comprised of two known *S. oneidensis*

substrates (Fe(III) and fumarate), has a comparable surface area to ferrihydrite, and presumably solubilizes its linker and metal node under biotic conditions (Figure 4.4a). Given its sharp, needle-like particle morphology, MIL-88A may compromise cell membranes, resulting in cell lysis[341–343]. Separately, we found that *S. oneidensis* did not exhibit a decline in cell viability in the absence of an electron acceptor and *E. coli* was able to grow unimpeded in the presence of MIL-88A (Figure C.3). Unlike *S. oneidensis*, *E. coli* does not readily establish biofilms on redox-active surfaces[344]. While growth dynamics were not continuously monitored, our endpoint measurements revealed that *E. coli* does not exhibit the sharp decline in cell viability that *S. oneidensis* displays in the presence of MIL-88A after 24 h. Taken together, this suggests that the morphology of MIL-88A is cytotoxic to biofilm forming bacteria, such as *S. oneidensis*, although the exact mechanism for this is unclear.

In one potential application, we showed that *S. oneidensis* operates synergistically with metal-organic frameworks to remediate large quantities of the environmental pollutant, Cr(VI). Specifically, the combination of biologically generated Fe(II) with a high surface-area porous material, especially MIL-100, enabled rapid reductive adsorption of Cr(VI) from solution. This synergism was supported by low Cr(VI) removal in experiments with material-free biological reduction of soluble Fe(III) and material-free abiotic Fe(II) addition (Figure C.11). Although *S. oneidensis* growth on ferrihydrite (a nonporous iron oxide) was capable of generating Fe(II), Cr(VI) adsorption was similarly diminished relative to bioreduced frameworks and cell viability was completely compromised after ten cycles. In addition to exhibiting higher adsorption capacity, MIL-100 was able to shield the bacteria from repeated Cr(VI) challenges. Higher material surface area (Table C.1) and higher levels of solubilized Fe(II) (Figure 4.4c) likely facilitated superior performance by MIL-100 cultures. Specifically, soluble Fe(II) provides a kinetically facile reduction pathway for Cr(VI), while the framework acts as a high surface area adsorbent. Moreover, Cr(III) can potentially exchange with Fe(III) as a structural node in MIL-100, which may further contribute to the high adsorption capacity measured for this framework[345]. As Fe(III) is continually reduced by *S. oneidensis*, then re-oxidized after Cr(VI) addition, the

Cr adsorption capacity of reduced MIL-100 is theoretically only limited by the amount of electron donor in the culture medium. In our long-term cycling experiment, the Cr adsorption capacity for MIL-100 was measured as 320 mg g^{-1}, a 523-fold increase relative to abiotic MIL-100. This capacity corresponds to an amount of reduced Cr(VI) that is approximately 75% of the theoretical maximum based on the abundance of lactate-derived electrons that can be anaerobically metabolized by *S. oneidensis* (4 electrons per molecule of lactate)[346]. Based on our metabolite measurements, up to half of the supplemented lactate can be consumed by *S. oneidensis* after 48 hours of Fe(III) reduction (Figure C.6). Since our long-term cycling experiment occurred well beyond this timescale, the large quantity of Fe(III) reduction and Cr(VI) reduction/adsorption lends further credence to build-up of reduced intracellular metabolites and/or metabolizing of H_2 as an electron donor.

Although we examined only a small selection of frameworks, we note that changes to metal node or linker identity can radically alter material structure/functionality and tailor frameworks to specific applications. In addition to iron, metal-organic frameworks can be constructed from a variety of biologically-relevant metal nodes, including manganese, chromium, and cobalt[310]. In contrast to metal oxides, the organic linker or other framework components can also be modified to act as secondary electron acceptors, such as with frameworks containing DMSO[347], porphyrins[348], or conductive linkers[349]. Our Cr(VI) adsorption results with MIL-100 suggest that *S. oneidensis* can be paired with other redox-active frameworks to improve Cr adsorption capacity or remediate additional environmental pollutants, such as U(VI)[350]. Alternatively, metal-organic frameworks may find use as substrates for other electroactive microbes (e.g., *Geobacter* spp.) or as redox mediators that support syntrophic cocultures[351,352]. Overall, our results show that pairing metal-organic frameworks with electroactive microbes can actuate vastly different biological (e.g., Fe(III) reduction rates) and chemical (e.g., Cr(VI) removal) responses, relative to iron oxides. As a result, metal-organic frameworks offer promise for studying the microbe-material interface and optimizing a variety of redox-based technologies.

4.5 Materials and Methods

4.5.1 Synthesis of metal-organic frameworks and iron oxides

MIL-100 was synthesized by first dissolving H_3BTC (1.68 g, 7.6 mmol) and NaOH (0.91 g, 22.8 mmol) in 24 mL H_2O. This solution was added dropwise to $FeCl_2 \cdot 4H_2O$ (2.26 g, 11.4 mmol) dissolved in 97 mL H_2O and stirred for 24 h at room temperature/ambient conditions. The precipitate was isolated, washed with water (3x at 25 °C for 12 h) and ethanol (1x at 25 °C for 12 h), and then dried at room temperature/ambient conditions[316]. Fe-BTC was synthesized by dissolving H_3BTC (0.263 g, 1.2 mmol) and NaOH (0.15 g, 3.8 mmol) in 10 mL of H_2O. This solution was added dropwise to $FeCl_3 \cdot 6H_2O$ (0.513 g, 1.9 mmol) dissolved in 10 mL H_2O and stirred for 10 min at room temperature/ambient conditions. The precipitate was isolated, washed with water (3x at 25 °C for 12 h) and ethanol (1x at 25 °C for 12 h), and then dried at room temperature/ambient conditions[317]. MIL-88A was synthesized by stirring a solution of fumaric acid (0.97 g, 8.4 mmol) and $FeCl_3 \cdot 6H_2O$ (2.27 g, 8.4 mmol) in 42 mL of H_2O for 1 h before transferring to a Teflon-lined steel autoclave (Parr). The reactor was heated at 65 °C for 12 h and then cooled down to room temperature. Precipitate from inside the reactor was subsequently washed with ethanol (3x at 25 °C for 12 h) and water (3x at 25 °C for 12 h), then dried at 120 °C for 10 h[318]. Ferrihydrite was synthesized by adding 1M NaOH dropwise to $FeCl_3 \cdot 6H_2O$ (5.4 g, 20.0 mmol) dissolved in 100 mL H_2O until the pH reached ~7.5. The solid was isolated by centrifugation, washed with water (3x at 25 °C for 10 min), and lyophilized immediately following washing for 48 h[319].

4.5.2 Strains and culture conditions

All anaerobic cultures and experiments were performed inside a humidified Coy anaerobic chamber (3% H_2/balance N_2 atmosphere). *S. oneidensis* MR-1 was obtained from ATCC® (700550™). Mutant strains, Δ*mtrC*Δ*omcA* and Δ*bfe*, were generously provided by JA Gralnick (University of Minnesota, Minneapolis, MN). For anaerobic pregrowths,

all strains were cultured in SBM buffered with 100 mM HEPES and supplemented with 0.05% casamino acids and 1X Wolfe's mineral mix[138]. The medium was adjusted to a pH of ~7.2. For pregrowth, sodium lactate (20 mM) and sodium fumarate (40 mM) were added as the carbon source and an electron acceptor, respectively. Once the bacteria reached stationary phase (ca. 18 h), they were pelleted by centrifugation (6000 x g; 20 min) and washed with SBM two times. A final addition of SBM was added to dilute the cells to OD_{600}=0.2.

4.5.3 Growth of MR-1 on metal-organic frameworks and iron oxides

Growth of MR-1 on the metal-organic frameworks was measured by CFU counting, nucleic acid staining (Syto™ 9), extracellular protein staining (SYPRO™ Ruby), and total protein biomass (Bradford assay). Cultures containing 20 mM sodium lactate and either MIL-100, Fe-BTC, MIL-88A, or ferrihydrite ($[Fe(III)]_0$=15 mM) in fresh SBM were prepared anaerobically and then inoculated with the washed MR-1. CFU/Fe(III) reduction studies and total protein biomass studies used an inoculating OD_{600}=0.002. Nucleic acid staining and extracellular protein staining reduction studies used an inoculating OD_{600}=0.02 to increase the fluorescent signal. Abiotic samples were prepared with the materials in SBM with lactate but with no cells. The cultures were incubated anaerobically at 30 °C. For CFU counting, an aliquot of the culture suspension was removed and serially diluted (10^0-10^{-7}). Each dilution (100 μL) was plated onto LB agar plates using sterile glass beads and incubated aerobically at 30 ºC overnight. Individual colonies on each plate were counted and the initial concentration of MR-1 was calculated. For the staining of bacterial nucleic acids, 200 μL of the culture suspension was removed and pelleted before removing the supernatant. The pellet was resuspended in 100 μL of 0.85% NaCl solution, mixed with 2X Syto™ 9 solution in a 96 well plate, and incubated at room temperature for 15 minutes in the dark. Fluorescence was measured with an excitation/emission of 485/530 nm using a BMG LabTech CLARIOstar Monochromator Microplate Reader. For the staining of biofilm matrix, 100 μL of the culture suspension was removed and pelleted before

removing the supernatant. The pellet was mixed with 200 μL of 1X SYPRO™ Ruby fluorescent dye in a 96 well plate. The plate was incubated in the dark at room temperature for 15 minutes before measuring fluorescence at an excitation/emission of 460/640 nm using a plate reader. The nucleic acid fluorescence and extracellular protein fluorescence for biotic samples was corrected by subtracting the abiotic total measurement. For the total protein biomass measurements, an 850 μL or 900 μL aliquot of the suspension was pelleted (10000 x g; 10 min) prior to resuspending in 90 μL of 0.5X SBM buffer. The samples were pelleted once more (10000 x g; 10 min) and resuspended in 90 μL 0.1 M NaOH. The samples were sonicated in a Bransonic 28100 ultrasonic bath (Branson) for 10 minutes, then heated at 95 °C for 40 minutes, and pelleted a final time (10000 x g; 10 min). The supernatant (10 μL) was mixed with 200 μL of the Better Bradford Reagent (ThermoFisher) in a 96 well plate and analyzed at 595 nm in a plate reader[353]. The measured total protein for biotic samples was corrected by subtracting the average abiotic total protein measurement. The corrected biotic values were used to normalize the Fe(III) reduction rate.

4.5.4 Reduction of metal-organic frameworks and ferrihydrite

Reduction of the metal-organic frameworks and ferrihydrite by MR-1 was tested by measuring Fe(II) concentrations in framework-bacteria suspensions over time. Suspensions containing 20 mM sodium lactate and either MIL-100, Fe-BTC, MIL-88A, or ferrihydrite ($[Fe(III)]_0$=15 mM) in fresh SBM were prepared anaerobically and then inoculated with the washed MR-1 to OD_{600}=0.002. Abiotic samples were prepared with the materials in SBM with lactate but with no cells. The suspensions were incubated anaerobically at 30 °C. At each time point, the material substrates were gently shaken to fully suspend all materials before removing an aliquot from the culture. Each aliquot was mixed with 6 M HCl in a 1:1 ratio, until full dissolution of the framework or oxide occurred. If the Fe(II) concentrations was large, the sample was further diluted with 1 M HCl. All samples were analyzed for Fe(II) using the ferrozine assay[354]. The ferrozine assay was

performed by mixing 15 μL of the diluted sampled with 235 μL of ferrozine solution in a 96-well plate. Absorbance was measured at 562 nm using a microplate reader. Ferrozine solution consisted of ferrozine (45 mg, 87 μmol) and ammonium acetate (22.5 g, 0.29 mol) in 45 mL H_2O. Rates of iron reduction were calculated using linear squares regression analysis and were normalized by the sample's corresponding total protein biomass measurement. A similar protocol was followed for reduction of the frameworks by Δ*mtrC*Δ*omcA* and Δ*bfe*. For experiments with heat-killed cells, washed *S. oneidensis* MR-1 cells were heated at 80 °C for 10 minutes. Lysed cell cultures were prepared by sonicating washed *S. oneidensis* MR-1 with a Qsonica 55 probe (Qsonica, LLC, Newtown, CT) for 90 s at 4 °C, maintaining between 10 and 15 W of output energy and alternating between 10 s "ON" and 5 s "OFF".

To assess the amount of Fe(II) contained in biotically-reduced MIL-100, Fe-BTC, and MIL-88A, abiotic and framework-bacteria suspensions were prepared identical to those utilized in reduction kinetics experiments. After 48 h, the framework suspension was centrifuged to pellet the solid, and the supernatant was separated. The isolated solid was washed three times with sterile water and resuspended with SBM using the same volume of initially removed supernatant. Fe(II) concentrations were quantified in the whole sample suspension, isolated supernatant and isolated/washed/resuspended framework. As shown in Figure 4.4c, the Fe(II) concentrations quantified in isolated supernatant and isolated framework were summed to compare to Fe(II) concentrations measured in the whole sample suspension.

4.5.5 Cr(VI) adsorption to MR-1 reduced metal-organic frameworks and ferrihydrite

Cr(VI) removal was tested using metal-organic frameworks or ferrihydrite that had been reduced by MR-1 for 24 h. Cultures containing MIL-100 ($[Fe(III)]_0$=15 mM) and 20 mM lactate in SBM were inoculated with MR-1 to OD_{600}=0.002, as previously described. After 24 h, $K_2Cr_2O_7$ was added to each of the cultures ($[Cr(VI)]_0$=70 μM) and Fe(II)

concentrations were analyzed. Cr(VI) concentration in the supernatant was analyzed using the DPC assay[355]. The DPC assay was performed by mixing 15 μL of sample with 235 μL of DPC solution in a 96-well plate. Absorbance was measured at 540 nm in a microplate reader. DPC solution consisted of DPC (12.5 mg, 103 μmol) in a mixture of 0.5 M H_2SO_4 (10 mL) and acetone (10 mL). MIL-100 was tested with higher concentrations of Cr(VI) (0.25, 0.50, and 1 mM) using the same procedure.

4.5.6 Cr(VI) cycling

Cr(VI) removal from a supernatant was tested over ten cycles with MR-1 reduced MIL-100, ferrihydrite, and fumarate. MIL-100, ferrihydrite, and fumarate were biotically reduced for 24 h and $K_2Cr_2O_7$ was added to each culture ($[Cr(VI)]_0$=0.50 mM). Every 24 h, $K_2Cr_2O_7$ ($[Cr(VI)]_0$=0.50 mM) was added, with ten total additions occurring. Fe(II) concentration and Cr(VI) concentration in the supernatant were monitored as previously described. A second cycling experiment was done using the same conditions, but adding 0.5 mM Cr(VI) until no more Cr(VI) was reduced in the supernatant, equaling 41 additions. To determine cell viability after 10 additions, aliquots of each sample (100 μL) were plated on LB agar plates 24 h after the last Cr(VI) addition and cells were grown aerobically at 30 ºC overnight. Following cycling, cycled samples were washed in fresh H_2O and then dried anaerobically. Prior to STEM imaging, the samples were suspended in ethanol (500 μL) and dropcast on TEM grids. STEM imaging and electron mapping of Fe and Cr was performed using a JOEL 2010F Transmission Electron Microscope.

4.5.7 Powder X-Ray Diffraction

PXRD was performed using a Rigaku R-Axis Spider X-Ray Diffractometer with curved image plate detector. The as-synthesized metal-organic frameworks were analyzed without modification. Following reduction of the materials by MR-1, the abiotic and biotic samples were washed with fresh H_2O to remove any residual salts from the medium and stored in anaerobic conditions prior to analysis. Immediately before analysis, the samples

were coated in mineral oil to prevent oxidation in the aerobic environment of the instrument. A sample of mineral oil run under the same instrument conditions was subtracted as background from the spectra.

4.5.8 Surface Area Measurements

Langmuir surface area measurements were conducted using N_2 (99.999%) gas adsorption collected on a Micromeritics ASAP 2020 Physisorption instrument. Approximately 60 mg of either Fe-BTC, MIL-100 or MIL-88A were activated under high vacuum at 120 °C with a ramp of 0.1 deg/min for 24 h before analysis.

4.5.9 Electron Microscopy

SEM was used to determine the extent of aggregation in the as-synthesized metal-organic framework. Images were collected using Zeiss Supra 40V SEM. TEM was used to determine particle morphology of cycled MIL-100. The TEM grids used for STEM and element mapping were imaged using a Thermo Fisher Tecnai TEM.

4.5.10 Leaching and Framework Stability Analysis

The metal-organic frameworks were tested for leaching and framework stability by exposing the materials to culture conditions for 48 h. The ferrozine assay was used to determine the Fe(III) concentration in the supernatants after the metal-organic frameworks ([Fe(III)=15mM). For Fe(II) analysis, samples were prepared as previously described. For total Fe analysis, the sample was mixed with 1 M hydroxylamine hydrochloride in a 1:1 ratio and analyzed by the ferrozine assay. Fe(III) concentrations were calculated by subtracting the Fe(II) concentration from the total Fe concentration.

NMR spectroscopy was used to determine the extent of fumarate leaching from MIL-88A ([Fumarate$^-$]=5 mM) in 1 mL of D_2O and stored anaerobically at 30 °C. After 48 h, the samples were centrifuged and the supernatant was removed. The supernatant was spiked with 1.0 mg of benzoic acid as an internal standard. A standard of fumaric acid (1.0

mg/mL) and benzoic acid (1.0 mg/mL) was mixed in 1 mL D_2O. An aliquot of the supernatant (50 μL) was diluted in 950 μL of D_2O and analyzed on an Agilent MR400 NMR (400 MHz).

Framework structural stability was tested by exposing the metal-organic frameworks to culture conditions for 48 h. Following exposure, the materials were washed and analyzed by PXRD.

4.5.11 Nucleic Acid and Extracellular Protein Staining

To assess biomass accumulation of *S. oneidensis* MR-1, nucleic acids and extracellular proteins were stained with fluorescent dyes. Cultures were prepared in SBM with 20 mM lactate and either MIL-100 or ferrihydrite ([Fe(III)]=15 mM). To improve the fluorescent signal, the inoculating concentration of washed cells was increased OD_{600}=0.02. Cultures were anaerobically incubated at 30 °C for 48 hours. For the staining of bacterial nucleic acids, 200 μL of the culture suspension was removed and pelleted before removing the supernatant. The pellet was resuspended in 100 μL of 0.85% NaCl solution, mixed with 2X Syto™ 9 solution in a 96 well plate, and incubated at room temperature for 15 minutes in the dark. Fluorescence was measured with an excitation/emission of 485/530 nm using a BMG LabTech CLARIOstar Monochromator Microplate Reader. For the staining of extracellular proteins, 100 μL of the culture suspension was removed and pelleted prior to removing the supernatant. The pellet was mixed with 200 μL of 1X SYPRO™ Ruby fluorescent dye in a 96 well plate. The plate was incubated in the dark at room temperature for 15 minutes before measure fluorescence at an excitation/emission of 460/640 nm using a plate reader. The nucleic acid fluorescence and extracellular fluorescence for biotic samples was corrected by subtracting the abiotic measurement.

4.5.12 Reduction of MIL-100 by *E. coli*

To demonstrate that the reduction of MIL-100 is not due to promiscuous reduction, a culture of MIL-100 ([Fe(III)]=15 mM) and 20 mM lactate in SBM was inoculated with stationary-phase *E. coli* (OD_{600}=0.002). *E. coli* MG1655, generously provided by Dr. Lydia Contreras (University of Texas, Austin, TX), was pregrown anaerobically in 40 mM fumarate and 20 mM lactate in SBM, washed twice and diluted to an OD_{600}=0.2 prior to culture inoculation. All cultures were incubated at 37 °C in an anaerobic environment. Fe(II) concentrations were analyzed using the ferrozine assay. An abiotic control was also tested. Experiments were performed in triplicate.

4.5.13 ICP-MS analysis

ICP-MS was used to analyze total Cr in the supernatant of biotically-reduced MIL-100 challenged with 0.5 mM Cr(VI). Cultures containing MIL-100 ([Fe(III)=15 mM) and 20 mM lactate were inoculated with MR-1 (OD_{600}=0.002, anaerobic pregrowth). MR-1 reduced MIL-100 until the [Fe(II)] = 2.8 mM after which cultures were challenged with 0.5 mM Cr(VI) and aliquots of the supernatant were removed for analysis. Samples were centrifuged (10000 x g, 1 min), frozen in liquid N_2 and stored at -20°C until further sample preparation. For the ICP-MS sample preparation, the samples were thawed and diluted 200-fold in 2% HNO_3 immediately prior to analysis. A 7500ce Agilent ICP-MS was used to analyze total Cr (LOD:0.54 ppb) and was verified using m/Z=52 and 53.

4.5.14 MR-1 reduction of Cr(VI)

Reduction of 100 μM Cr(VI) by MR-1 was tested by inoculating a culture of 20 mM lactate and 50 μM $K_2Cr_2O_7$ in SBM with stationary phase MR-1 (OD_{600}=0.002, anaerobic pregrowth). Cultures were stored at 30 °C in anaerobic conditions for 24 h. Cr(VI) concentrations were analyzed using the DPC assay. An abiotic control was also tested.

4.5.15 Cr(VI) reduction by $FeCl_2$

Cr(VI) reduction by abiotic Fe(II) was tested by mixing a solution of $FeCl_2 \cdot 4 \cdot H_2O$ (either 0.5 mM, 1.0 mM or 2.0 mM), 20 mM lactate and 0.5 mM Cr(VI) in SBM (pH=7.2). Solutions were stored in anaerobic conditions at 30 °C for 24 h. Cr(VI) concentrations were determined using the DPC assay.

4.5.16 Cr(VI) reduction by MR-1 reduced Fe(III)-citrate

Cr(VI) reduction by biotically reduced Fe(II) was tested by inoculating a culture of Fe(III)-citrate (5 mM) and 20 mM lactate in SBM with stationary phase MR-1 (OD_{600}=0.002, anaerobic pregrowth). MR-1 reduced Fe(III)-citrate until Fe(II) concentrations for 8 h, or when Fe(II) concentrations were comparable to those observed at 24 h with MR-1 and MIL-100. Fe(II) concentration in the Fe(III)-citrate and MR-1 cultures was 2.5 mM after 8 h. Once Fe(III) reduction was established, the cultures were challenged with 0.5 mM Cr(VI). After 12 h, the cultures were challenged again with 0.5 mM Cr(VI). Fe(II) and Cr(VI) concentrations were monitored throughout the experiment using the ferrozine and DPC assays, respectively. An abiotic control was also tested using the same procedure.

4.5.17 Chemicals and reagents

Trimesic acid (H_3BTC, Sigma-Aldrich, 95%), sodium hydroxide (NaOH, VWR, pellets), ferrous chloride tetrahydrate ($FeCl_2 \cdot 4H_2O$, JT Baker), ferric chloride hexahydrate ($FeCl_3 \cdot 6H_2O$, Fisher-Scientific, ACS grade), fumaric acid ($HO_2CCHCHCO_2H$, Alfa Aesar, 99%), red hematite (Fe_2O_3, Strem Chemicals, 99.8% Fe), magnesium oxide (MgO, Alfa Aesar), oxalic acid ($C_2H_2O_4$-, VWR, 10% w/v), HEPES buffer (4-(2-hydroxyethyl)-1-piperazineethanesulfonic acid, IBI Scientific), potassium phosphate dibasic (K_2HPO_4, Sigma-Aldrich), potassium phosphate monobasic (KH_2PO_4, VWR), sodium chloride (NaCl, VWR), ammonium sulfate $(NH_4)_2SO_4$, Fisher Scientific), magnesium(II) sulfate heptahydrate ($MgSO_4 \cdot 7H_2O$, Sigma-Aldrich), EDTA acid disodium salt dihydrate

($C_{10}H_{14}N_2Na_2O_8 \cdot 2H_2O$, VWR), manganese(II) sulfate monohydrate ($MnSO_4 \cdot H_2O$, VWR), ferrous sulfate heptahydrate ($FeSO_4 \cdot 7H_2O$, Alfa Aesar), cobalt(II) nitrate hexahydrate ($Co(NO_3)_2 \cdot 6H_2O$, Strem Chemicals), calcium chloride dihydrate ($CaCl_2 \cdot 2H_2O$, Sigma-Aldrich), zinc(II) sulfate monohydrate ($ZnSO_4 \cdot H_2O$, Strem Chemicals), cupric sulfate pentahydrate ($CuSO_4 \cdot 5H_2O$, VWR), aluminum potassium sulfate ($AlK(SO_4)_2$, Acros Organics), boric acid (H_3BO_3, VWR), sodium molybdate dihydrate ($Na_2MoO_4 \cdot 2H_2O$, Beantown Chemical), sodium selenite (Na_2SeO_3, Acros Organics), sodium tungstate dihydrate ($Na_2WO_4 \cdot 2H_2O$, Alfa Aesar), nickel(II) chloride hexahydrate ($NiCl_{-2} \cdot 6H_2O$, Alfa Aesar), Syto™ 9 green fluorescent nucleic acid stain (ThermoFisher Scientific), SYPRO™ Ruby protein gel stain (ThermoFisher Scientific), Better Bradford Reagent (ThermoFisher Scientific) and casamino acids (VWR) were used as received. Sodium DL-lactate ($C_3H_5NaO_3$, VWR, 60% in water) was filtered using 0.2 μm PES filters. Sodium fumarate ($Na_2C_4H_2O_4$, VWR) was diluted in H_2O and then filtered using 0.2 μm PES filters. LB Lennox agar powder (VWR) was dissolved in H_2O and sterilized at 121°C and 100 kPa for 1 h. Hydrochloric acid (HCl, Sigma-Aldrich, 37%) was diluted in H_2O prior to use. Ferrozine (3-(2-pyridyl)-5,6-bis(4-sulfophenyl)-1,2,4-triazine disodium salt hydrate, TCI Chemicals), ammonium acetate ($NH_4CH_3CO_2$, VWR), hydroxylamine hydrochloride ($HONH_2 \cdot HCl$, Alfa Aesar, ACS grade), potassium dichromate ($K_2Cr_2O_7$, Alfa Aesar, ACS grade), 1,5-diphenylcarbazide (DPC, Alfa Aesar), and acetone ($(CH_3)_2CO$, Fisher Scientific, ACS grade) were used as received. Sulfuric acid (H_2SO_4, VWR, 95-97%) was diluted in H_2O before use. Iron(III) citrate ($FeC_6H_5O_7$, Alfa Aesar, Fe(III) 16.5-20%, Fe(II) max 5%) was used as received. Deuterium oxide (D_2O, Sigma-Aldrich, 99.9%) was used for NMR as received. Nitric acid (HNO_3, Sigma-Aldrich, trace mineral grade) was diluted to 2% for ICP-MS analysis. Ultrapure water was produced by a MilliQ Integral Water Purification System.

4.5.18 Statistical Analysis

Unless otherwise noted, data are reported as mean ± S.D. of N = 3 biological replicates, as this sample size was sufficiently large to detect significant differences in

means. Significance was calculated using an unpaired two-tailed Student's *t*-test (α=0.05) or ANOVA with post-hoc Dunnett's test in Prism 8 by GraphPad Software (San Diego, CA).

Chapter 5: Tuning extracellular electron transfer by *Shewanella oneidensis* using transcriptional logic gates[4]

5.1 Chapter Summary

Extracellular electron transfer (EET) pathways, such as those in the bacterium *Shewanella oneidensis*, interface cellular metabolism with a variety of redox-driven applications. However, designer control over EET flux in *S. oneidensis* has proven challenging since a functional understanding of its EET pathway proteins and their effect on engineering parameterizations (e.g., response curves, dynamic range) is generally lacking. To address this, we systematically altered transcription and translation of single genes encoding parts of the primary EET pathway of *S. oneidensis*, CymA/MtrCAB, and examined how expression differences affected model-fitted parameters for Fe(III) reduction kinetics. Using a suite of plasmid-based inducible circuits maintained by appropriate *S. oneidensis* knockout strains, we pinpointed construct/strain pairings that expressed *cymA*, *mtrA*, and *mtrC* with maximal dynamic range of Fe(III) reduction rate. These optimized EET gene constructs were employed to create Buffer and NOT gate architectures, that predictably turn on and turn off EET flux, respectively, in response to IPTG. Furthermore, we found that response functions generated by these logic gates (i.e., EET activity vs. inducer concentration) were comparable to those generated by conventional synthetic biology circuits, where fluorescent reporters are the output. Our results provide insight on programming EET activity with transcriptional logic gates and suggest that previously developed transcriptional circuitry can be adapted to predictably control EET flux.

[4]Adapted from Dundas, C.M., Walker, D.J.F., Keitz, B.K. (2020) Tuning Extracellular Electron Transfer by *Shewanella oneidensis* Using Transcriptional Logic Gates. *ACS Synth. Biol.* doi:10.1021/acssynbio.9b00517. Christopher M. Dundas conceived the project, designed the genetic constructs, performed the experiments, analyzed the results, and wrote the chapter.

5.2 INTRODUCTION

Extracellular electron transfer (EET) is an anaerobic respiratory mechanism through which electroactive microbes interact with and influence their environment[64]. For example, EET flux can be harnessed for power generation in microbial fuel cells[58], the remediation of environmental pollutants[237], and for material synthesis[31,39]. In theory, EET can connect biological computation with modern electronics, potentially enabling the creation of new sensors and other hybrid living-electronic devices[128]. Because redox-active proteins and metabolites mediate microbial electron transfer, these applications have the potential for genetic and metabolic optimization. However, strict control over expression/activity of metabolic and proteomic elements governing EET flux and thus programmable control over cellular electron flux remains challenging.

Shewanella oneidnesis is a facultative bacterium that couples carbon oxidation to EET flux[61]. The EET pathways of *S. oneidensis* are common engineering targets, owing to the bacteria's favorable growth characteristics and genetic tractability. In the absence of oxygen, these pathways facilitate respiration onto a variety of technologically-relevant metal species, including Fe(III)[62], Mn(IV), and Pd(II)[156]. The primary EET pathway in *S. oneidensis* is the CymA/MtrCAB conduit (Figure 5.1), which is comprised of a periplasmic/outer membrane *c*-cytochrome network that links carbon metabolism to the reduction of inorganic substrates[356]. Manipulating EET in *S. oneidensis* has been predominantly explored in the context of bioelectrochemical applications[90]. For example, a frequent power generation goal to increase EET flux above wild-type *S. oneidensis* levels can be accomplished through overexpression of flavin biosynthesis enzymes[130]. However, controlled expression of the CymA/Mtr components has received relatively little attention outside of electrode-based characterizations.

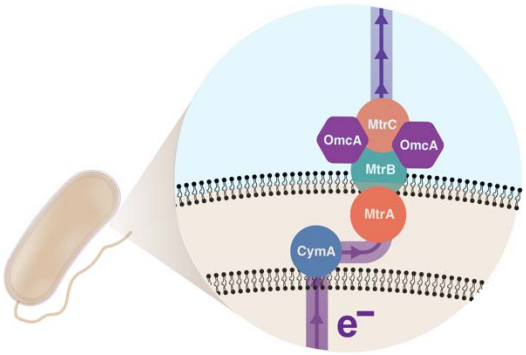

Figure 5.1: CymA/MtrCAB extracellular electron pathway in *S. oneidensis* MR-1.

While electron transfer rates below wild-type levels are advantageous in certain applications and can be accomplished using genomic deletion strains[86], programmable expression of EET proteins remains a non-trivial engineering task. Despite a few examples of inducible EET flux via circuits that control Mtr protein expression[129,134,136,214], basic engineering parameterizations, such as output/input response curves[227] (i.e., EET flux vs. inducer concentration) and dynamic range optimization (i.e., induced EET rate/uninduced EET rate), have not been systematically studied. It is not clear the magnitude to which each EET protein affects these parameterizations nor the relative effect of each pathway component. Additionally, many previously engineered circuits exhibited "leaky" expression of EET genes[136,298]. Finally, most EET genetic circuits have focused on "turning on" EET activity, but "turning off" EET activity at the protein expression level remains largely unexamined[215]. Taken together, an overall picture of how controlled changes in CymA/Mtr protein expression relate to changes in EET flux is lacking. Developing this understanding is critical for adopting synthetic biology approaches to control EET activity and expanding the versatility of EET in applications such as sensing and catalysis.

To address these challenges, we designed a well-defined and modular expression system for the CymA/Mtr proteins that could be used to rapidly parameterize electroactivity by engineered *S. oneidensis* strains. Transcriptional regulation can be harnessed to precisely control protein expression and design synthetic biology circuits that behave similarly to electronic circuits[197,198,211]. By pairing transcriptional regulators (e.g.,

repressors, activators) with cognate promoter DNA sequences, expression of promoter-downstream genes can be modulated based on the presence/absence of inducing molecules. Using this regulation scheme, transcriptional logic gates can be constructed that facilitate rational programming of complex cellular functions[20,21,357]. We hypothesized that rigorous control of EET activity could similarly be enabled using transcriptional logic gates that control expression of single EET genes. By tuning logic gate elements, including RBS sequences and regulatory topology, we predicted that EET activity could exhibit response functions comparable to those observed with fluorescent reporters. Transcriptional control over individual EET components would simplify programming of EET flux and potentially facilitate its integration into previously developed genetic circuits.

In this work, we developed a suite of plasmids to control expression of the EET genes *mtrC, mtrA*, and *cymA*. *S. oneidensis* strains with appropriate genomic deletions were transformed by these plasmids, and the effects of EET gene transcription and translation were systematically interrogated. When evaluating genetic designs, Fe(III) reduction was used as a high throughput reporter of EET activity. *In situ* reduction kinetics were fitted to transcription-governed models, which allowed us to parameterize strain electron transfer rates and optimize inducible EET turn-on behavior, including dynamic range and fitting to Hill models of gene transcription. After identifying transcriptionally responsive EET constructs, we further demonstrated their utility by constructing NOT gates that functionally turn off EET activity in response to IPTG. Our results show that EET activity can be programmed via expression of single genes and will provide insight on the amenability of EET pathway components for future engineering efforts.

5.3 Results

5.3.1 High Throughput and Real-Time Quantification of Microbial Fe(III) Reduction

To rapidly prototype EET genetic circuits, we developed a simple and high throughput means to detect expression-driven changes in EET flux (Figure 5.2a). Soluble Fe(III) reduction is a common assay for microbial EET activity and can be measured using

the colorimetric dye, ferrozine. Ferrozine complexes microbially generated Fe(II) and has an absorption peak at 562 nm[354]. Inspired by previous *Shewanella* studies[358–360] and a recent report that analyzed the electroactivity of several microorganisms *en masse*[70], we found that adding ferrozine directly to cell suspensions in anaerobically sealed 96-well plates enabled high throughput and real-time monitoring of Fe(III) reduction and EET activity (Figure D.1). Each experimental 96-plate well was filled with *Shewanella* Basal Medium that contained 1 mg mL^{-1} ferrozine, which showed minimal absorbance change in the absence of bacterial inoculum. In contrast, wells containing ferrozine and *S. oneidensis* cells exhibited color changes attributable to Fe(III) reduction. As plates also contained abiotic Fe(II) standards, this setup enabled rapid detection of Fe(II) levels up to 96 μM across varying biological and chemical conditions. For example, when adding ferrozine to suspensions of *S. oneidensis* MR-1 (wild-type), we observed distinct Fe(III) reduction profiles that follow known *S. oneidensis* metabolisms on different carbon sources[264]. Bacteria cultured with lactate and pyruvate displayed fast Fe(III) reduction kinetics, relative to starved cultures and those supplemented with metabolically inaccessible acetate (Figure 5.2b). We also measured drastic kinetic differences between *S. oneidensis* MR-1 and previously characterized Fe(III) reduction-deficient strains[86]. Cytochrome knockout strains exhibited markedly slower Fe(III) reduction levels, relative to *S. oneidensis* MR-1 (Figure 5.2c). Together, these results demonstrate that our assay provides a high-throughput means to quantify engineered EET activity via microbial Fe(III) reduction kinetics.

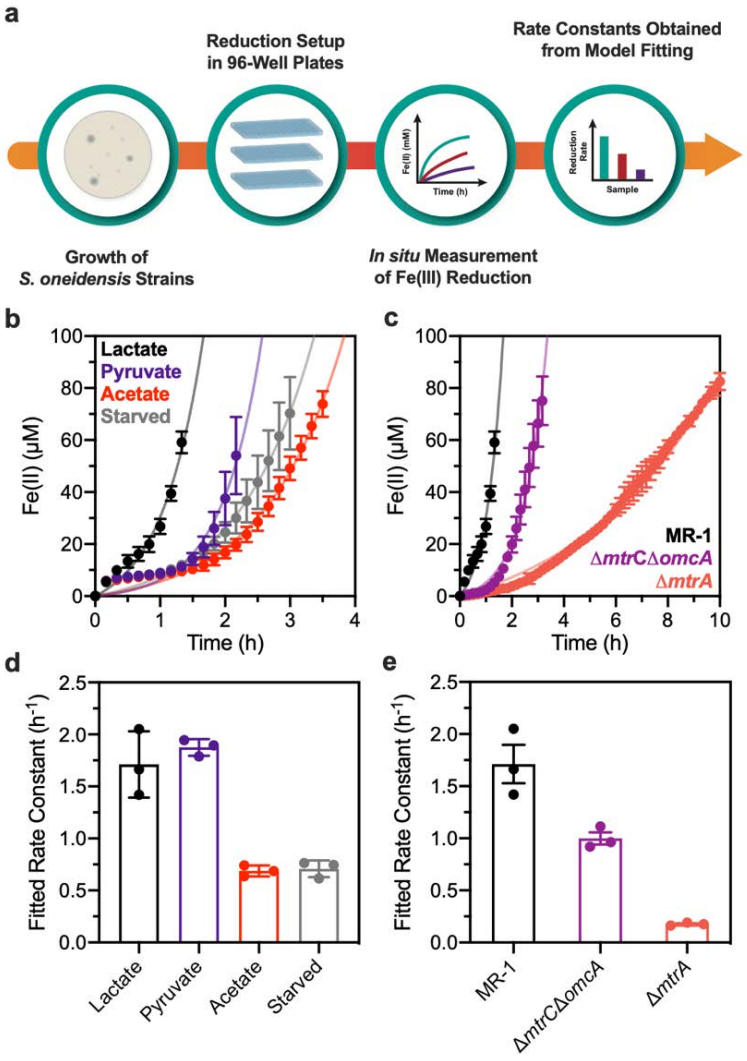

Figure 5.2: Measurement and modeling of Fe(III) reduction kinetics by *S. oneidensis*.

(a) General workflow for 96-well plate Fe(III) reduction setup, kinetic measurements, and obtaining fitted rate constants. (b) Raw Fe(III) reduction kinetics for *S. oneidensis* MR-1 cultured with 1 mg mL^{-1} ferrozine, 5 mM Fe(III) citrate, and either 20 mM sodium lactate (black), 20 mM sodium pyruvate (purple), 20 mM sodium acetate (red) or no carbon source (grey). (c) Raw Fe(III) reduction kinetics for *S. oneidensis* MR-1 (black), Δ*mtrC*Δ*omcA* (purple), and Δ*mtrA* (red) cultured with 1 mg mL^{-1} ferrozine, 5 mM Fe(III) citrate, and 20 mM lactate. Fitted rate constants from the carbon source experiments (b) and different *S. oneidensis* strains (c) are shown in (d) and (e), respectively. Rate constants were obtained by fitting raw kinetic data to a Monod-type model. For (b) and (c), all data represent the mean ± s.d. of raw Fe(II) levels. For (d) and (e), all data represent the mean ± s.e.m of fitted rate constants. All experiments were performed with n = 3 biological replicates.

5.3.2 A Monod-type Model Connects Steady-State Gene Expression to Fe(III) Reduction

Having established a platform for directly measuring Fe(III) reduction kinetics by various *S. oneidensis* strains and conditions, we next developed a genetic and mathematical framework that could tie EET gene expression to Fe(III) reduction. Despite functional redundancy by other cytochromes and electron transfer proteins[111], the CymA/MtrCAB pathway is the primary conduit for electron transfer to soluble Fe(III) by *S. oneidensis*. Knockout strains that lack just one protein in this conduit exhibit significantly reduced rates of Fe(III) reduction relative to wild-type. Given these results, we hypothesized that complementing appropriate knockout strains with a single EET gene from the CymA/MtrCAB conduit would cause Fe(III) reduction kinetics to be rate limited and controllable by expression of that gene. To test this, we designed plasmids that placed *mtrC*, *mtrA*, and *cymA* downstream of the promoter $P_{tacsymO}$[361], which is under control of the plasmid-expressed transcriptional regulator, LacI[362]. These genes were chosen as they are all cytochromes, span a range of sizes and cellular localizations, and have precedence for altering EET flux via genetic circuits in *S. oneidensis*. Constructed plasmids were used to transform the following knockout strains when appropriate: Δ*mtrC*Δ*omcA*Δ*mtrF*, Δ*mtrA*, Δ*cymA*. These strains exhibit substantially lower Fe(III) reduction capabilities relative to *S. oneidensis* MR-1 that can be restored by complementation[86,99]. With addition of IPTG and use of various regulator topologies, we varied transcriptional flux for each gene and systematically examined expression effects on Fe(III) reduction rate.

To facilitate comparisons between different tested conditions, we identified cell-intrinsic metrics to analyze our Fe(III) kinetic data. While microbial Fe(III) reduction rates are often normalized by bulk biomass, measurements of cell concentration or protein levels were challenging to perform during *in situ* kinetics. Previous modeling of soluble Fe(III) reduction by *Shewanella* spp. has leveraged Monod-type models to analyze microbial kinetic data[232]. With these exponential models, the fitted exponential constant is a cell-intrinsic, biomass-independent, parameter that determines substrate utilization rates (see section 5.5.4). Indeed, we found that a Monod-type model fit well to our Fe(II) kinetic data

and that qualitative trends in raw Fe(III) reduction kinetics matched fitted rate constants for *S. oneidensis* MR-1 cultured on different carbon sources (Figure 5.2d) and between different *S. oneidensis* strains (Figure 5.2e). Using the Monod-type model, extrapolated Fe(II) kinetics from our ferrozine-containing experiments also match previous measurements with these strains in ferrozine-free experiments over longer timescales[86]. Moreover, culture supplementation with 5 mM Fe(III) citrate was sufficiently high enough such that the fitted rate constant was not appreciably affected by substrate limitation in the range of Fe(II) quantification (0 to 96 μM) (Figure D.2).

Another benefit of the Monod-type model is that it can directly relate plasmid-based EET gene expression to Fe(III) reduction rate. Similarly to Michaelis-Menten kinetics, the fitted Fe(III) reduction rate constant can be assumed to be proportional to cellular concentration of the rate-limiting protein (i.e., the expressed EET protein) (see section 5.5.4)[363]. Since EET protein levels are proportional to steady-state mRNA levels during exponential growth[364], we predicted that transcriptional logic gate regulation of EET genes would control Fe(III) reduction rates. Thus, the fitted exponential rate constant may serve as a valuable parameter to evaluate how various genetic constructs/experimental conditions affect Fe(III) reduction kinetics.

5.3.3 RBS Strength Tunes Dynamic Range of Inducible Fe(III) Reduction

Towards designing more complex EET behavior, an important preliminary objective was to determine the dynamic range over which EET gene circuits can turn cellular electron flux "on" relative to an uninduced "off" state. Typically, dynamic range of inducible systems is determined by measuring reporter activity (e.g., GFP fluorescence) under conditions of maximal induction and in the absence of inducer[19]. These reporter measurements serve as a proxy for the maximum and minimum expression of the reporter gene and can be normalized by cell number or taken at the single cell level. In contrast, our system measures Fe(III) reductase activity in a bulk cell suspension, which makes similar normalizations challenging. Nonetheless, we predicted the fitted reduction rate constants

would vary with EET gene expression, and that the ratio of fitted constants could be used to determine the dynamic range of inducible EET circuits.

Maximizing dynamic range in inducible systems is necessary for practical applications, since it affords high signal-to-noise ratios when actuating cellular responses. Thus, we sought to identify inducible EET gene constructs that exhibited high dynamic range, and thus strong control over EET activity. Although dynamic range in our circuit is ultimately determined by changing gene transcription rates, gene translation strength also affects the magnitude of expression levels. For example, even in the absence of inducer, leaky transcription of inducer-regulated genes may occur. If the gene possesses high translational strength, low levels of transcript may be sufficient to saturate protein expression indistinguishably from maximal induction. Indeed, previous LacI regulated *mtrC* constructs we and others have utilized exhibit such behavior[293,298]. Alternatively, genes with weak translational strengths may exhibit no protein expression under inducing conditions. Since the ribosome binding site (RBS) sequence modulates gene translation rate, this sequence can be optimized for each expressed gene to find a "transcriptional window" that exhibits minimal leaky expression and high dynamic range. Computational tools developed by Salis et al. are frequently utilized to predict and forward engineer gene translation rates[228]. With their RBSLibrary Calculator, users provide the DNA sequences for a target gene, the desired RBS-upstream region, and the 16S rRNA sequence of the host organism to generate a library of candidate RBS sequences with a spectrum of predicted translational strengths[365,366].

We leveraged this tool to generate/predict RBS sequences that would optimize the dynamic range of inducible EET gene constructs. For *mtrC*, *mtrA*, and *cymA*, we assembled a small library of plasmids (5 to 6 library members per gene) that varied only in RBS sequence (Figure 5.3a, Table D.2). As mentioned above, each plasmid was used to transform an appropriate knockout strain of *S. oneidensis* to avoid native chromosomal expression (Figure 5.3b-d). To permit insulation from genetic context and potentially enable combination of different EET genes in future assemblies, we also added a self-cleaving ribozyme downstream of the $P_{tacsymO}$ promoter and upstream of each RBS[367].

Despite the presence of unique ribozymes for each EET gene, the RBSLibrary Calculator includes these different RBS-upstream sequences into translation strength calculations and outputs comparable predictions. We report translation strength for each plasmid as the ΔG_{total}, which is the predicted change in Gibbs free energy associated with mRNA binding to the host ribosome relative to the unbound state of both components. Under ideal conditions, the ΔG_{total} for a given gene should be linearly proportional to the logarithm of that gene's translation rate (and thus steady-state protein levels), with more negative ΔG_{total} values corresponding to higher translation rates[228].

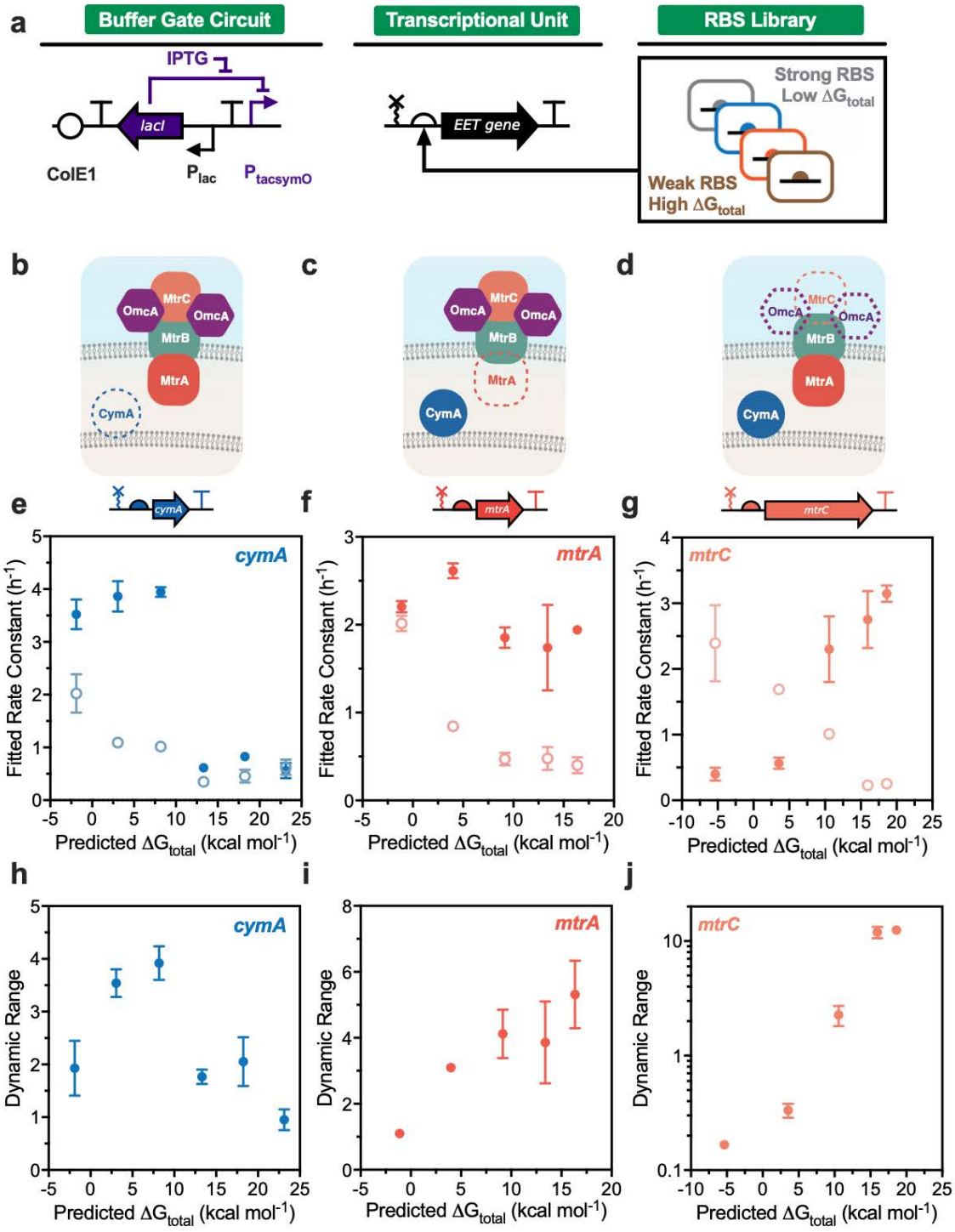

Figure 5.3: Dynamic range optimization for inducible EET circuits.

Figure 5.3: Dynamic range optimization for inducible EET circuits. (a) Diagram of the RBS library/IPTG inducible circuit (Buffer gate) used to control each EET gene transcriptional output. (b) Strain backgrounds and transcriptional unit pairings that were used to assay each RBS library for *cymA* (Δ*cymA*+pCD26r#), (c) *mtrA* (Δ*mtrA*+pCD25r#), and (d) *mtrC* (Δ*mtrC*Δ*omcA*Δ*omcA*+pCD24r#). Dashed outlines represent proteins removed via genomic deletion. Induced (1500 μM IPTG, filled circles) and uninduced (0 μM IPTG, open circles) Fe(III) reduction rate constants for the (e) *cymA*, (f) *mtrA*, and (g) *mtrC* RBS libraries. *cymA* circuit strains were pregrown aerobically and *mtrA*/*mtrC* circuit strains were pregrown anaerobically. For all experiments, IPTG was supplemented immediately prior to measuring Fe(III) reduction kinetics. Rate constants were obtained by fitting raw kinetic data to a Monod-type model. Dynamic range of inducible Fe(III) reduction for the (h) *cymA*, (i) *mtrA*, and (j) *mtrC* RBS libraries. Dynamic range was calculated as the ratio of induced (1500 μM IPTG) and uninduced (0 μM IPTG) fitted rate constants for each replicate. All data represent the mean ± s.e.m. of fitted rate constants or dynamic range for n = 3 biological replicates. Raw data for all replicates is shown in Figure D.3.

To analyze dynamic range of EET activity for each library member, we measured Fe(III) reduction kinetics in the presence of 0 and 1500 μM IPTG. These conditions facilitate minimal and maximal transcription in our circuit, as determined by sfGFP expression (Figure 5.4b). To maximize differences in EET protein expression, we chose to induce cells with IPTG immediately prior to Fe(III) reduction. Cells were pregrown uninduced either anaerobically on lactate/fumarate (*mtrC, mtrA*) or aerobically on lactate (*cymA*) for ca. 18 hours and diluted 100-fold into growth medium containing ferrozine and IPTG. Aerobic pregrowth is required for *cymA*-deficient strains due to the protein's global role in several anaerobic respiratory pathways[99,356]. After addition of 5 mM Fe(III) citrate, measurement of Fe(III) reduction kinetics began. In the absence of IPTG, we observed that fitted rates constants for all tested genes monotonically increased with more negative ΔG_{total} (Figure 5.3e-g). This result is consistent with increases in leaky gene expression as translation strength increases and validates the predictive power of the RBSLibrary Calculator in *S. oneidensis*. In contrast, fitted reduction rate constants from IPTG-containing samples showed qualitatively different trends based on the tested gene. With *cymA*, fitted rate constants were comparable for induced and uninduced strains harboring weaker translating library members (Figure 5.3e). However, rate constants increased to comparable levels for *cymA* strains harboring constructs with predicted ΔG_{total} less than 8.2

kcal mol^{-1}. Given the increase in reduction rate constant observed for all uninduced strains with increasing translation strength, a maximum in dynamic range was observed at a relatively intermediate translation strength within our *cymA* library (pCD26r4, ΔG_{total} = 8.19 kcal mol^{-1}, dynamic range = 3.9 ± 0.3) (Figure 5.3h). In contrast, maximums in dynamic range were observed for the weakest translating library members of *mtrA* (pCD25r0, ΔG_{total} = 16.4 kcal mol^{-1}, dynamic range = 5.3 ± 1.0) and *mtrC* (pCD24r1, ΔG_{total} = 18.6 kcal mol^{-1}, dynamic range = 12.5 ± 0.3) strains (Figure 5.3i-j). For induced *mtrA* strains, the fitted rate constants showed minimal change across varying translation strength (Figure 5.3f). Consequently, dynamic range increased with decreasing translation strength as the background uninduced reduction increases. Interestingly, induced *mtrC* strains exhibited a decrease in fitted rate constant with increasing translation strength, which fell below uninduced levels for constructs with predicted ΔG_{total} less than 5 kcal mol^{-1} (Figure 5.3g). This result suggests that *mtrC* expression imposes a metabolic burden at higher translation strengths[368]. Raw kinetic data from each of the optimal RBS/gene combinations show that different timescales of Fe(III) reduction arise based on construct identity (Figure D.3). Together, these results highlight the ability of RBS engineering to modulate EET activity and facilitated the identification of three inducible EET plasmids with minimal leakiness and dynamic ranges spanning ca. 4 to 12 in their respective strain backgrounds.

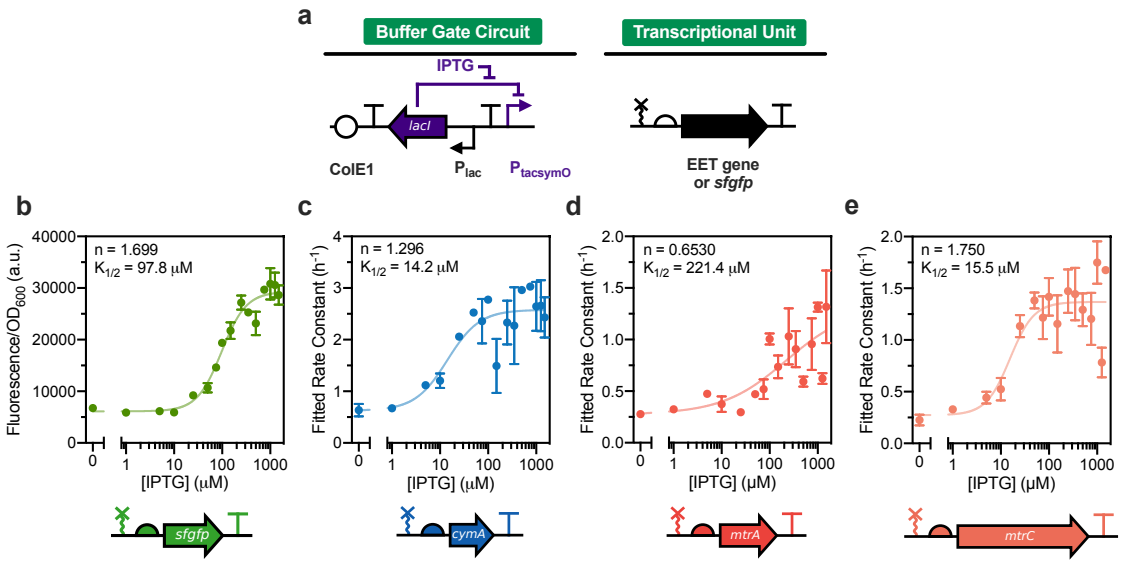

Figure 5.4: Buffer gate response functions under steady-state EET gene expression.

(a) Diagram of Buffer gate circuit used to control each EET gene or *sfgfp* transcriptional output. (b) Fluorescence/OD_{600} response function generated by *S. oneidensis* MR-1 expressing the *sfgfp* Buffer gate circuit. Cells were induced with IPTG for 18 hours during anaerobic growth on lactate/fumarate. To produce mature and functional sfGFP, translation was arrested with 2 mg mL^{-1} kanamycin sulfate and cell aliquots were transferred to an aerobic shaking incubator (30 °C, 250 RPM) for 1 hour prior to fluorescence/optical density measurements. (c) Fe(III) reduction response function generated by aerobically pregrown *S. oneidensis* Δ*cymA* expressing the *cymA* Buffer gate circuit (pCD26r4). (d) Fe(III) reduction response function generated by anaerobically pregrown *S. oneidensis* Δ*mtrA* expressing the *mtrA* Buffer gate circuit (pCD25r0). (e) Fe(III) reduction response function generated by anaerobically pregrown *S. oneidensis* Δ*mtrC*Δ*omcA*Δ*mtrF* expressing the *mtrC* Buffer gate circuit (pCD24r1). For Fe(III) reduction experiments, all strains were pre-induced with IPTG for 18-24 hours prior to measuring Fe(III) reduction kinetics. Cultures were also supplemented with IPTG during kinetic measurements. Rate constants were obtained by fitting raw kinetic data to a Monod-type model. The solid line and Hill parameters shown in each graph were obtained by fitting individual replicates to a four-parameter activating Hill function with weighted error. To improve Hill function fitting for (d), the minimum and maximum Hill function values were constrained by the mean fitted rate constants at 0 and 1500 μM IPTG, respectively. All data represent the mean ± s.e.m. of fitted rate constants for n = 3 biological replicates. Raw data for all replicates is shown in Figure D.13.

5.3.4 Inducible Fe(III) Reduction Occurs in the Absence of Ferrozine

To confirm that inducibility was not an artifact of our real-time kinetics setup, we also performed inducible expression for each optimized EET gene in lactate/Fe(III) citrate medium that lacked ferrozine. Indeed, we observed that Fe(III) reduction remained highly inducible via IPTG for each construct (Figure D.4). In these experiments, we concomitantly measured viable cell density and observed comparable, albeit slightly higher, growth yields for induced samples relative to uninduced. Although growth dynamics were not continuously monitored, cell concentrations for each strain differed based on the presence of IPTG by at most ca. 2-fold after 8 hours, while Fe(II) levels varied 7- to 65-fold. This result suggests that relative differences in biomass do not appreciably contribute to observed differences in Fe(III) reduction rate between induced/uninduced samples and that inducible Fe(III) reduction is primarily controlled by EET protein expression. Additionally, our viability measurements show that inducibility is not due to spurious effects from cell lysis or plasmid maintenance. We also examined the early timescale of inducible Fe(III) reduction for the optimized *mtrC* construct in the absence of ferrozine. Similar to ferrozine-containing experiments, Fe(II) concentration increased in the presence of IPTG after ca. 2-3 hours, while uninduced samples remained at baseline levels (Figure D.5). Collectively, these results demonstrate that ferrozine does not markedly alter inducible Fe(III) reduction and further validate our real-time methodology as a means to assay EET gene expression.

5.3.5 Reduction Rate Response Functions from Steady-State EET Gene Expression

Using our translation-optimized EET gene expression plasmids, we next examined how Fe(III) reduction kinetics changed with varying transcription rate. Since our RBS library screening aided in identifying RBS/EET gene pairs that display high dynamic range between maximal (1500 μM IPTG) and minimal (0 μM IPTG) induction, we hypothesized that graded EET activity would be measured when testing intermediate inducer concentrations. Given that EET activity in our system should be proportional to steady-state mRNA levels of the expressed EET gene and transcriptionally regulated via LacI (Figure 5.4a), we further reasoned that generated response functions (i.e., fitted rate

constant vs. IPTG concentration) may exhibit Hill function-type responses to changing IPTG concentration and functionally behave as Buffer logic gates.

To promote steady-state behavior and minimize simultaneous effects of growth and dynamic protein expression, we initially pre-induced each EET construct at various IPTG concentrations for 24-hours in lactate/fumarate-containing growth medium. Subsequently, these cultures were diluted 100-fold into growth medium containing the same concentrations of IPTG and ferrozine, and Fe(III)-citrate was finally added prior to kinetic measurements. As predicted, we observed that fitted rate constants increased for all tested EET genes with increasing concentration of IPTG (Figure 5.4c-e). Generally, each response function followed a sigmoidal shape and could be modeled using an activating Hill function. Similar fitted cooperativity (n = 1.296 and 1.750) and threshold-response ($K_{1/2}$ = 14.2 and 15.5 μM IPTG) values were observed between *cymA* and *mtrC* (Figure 5.4c,e). These fitted Hill parameters also comparable favorably to those generated by a fluorescent *sfgfp* circuit that was anaerobically induced with IPTG under steady-state expression (n = 1.699, $K_{1/2}$ = 97.8 μM IPTG) (Figure 5.4b). This is expected if transcription of each gene is controlled by the same regulator (LacI) and promoter ($P_{tacsymO}$) and was evidence that gene transcription rate limits EET activity in our constructs. While the *mtrA* construct exhibited a more gradual increase in Fe(III) reduction rate (n = 0.6530, $K_{1/2}$ = 221.4 μM IPTG), it still demonstrated an ability to turn-on EET activity in response to IPTG (Figure 5.4d). Given that empty vector controls showed baseline or lower than uninduced rates of Fe(III) reduction (Figure D.6), increases in EET activity appear to be due to IPTG-driven increases in EET gene expression for all Buffer gate constructs.

To verify if differential EET activity arose from transcriptional control of EET protein levels, we analyzed whole cell lysate from each EET gene expression construct via SDS-PAGE and heme-staining. For the *mtrC* construct, we observed high molecular weights bands (ca. 250 kDa) that increased in intensity with increasing concentration of supplemented IPTG (Figure D.7a). Bands in this size range have previously been associated with MtrC-containing complexes[369]. For the *cymA* construct a faint but noticeable band migrated around the size of CymA (19 kDa) (Figure D.7c)[108]. While IPTG-

dependent differences could not be discerned by the naked eye, densitometry analysis indicated that band intensity increased with IPTG concentration above uninduced levels (Figure D.7d). Although we could not identify bands whose formation/disappearance was a result of MtrA expression (Figure D.7b), the MtrC/CymA heme staining results are evidence that functional cytochromes can be generated from our expression system. Together, this data demonstrates that transcriptionally regulated *cymA, mtrA, and mtrC* constructs can controllably turn on EET activity (i.e., Buffer gate behavior) and suggests that changes in protein expression are linked to changing Fe(III) reduction rates.

5.3.6 A Polynomial Model Describes Dynamic Gene Expression and Fe(III) Reduction

While these previous experiments demonstrated that our inducible constructs afforded predictable control over EET activity under conditions closest to steady-state protein expression, there are many applications where dynamic control of protein expression and EET activity would be advantageous (e.g., sensing, catalysis)[214,293]. Thus, we also examined EET response functions by the *cymA*, *mtrA,* and *mtrC* constructs in response to non-steady state gene expression. As described above, we previously fit Fe(III) reduction kinetics to a Monod model of substrate utilization. However, a major assumption of Monod models is that transcriptomic and proteomic changes during growth do not affect the fitted rate constant[370]. In practice, this means that engineered changes to mRNA and protein levels should rapidly reach steady-state. As this may not be the case under certain experimental conditions, we also examined a model that accounted for the dynamics of protein expression immediately after induction. Under the assumption of constant biomass (i.e., minimal growth) and rapid equilibrium of steady-state mRNA levels, a simplified dynamic induction model predicts a linear increase in the cellular concentration of expressed EET proteins with time (see section 5.5.5). The minimal growth assumption appears valid based on comparable cell counts measured for each induced/uninduced EET construct during dynamic expression (Figure D.4). While this model exhibits an accelerating Fe(III) reduction rate similar to Monod-based exponential models, kinetics are

more accurately described by a second-order polynomial. Using this polynomial model, the fitted constant preceding the time-squared term is also predicted to be proportional to steady-state mRNA levels and should be controllable in our system. As our system is likely somewhere in-between the limits of no-growth/dynamic protein levels and cell growth/steady-state protein levels, we expected that both models could aid characterization of dynamic EET gene expression and Fe(III) reduction.

5.3.7 Dynamic Expression of EET Genes Predictably Controls Reduction Rate

To evaluate dynamic expression of EET genes, cells were pregrown in the absence of inducer and induced with IPTG immediately prior to Fe(III) citrate addition. Initially, we mimicked our steady-state experiments by preculturing the *mtrA* and *mtrC* constructs anaerobically and the *cymA* construct aerobically. Using the polynomial model to fit Fe(III) reduction kinetics, the response function generated by the *cymA* construct fit strongly to an activating Hill equation (n = 1.176, $K_{1/2}$ = 79.54 μM) (Figure 5.5b) and fitted Hill parameters were comparable to the response function generated via steady-state *cymA* expression (Figure 5.4c). Rate constants obtained from the Monod-type model yielded similar *cymA* response function behavior (Figure D.8f). In contrast, response functions generated by the *mtrA* and *mtrC* strains fit poorly to Hill models and exhibited low Hill coefficients (n = 0.5492 to 0.7049) for both polynomial and Monod-type model fitting (Figure D.8b-e). While polynomial model fitting produced response functions with higher Hill coefficients relative to the Monod-type model, coefficient values for each construct were still substantially lower than what was expected based on the *cymA* and sfGFP circuits (Figure 5.4b). While the *mtrC* construct exhibited a steep EET turn-on under steady-state expression, turn-on behavior under dynamic expression was substantially more graded. The slope of the *mtrA* dynamic expression response function was similar to its steady-state expression counterpart and to the *mtrC* dynamic expression response function. Together, this was suggestive that other cellular processes (e.g., protein maturation/localization, background Fe(III) reduction) decrease sensitivity of the EET output to IPTG during dynamic induction.

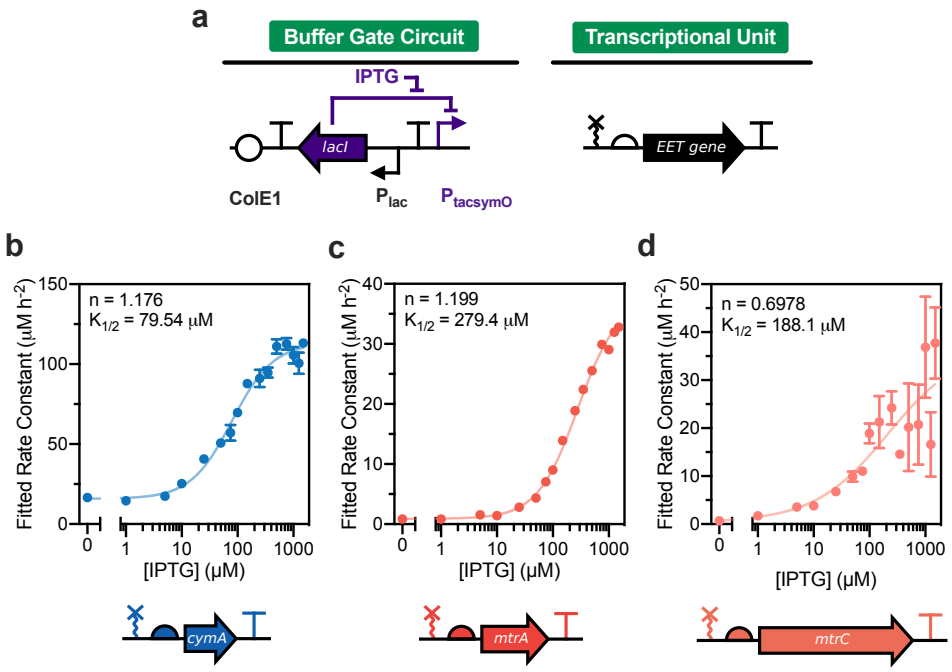

Figure 5.5: Buffer gate response functions under dynamic EET gene expression and from aerobic pregrowth.

(a) Diagram of Buffer gate circuit used to control each EET gene transcriptional output. (b) Fe(III) reduction response function generated by *S. oneidensis* Δ*cymA* expressing the *cymA* Buffer gate circuit (pCD26r4). (c) Fe(III) reduction response function generated by *S. oneidensis* Δ*mtrA* expressing the *mtrA* Buffer gate circuit (pCD25r0). (d) Fe(III) reduction response function generated by *S. oneidensis* Δ*mtrC*Δ*omcA*Δ*mtrF* expressing the *mtrC* Buffer gate circuit (pCD24r1). In these experiments, all strains were pregrown aerobically and IPTG was supplemented immediately prior to measuring Fe(III) reduction kinetics. Rate constants were obtained by fitting raw kinetic data to a polynomial model. The solid line and Hill parameters shown in each graph were obtained by fitting individual replicates to a four-parameter activating Hill function with weighted error. All data represent the mean ± s.e.m. of fitted rate constants for n = 3 biological replicates.

Encouraged by the predictability of the *cymA* response function, we hypothesized that aerobic pregrowth conditions may facilitate higher sensitivity of EET flux to IPTG. Most of the EET machinery is downregulated under aerobic conditions, which we predicted could minimize background Fe(III) reduction[242,371]. Furthermore, dynamic expression in parallel with aerobic to anaerobic transition may ensure that all EET pathways, including

those under exogenous control, turn on simultaneously. Thus, we examined dynamic expression by the *mtrA* and *mtrC* constructs after aerobic pregrowth. Excitingly, we found that response functions for the *mtrA* construct fit more strongly to activating Hill models (Figure 5.5c). Kinetic fitting using both the polynomial and Monod-type models generated similar values for fitted Hill parameters (Figure D.8g). Additionally, the fitted Hill coefficients for the *mtrA* construct were comparable to those for *cymA* and *sfgfp* circuits and overall kinetic variability significantly decreased. In contrast, the *mtrC* construct only showed a marginal improvement in fitting to all models (Figure 5.5d, D.8h). These collective results demonstrate that our engineered *cymA*, *mtrA*, and *mtrC* constructs can controllably turn on EET activity in response to both steady-state and dynamic transcriptional cues.

5.3.8 NOT Gate Circuits Turn Off Fe(III) Reduction in the Presence of IPTG

Having developed a set of EET gene expression constructs that turn on EET activity via transcriptional regulation, we next asked if similar genetic designs could be leveraged to turn off cellular electron flux. The NOT gate is the simplest expression-based logic gate that inverts the signal from an inducer molecule to turn off expression of a target gene[211,372]. Mechanistically, an inducer molecule (e.g., IPTG) stimulates expression of a repressor protein, which subsequently downregulates the target gene. Since our *cymA* and *mtrC* constructs were optimized to exhibit maximal transcriptional responsiveness with high dynamic range, we hypothesized that converting their Buffer gate constructs into NOT gate designs would enable transcriptional downregulation of these genes. Accordingly, NOT gate genetic architectures should facilitate EET turn-off behavior in the presence of IPTG.

We designed NOT gate plasmids for the *cymA* and *mtrC* constructs, using TetR as the repressor that regulates EET gene transcription (Figure 5.6a)[373]. NOT gate transcriptional outputs were identical to our optimized Buffer gate designs for *cymA* and *mtrC* (i.e., ribozyme-optimized RBS-target gene-terminator), but instead of regulation via $P_{tacsymO}$, each transcriptional unit was placed downstream of the promoter P_{tet}. Genes under control of P_{tet} are constitutively expressed in the absence of the TetR and downregulated

in its presence. In our NOT gate plasmids, TetR expression was controlled via LacI/$P_{tacsymO}$. Thus, IPTG should elevate TetR levels and subsequently decrease EET gene expression in appropriate knockout strains (Δ*mtrC*Δ*omcA*Δ*mtrF* and Δ*cymA*) transformed by these plasmids. Although EET activity can readily be turned on through dynamic expression of EET genes, turning off EET activity via transcriptional regulation is more challenging. Using NOT gate architectures, regulated EET genes are maximally expressed in the absence of inducer. Upon adding IPTG, not only must downregulation of EET gene transcription be considered, but also the fate of preexisting EET proteins. While EET proteins can potentially be diluted through cell division[234], this process may occur at timescales slower than what is required for functional NOT gate behavior.

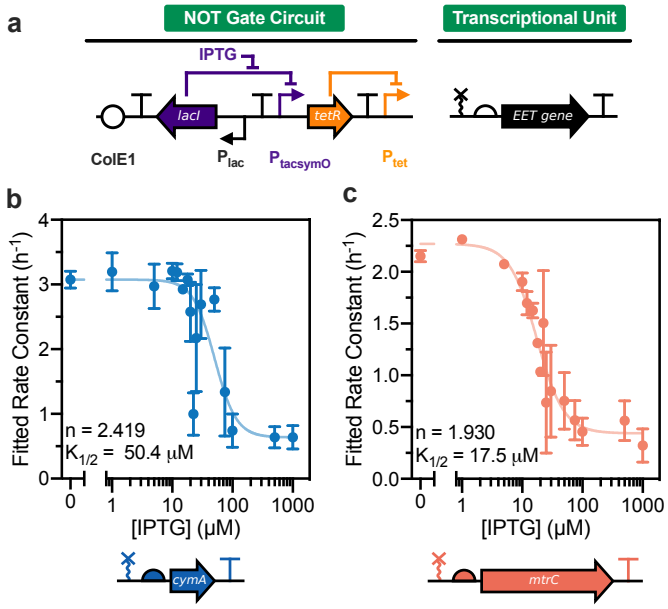

Figure 5.6: NOT gate response functions under steady-state EET gene expression.

(a) Diagram of NOT gate circuit used to control each EET gene transcriptional output. (b) Fe(III) reduction response function generated by aerobically pregrown *S. oneidensis* Δ*cymA* expressing the *cymA* NOT gate circuit (pCDd3r4). (c) Fe(III) reduction response function generated by anerobically pregrown *S. oneidensis* Δ*mtrC*Δ*omcA*Δ*mtrF* expressing the *mtrC* NOT gate circuit (pCDd1). In these experiments, all strains were pre-induced with IPTG for 18-24 hours prior to measuring Fe(III) reduction kinetics. Cultures were also supplemented with IPTG during kinetic measurements. Rate constants were obtained by fitting raw kinetic data to a Monod-type model. The solid line and Hill parameters shown in each graph were obtained by fitting individual replicates to a four-parameter deactivating Hill function with weighted error. To improve Hill function fitting for (b), the maximum and minimum Hill function values were constrained by the mean fitted rate constants at 0 and 1500 μM IPTG, respectively. All data represent the mean ± s.e.m. of fitted rate constants for n = 3 biological replicates.

To avoid complications from dynamic expression/induction and achieve steady-state expression levels, an 18-24 hour IPTG pre-induction was performed for each NOT gate prior to Fe(III) reduction. Response functions were generated using a range of IPTG concentrations and we found that fitted rate constants were reasonably approximated by deactivating Hill functions for both the *cymA* (n = 2.419; $K_{1/2}$ = 50.4 μM) and *mtrC* (n = 1.930; $K_{1/2}$ = 17.5 μM) constructs (Figure 5.6b-c). In the absence of IPTG, both constructs

exhibited rapid Fe(III) reduction and fitted rate constants were similar to those observed with our maximally induced EET turn-on circuits. This suggested that both *mtrC* and *cymA* were being constitutively expressed as expected from the NOT gate design. In contrast, cells preinduced with high levels of IPTG exhibited slower Fe(III) reduction kinetics, with fitted rate constants comparable to both uninduced *mtrC* and *cymA* Buffer gate constructs. To control for the effect of TetR expression on Fe(III) reduction, we also constructed an empty NOT gate plasmid that increased TetR expression in response to IPTG, but lacked an EET gene downstream of the P_{tet} promoter. All knockout strains transformed by this plasmid exhibited low levels of Fe(III) reduction and minimal change in reduction rate with IPTG addition (Figure D.9). While, *S. oneidensis* MR-1 transformed by this plasmid exhibited a slight drop in Fe(III) reduction in the presence of IPTG, induced and uninduced rate constants remained substantially higher than empty vector or NOT gate transformed knockout strains. This further evidenced that changes in Fe(III) reduction were due to NOT gate-controlled EET gene expression and not spurious effects from varying TetR levels.

We briefly examined dynamic expression experiments with the *mtrC* NOT gate. As predicted, only a marginal decrease in Fe(III) reduction rate was observed when IPTG was added immediately prior to kinetic measurements (ca. 35%) relative to decreases observed with steady-state expression (ca. 85%) (Figure D.10, Figure 5.6c). Attempts to accelerate growth-based protein turnover with addition of fumarate were similarly hampered by poor EET turn-off behavior, relative to steady-state experiments (Figure D.10). Although dynamic expression will require further optimization, our results indicate that it is possible to program EET turn-off by downregulating expression of EET genes.

5.4 Discussion and Conclusions

Developing rigorous and predictable control over EET flux is of critical importance to expand the utility of electroactive microbes in redox-driven technologies[90,91]. In this work, we asked if expression of single EET genes (*cymA*, *mtrA*, *mtrC*) in *S. oneidensis* knockout strains could enable such control. By making simple and systematic changes to

translation and transcription of these genes, we explored the design space of programmable Fe(III) reduction kinetics.

Although there are notable examples of engineered genetic circuits that control EET activity in *S. oneidensis*, many of these circuits simultaneously regulate multiple genes (e.g., *mtrCAB* operon[136,215], NADH/flavin metabolite pathways[130,131]) or lack detailed engineering parameterizations typically measured for fluorescence-parameterized circuits (e.g., response functions, dynamic range optimization). Although more systematic optimizations have been performed to incorporate the Mtr proteins into *Escherichia coli*, this organism requires extensive engineering to facilitate proper functioning of pathway components[277,298,368]. Since the underpinnings of EET performance can be challenging to interpret, we adopted a reductionist approach by studying single EET genes and their contribution to EET flux. Expressing each gene in appropriate *S. oneidensis* knockout strains allowed us to abrogate native expression, functionally generate each EET protein and associated conduit proteins, and isolate each gene's influence on EET parameters. Moreover, we chose to target the CymA/Mtr conduit since these proteins are somewhat orthogonal to overall cellular metabolism, relative to more universal metabolites (e.g. NADH, flavins, quinones). In contrast to electrode-based setups, Fe(III) reduction provided a convenient and high throughput assay to analyze EET activity. Notably, our results demonstrate that fitted Fe(III) reduction rate constants from engineered strains follow predictable behavior, akin to circuits where fluorescent reporters are the output[211]. While cellular physiology likely differs between knockout strains (e.g., loss of one cytochrome may upregulate expression/maturation of others)[368] and absolute kinetics are subject to change based on plasmid composition (e.g., origin of replication, resistance marker)[80,361], our system could identify pairings of engineered plasmids and genetic backgrounds that yielded the desired circuit function.

For example, a major challenge in the electromicrobiology community is engineering of EET circuits that exhibit minimal leakiness and high signal-to-noise outputs[90]. More broadly, developing genetic circuits with these properties is a ubiquitous goal in synthetic biology[211,227]. With other engineered genetic circuitries, RBS optimization

for target genes is typically performed to address this[373]. Thus, we developed a small library of plasmids for each tested EET gene to first identify the range of inducibility afforded by different RBS sequences/translation strengths. After analyzing Fe(III) reduction kinetics by all library members, we pinpointed RBS sequences for each EET gene that facilitated the highest dynamic range in EET activity. Notably, the optimal *mtrC* and *mtrA* plasmids possessed the weakest translation strength in their respective libraries (Figure 5.3f-g). Like other outer membrane proteins, MtrC has a low turnover rate (half-life ca. 16 hours) relative to intracellular proteins[374]. MtrC also forms a large multi-protein complex (MtrCAB) that may further stabilize it from degradation[103,375]. Moreover, we observed that dynamic range of *mtrC* constructs decreased below 1 with increasing translation strength (Figure 5.3j), which suggested that high levels of MtrC expression impose a metabolic burden[368]. Taken together, these factors may explain why only the weakest translation strength construct facilitated high dynamic range. While the degradation rate of MtrA has not been studied, it is also part of the MtrCAB complex, and thus its RBS library likely exhibits similar trends to *mtrC* due to low protein turnover[376]. Conversely, the small size of CymA (19 kDa) relative to MtrC (76 kDa) and MtrA (35 kDa), along with its more intracellular localization, may increase its susceptibility to proteolytic degradation and result in a higher turnover rate. This would also explain why the optimal *cymA* construct possessed a more intermediate translation strength (Figure 5.3e). Overall, we identified transcriptional units (ribozyme, RBS, and terminator sequences) for *cymA, mtrA*, and *mtrC* that exhibited a spectrum of dynamic ranges, which could inform the choice of EET construct based on application needs.

We leveraged RBS optimization of each EET gene to forward engineer EET turn-on and turn-off behavior in response to logic gate-driven transcriptional cues. While there are several means to regulate the expression and activity of electron transfer proteins within cells[215,377], a benefit of transcriptional logic gates is that desired gene expression behavior is relatively straightforward to program. Using the two simplest logic gates, we validated our underlying hypothesis that EET flux can be precisely controlled via transcriptional modulation of single EET genes. Upon addition of IPTG to each Buffer gate strain,

increases in EET protein levels were concomitant with increases in Fe(IIII) reduction rate (Figures 5.4-5.5). Although direct measurement of MtrA protein expression posed challenges, our heme staining results suggest that MtrC and CymA are being functionally expressed (Figure D.7). We also note that all of our circuit plasmids rescued Fe(III) reduction deficiencies that have been previously characterized via knockout complementation[86,99]. Additionally, minimal changes in cell growth were observed between induced/uninduced strains, further suggesting that kinetic differences were a result of protein expression (Figure D.4). Furthermore, we observed that fitted Fe(III) reduction rate constants vs. inducer IPTG concentrations (i.e., EET response functions) fit well to Hill models for both our Buffer and NOT gate architectures (Figures 5.4-5.6). Since fluorescent protein-based response functions can be readily parameterized by such models (Figure 5.4b)[227], these collective results support a scheme whereby transcriptional regulation controls EET protein levels and thus EET flux. Excitingly, our NOT gate circuits were able to dial down EET activity, albeit only at steady-state protein expression levels. As shown from our experiments, utilizing NOT gate architectures under dynamic conditions remains an outstanding challenge and is likely due to limited turnover of the expressed EET proteins (Figure D.10). Since growth-based dilution is the primary contributor to protein level decreases[234], future studies can potentially optimize bacterial respiration onto secondary substrates to improve such decreases for target EET proteins. Altogether, our system demonstrates that EET genes may serve as useful outputs for other transcriptionally controlled circuits, such as two-component sensors and stimuli-responsive logical operators[21,378].

As determined by the value of fitted Hill coefficients, the sensitivity of EET turn-on activity to IPTG appears to strongly depend on the identity of the expressed EET gene/genetic background and strain pregrowth conditions. As our sfGFP Buffer gate and EET turn on circuits utilize the same transcriptional regulatory mechanism (Figure 5.4a), fitted Hill coefficients should be comparable for both systems if transcriptional control rate-limits functional activity. Hill parameters for EET response functions that deviate from those measured via sfGFP suggests that other cellular processes compete with

transcriptional control[227,368]. For example, *cymA* and *mtrC* strains that were preinduced with IPTG exhibited Hill coefficient values closest to those determined for sfGFP (n = 1-2) (Figure 5.4b-c,e), suggesting strong transcriptional control is facilitated via steady-state protein expression. For dynamic expression experiments, we observed lower than expected Hill coefficients (n < 1) for anaerobically pregrown *mtrC* and *mtrA* strains (Figure D.8). This lower sensitivity to IPTG is reasonable given that these genes encode proteins with numerous post-translational processing steps (e.g., maturation, periplasmic/extracellular localization) that may rate-limit their functional activity when dynamically expressed[368]. Moreover, other cytochromes may be expressed during anaerobic pregrowth that contribute to background Fe(III) reduction[86].

Interestingly, we observed that some aerobically pregrown strains (*cymA* and *mtrA*) exhibited a more characteristically sensitive response to IPTG during dynamic expression and fit better to Hill models relative to anaerobic pregrowth (Figure 5.5b-c). Given that relative growth rates for these strains were not significantly different based on the presence/absence of IPTG (Figure D.4), we primarily attribute this sensitivity to a decrease in background reduction from spurious EET pathway expression. Under aerobic conditions, much of the EET machinery in downregulated in *S. oneidensis*[242,371]. Even when switched to anaerobic conditions, Fe(III) reduction capabilities by aerobically pregrown *S. oneidensis* are considerably diminished relative to anaerobic pregrowth[379]. Thus, the switch to anaerobic Fe(III) respiring conditions likely causes reduction by aerobically pregrown strains to be more rate-limited by plasmid-based EET gene expression. For example, the *mtrA* construct's genetic background (Δ*mtrA)* has functional redundancy by other cytochromes and is less "insulatory" than the other tested strains (Δ*mtrC*Δ*omcA*Δ*mtrF* and Δ*cymA*)[86,111], which may explain why the aerobic pregrowth facilitated markedly higher IPTG sensitivity (Figure 5.5c). Future engineering efforts may seek to identify other strain backgrounds that improve transcriptional control of EET activity. Collectively, our results demonstrate that inducible EET activity can follow a spectrum of sensitivity to inducer stimuli, which may be advantageous based on application

needs such as switch-like behavior for computation or graded responses for sensing/detection[204,214,380].

Logic gate formalisms were originally intended to abstract electrical circuit construction and aid the development of more complex electronic devices. Synthetic biologists have adapted these concepts to generate countless transcriptional circuits[26], which range from simple Buffer gates[111] (a single inducer causes gene expression "turn on") to complex multi-layered logic constructs[19,201,204,380,381], where one regulator modulates the expression of multiple regulators and actuators. In this work, we showed that transcriptional logic gate regulation can be extended to EET protein expression and can consequently control electron transfer to soluble Fe(III). Notably, simple exponential and polynomial relationships captured the dynamics of Fe(III) reduction. From these models, we demonstrated that EET protein actuations can be parameterized similarly to other transcriptionally controlled logic gates (i.e., fitting rate constants to Hill models) and rationally programmed to exhibit desired behavior. Although we only examined the two simplest transcriptional logic gates, the ability to turn on and turn off EET flux is foundational for constructing more complex circuit architectures. Given the respiratory flexibility of the CymA/Mtr pathway, our system is potentially extendable to other metals and EET acceptors. We expect that this work will serve as the basis for future engineering of logic gate-driven EET activity and further blend the fields of synthetic biology and electrical engineering.

5.5 Materials and Methods

5.5.1 DNA and Strain Construction

All bacterial strains, plasmids, genetic circuit maps, and sequence information for each genetic part are detailed in Appendix D. All plasmids were assembled via Golden Gate cloning procedures using enzymes (BsaI, SapI, BsmBI) and buffers from New England Biolabs. DNA fragments used in Golden Gate cloning[382] were generated via partial/whole-plasmid PCR (Phusion High Fidelity DNA Polymerase, New England

Biolabs) or commercially synthesized (gBlocks, Integrated DNA Technologies). Generally, 10 µL Golden Gate reactions were set up that contained 10 fmol of pCD plasmid backbone and 40 fmol of each gBlock and/or PCR insert (as necessary). In a thermocycler, Golden Gate reactions were cycled 25 times: 90 s at 37 °C (for BsaI and SapI) or 42 °C (for BsmBI) followed by 3 minutes at 16 °C. After the 25 cycles, reactions were incubated at 37 °C (for BsaI and SapI) or 55 °C (for BsmBI) for 5 minutes, 80 °C for 10 minutes, and then held at 4 °C.

Golden Gate reactions were used to directly transform freshly prepared electrocompetent *S. oneidensis* strains. To prepare electrocompetent *S. oneidensis*, bacterial stocks stored in 22.5% glycerol at -80 ºC were streaked onto LB agar plates and grown aerobically overnight at 30 ºC. Single colonies were used to inoculate 5 mL of LB medium and grown aerobically in a shaking incubator (30 °C and 250 rpm). After 18 hours, the entire 5 mL culture was washed 3 times with sterile 10% glycerol at room temperature and concentrated to ~300 µL. 2 µL of Golden Gate reaction was mixed with 30 µL of concentrated electrocompetent *S. oneidensis*, transferred to a 1 mm electroporation cuvette, and electroporated at 1250 V. To recover electroporated cells, 250 µL of LB was immediately added post-electroporation and cells were incubated/shaken at 30 °C and 250 rpm. After 2 h of recovery, 100 µL of cell suspension was plated onto LB agar plates containing 25 µg mL-1 kanamycin sulfate and incubated overnight at 30 °C to obtain single colonies (generally 5-100 colonies observed for 1-3 part assemblies). Single colonies were used to inoculate LB liquid medium containing 25 µg mL^{-1} kanamycin sulfate and incubated/shaken overnight at 30 °C and 250 rpm. These cultures were used to generate 22.5% glycerol stocks, which were stored at -80 °C, and harvest assembled plasmid for Sanger sequencing (DNA Sequencing Facilities, University of Texas at Austin).

5.5.2 RBS Library Design

Ribosome binding site (RBS) sequences with variable translation strength were computationally designed for each EET gene (*cymA*, *mtrA*, and *mtrC*) using the RBS Library Calculator (v2.0) from Salis et al.[365,366]. The calculator was utilized in

design/search mode with the DNA sequence of each gene, the 16S rRNA sequence of *Shewanella oneidensis* MR-1, and the constant upstream region of each unique ribozyme after self-cleavage serving as software inputs (see Table D.2). The target minimum translation initiation rate (0.1 a.u.), target maximum translation initiation rate (1,000,000 a.u.), and target library size (64 members) were chosen such that output RBS sequences covered a broad translational space. One RBS sequence for *mtrC* (pCD24) was not designed using the RBS Library Calculator, and was instead derived from the BioBrick collection, B0032. The translational strength of this sequence (ΔG_{total} = -5.34 kcal mol^{-1}) was calculated using the RBS Calculator (v2.0) using the same software inputs used for library construction. Translation strengths for each sequence were reported as ΔG_{total}, which is related to translation initiation rate (r) according to the exponential relationship $r \propto \exp(-\beta \Delta G_{total})$.

5.5.3 Measurement of Fe(III) Reduction Kinetics by *S. oneidensis*

Except where noted, all Fe(III) reduction experiments were monitored *in situ* using 96-well plates that contained *S. oneidensis*, lactate, Fe(III) citrate, and ferrozine[354]. The general protocol for an Fe(III) reduction setup was as follows. Bacterial stocks stored in 22.5% glycerol at -80 ºC were streaked onto LB agar plates (for wild-type and knockout strains) or LB agar with 25 μg mL^{-1} kanamycin (for plasmid-harboring strains). For anaerobic pregrowths, plates were brought into an anaerobic chamber (3% H_2, balance N_2, Coy) and single colonies were used to inoculate a pregrowth medium consisting of SBM supplemented with 100 mM HEPES, 1X trace mineral supplement (ATCC), 0.05% casamino acids, 20 mM sodium lactate as the electron donor, and 40 mM sodium fumarate as the electron acceptor. For dynamic expression and growth of strains absent of plasmid, this culture medium was inoculated and statically incubated in an anaerobic chamber at 30 ºC for 18-24 hours. For steady-state expression experiments, this culture medium was inoculated and statically incubated in an anaerobic chamber at 30 ºC for 6 hours. Afterwards, cultures were diluted 25-fold (10 μL into 250 μL final volume) into 96-well plates containing preinduction medium. Preinduction medium was identical to the

SBM/lactate/fumarate pregrowth medium, but also contained varying concentrations of IPTG. These cultures were statically incubated in an anaerobic chamber at 30 ºC for an additional 18-24 hours. Aerobic pregrowths were identical to the above except that single colonies were used to inoculate pregrowth medium that lacked 40 mM sodium fumarate and grown aerobically in a shaking incubator (250 rpm, 30 ºC). All cultures were performed in biological triplicate where each culture was derived from a single picked colony. 25 μg mL^{-1} kanamycin sulfate was added to pregrowth and preinduction media for strains harboring plasmids. Optical density for each overnight growth was monitored by pipetting 100 μL (for preinduced samples) or 250 μL cell suspension aliquots into 96-well plates and measuring absorbance at 600 nm using a BMG LABTECH CLARIOstar plate reader. The plate reader software converted measured optical density values into standard 10 mm cuvette readings based on the plate dimensions (96-well flat bottom, sterile, Greiner) and utilized liquid volume.

In situ Fe(III) reduction was set up within an anaerobic chamber using degassed media and solutions. Immediately prior to each experiment, 24 mg of ferrozine was dissolved in 12 mL of 2x SBM solution that was supplemented with 200 mM HEPES, 0.1% casamino acids, and 2X trace mineral supplement (ATCC). A master mix was generated that combined the 2X SBM/ferrozine with sodium lactate and kanamycin sulfate, such that the final concentrations of these components would be 1X casamino acid/trace mineral solution supplemented SBM, 1 mg mL^{-1} ferrozine, 20 mM sodium lactate, and 25 μg mL^{-1} kanamycin sulfate, within a final 250 μL solution. 220 μL aliquots of this master mix were pipetted into each 96-well plate well and subsequently mixed with 10 μL of appropriate IPTG stock. Next, (un)induced *S. oneidensis* pregrowth was diluted 4-fold (25 μL into 75 μL SBM supplemented with kanamycin) in a separate 96-well plate. 10 μL of this 4-fold dilution was used to inoculate the 96-well plate containing the Fe(III) reduction mixture (final dilution equal to 100-fold from overnight pregrowth). Lastly, 10 μL of 125 mM Fe(III) citrate was added to each well such that the final concentration was 5 mM Fe(III). To generate an Fe(II) calibration curve, freshly prepared Fe(II) sulfate stocks dissolved in sterile water were also added to each 96-well plate. 10 μL of each Fe(II)

stock,10 µL of sterile water, and 10 µL abiotic SBM were mixed with 220 µL of master mix such that the final concentration of Fe(II) standards ranged from 0 to 96 µM Fe(II).

After addition of all plate components, the 96-well plate was sealed with a sterile and optically transparent sealing film (PCR-SP-S, AxySeal Scientific) and covered with a polystyrene plate lid (Eppendorf) that had silicone grease lining the edges. This plate was removed from the anaerobic chamber and placed within a BMG LABTECH CLARIOstar plate reader with temperature control set to 30 ºC. Without shaking, the absorbance at 562 nm was measured every 10 minutes for at least 14 hours. For the ferrozine-free experiment, the Fe(III) reduction setup was identical to the above except that ferrozine was not dissolved in the 2X SBM. Instead, the 96-well plate was kept within an anaerobic chamber at 30 ºC for the entirety of the experiment. Aliquots were taken and either acidified in equal volume 1 N HCl for measurement of Fe(II) levels or used for serial dilutions to perform colony counting on LB agar plates containing 25 µg mL^{-1} kanamycin sulfate. Plated dilutions were grown aerobically overnight at 30 ºC.

5.5.4 Derivation of Monod-type Model for Fe(III) Reduction

General relationship between cell growth and Fe(III) Reduction

Monod-type models can be used to relate extracellular electron transfer (EET) and growth of electroactive microorganisms[232]. Generally, these models are of the form:

$$\frac{dN}{dt} = \mu N \qquad \text{(Eq. 1)}$$

$$\mu = \mu_{max} \frac{S}{K_S + S} \qquad \text{(Eq. 2)}$$

where N is the concentration of cells in suspension, μ is the specific growth rate, μ_{max} is the maximum specific growth rate, and S is the concentration of the growth rate-limiting substrate. Although in many situations the growth rate-limiting substrate is a carbon source[363], it can also be an electron acceptor, which in our system is soluble Fe^{III}. In

Monod-type models, μ is function of medium composition/cell-intrinsic physiology and, as discussed further below, can be assumed to remain constant.

Since cells utilize Fe^{III} to generate further biomass, the following relationship arises in our system:

$$\frac{dN}{dt} = -Y\frac{dFe^{III}}{dt} \qquad \text{(Eq. 3)}$$

where Y is the yield coefficient that relates substrate utilization to biomass generation. Combining (3) with (1) generates

$$\frac{dFe^{III}}{dt} = -\frac{\mu}{Y}N \qquad \text{(Eq. 4)}$$

Assuming constant Y during metal reduction, (3) can also be integrated to

$$N = N_0 + Y(Fe_0^{III} - Fe^{III}) \quad \text{(Eq. 5)}$$

By inserting (5) into (4), the following relationship is obtained

$$\frac{dFe^{III}}{dt} = -\frac{\mu}{Y}(N_0 + Y(Fe_0^{III} - Fe^{III})) \qquad \text{(Eq. 6)}$$

Equation (6) can be used to directly model microbial Fe^{III} reduction kinetics and obtained fitted values for Y and μ. However, since the microbial reduction product Fe^{II} is typically what is experimentally quantified, (6) can be rewritten using the following mass conservation relations

$$\frac{dFe^{III}}{dt} = -\frac{dFe^{II}}{dt} \qquad \text{(Eq. 7)}$$

$$Fe^{II} = Fe_0^{II} + Fe_0^{III} - Fe^{III} \quad \text{(Eq. 8)}$$

to generate

$$\frac{dFe^{II}}{dt} = \frac{\mu}{Y}(N_0 + Y(Fe^{II} - Fe_0^{II})) \qquad \text{(Eq. 9)}$$

This differential equation can be integrated to

$$Fe^{II} - Fe_0^{II} = \frac{N_0}{Y}(\exp(\mu t) - 1) \qquad \text{(Eq. 10)}$$

Under steady-state gene expression, (10) is the exponential model that was used to fit kinetic data from our experiments and obtain values for μ. We note that despite a generally strong fit of (10) to much of our experimental data, fitted values for μ appear higher than what has been experimentally measured for *Shewanella oneidensis* growth rates. Obtaining unrealistic growth rate values is a known issue when performing kinetic experiments with high S_0/N_0 ratios[370]. Since *S. oneidensis* also performs EET for energy maintenance in addition to cell growth, our fitted μ values are likely a combination of these factors. Thus, we elected to refer to μ as the fitted rate constant and not fitted growth rate.

Comment on assumption of constant μ

In many conditions, μ can be assumed to remain constant when $S >> K_S$. Alternatively, μ can be assumed to remain constant when $S_0 >> \Delta S$, where ΔS is the change in S over the course of the experiment. Our setup is the latter scenario, as we are only fitting Fe^{II} kinetics when Fe^{II} concentration ranges from 0 to 96 μM. As shown in Figure D.2, we experimentally fit K_S and determined its value to be 1889 μM, which compares favorably to previous measurements. (2) appears to accurately relate fitted rate constants to starting Fe(III) citrate concentration, which further validates that our kinetics follow a Monod-type relationship. Moreover, given the fitted K_S value, our typical starting Fe(III)

citrate concentration S_0 of ca. 5000 μM, and ΔS being at most 96 μM, μ deviates based on changing S values by at most ca. 0.5%. This supports the validity of our assumption that fitted μ values are not affected by changing Fe^{III} concentration under our experimental conditions.

Relationship between fitted rate constant and EET gene expression

The fitted rate constant from the Monod-type model controls the rate of microbial Fe(III) reduction within our system. When the cellular concentration of a single protein P_{EET} rate-limits reduction of Fe(III), an additional relationship can be assumed for the Monod-type model that is similar to Michaelis-Menten enzyme kinetics.

$$\mu = \mu_{max} P_{EET} \frac{S}{K_S + S} \quad \text{(Eq. 11)}$$

Since we expressed this EET protein in appropriate knockout strains of *S. oneidensis,* inducible control of P_{EET} can control Fe(III) reduction. The dynamics of inducible protein expression are well studied and can be modeled using the following equations

$$\frac{dm_{EET}}{dt} = k_{tx}\left(MIN + (MAX - MIN)\frac{I^n}{K_{1/2}^n + I^n}\right) - d_m m_{EET} \quad \text{(Eq. 12)}$$

$$\frac{dP_{EET}}{dt} = k_{tl} m_{EET} - d_P P_{EET} \quad \text{(Eq. 13)}$$

where m_{EET} is the cellular mRNA concentration of the target EET gene, k_{tx} is a rate constant for this gene transcription, and d_m is the degradation rate constant for this transcript. The expression $\left(MIN + (MAX - MIN)\frac{I^n}{K^n + I^n}\right)$ is a quasi-empirical Hill function that describes LacI/IPTG regulation of EET gene transcription. The amount of EET gene mRNA generated depends on IPTG supplemented (I) and values for MIN, MAX,

n, and $K_{1/2}$, which are typically obtained by model fitting. k_{tl} is the rate constant for mRNA translation and d_P is the protein degradation rate constant.

The steady-state approximation is frequently applied to (12), which causes m_{EET} to follow a Hill function relationship

.

$$m_{EET,ss} = \frac{k_{tx}}{d_m}(MIN + (MAX - MIN)\frac{I^n}{K_{1/2}^n + I^n}) \qquad \text{(Eq. 14)}$$

After applying the steady-state approximation to (13), a linear relationship is derived between m_{EET} and P_{EET}

$$P_{EET,ss} = \frac{k_{tl}}{d_P} m_{EET} \qquad \text{(Eq. 15)}$$

which can further be used with (14) to model $P_{EET,ss}$ as a Hill function in response to IPTG

$$P_{EET,ss} = \frac{k_{tl}}{d_P}\frac{k_{tx}}{d_m}(MIN + (MAX - MIN)\frac{I^n}{K_{1/2}^n + I^n}) \qquad \text{(Eq. 16)}$$

Given our assumption shown in (11), (16) predicts that μ can be described by a Hill function in response to IPTG. We note that d_P is typically assumed to be equal to cellular growth rate. While the fitted μ values are related to growth rate, directly including them in d_P likely leads to physiologically-unmeaningful dilution rates, since μ is a combination of growth rate and energetic maintenance requirements[370]. Based on comparable cell growth observed between induced/uninduced strains as shown in Figure D.4, we primarily attribute drastic differences in fitted μ values (Figure 5.3) as a result of maintenance requirements.

5.5.5 Derivation of Polynomial Model for Fe(III) Reduction

Dynamic protein expression model

The Monod-type model assumes that the cellular concentration of the Fe(III) reduction rate-limiting protein P_{EET} is unchanging with time. This assumption is primarily valid during steady-state induction experiments. In contrast, P_{EET} is expected to vary with time when performing dynamic expression experiments. This motivates the development of another model that captures the dynamics of protein concentration and can relate a fitted Fe(III) reduction parameter to P_{EET}.

While the Monod-type model assumes constant P_{EET} and changing cell concentration, another limit may be examined where P_{EET} varies with time and cell concentration remains relatively constant. This assumption affects (13), as the value of d_P, or essentially the cell growth rate, tends to 0:

$$\frac{dP_{EET}}{dt} = k_{tl} m_{EET,ss} \quad \text{(Eq. 17)}$$

(17) implies that there is negligible growth-based dilution/protein degradation relative to the timescale of mRNA transcription/translation. (17) can be integrated to

$$P_{EET} = k_{tl} m_{EET,ss} t \quad \text{(Eq. 18)}$$

which shows that P_{EET} varies linearly with time and the steady-state concentration of EET gene mRNA m_{EET}. (18) can be further related to IPTG induction by replacing $m_{EET,ss}$ with (14)

$$P_{EET} = k_{tl} \frac{k_{tx}}{d_m} (MIN + (MAX - MIN) \frac{I^n}{K_{1/2}^n + I^n}) t \quad \text{(Eq. 19)}$$

Thus, P_{EET} is shown to vary linearly with time and the rate of P_{EET} increase depends on supplemented IPTG concentrations.

Connection of dynamic protein expression with Fe(III) reduction

To relate Fe(III) reduction rate to P_{EET}, a variation of (4) can be assumed:

$$\frac{dFe^{III}}{dt} = -N_0(k_{EET}P_{EET} + k_{background}) \qquad \text{(Eq. 20)}$$

From (20), it is shown that $\frac{dFe^{III}}{dt}$ is proportional to the initial cell number and the cellular concentration of the rate-limiting EET protein P_{EET}. k_{EET} is a rate constant that relates Fe(III) reduction to P_{EET}. (20) also captures background Fe(III) reduction that is independent of P_{EET} via the rate constant $k_{background}$. Background Fe(III) reduction is assumed to be unchanging with time and proportional to initial cell number. (19) can be inserted into (20) to account for how P_{EET} changes with time/IPTG concentration:

$$\frac{dFe^{III}}{dt} = -N_0(k_{EET}k_{tl}\frac{k_{tx}}{d_m}(MIN + (MAX - MIN)\frac{I^n}{K_{1/2}^n + I^n})t + k_{background}) \quad \text{(Eq. 21)}$$

Integrating (21) and replacing Fe(III) variables with the mass conservation Fe(II) relations yields the second-order polynomial relationship

$$Fe^{II} - Fe_0^{II} = N_0\,(k_{EET}k_{tl}\frac{k_{tx}}{2d_m}(MIN + (MAX - MIN)\frac{I^n}{K_{1/2}^n + I^n}t^2 + k_{background}t) \quad \text{(Eq. 22)}$$

Under dynamic gene expression, (22) is the polynomial model that was used to fit kinetic data from our experiments. Note that (22) predicts fitted constants preceding the t^2 term (which we refer to as μ_{poly}) should follow a Hill function relationship based on supplemented IPTG concentration. For clarity, μ_{poly} is defined as

$$\mu_{poly} = N_0\, k_{EET} k_{tl} \frac{k_{tx}}{2d_m} \left(MIN + (MAX - MIN) \frac{I^n}{K_{1/2}^n + I^n}\right) \text{ (Eq. 23)}$$

Together, (22) and (23) provide another model and fitted rate constant that can be used to parameterize inducible EET activity. Although we chose to examine dynamic protein expression under the no growth assumption to simplify the derived model, we note that growth is likely occurring. Thus, it may be possible to model reduction kinetics using other equations that combine aspects of (10) and (22), potentially through summed weighting.

5.5.6 Reduction Kinetics and Rate Constant Response Function Fitting

Prior to kinetic fitting, the initial Fe(II) concentrations were subtracted from every timepoint within each replicate (i.e., $Fe^{II} - Fe_0^{II}$). These subtracted Fe(II) concentrations, Fe_{subt}^{II}, were then fit to either $Fe_{subt}^{II} = K\,(\exp(\mu t) - 1)$ (exponential model) or $Fe_{subt}^{II} = \mu_{poly} t^2 + K_2 t + K_3$ (polynomial model) to obtain μ and μ_{poly} rate constants, respectively. Response functions for Buffer gate circuits (fitted rate constants vs. IPTG) were modeled using a four-parameter activating Hill function $y = MIN + (MAX - MIN)\frac{I^n}{K_{1/2}^n + I^n}$. Response functions for NOT gate circuits were modeled using a four-parameter deactivating Hill function $y = MIN + (MAX - MIN)\frac{K_{1/2}^n}{K_{1/2}^n + I^n}$. Individual replicate kinetic fitting was performed using least-squares regression with no weighting. Response function fitting was performed using least-squares regression weighting by $\frac{1}{y^2}$ and each replicate y value was treated as an individual point. All fitting was performed in Prism 8.3 (GraphPad Software). Dynamic range was calculated as the ratio of induced (1500 μM IPTG) and uninduced (0 μM IPTG) fitted rate constants for each replicate, and the mean ± s.e.m. was determined.

Chapter 6: Genetic control of radical cross-linking in a semisynthetic hydrogel[5]

6.1 Chapter Summary

Enhancing materials with the qualities of living systems, including sensing, computation, and adaptation, is an important challenge in designing next-generation technologies. Living materials address this challenge by incorporating live cells as actuating components that control material function. For abiotic materials, this requires new methods that couple genetic and metabolic processes to material properties. Toward this goal, we demonstrate that extracellular electron transfer (EET) from *Shewanella oneidensis* can be leveraged to control radical crosslinking of a methacrylate-functionalized hyaluronic acid hydrogel. Crosslinking rates and hydrogel mechanics, specifically storage modulus, were dependent on various chemical and biological factors, including *S. oneidensis* genotype. Bacteria remained viable and metabolically active in the networks for a least one week, while cell tracking revealed that EET genes also encode control over hydrogel microstructure. Moreover, construction of an inducible gene circuit allowed transcriptional control of storage modulus and crosslinking rate via the tailored expression of a key electron transfer protein, MtrC. Finally, we quantitatively modeled hydrogel stiffness as a function of steady-state *mtrC* expression, and generalized this result by demonstrating the strong relationship between relative gene expression and material properties. This general mechanism for radical crosslinking provides a foundation for programming the form and function of synthetic materials through genetic control over extracellular electron transfer.

[5]Adapted from Graham, A.J., Dundas, C.M., Hillsley, A., Kasprak, D.S., Rosales, A.M., Keitz, B.K. (2020) *ACS Biomater. Sci. Eng. 6*(3), 1375-1386. Christopher M. Dundas performed experiments, designed and built the *sfgfp* and *mtrC* expression plasmids, analyzed the results, and contributed to writing the chapter.

6.2 INTRODUCTION

Nature uses hierarchical and genetically-encoded instructions to construct functional materials with specific self-assembly, regulatory, healing, and morphological properties[383]. Inspired by such processes, engineered living materials (ELMs) employ the autonomy of living cells to synthesize and control material structures across multiple scales with user-designed functions that are directly coupled to gene expression[32,40,41,148]. Living materials containing microbes, including biofilms, bacterial cellulose, curli fibers, and synthetic gels loaded with bacteria, are of prominent interest due to their potential application in tissue engineering, 3D printing, soft robotics, metabolic engineering, and living sensors[384–388]. Bacteria are particularly attractive as ELM components due to their natural sensing capabilities and programmability. For example, engineered bacteria can act as cellular actuators integrated within the ELM, tailoring its synthesis and function through overexpression, mutagenesis, and gene circuitry.

Not surprisingly, the majority of ELMs rely on materials natively produced by the host organism. For example, several amyloid-based materials have been synthesized by genetically tractable bacteria, such as aggregates of CsgA in *Escherichia coli*[389,390] and TasA in *Bacillus subtilis*[391]. Genetic fusions have allowed these fibrous matrices to bind specific molecules, conduct electricity, perform catalytic reactions, and adhere to complex surfaces[392–395]. Apart from amyloids, extracellular polymerization of bacterial cellulose has been engineered using quorum sensing circuits and mutagenesis to create sturdy materials for tissue engineering and sensing applications [235,396]. Despite these advances, significant drawbacks of natural materials include their limited chemical functionality, robustness, homogeneity, and scalability compared to engineered synthetic materials[397]. For example, manufactured soft materials such as polymers and hydrogels are easily-functionalized and versatile, facilitating their adoption in diverse environments. However, synthetic materials largely lack the dynamic adaptability and environmental responsiveness found in natural systems. Introducing these qualities to synthetic materials could synergistically enhance ELMs and enable new applications that combine the precision and chemical diversity of engineered materials with the autonomy and evolvability of living cells. However, such

designs will require methods for bacteria to control synthetic material properties at the genotypic level. Similarly, robust transcriptional control and quantitative prediction of the relationship between gene expression and material properties are needed for ELMs to approach the design precision of engineered materials.

Toward this goal, we recently developed a cell-controlled radical polymerization reaction using extracellular electron transfer (EET) from the organism *Shewanella oneidensis*[293]. EET is a form of anaerobic respiration that couples carbon oxidation to the reduction of extracellular metals or metal oxides[64]. In *S. oneidensis*, the Mtr protein pathway is the primary source of EET flux in anaerobic *S. oneidensis* metabolism (Figure 6.1a). Specifically, the outer membrane cytochromes MtrC and OmcA are terminal reductases in this pathway and responsible for direct electron transfer onto extracellular metal species such as Fe and Cu[86,293]. MtrF is a homologue to MtrC and can similarly reduce a variety of metals[398]. In our previous polymerization platform, we redirected EET flux to a metal catalyst, which controlled a polymerization governed by the atom-transfer radical polymerization (ATRP) mechanism. Importantly, we demonstrated that control over polymer production was directly coupled to cell metabolism and genetically encoded through these EET proteins. Since ATRP is a versatile platform for soft material synthesis[399], we hypothesized that EET-powered catalysis could be extended to control radical crosslinking in a synthetic hydrogel. While there are numerous examples of incorporating live cells into polymer networks, network properties such as crosslink density, mesh size, degradation, and elastic modulus have generally been designed independent of cell activity. In addition, previous attempts to incorporate cells as live crosslinking agents in synthetic hydrogels have relied on the activity of glucose peroxidase or extracellular functionalization of cells after growth[400–404], which compromise cell viability through the creation of toxic reactive oxygen species or are not under cellular control. Cell-free gelation systems using bacterial lysates[405] or secreted recombinant peptides[406] have also been explored, but removing the living component prevents continued material responsiveness. We envisioned that controlling radical crosslinking via EET gene

expression would capitalize on the programmability of bacteria and enable the use of stimuli-responsive synthetic biology circuits to control material function.

Here, we demonstrate that EET from *S. oneidensis* can be used to control radical crosslinking of a semi-synthetic methacrylated hyaluronic acid (MeHA) hydrogel (Figure 6.1a). First, we show that EET is required for gelation, and that organisms without this metabolic capability (i.e., *E. coli*) are unable to crosslink gels on a comparable time scale or in a controllable manner. Gels did not form unless a constant source of electron flux, radical initiator, and metal catalyst were present. Additionally, the facultative metabolic capability of *S. oneidensis* enabled crosslinking under benchtop conditions without dedicated oxygen removal. Analysis of cell motility and metabolic activity reveled that bacteria remain viable and responsive in the gels for a minimum of one week, and that degree of crosslinking by EET affected cell movement. Next, we found that crosslink density was a strong function of bacterial genetics, as cytochrome knockout strains synthesized gels more slowly and with decreasing stiffness correspondent to the number of removed EET genes. Finally, transcriptional circuits based on controlling the expression of *mtrC* with the LacI repressor enabled tunable crosslinking rates and hydrogel mechanical properties. We found that hydrogel storage modulus fit well to inducible gene expression models, directly linking steady-state gene expression to a quantifiable and macroscopic material property. Overall, our results suggest that transcriptional control over EET can be used to predictably interface the properties of living systems with potentially any material amenable to radical crosslinking.

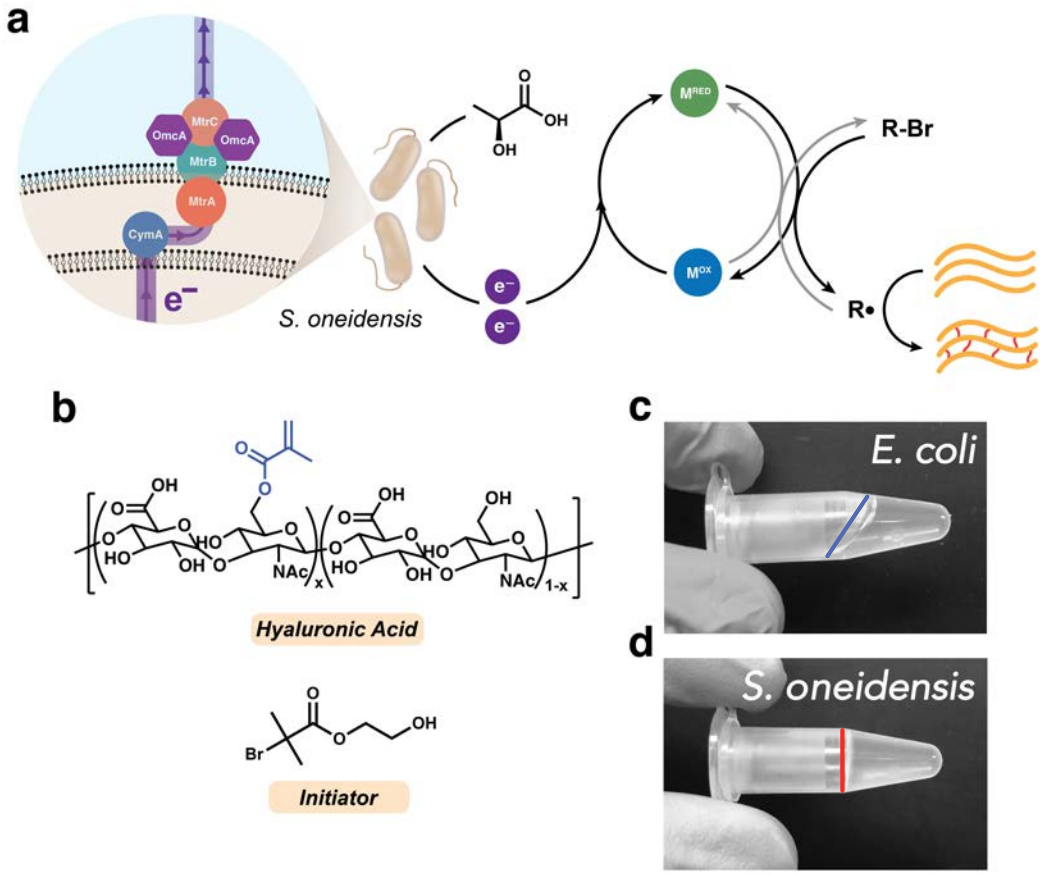

Figure 6.1: Extracellular electron transfer from *S. oneidensis* controls radical crosslinking of a semi-synthetic hydrogel.

(a) The Mtr pathway of *S. oneidensis* directs metabolic electron flux to a metal catalyst, which generates a radical from a halogenated initiator and crosslinks acrylate-based functional groups. (b) Chemical structures of the macromer, methacrylated hyaluronic acid (MeHA), and the radical initiator, 2-hydroxyethyl 2-bromoisobutyrate (HEBIB). (c) Crosslinking reaction mixture inoculated with *E. coli*, which does not possess EET machinery, does not form gels as indicated by liquid flow. Air-liquid interface is highlighted. (d) Crosslinking reaction mixture inoculated with *S. oneidensis* MR-1 forms a solid gel as confirmed by inversion test. Air-liquid interface is highlighted.

6.3 RESULTS

6.3.1 Extracellular Electron Transfer from Live *S. oneidensis* Controls Aerobic Radical Crosslinking

To initially validate our hypothesis that EET-controlled ATRP could be used to form a crosslinked hydrogel, we first synthesized a 65% methacrylated hyaluronic acid (MeHA) macromer using an established protocol[407] (Figure 6.1b, E.1). Hyaluronic acid is a common naturally-derived biomaterial platform that is attractive for our application due to its biocompatibility and chemical versatility[408]. The high density of functional groups was chosen to increase likelihood of successful crosslinking and to minimize the effect of radical scavenging by oxygen. In initial experiments, MeHA was dissolved at 3 wt.% in *Shewanella* Basal Medium (SBM) supplemented with 0.05 % w/v casamino acids (Table E.2-E.3), and the dissolved macromer was mixed with a radical initiator, 2-hydroxyethyl 2-bromoisobutyrate (HEBIB, 500 μM), a copper ATRP catalyst with Tris(2-pyridylmethyl)amine ligand (Cu-TPMA, 10 μM), and inoculated with anaerobically pregrown *S. oneidensis* MR-1 cells (initial OD_{600} = 0.2 in the gel, ca. 4 x 10^8 CFU • mL^{-1}). Lactate (20 mM) was the electron donor and fumarate (40 mM) was the primary electron acceptor. Gels were initially tested in anaerobic environments to promote EET metabolism and eliminate any effects of oxygen quenching. After mixing, the solution was placed in a humidified anaerobic chamber and was monitored via inversion testing. After 2 h, solutions containing *S. oneidensis* crosslinked to form polymer networks, whereas solutions containing *E. coli* did not (Figure 6.1c-d). Consistent with our previous results[293], these data suggest that electron flux to the metal catalyst from EET-based metabolism is required for radical generation and crosslinking.

After successful preliminary crosslinking reactions, we more thoroughly investigated the mechanical properties of the gels using shear oscillatory rheology. Gel precursor solutions were inoculated with cells and placed between two hydrophobically-treated glass slides with a silicone spacer, allowed to crosslink, and swollen overnight at room temperature in 1x PBS. Gel mechanical properties were then quantified on a

rheometer by measuring storage and loss moduli. Storage modulus (G') is a measure of the elastic response to applied shear, wherein the network recovers. In contrast, loss modulus (G'') is a measure of viscous, non-recoverable dissipation of applied shear. The storage modulus of biological tissues and common biomaterial platforms, such as extracellular matrix mimics, typically range from 0.01 to 100 kPa[409]. Storage and loss moduli for EET-crosslinked gels were determined from the linear viscoelastic regime as determined by strain and frequency sweeps (Figure E.2), and calculated using a 0.01 to 100 Hz frequency sweep at 0.1% strain. Gels formed in anaerobic environments exhibited a storage modulus of ~2500 Pa and a loss modulus of ~20 Pa (Figure E.3) and were predominately elastic, as indicated by significantly larger G' compared to G''. Taking advantage of its facultative metabolism, we next tested radical crosslinking of hydrogels by *S. oneidensis* under ambient as opposed to anaerobic conditions. Using the same reagent concentrations as above with aerobically pregrown cells (henceforth, standard conditions), *S. oneidensis* formed crosslinked networks at 30 ºC without dedicated oxygen removal. Gels formed in both aerobic and anaerobic environments yielded comparable mechanical properties, indicating insignificant oxygen inhibition under ambient conditions (Figure E.3). Aerobic gels prepared by *S. oneidensis* were also mechanically similar to acellular gels crosslinked using UV light and the photoinitiator lithium phenyl-2,4,6-trimethylbenzoylphosphinate (LAP, 500 μM) (Figure E.4). In addition, controls lacking (a) EET-active bacteria, (b) radical initiator, (c) metal catalyst, or (d) methacrylate functional group did not form measurable gels within 2 h (Figure 6.2a, E.5). Methacrylate functional group conversion in the hydrogels was also measured by ^{1}H-NMR spectroscopy after hyaluronidase digestion, confirming the crosslinking mechanism (Figure E.6). Together, these results demonstrate that EET-crosslinked hydrogels can be synthesized under ambient or anaerobic conditions using electroactive bacteria to form mechanically robust networks that are typical of this macromer.

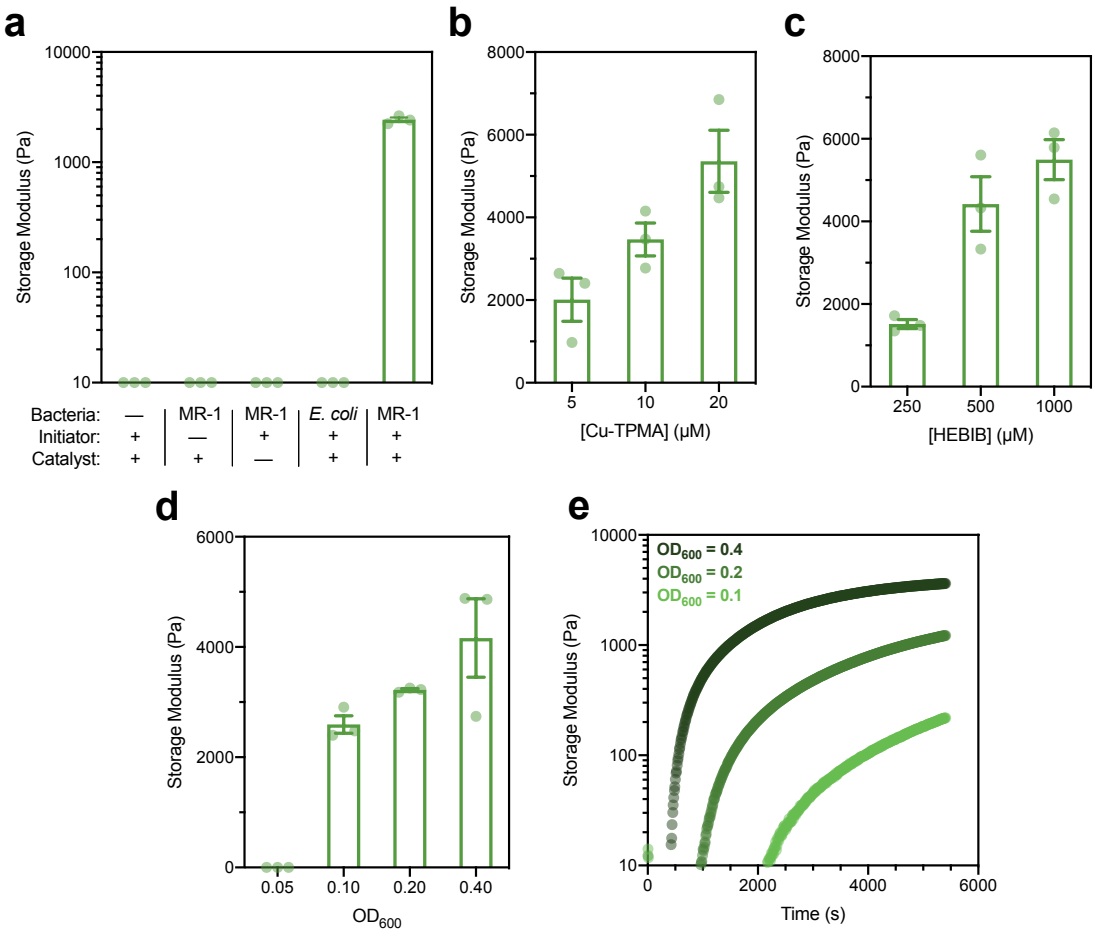

Figure 6.2: Living hydrogel materials crosslinked by *S. oneidensis* MR-1 can be chemically or biologically tuned.

(a) Storage moduli of hydrogels crosslinked without various components, measured by rheology after 2 hours of crosslinking. Many gels did not form and could not be characterized. (b) Storage moduli of hydrogels crosslinked for 2 hours with varying concentrations of Cu-TPMA (catalyst); one-way ANOVA $p = 0.018$. (c) Storage moduli of hydrogels crosslinked for 2 hours with varying concentrations of HEBIB (radical initiator); one-way ANOVA $p = 0.0027$. (d) End-point storage moduli at 2 hours and (e) *in situ* rheology of hydrogels crosslinked with varying optical densities of *S. oneidensis* MR-1 in the reaction, and therefore varying total electron transfer; one-way ANOVA $p = 0.0002$. Gels did not form using $OD_{600} = 0.05$ cells in either experiment. (a-d) Data are shown as mean ± SEM, $n = 3$ biological replicates.

The crosslinking kinetics and mechanical properties of polymer networks strongly depend on a variety of chemical factors such as catalyst and ligand identity, rate of initiation, and initiator structure[410]. Thus, we next explored the tunable range of hydrogel stiffness after 2 h of crosslinking by altering the concentration and identity of the chemical components in our system (frequency sweeps, Figure E.7). First, we varied the concentration of the metal catalyst from 5 μM to 20 μM. Greater catalyst concentrations were not considered due to copper-induced transcriptional responses in *Shewanella* at concentrations greater than 20 μM[263]. Increasing catalyst concentration correspondingly increased gel modulus (Figure 6.2b), likely due to increased methacrylate conversion from greater radical production. Second, we varied the concentration of the initiator over the range of 250 to 1000 μM, which should in turn also tailor radical concentration. As expected, increasing gel stiffness was a function of increasing initiator concentration (Figure 6.2c). An additional advantage of ATRP over hydroxyl radicals is the potential for using structurally well-defined radical initiators. Consistent with this expectation, we found that a PEG-based initiator, poly(ethylene glycol) bis(2-bromoisobutyrate) ($M_{n,avg}$ = 700 g/mol), also successfully crosslinked EET-controlled gels at a variety of concentrations (Figure E.8). MeHA macromers of varying methacrylate percentages also crosslinked as expected, exhibiting crosslink density saturation around 65% functionalization (Figure E.9). Overall, EET-controlled hydrogels exhibited a modulus range of about 1-6 kPa for the conditions tested, which is typical of chain-growth crosslinked MeHA hydrogels and within range for a variety of applications, such as biofilm and tissue mimetics[407,409,411]. These results also indicate that traditional approaches to tuning hydrogel mechanics through chemical mechanisms are still applicable when using EET-controlled crosslinking.

Next, we investigated the role of *S. oneidensis* cell density, and thus aggregate EET flux, on hydrogel modulus. Below a certain critical inoculum (ca. initial OD_{600} = 0.1), the rate of bacterial oxygen consumption was not fast enough to overcome oxygen diffusion and radical quenching. As expected, hydrogels formed with sufficient cell density, and stiffness strongly correlated with OD_{600} (Figure 6.2d). Based on these results, we predicted that crosslinking rate would also be coupled to EET and inoculating cell density. To

confirm this, we performed rheological measurements *in situ*, which provided real-time measurement of mechanical properties during crosslinking, at 1 Hz and 0.1% strain. Gels formed at higher initial cell concentrations were not only stronger, but formed more quickly (Figure 6.2e). Consistent with end-point experiments, *in situ* rheology measurements also confirmed that a critical concentration of cells was necessary for oxygen depletion. Together, these results demonstrate that cells play a direct role in crosslinking, and overall stiffness and crosslinking rate can be controlled by cell inoculum. They also suggest that genetic and metabolic manipulations to tune EET flux could be used to influence gel mechanics.

6.3.2 *S. oneidensis* Remains Viable and Metabolically Active in the Network

For a living material to maintain adaptability, it is critical that the actuating components (i.e., cells) remain viable and encased in the network. The various components of our system, including the Cu catalyst, initiator, and presence of radicals could affect cell viability. Thus, we assessed cell viability and activity after crosslinking. EET-crosslinked gels formed in standard conditions were swollen overnight in 1x PBS after modulus measurements, and stained using live/dead fluorescent dyes. Even after mechanical stresses induced by swelling and rheometer measurements, cells maintained approximately 100% viability 5 days after crosslinking (Figure E.10). In addition, cells exposed to crosslinking conditions, but released from the gel surface during swelling could successfully inoculate new cultures in fresh growth media, indicating viability; these cultures were also able to crosslink new hydrogels with identical properties (Figure E.11).

Since new cultures could be inoculated using cells released during swelling, we next quantified escape or leakage of bacteria from the gels after crosslinking. At the functional group density and crosslink molecular weight of our material, the mesh size of a fully converted gel should be on the order of 10-50 nm[412,413], allowing for catalyst and electron shuttle diffusion. However, because this is considerably smaller than average bacterial dimensions, there should be minimal cell movement. To test this prediction, crosslinked gels were prepared at standard conditions, swollen in 1 mL of 1x PBS, and the

optical density of the surrounding media was measured. An initial, low optical density of cells was detected immediately upon swelling. We hypothesized that this was due to an instantaneous egress of cells on the periphery of the gels and not contained in the network. After washing gels 3x with 1 mL PBS to remove this outer layer of cells, no increase in optical density was detected. Furthermore, colony counting confirmed that escaped cells after 24 h of swelling accounted for < 0.005% of the inoculating density (Figure E.12), suggesting embedded cells do not escape the network in significant numbers.

Real-time responses within the network and design of new functions require an understanding of spatiotemporal cell behavior within the gels during synthesis. Therefore, we next visualized the relationship between genotype, crosslink density, and cell movement during gelation. We constructed an inducible *sfgfp* expression plasmid under the control of the LacI repressor protein and its cognate promoter, P_{tac}. Cells were transformed with this vector such that sensing of isopropyl ß-D-1-thiogalactopyranoside (IPTG) would induce a fluorescent response indicative of metabolic activity. We developed two reporter strains by transforming both *S. oneidensis* MR-1 and Δ*mtrC*Δ*omcA*Δ*mtrF* (an EET-deficient knockout) with this construct. Strains were grown overnight in 1000 μM IPTG, washed, and inoculated into standard gelation mixtures. The solution was then pipetted onto a glass slide and sealed under a coverslip, such that crosslinking occurred in the sealed layer. Bacterial movement was monitored by time-lapse imaging using GFP fluorescence. Cells were uniformly dispersed within the network throughout gelation. For both *S. oneidensis* MR-1 and Δ*mtrC*Δ*omcA*Δ*mtrF*, a significant degree of bacterial motion was visible upon inoculation, both by convective flow of the reaction mixture and by flagella-based swimming[414]. Minutes after inoculation, cell movement and bulk fluid motion was arrested in the *S. oneidensis* MR-1 sample as crosslinking proceeded (0 h, Movies S1; 2 h, Movie S2). Contrastingly, movement both from flow and swimming were still perceptible after 2 h in the Δ*mtrC*Δ*omcA*Δ*mtrF* sample, indicating that minimal crosslinking occurred (0 h, Movies S3; 2 h, Movie S4). Quantification of cell movement revealed that average cell displacement over 5 seconds was significantly greater for the knockout strain at both 0 and 2 h (Figure 6.3a, E.13)[415]. A decrease in cell movement for

the Δ*mtrC*Δ*omcA*Δ*mtrF* mutant was also observed at 2 h, which is likely a result of background crosslinking (described below). Movement was not significantly different between the two strains in non-functionalized hyaluronic acid solution, suggesting the observed motility differences were due to crosslinking, even at early times immediately following inoculation (Figure E.14). These results confirm that cells become trapped in the polymer network as it forms, and suggest that bacterial genotype encodes control over bulk and microscopic properties such as crosslink density and mesh size, affecting flow, diffusion, and cell movement within the material.

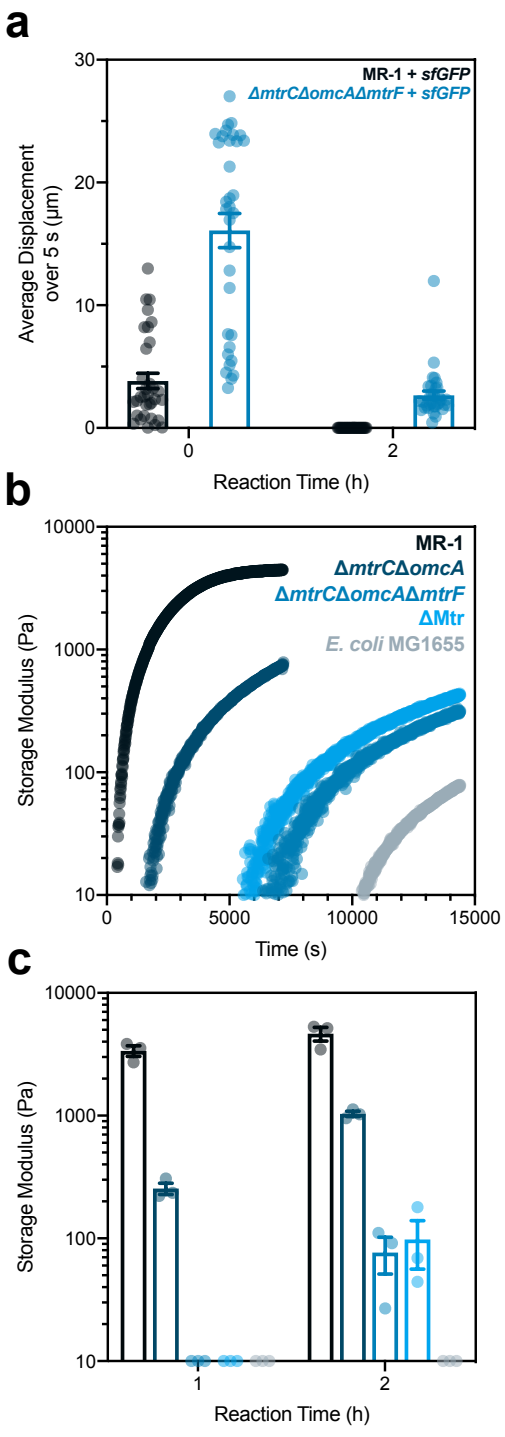

Figure 6.3: Cell motility, synthesis rate, and crosslink density within living hydrogels are governed by *S. oneidensis* genetics and EET machinery.

Figure 6.3: Cell motility, synthesis rate, and crosslink density within living hydrogels are governed by *S. oneidensis* genetics and EET machinery. (a) Average cell displacement within the gels measured by microscopy over 5 second time-lapses at both 0 and 2 hours into crosslinking; student t-test $p < 0.0001$ between strains at $t = 0$ and 2 hours. (b) *In situ* and (c) end-point rheology measurements of hydrogels crosslinked by *S. oneidensis* strains with various EET genes knocked out. *E. coli* was included as an EET-deficient control; student t-test $p < 0.0001$ for MR-1 compared to other strains at $t = 1$ and 2 hours. Data are shown as mean ± SEM, (a) $n = 33$ tracked cells or (c) $n = 3$ biological replicates.

Although the cells remained viable for days in the crosslinked gels, we wished to assess their continued sensing and metabolic capabilities over long periods after crosslinking. Gels synthesized at standard conditions with sfGFP plasmid-carrying *S. oneidensis* MR-1 were swollen in 1x PBS for varying lengths of time after crosslinking, then induced for 24 h with 1000 μM IPTG. Significant fluorescence was detected by microscopy in induced samples up to 1 week after crosslinking, but was not detectable in uninduced samples (Figure E.15). Together, these results indicate that the bacteria remain viable, trapped, and maintain transcriptional and translational capabilities for extended periods after crosslinking.

6.3.3 Bacterial Genetics Govern Crosslink Density

Understanding the genetic link between EET and crosslinking is critical for biologically controlling hydrogel structure and function. Toward this goal, we employed various EET knockout strains in crosslinking reactions: Δ*mtrC*Δ*omcA*, Δ*mtrC*Δ*omcA*Δ*mtrF*, and ΔMtr. The knockout ΔMtr refers to a strain with a large number of EET genes removed from the genome, and should provide minimal electron flux to the catalyst (Table E.1)[86,111]. *E. coli* MG1655 was also included as an EET-deficient control. We measured *in situ* crosslinking kinetics using these strains, and compared crosslinking rates and density. Both crosslinking rate and hydrogel storage modulus strongly corresponded with bacterial genotype, where decreasing number of EET genes led to decreased crosslinking rates and weaker moduli (Figure 6.3b). Although MtrC is the primary terminal reductase for many metal substrates, our results show that MtrF exhibits compensatory reduction of Cu in the Δ*mtrC*Δ*omcA* knockout compared to the

Δ*mtrC*Δ*omcA*Δ*mtrF* knockout. The strong similarity between gels formed by the Δ*mtrC*Δ*omcA*Δ*mtrF* and ΔMtr knockouts further demonstrates that outer membrane cytochromes are primarily responsible for electron transfer to the Cu catalyst and subsequent crosslinking activity. The minimal, delayed crosslinking activity of *E. coli* suggests that background radical generation or non-specific Cu reduction can produce weak gels at extended times. In separate experiments, we corroborated these *in situ* results using end-point, swollen gel measurements after 1 and 2 h of crosslinking (Figure 6.3c, E.16). *S. oneidensis* MR-1 and Δ*mtrC*Δ*omcA* formed gels the fastest and were measurable at 1 h, whereas the other strains did not form measureable gels by this time. Measurable networks were formed by Δ*mtrC*Δ*omcA*Δ*mtrF* and ΔMtr at 2 h, but were significantly weaker than gels formed by the strains containing more EET machinery. Overall, these results show that bacterial genotype directly governs gel modulus and suggests that material properties can be controlled through more sophisticated regulation of EET.

6.3.4 Transcriptional Regulation of Extracellular Electron Transfer Yields Tunable Crosslinking Activity

For ELMs to emulate the adaptability of biological materials, the actuating components should continually sense and respond to their environment. Environmental stimuli should then induce a transcriptional response and impart control over material properties. Toward this goal, we constructed an inducible *mtrC* expression plasmid using the same genetic circuit outlined before, but replacing *sfgfp* with *mtrC* (Figure 6.4a, Figure E.17-E.18). We transformed the Δ*mtrC*Δ*omcA*Δ*mtrF* strain with this plasmid, such that IPTG would sequentially activate *mtrC* expression, electron transfer, and crosslinking activity. Upstream of the *mtrC* gene, a computationally-predicted weak synthetic ribosome binding site was employed to optimize control over EET and minimize leaky expression[365]. SDS-PAGE and heme staining of total protein from induced and uninduced cell lysates validated inducible MtrC protein production after overnight growth in IPTG-containing medium. High molecular weight bands corresponding to the size of the MtrCAB complex were observed in induced Δ*mtrC*Δ*omcA*Δ*mtrF*+*mtrC* samples and a wild-type control, but

not in uninduced and empty vector Δ*mtrC*Δ*omcA*Δ*mtrF* samples (Figure E.19). Functional steady-state expression of *mtrC* in response to IPTG was further validated by measuring Fe^{3+} reduction with the ferrozine assay. After 2 h of reduction, Fe^{2+} concentration increased with the presence of inducing molecule, indicating functional MtrC activity and no leaky EET response over an uninduced control (Figure E.20). Next, we verified tailored crosslinking activity in response to varying transcriptional activation. *In situ* gelation kinetics were assessed after overnight growth in media containing a range of inducing molecule concentrations. Crosslinking activity was a strong function of IPTG concentration, spanning orders of magnitude in storage modulus (Figure 6.4b). Crosslinking kinetics also corresponded to inducer presence, indicating that both synthesis rate and final material modulus can be customized through differential steady-state gene expression. Both an induced empty vector control and a complemented strain with no IPTG did not form measurable gels in 2 h. Thus, transcriptional regulation over EET gene expression in response to an environmental signal imparts programmable control over hydrogel stiffness.

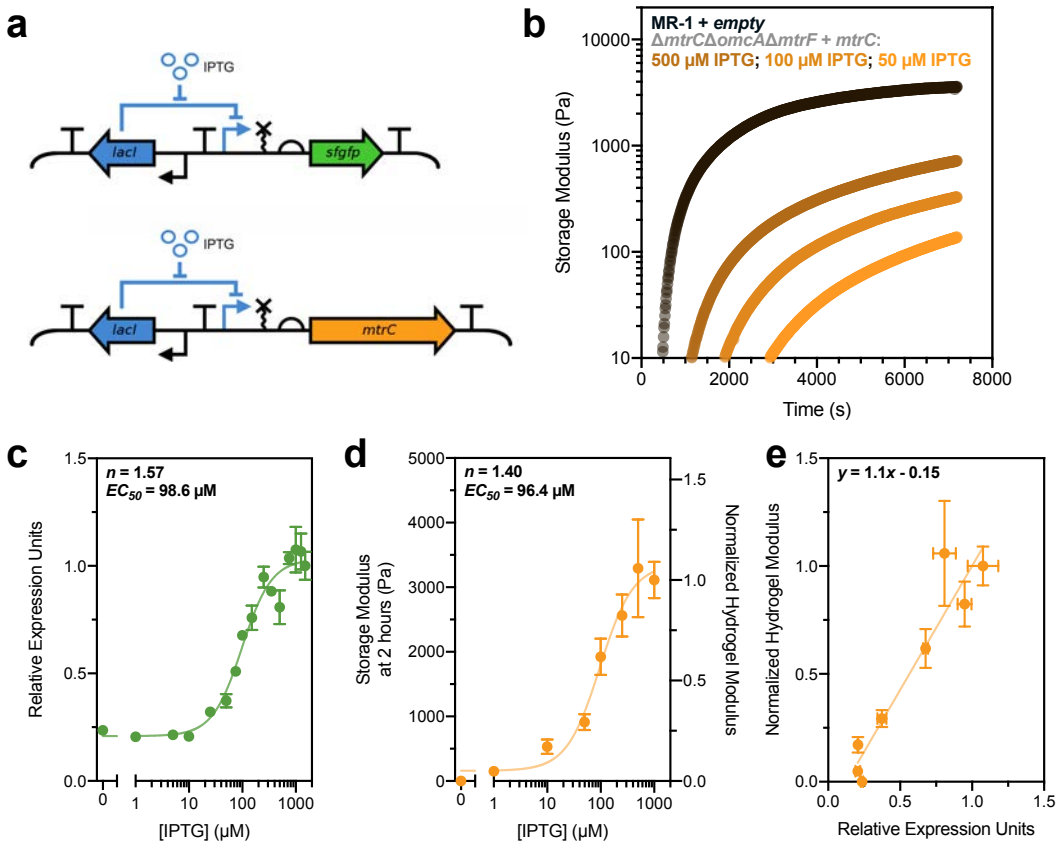

Figure 6.4: Modeling gene expression allows quantitative prediction of living hydrogel properties.

(a) Genetic circuits utilized in this study placing either *sfgfp* or *mtrC* under inducible control of IPTG via the LacI repressor and P_{tac} promoter. (b) *In situ* rheology of hydrogels crosslinked by *S. oneidensis* with steady-state induced *mtrC* levels at various IPTG concentrations. Δ*mtrC*Δ*omcA*Δ*mtrF*+empty and Δ*mtrC*Δ*omcA*Δ*mtrF*+*mtrC* with 0 μM IPTG were also tested, but did not form gels on the time scale shown. (c) Hill function analysis of sfGFP fluorescence, denoted as relative expression units by normalization to fluorescence at maximum induction, as a function of IPTG concentration. (d) Hill function analysis of hydrogel storage modulus after 2 hours of crosslinking as a function of IPTG concentration. Right y-axis is storage modulus normalized to average modulus at maximum induction. (e) Normalized hydrogel stiffness plotted as a function of relative expression units for corresponding IPTG concentrations. The fit was determined by performing linear regression on the paired data (R^2 = 0.80). (c-e) Data are shown as mean ± SEM, n = 3 biological replicates.

6.3.5 Modeling Gene Expression Enables Predictable Material Properties

Due to successful transcriptional regulation of *mtrC*, we hypothesized that a material property such as storage modulus could be predicted from inducible gene expression models. Since the *sfgfp* and *mtrC* circuits have identical transcriptional regulation, we tested whether both fit to activating Hill function models. First, we measured the response function of the *sfgfp* circuit in *S. oneidensis* MR-1 by inducing overnight cultures in a variety of IPTG concentrations. Steady-state fluorescence was quantified using a plate reader, and normalized to optical density (Figure 6.4c). As expected, relative expression (i.e., normalized fluorescence) was a strong function of IPTG concentration, and fit well to a Hill function with a hillslope of n = 1.57 and a half-maximal effective concentration of EC_{50} = 98.6 μM (Table E.5). These results indicate that our circuit generates a predictable transcriptional response. Next, end-point gel measurements were used to examine storage modulus as a function of steady-state cytochrome (MtrC) expression. Gels were crosslinked for 2 h since our *in situ* results indicated this time would provide sufficient differentiation between induced cultures at varying IPTG concentrations. Specifically, Δ*mtrC*Δ*omcA*Δ*mtrF* complemented with LacI-regulated *mtrC* was grown overnight in a variety of IPTG concentrations and allowed to react for 2 h at standard gelation conditions. We found that, similar to sfGFP fluorescence, hydrogel storage moduli were also under strong transcriptional control and could be modeled using a Hill function with n = 1.40 and EC_{50} = 96.4 μM (Figure 6.4d). As the sfGFP signal is effectively a measure of the transcriptional rate at different IPTG concentrations[231], the similarity between fitted constants for *sfgfp* expression and hydrogel stiffness suggests that transcriptionally-regulated MtrC levels can predictably control hydrogel properties via a linear model (see section 6.5.9). To further visualize this relationship, we plotted normalized storage modulus as a function of relative expression units for each corresponding IPTG concentration and indeed observed a linear correlation (Figure 6.4e). The slope and intercept obtained by linear regression of the paired data are similar to the fit predicted by the individual Hill functions, corroborating the model between steady-state gene expression and hydrogel modulus. Together, these results demonstrate that EET gene

expression can be modulated to control ELM properties (e.g., gel stiffness), and that fluorescence-parameterized models for existing and new genetic circuits may be adapted to design, predict, and control more complex macroscopic material outputs.

6.4 Discussion and Conclusions

We showed that *S. oneidensis* can genetically control radical crosslinking in a semi-synthetic hydrogel via electron transfer to a redox-active polymerization catalyst. Similar to other crosslinking chemistries, storage modulus was dependent on catalyst and initiator concentrations as well as initial cell density. A significant advantage of our system is that it is theoretically amenable to any substrate that can undergo radical crosslinking and support microbial life. We used methacrylate-functionalized hyaluronic acid, but other semi-synthetic materials based on functionalized alginate, collagen, and cellulose, as well as completely synthetic substrates, such as PEG, should show similar behavior. In addition to flexibility in macromer structure, our design also allows for a variety of well-defined ATRP initiators to be used as crosslinking agents. For example, we showed two traditional ATRP initiators, HEBIB and bis-brominated PEG, could both form crosslinked hyaluronic acid hydrogels. Similar to other radical crosslinking methodologies, bacteria-controlled crosslinking is also compatible with various biochemical modifications including the installation of integrin recognition motifs (e.g., RGD), orthogonal crosslinking chemistries (e.g., Michael addition), and other common polymer engineering paradigms. The chemical flexibility and general compatibility with a variety of polymer network scaffolds should facilitate the use of our platform in tissue engineering, 3D printing, soft robotics, and drug delivery. While utilizing bacteria for applications requiring mammalian biocompatibility is challenging, potential uses include platforms for studying cell-microbe interactions mediated by the extracellular matrix, such as tissue repair[416] and the gut lumen[417].

In contrast to other biologically-driven radical crosslinking methods, most notably hydroxyl radicals generated from glucose oxidase, EET-controlled crosslinking did not negatively impact cell health. Cells remained viable at least one week following gelation and transformed cells could express *sfgfp* in response to an external stimulus. We also

observed genotypic changes in cell motility and convective flow as a result of EET-dependent crosslinking, implying genetic control over gel microstructure. Overall, our design avoids cell viability concerns associated with other radical crosslinking methodologies and could enable synthetic platforms for studying biofilm formation[418], trapping[275], or functionalizing cells[248].

We found that crosslinking activity and overall hydrogel stiffness were governed by EET cytochrome expression. Specifically, *S. oneidensis* MR-1 with wild-type EET pathways generated stiff gels within an hour while negative controls containing *E. coli* MG1655, which lacks EET machinery, did not form gels on comparable timescales. At longer time scales (ca. 2-4 hours), EET-knockout strains and *E. coli* showed some crosslinking activity. This background radical generation could be caused by non-specific copper reduction (e.g., release or secretion of cytosolic reducing agents) or spurious radical activation. To further reduce background crosslinking, decreasing catalyst and/or initiator concentration, lowering cell density, or changing the identity of chemical components could all potentially be tuned. Overall, the strong link between *S. oneidensis* genetics and crosslinking rate and density lays the foundation for developing more sophisticated EET-based regulation of material properties.

Using *in situ* and end-point rheology measurements, we showed that hydrogel crosslinking is directly linked to *mtrC* expression levels, which has a number of implications for adaptable and dynamic materials. Interestingly, placing *mtrC* under the control of the LacI repressor generated a hydrogel stiffness response function that is characteristic of inducible gene expression. This response function mirrored one generated from *sfgfp* expression in the same construct, indicating robust transcriptional control over both gene expression and material properties. More importantly, our results suggest that previously characterized genetic circuits, including genetic logic gates, designed to express fluorescent reporters could be readily adapted to control *mtrC* expression and gel stiffness[211]. Although the ultimate stiffness of the hydrogel will depend on the specific crosslinking chemistry, our observation of canonical Hill function responses demonstrates that changes in hydrogel stiffness governed by transcriptional regulation can be partially

predicted. Overall, our results suggest that a variety of transcriptional circuits could be extended to control the macroscopic properties of synthetic materials in a predictable and programmable manner. Additionally, robust genetic control over crosslinking should complement other stimuli-responsive hydrogel designs, including integration of biochemical signals[419–421], actuators[422,423], and complex geometric designs[424].

The gel stiffness response function was measured after 2 h of gelation since *in situ* measurements indicated this would be sufficient time to distinguish between differentially induced cells. Because crosslinking is a dynamic process, the hydrogel response function also varies as a function of time, even at steady-state expression levels of MtrC. For example, at early times (< 1 h), it is exaggerated since measurable gels do not form at low induction levels (Figure E.21). At longer timescales, the response function begins to collapse as background polymerization starts to compete with EET-driven crosslinking. Applications leveraging genetic control over material properties will require both an understanding of how EET influences crosslinking kinetics and the optimization of real-time transcriptional responses. Understanding how cells coordinate transient gene expression to control dynamic outputs such as cell motility, morphogenesis, biofilm structure, or extracellular matrix construction are ongoing challenges in developmental and systems biology[425]. Similarly, we are currently investigating how to match gene expression to the polymerization kinetics in our system[227]. Overall, continued optimization of MtrC (or other EET protein) expression and material chemistry should allow for actuation of material changes over timescales similar to transcription and translation, as well as predictive models that relate gene expression to material function.

Overall, we found that extracellular electron transfer from *S. oneidensis* could power a radical polymerization catalyst and form a semi-synthetic hydrogel composed of functionalized hyaluronic acid. A variety of chemical and biological factors controlled crosslinking kinetics and the resulting storage moduli of the gels, demonstrating a tunable and adaptable platform. Most importantly, we found that robust transcriptional control over *mtrC* expression and metabolic electron flux enabled precise and predictable control over hydrogel mechanical properties. While cells are frequently incorporated into polymer

networks, our platform allows for a variety of network properties including crosslink density, mesh size, degradation, diffusion, and elastic modulus to be controlled through cellular metabolism and gene expression. In summary, our results provide a powerful foundation for programming adaptive and responsive behavior into the vast functional space of synthetic materials through the conduit of biological electron transfer.

6.5 MATERIALS AND METHODS

6.5.1 Chemicals and Reagents

Sodium hyaluronate (72 kDa, Lifecore Biomedical), methacrylic anhydride (Sigma-Aldrich, 94%), copper(II) bromide ($CuBr_2$, Sigma-Aldrich, 99%), tris(2-pyridylmethyl)amine (TPMA, Sigma-Aldrich, 98%), 2-hydroxyethyl 2-bromoisobutyrate (HEBIB, Sigma-Aldrich, 95%), poly(ethylene glycol) bis(2-bromoisobutyrate) (PEGBBIB, $M_{n,avg}$ = 700 g/mol, Sigma-Aldrich, PDI ≤ 1.1) sodium DL-lactate ($NaC_3H_5O_3$, TCI, 60% in water), sodium fumarate ($Na_2C_4H_2O_4$, VWR, 98%), HEPES buffer solution ($C_8H_{18}N_2O_4S$, VWR, 1 M in water, pH = 7.3), potassium phosphate dibasic (K_2HPO_4, Sigma-Aldrich), potassium phosphate monobasic (KH_2PO_4, Sigma-Aldrich), sodium chloride (NaCl, VWR), ammonium sulfate ($(NH_4)_2SO_4$, Fisher Scientific), magnesium (II) sulfate heptahydrate ($MgSO_4•7H_2O$, VWR), trace mineral supplement (ATCC), casamino acids (VWR), silicone oil (Alfa Aesar), isopropyl ß-D-1-thiogalactopyranoside (IPTG, Teknova), kanamycin sulfate ($C_{18}H_{38}N_4O_{15}S$, Growcells), nail polish (Electron Microscopy Sciences), BacLight Live/Dead Stain (Invitrogen), deuterium oxide (D_2O, Sigma-Aldrich, 99.9%), hyaluronidase from bovine testes (Sigma-Aldrich, Type I-S, 400-1000 units/mg), hydrogen peroxide solution (H_2O_2, Sigma-Aldrich, 30% in H_2O), and 3,3',5,5'-Tetramethylbenzidine (TMBZ, Alfa Aesar, 98%) were used as received. All media components were autoclaved or sterilized using 0.2 µm PES filters.

6.5.2 Methacrylated Hyaluronic Acid Synthesis and Purification

MeHA was functionalized using methacrylic anhydride according to an established protocol(29). Briefly, ~72 kDa HA macromer (1.5 g, 3.81 mmol, 1.0 eq) was dissolved at 1 wt.% in DI water (150 mL), cooled on ice, and adjusted to pH = 8.5 using 5 N NaOH. The pH was maintained between 7.5 – 8.5 using NaOH while methacrylic anhydride (8.44 mL, 56.7 mmol, 14.9 eq) was added in 750 µL aliquots every ~5 minutes. Once all the methacrylic anhydride was added, the pH was maintained between 7.5 – 8.5 for 4 hours, then the reaction stoppered and stirred overnight at room temperature. The reaction solution was dialyzed using 6 – 8 kDa dialysis tubing in DI water while stirring for two weeks. The mixture was then frozen and lyophilized. Methacrylate functionalization was quantified by ^{1}H-NMR spectroscopy and determined to be ~65% from integration of the vinyl group relative to the HA backbone (Figure E.1). Functionalized MeHA solution was passed through a basic alumina column immediately prior to crosslinking reactions. Methacrylate functional group conversion was quantified by adding 10 µL of 50 mg/mL hyaluronidase solution in 1x PBS to 50 µL hydrogels and degrading overnight at 37 ºC in an incubator with 250 RPM shaking. Liquified solutions were diluted in 550 µL of D_2O and the methacrylate peak quantified using ^{1}H-NMR spectroscopy.

6.5.3 Bacteria Strains and Culture

Bacterial strains and plasmids are listed in Table E.1. Cultures were prepared as follows: bacterial stocks stored in 20% glycerol at -80 ºC were streaked onto LB agar plates (for wild-type and knockout strains) or LB agar with 25 µg/mL kanamycin (for plasmid-harboring strains) and grown overnight at 30 ºC for *Shewanella*, 37 ºC for *E. coli*. Single colonies were isolated and inoculated into *Shewanella* Basal Medium (SBM) supplemented with 100 mM HEPES, 0.05% trace mineral supplement, 0.05% casamino acids, and 20 mM sodium lactate (2.85 µL of 60% w/w sodium lactate per 1 mL culture) as the electron donor. Aerobic cultures were pregrown in 15 mL culture tubes at 30 ºC and 250 rpm shaking. Anaerobic cultures were pregrown using the same procedure outlined above, but

in degassed growth medium in a humidified anaerobic chamber and supplemented with 40 mM sodium fumarate (40 µL/mL of a 1 M stock) as the electron acceptor. Cultures were washed 3x after pregrowth using SBM supplemented with 0.05% casamino acids (degassed for anaerobic cultures). OD_{600} was measured using a NanoDrop 2000C spectrophotometer and normalized to 2.0 for 10-fold dilution into gel mixtures (5 µL of OD_{600} = 2.0 concentrated cell culture into 45 µL of gel mixture) unless otherwise noted.

6.5.4 MeHA Hydrogel Crosslinking using *S. oneidensis*

$CuBr_2$, TPMA, and HEBIB stock solutions were prepared according to previously established protocol[21]. For three 50 µL hydrogel discs that were analyzed by rheology, a reaction mixture was prepared as follows: MeHA was dissolved at 3.76 wt.% in SBM with 0.05% casamino acids and aliquoted into an autoclaved microfuge tube (119.2 µL). 400 µM Cu-TPMA (3.75 µL), 69 mM HEBIB (1.09 µL), 60% sodium lactate (0.428 µL), and 1 M sodium fumarate (6 µL) were added to the MeHA solution and mixed. Per 50 µL gel mixture, the remaining 1.5 µL was used for antibiotic and inducing molecule addition where necessary, otherwise 1.5 µL of SBM with casamino acids was added. Final concentrations in solution were 3 wt.% MeHA, 10 µM Cu-TPMA, 500 µM HEBIB, 20 mM lactate, and 40 mM fumarate. This solution was distributed into three autoclaved microfuge tubes of 45 µL aliquots to which 5 µL of OD_{600}-normalized cells were added. The gel solutions were mixed and dispensed onto hydrophobically-treated glass slides with a 0.5 mm silicone spacer separating the two glass layers. Slides were sealed with a binder clip and allowed to react at 30 ºC for two hours unless otherwise noted. Hydrogels were removed from the slides using a razor blade and placed into 3 mL baths of 1x PBS overnight to swell to equilibrium. Hydrogels analyzed by *in situ* rheology were prepared using the same mixture outlined above, but inoculated with cells and immediately placed on the rheometer for analysis.

6.5.5 Rheological Analysis

End-point rheological analysis: swollen hydrogels prepared as outlined above were analyzed by oscillatory shear rheology using a TA Instruments Discovery HR-2 Rheometer with an 8 mm parallel plate geometry. Hydrogels were loaded onto a Peltier plate and excised to 8 mm diameter using a biopsy punch. The geometry gap was then lowered until the measured axial force was above 0.02 N (usually between 500 – 800 μm, depending on the crosslink density and swelling ratio). Storage and loss moduli were measured using frequency sweeps from 0.01 to 100 Hz at a constant strain of 0.1%. Moduli for a single gel were quantified by averaging the linear viscoelastic region of each frequency sweep.
In situ rheological analysis: hydrogels measured by *in situ* oscillatory shear rheology were prepared using the mixtures and rheometer outlined above. Immediately after inoculating reaction mixtures with cells, 80 μL of mix was loaded onto the Peltier plate, which was maintained at 30 ºC. A 20 mm parallel plate geometry was lowered onto the solution while spinning such that the mixture coated the entire geometry surface and filled the gap (~350 μm gap size). The edges of the geometry and gap were then coated with silicone oil to prevent evaporative losses. *In situ* crosslinking was monitored using 1 Hz oscillation and 0.1% strain over variable lengths of time (1.5 – 8 hours).

6.5.6 Microscopy and Cell Tracking

All microscopy was performed using a Nikon Ti2 Eclipse inverted epifluorescence microscope. Cells assessed for viability by microscopy were crosslinked using standard conditions and the resulting gels swollen in 1x PBS at room temperature for varying lengths of time. The gels were then incubated in the dark in the BacLight Live/Dead stain mix (1.5 μL/mL Syto9, 2.5 μL/mL propidium iodide in 0.85% NaCl solution) for 30 minutes. Stained gels were then washed by pipetting 3x in 1 mL PBS to remove unbound dye. Gels were loaded onto glass microscope slides and a no. 1 coverslip placed on top. The gel thickness prevented using nail polish to seal the sides, but evaporative losses were not noticeable over the course of the experiment (~30 min). Fluorescence for each stain (green

for Syto9, red for propidium iodide) was measured using GFP and Texas Red excitation/emission filter cubes on a Nikon Ti2 Eclipse, as outlined previously[21]. To assess metabolic activity, gels were crosslinked with *sfgfp*-harboring strains and allowed to swell in 1x PBS for varying lengths of time. sfGFP fluorescence was assessed before induction to ensure there was no detectable background fluorescence. Gels were then incubated in 0 μM or 1000 μM IPTG in PBS for 24 h and monitored by fluorescence using the GFP channel.

Cells tracked by microscopy during crosslinking were prepared with reaction mixtures as outlined above. Upon cell inoculation, the crosslinking mixture was loaded onto glass slides, covered, and sealed with nail polish. The slides were loaded onto the microscope and cell movement monitored using the Time-lapse function in NIS-Elements. Images were taken every 1 s or 5 s with 100 or 300 ms exposure time using the GFP channel. Time-lapse images were edited and quantified using TrackMate in Fiji 1.0. Images were first background subtracted and equally brightened by thresholding. The top 50 highest quality cells were selected, as determined by the TrackMate user interface, and tracked over 5 or 10 s. The highest quality tracks, as determined by the software, were used to quantify average total displacement over the time-lapse. The number of tracks used to calculate the average was the maximum number of tracks from the image with the fewest tracks at each time point (e.g., if *S. oneidensis* MR-1 had 100 high-quality tracks and *S. oneidensis* JG596 had 50 high-quality tracks at the 0 h time point, the 50 highest-quality tracks from each image were used).

6.5.7 Plasmid Construction

DNA sequences and plasmid maps for each genetic part and plasmid used in this study are given in the Figures E.17-E.18 and Table E.4. All plasmids were assembled via Golden Gate cloning using enzymes and buffers from New England Biolabs. In addition to T4 Ligase, Golden Gate reactions contained either SapI for *mtrC* plasmid assembly or BsaI for *sfgfp* and empty plasmid assembly. The pCD backbone was assembled by PCR amplifying (Phusion, New England Biolabs) regions of pSR58.6 (B0015 and T0

terminators, ColE1 origin of replication), pTKEI-tLOV (kanamycin resistance), and pAL-rfp_(RP4 origin of transfer). To construct the gene expression unit (insulating terminators, RiboJ ribozyme, and *lacI* regulation unit), a gBlock was synthesized (Integrated DNA Technologies) and used in Golden Gate cloning. *sfgfp* and *mtrC* were PCR amplified from pSR58.6 and purified *Shewanella oneidensis* MR-1 genomic DNA, respectively, with ribosome binding sites and Golden Gate restriction enzyme sites added via oligonucleotide primers. Generally, 10 µL Golden Gate reactions that contained 10 fmol of pCD plasmid backbone and 40 fmol of each gBlock and/or PCR insert (as necessary) were used. In a thermocycler, Golden Gate reactions were cycled 25 times: 90 s at 37 °C followed by 3 minutes at 16 °C. After the 25 cycles, reactions were incubated at 37 °C for 5 minutes, 80 °C for 10 minutes, and then held at 4 °C.

Golden Gate reactions were used to directly transform freshly prepared electrocompetent *S. oneidensis* strains[78]. To prepare electrocompetent *S. oneidensis*, 5 mL of overnight *S. oneidensis* growth in LB medium at 30 °C was washed 3 times with sterile 10% glycerol at room temperature and concentrated to ~300 µL. 2 µL of Golden Gate reaction was mixed with 30 µL of concentrated electrocompetent *S. oneidensis*, transferred to a 1 mm electroporation cuvette, and electroporated at 1250 V. To recover electroporated cells, 250 µL of LB was immediately added post-electroporation and cells were incubated/shaken at 30 °C and 250 rpm. After 2 h of recovery, 100 µL of cell suspension was plated onto LB agar plates containing 25 µg mL^{-1} kanamycin sulfate and incubated overnight at 30 °C to obtain single colonies (generally 5-100 colonies observered for 1-3 part assemblies). Single colonies were used to inoculate LB liquid medium containing 25 µg mL^{-1} kanamycin sulfate and incubated/shaken overnight at 30 °C and 250 rpm. These cultures were used to generate 22.5% glycerol stocks, which were stored at -80 °C, and harvest assembled plasmid for Sanger sequencing (DNA Sequencing Facilities, University of Texas at Austin).

6.5.8 Verification of MtrC Inducible Expression and Functional Activity

Heme staining was performed by adapting previously described methods[426]. 5 mL of uninduced (0 μM IPTG) and induced (1000 μM IPTG) *S. oneidensis* strains were anaerobically cultured overnight in SBM containing 20 mM lactate and 40 mM fumarate. The total culture was washed once in 1x PBS, concentrated to 500 μL, and lysed by sonication. The cell lysate was centrifuged for 10 minutes at 10,000 rcf, and the supernatant was transferred to a separate tube. The pellet was resuspended in 100 μL 1x PBS, and the total protein concentration of both lysate fractions was determined by Bradford assay. 10 μg of protein from the supernatant and pellet were loaded into each well of a 12% Bis-Tris SDS-PAGE gel and run for ca. 120 minutes at 110 V. The gel was stained in a 3:7 mixture of 6.3 mM TMBZ in methanol:0.25 M sodium acetate (pH 5.0) for 2 h in the dark. Heme-containing protein bands were visualized upon addition of 30 mM hydrogen peroxide for 30 min.

Ferrozine assay[354] was performed to determine functional activity of MtrC-expressing strains. Strains were anaerobically grown overnight in IPTG-free SBM containing 20 mM lactate and 40 mM fumarate. Within in anaerobic chamber, cells were diluted 100-fold into 96-well plate wells filled SBM containing 20 mM lactate, 5 mM Fe(III)-citrate, and 1 mg mL^{-1} ferrozine (final total volume of 250 μL per well). Each well contained either 0 or 750 μM IPTG and Fe(II) standards were also added to the plate. Immediately after addition of cells and Fe(III), the plate was sealed with optically transparent sealing film and a plate cover lined with silicone grease. The plate was then removed from the anaerobic chamber and statically incubated at 30 °C. Absorbance at 562 nm was periodically measured using a BMG LABTECH CLARIOstar plate reader.

6.5.9 Models of Inducible Gene Expression and Storage Moduli

Hill Function Model

The activating Hill function has been extensively used to describe inducible gene expression[227]. Its general form is depicted below:

$$y = Min + (Max - Min)\frac{[I]^n}{EC_{50}{}^n + [I]^n} \quad \text{(Eq. 24)}$$

where y corresponds to storage modulus (G') or relative expression units (REU), Min corresponds to the lower-bound plateau value, Max corresponds to the upper-bound plateau value, $[I]$ corresponds to IPTG concentration, n corresponds to the hillslope, and EC_{50} corresponds to the half-maximal effective concentration.

Derivation of Linear Relationship Between REU and G'

We observed that inducible transcriptional rate/sfGFP fluorescence (REU, Figure 6.4c) and hydrogel storage modulus (G', Figure 6.4d) fit well to (24) and that similar n and EC_{50} values were obtained from fitting the model to each data set. Assuming the fitted n and EC_{50} values are identical for REU and G', the $[I]$, n and EC_{50} terms can be rewritten as an expression that relates G' as a function of REU. This expression dependent on experimental REU values and fitted Hill function parameters is shown below:

$$\frac{[I]^n}{EC_{50}{}^n + [I]^n} = \frac{REU - Min_{REU}}{(Max_{REU} - Min_{REU})} \quad \text{(Eq. 25)}$$

By inserting (25) into (24), where G' is the dependent variable, a linear relationship of the form $y = mx + b$ is obtained. The final relationship is depicted below:

$$G' = \frac{(Max_{G'} - Min_{G'})}{(Max_{REU} - Min_{REU})} REU + \left(Min_{G'} - \frac{(Max_{G'} - Min_{G'})}{(Max_{REU} - Min_{REU})} Min_{REU}\right) \quad \text{(Eq. 26)}$$

Using the normalized Hill function-derived values for each Max and Min value, (26) is predicted:

$$G' = 1.25REU - 0.21 \quad \text{(Eq. 27)}$$

which is similar to the fitted values obtained from linear regression (Figure 6.4e). Assuming $[MtrC]$ is proportional to transcriptional rate (REU)[231], this generates a linear relationship between G' and $[MtrC]$.

6.5.10 Quantification and Modeling of Inducible Constructs

The Δ*mtrC*Δ*omcA*Δ*mtrF*+*sfgfp* and +*mtrC* strains were anaerobically pregrown overnight using the same conditions outlined above, with the addition of 25 μg mL^{-1} kanamycin and varying IPTG concentrations. Anaerobic conditions were used for pregrowth to optimize expression of Mtr pathway components besides *mtrC*. Cells were anaerobically washed 3x in degassed SBM with 0.05% casamino acids, normalized to OD_{600} = 2.0, and diluted 10-fold into reaction mixtures (also containing kanamycin and IPTG) prepared in ambient conditions. Prior to measuring sfGFP fluorescence, protein translation was arrested by supplementing a 100 μL aliquot of cell suspension with kanamycin sulfate to a final concentration of 2 mg mL^{-1}. Subsequently, this suspension was shaken aerobically for 1 h at 30 °C to allow for sfGFP maturation. sfGFP fluorescence (488/530 nm) and cell suspension absorbance (600 nm) was measured using a BMG LABTECH CLARIOstar plate reader to yield fluorescence • $absorbance^{-1}$ for each sample. For each sample, the background fluorescence • $absorbance^{-1}$ from an empty vector (pCD8) control was subtracted. The background subtracted values were then normalized to the average fluorescence • $absorbance^{-1}$ value at maximum induction (1500 μM IPTG) to give relative expression units. Crosslinking strains complemented with *mtrC* were allowed to form gels for two hours, and the gels allowed to swell overnight in 1x PBS at room temperature. Gels were then analyzed by oscillatory shear rheology as outlined above. A

nonlinear fitting algorithm in GraphPad Prism 8.0 was used to fit inducible gene expression and hydrogel storage modulus to the following activating Hill function: $y = Min + (Max - Min)\frac{[I]^n}{EC_{50}{}^n + [I]^n}$. Normalized hydrogel storage modulus and relative expression units were plotted for values at corresponding IPTG concentrations and modeled using a linear regression. Fitting parameters and "goodness of fit" can be found in Table E.5.

6.5.11 Statistical Analysis

Unless otherwise noted, data are reported as mean ± SEM of n = 3 biological replicates. Significance was calculated in GraphPad Prism 8.0 using either a two-tailed unpaired student t-test or a one-way ANOVA (α = 0.05).

Chapter 7: Conclusions and Future Work

7.1 Introduction

The work reported in this dissertation has substantially increased our knowledge on engineering inorganic and traditionally "abiotic" processes using the genetics and metabolism of *Shewanella oneidensis*. This bacterium has proven to be an ideal chassis for controlling material syntheses/transformations, as its ability to perform extracellular electron transfer (EET) facilitates genotype-phenotype linkage between genetically encoded respiratory proteins and electron transfer to synthetic metal catalysts/nanomaterials. Importantly, we demonstrated that this linkage can modulate the properties and functioning of materials (i.e., organic polymers, inorganic nanoparticles, and metal-organic frameworks) based on the expression and availability of EET pathway components (Chapter 2-4). This linkage motivated use of synthetic biology workflows to design transcriptionally controlled gene circuits that predictably alter EET flux (Chapter 5). Precise transcriptional regulation of EET activity subsequently enabled tuning of the formation and physical properties of semisynthetic hydrogels (Chapter 6). Taken together, these conceptual and experimental findings may serve as the foundation for future bioengineering of redox-driven chemistries and use of EET as a programmable cellular actuator.

7.2 Chapter 2 Summary and Outlook

Cell-directed synthesis of functional molecules and materials has been an engineering goal since the beginning of recombinant DNA technology[427]. However, the formation or rearrangement of chemical bonds in biological products has been mostly limited to those directly controlled by enzymes or other biologically derived metabolites/biomolecules[27]. In Chapter 2, we demonstrate that activation of a synthetic metal catalyst by EET from *S. oneidensis* facilitates biological control over atom transfer radical polymerization (ATRP) reactions and products – a process not observed in nature

or directly catalyzed by any known biomolecules. Whereas conventional synthetic chemistry setups activate ATRP catalysts using electrons derived from sacrificial reducing agents or electrodes[246,273], we demonstrated that EET proteins and respiratory metabolism enable reduction of an EDTA- or TPMA-chelated Cu(II) catalyst that 'turns on' the radical polymerization. Reactions containing a catalyst and *S. oneidensis* yielded well-controlled first-order reaction kinetics and predictable polymer molecular weight/polydispersity.

Although the metal catalyst (and not the bacteria) is what directly initiates and propagates the radical on the growing polymer chain[428], the oxidation state of the metal largely governs its catalytic activity. Importantly, we found that *S. oneidensis* can modulate this oxidation state and, consequently, the polymerization reaction through changes to EET activity at the genetic (i.e., knockout/complementation of outer membrane cytochrome genes) and metabolic (i.e., cells fed different carbon sources) level. Manipulations to EET flux drastically affected the measured rate of polymerization for a synthetic polymer (namely, $OEOMA_{500}$) and were evidence that this material synthesis could be optimized through genetic engineering. For example, genetic circuits that oscillate EET activity[198,208,429] or biosynthesize monomers[10] could potentially be used to autonomously generate functional block copolymers *in situ*[430]. To our knowledge, this work was the first clear demonstration that *S. oneidensis* EET activity is necessary and sufficient to control a synthetic redox-driven polymerization reaction. Follow-up studies by our group have shown that *S. oneidensis*-controlled ATRP is extendable to use of other metal catalysts (e.g., Co, Fe, Ni) and monomers (e.g., styrene)[431], and can be leveraged to control soft material synthesis (e.g., hydrogels – see Chapter 6). More broadly, our work suggests that other controlled radical polymerizations (e.g., RAFT)[432,433] and potentially any biocompatible metal-catalyzed redox process (e.g., azide-alkyne cycloaddition)[434–436] may be regulated using microbial electroactivity.

7.3 Chapter 3 Summary and Outlook

There are numerous examples of metal nanoparticle synthesis by bacteria[39], but a lack of simple genetic factors to control particle properties has bottlenecked application of

this biotechnology. In Chapter 3, we test the hypothesis that availability of *S. oneidensis* EET pathway components affects Pd nanoparticle properties and determine genotype-phenotype relationships between specific proteins/metabolites and the size and cellular localization of nanoparticles. Our knockout and complementation experiments determined that expression of the MtrC cytochrome is necessary and sufficient for robust Pd(II) reduction and nucleation of large nanoparticle aggregates (>50 nm) on the *S. oneidensis* outer membrane. Strains lacking MtrC expression formed small intracellular particles (10-25 nm) confined to the periplasm. These results are consistent with other studies showing that MtrC localizes to the outer membrane[83,109,110] and is the terminal reductase in the *S. oneidensis* EET pathway[86]. We also found that supplementing cultures with flavins (EET-enhancing cofactors of MtrC)[110,118] above cell-secreted concentrations leads to an increase in the number of Pd nucleation sites per cell. Collectively, these results provide a handle to control Pd particle formation through MtrC expression and suggest that flavin-bound MtrC serves as the binding site for cell surface-displayed nanoparticles.

Although the nature of particle binding remains to be directly tested (e.g., colocalization of labeled Pd/MtrC)[239,437], these results are proof-of-principle for developing genetically controlled Pd nanoparticle whole cell sensors and devices[438]. Since palladium is an effective catalyst for many fluorescence turn-on[439,440] and carbon-carbon coupling reactions[441,442], analyte sensing could be accomplished through stimuli-responsive MtrC expression circuits that generate signal-amplifying Pd nanoparticles[229,378]. Towards biopatterned inorganic and electronic structures[13,32,192,193], similar expression control of MtrC using pattern-forming morphogenetic circuits could generate well-defined spatial arrangements of bio-Pd nanomaterials[443–446]. Moreover, nanoparticle morphology and catalytic activity can potentially be optimized by applying protein engineering methodologies to MtrC. Manipulation of the cytochrome's redox activity may alter Pd(II) reduction rates[110] and further aid in determining the mechanism of particle binding[302]. Given the wide redox potential window of *S. oneidensis* EET proteins[116], our genetic approach to control particle properties can likely be leveraged with other nanoparticle-forming metals, such as Ag and Au[153–155].

7.4 Chapter 4 Summary and Outlook

Electroactive bacteria are frequently used in conjunction with functional insoluble materials, such as iron oxides and electrodes[64,226]. However, limited chemical tunability with these materials has made it challenging to rigorously control the biotic-abiotic interface (e.g., biofilm establishment, electrical conductivity). In Chapter 4, we provide the first report of *S. oneidensis* cultured on a tunable class of materials that are analogous to naturally occurring minerals: metal-organic frameworks. Similar to *S. oneidensis* iron oxide substrates, these frameworks contain redox-active Fe(III), which we hypothesized could be used as an electron acceptor in EET. Unlike oxide-type minerals, these materials exhibit extremely tunable morphologies, high surface areas, and well-defined crystal structures[447]. We observed that *S. oneidensis* can couple growth/carbon metabolism to EET-based reduction of Fe(III) in these materials, and that significant amounts of reactive Fe(II) are retained within the material structure. In a practical application, we demonstrated that a synergistic interaction between the bacterium and framework-bound Fe(II) enables cyclable remediation of the environmental toxin Cr(VI). Our bacteria-framework system sequesters chromium better than either component in isolation and has among the highest reported capacities for Cr(VI) removal. More generally, our results demonstrate that metal-organic frameworks can be leveraged as tunable ecosystems that control the rate and activity of *S. oneidensis* EET through material properties

Use of metal-organic frameworks as microbial substrates may find immediate application for studying other electroactive microbes. Since the isolation of model exoelectrogens *S. oneidensis* and *Geobacter sulfurreducens* in the late 1980s[62,63], metal oxides have remained the dominant electrode-free means to characterize EET with insoluble materials. Given their poorly defined composition, limited tunability, and susceptibility to thermodynamic phase changes, these substrates can be challenging to experimentally utilize. Differences between laboratory-synthesized oxides and naturally occurring minerals likely contribute to difficulties in isolating monocultures of environmentally observed electrogens, such as cable bacteria[448] and methanotrophic archaea[72]. The increased chemical and material tunability of frameworks could provide

growth conditions more conducive for isolation and facilitate characterization of EET activity at heterogeneous interfaces (e.g., extracellular cytochrome matrices)[236,449]. As we showed with our bacteria-framework chromium remediation scheme, traditionally abiotic applications that leverage these materials (e.g., catalysis, gas storage) may also be enhanced by addition of electroactive microbes[311,312].

7.5 Chapter 5 Summary and Outlook

Despite the promise of EET as a means for sustainable electricity generation and construction of bioelectronic devices, these applications remain largely unrealized due to a lack of control over EET activity in *Shewanella* and other electroactive bacteria[90,210]. Key to enabling this control is development of genetic tools that precisely regulate EET flux and enable construction of more sophisticated cellular circuitry. In Chapter 5, we engineer such tools by making simple and systematic changes to transcription/translation for single EET genes in *S. oneidensis* (i.e., *cymA*, *mtrA*, *mtrC*), which enabled generation of functional Buffer and NOT logic gate circuits. While the RBSCalculator has become a staple of synthetic biology workflows[365,366], to our knowledge it had not previously been tested in *S. oneidensis*. In addition to demonstrating its rational prediction of translation strength in the bacterium, we show that the calculator facilitates optimization of ON/OFF dynamic range for inducible EET activity. Using optimized RBS/EET gene pairs, a high throughput EET characterization assay, and a simple gene expression-metal reduction model, we constructed Buffer and NOT gate architectures that yield ON and OFF EET activity, respectively, by engineered *S. oneidensis* strains. Logic gate activity was regulated at the transcriptional level based on the presence of an inducer molecule. Notably, the Hill function-type EET responses by these logic gates closely mimic those observed with typical fluorescent reporter outputs[211]. Collectively, our genetic designs demonstrate that single EET genes can exert master control over cellular electron flux and represent functional building blocks for designer EET activity.

Although synthetic biology has significantly advanced through development of genetic sensing and computation machinery, genetic actuators are relatively limited to

fluorescent/luminescent reporters. While other useful protein-based outputs have been coupled to complex circuit architectures (e.g., nitrogen fixation enzymes, acoustic reporters)[12,205,450], these systems typically serve narrowly defined objectives. Based on our results, EET proteins may be leveraged as versatile genetically encoded actuators that can perform a myriad of functions (e.g., electricity generation, material synthesis, redox catalysis). Indeed, all the material syntheses/transformations described in Chapters 2-4 and Chapter 6 can potentially be controlled through EET gene expression circuits. Furthermore, we showed that the transcriptional logic gate paradigm can regulate microbial electroactivity, which suggests that previously developed genetic circuits exhibiting memory[197,200], multi-signal integration[21,229], and spatiotemporal dynamics[198,204,208] could be used to drive EET outputs. Given the direct connection between genetically encoded EET proteins and cellular electron flux, it is tempting to envision strict control over electronics through synthetic biology – an idea not too far off from how the field began[26]!

7.6 Chapter 6 Summary and Outlook

Hydrogels are widely applied in tissue engineering and soft robotics due to their biocompatibility, potential for chemical functionalization, and tunable mechanical properties (e.g., stiffness)[383,384,451,452]. Although enzymatic degradations can lower gel stiffness and enable *in situ* remodeling during cell proliferation/differentiation[453], stimuli-responsive increases in stiffness are limited to physical methods (e.g., photoactivation)[424]. In Chapter 6, we demonstrate that *S. oneidensis* EET can facilitate biologically controlled increases in gel stiffness via ATRP-controlled cross-linking of methacrylated hyaluronic acid macromers. Similar to the homopolymer system described in Chapter 2, macromer cross-linking follows a controlled radical polymerization process that is activated by EET-based reduction of a Cu(II) catalyst. Gel stiffness was proportional to inoculating cell density and attenuated by *S. oneidensis* strains with diminished EET activity. Together, this suggested that altering EET flux to the catalyst might tune cross-link density and gel stiffness. To test this hypothesis, we used an *S. oneidensis* strain carrying the *mtrC* Buffer gate circuit described in Chapter 5 and found that gel stiffness was inducible by IPTG.

Stiffness followed a Hill function-type response, which implies that stiffness is directly tied to cellular MtrC expression levels. Together, these results highlight another synthetic material whose formation is controlled by *S. oneidensis* and is further evidence that EET gene expression circuits can be used to program EET-based actuations (i.e., gel cross-linking/stiffness).

Our results are a powerful demonstration that EET can control material properties at a macroscopic scale. Formed gels could be physically touched and manipulated, while retaining metabolically active cells within the hydrogel matrix. Accordingly, they are an excellent example of living materials, and could be further engineered to sense/respond to target biological or environmental stimuli (e.g., drug delivery, wound repair)[32,453–455]. Separately, our *S. oneidensis*-hydrogel system could be leveraged to design more complex material architectures using genetic circuitry[456–458]. Understanding the design rules for pattern formation and generation of 2D/3D structures is an ongoing challenge in developmental and synthetic biology[459]. Since our system provides a direct linkage between EET activity and gel stiffness, previously engineered pattern-forming circuits could be adapted to express MtrC and control hydrogel synthesis[201,443,446]. In such a scheme, we hypothesize that 2D/3D arrangements of *S. oneidensis* cells expressing MtrC would be able to synthesize macroscopic hydrogels within the circuit-defined boundaries of gene expression patterns. Such a system may help understand fundamental limits of cell-cell communication/differentiation and further aid in the production of functional living materials[41].

7.7 Proposed Research and Final Comments

The technical advancements reported in this dissertation collectively demonstrate that EET is a powerful modality to genetically control inorganic and abiotic technologies. Looking forward, two questions can be asked that build upon this work and potentially expand the utility of EET-based actuations. First, can novel EET proteins be engineered to interact with substrates that are unreactive with the wild-type proteins? And second, can programmable EET activity be transferred to microorganisms residing in functionally

relevant environments (e.g., plant root rhizosphere, gut microbiota)? Future work will focus on addressing these questions by leveraging the findings and tools developed in this dissertation.

The first question is frequently posed in the enzyme engineering community for non-EET proteins – how do we engineer a protein to catalyze a new reaction? Despite the wide substrate range of *S. oneidensis* EET proteins, there are many molecules and metals that are inert to reduction by the bacterium[460–462]. In some cases, steric hindrance appears to limit reduction due to excessive molecule size or bulky chelation of certain metal complexes[398,463]. Thermodynamic limits may also play a role, as electrochemical measurements place the lower end of the MtrC redox potential window at -350 mV vs SHE[116,464]. This may cause extracellular reduction of substrates with reduction potentials below this value to be energetically unfavorable[464,465]. However, since many biologically-metabolized electron donors have lower reduction potentials (e.g., glucose/pyruvate, -720 mV vs. SHE; formate/CO_2, -420 mV vs. SHE)[55,95,466], EET-based reduction of compounds with lower potentials would appear feasible. Taken together, there is strong motivation to develop workflows for engineering the activity of MtrC and other EET proteins, as it could expand the substrate range of microbial electroactivity and further enable biological control over electronic and material science platforms.

Changes to the MtrC polypeptide sequence may increase its substrate promiscuity and alter its heme environments to carry electrons with lower reduction potentials[467]. Based on the MtrC crystal structure, four of the protein's ten hemes are hypothesized to be the sites of electron transfer to substrates and may serve as engineering targets[88]. Directed evolution has taught us that reactivity towards previously inert substrates can be rapidly engineered for proteins after repeated mutagenesis and screening/selection cycles[468]. Similarly, this method could be applied to alter MtrC activity and screen for degradation of recalcitrant dye substrates[460], which are amenable to high throughput characterization. Libraries of MtrC mutants could be generated by performing site saturation mutagenesis at residues that are non-essential ligands for the heme-bound Fe[469,470]. With other catalytic cytochromes, these residues have proven amenable to mutation and can exert drastic effects

on the redox potential and sterics around the heme site[24,25,471]. Our *mtrC* Buffer gate circuits described in Chapter 5 could be used to express the mutant library, as presumably the dynamic range-optimized RBS sequences would facilitate rigorous control over when mutant MtrC are expressed. While augmented dye reduction would be useful in a bioremediation setting, results from this effort could more have broader implications on design strategies when engineering MtrC to react with more challenging and lower throughput substrates (e.g., non-colorimetric metal complexes)[461,462,464].

While *S. oneidensis* has proven to be an excellent model organism when studying EET behavior, it does not naturally associate with multicellular hosts[61]. As a result, its EET activity has not been used in probiotic-type treatments and has been restricted to *in vitro* systems (e.g., bioreactors, microbial fuel cells). Given the ability of EET to control material formation, catalytic transformations, and potentially remodel the environment through redox interactions, EET-capable endosymbiotic bacteria could be practical tools in human health and agricultural settings. For example, root-associated rhizobacteria could potentially ameliorate iron starvation in plants[472,473] by mobilizing Fe(II) through EET-based reduction of mineral-bound Fe(III)[474,475]. Such beneficial bacteria could be used as growth inoculants in iron-poor soils and global regions with populations experiencing iron-deficiency[68,476,477]. Alternatively, probiotic oral/gut bacteria could be developed that leverage EET to outcompete pathogens for iron and other redox-active nutrients[70,478–480]. These probiotics could also be leveraged to activate pro-drugs using EET and localize their effect to diseased regions of the body that are colonized by these microbes (e.g., colorectal cancers)[481]. Taken together, developing new strains of electroactive host-associating bacteria could expand the utility of EET and endow multicellular organisms with redox capabilities that are challenging to directly engineer in eukaryotic systems.

At present, expression of EET pathways in a foreign host has chiefly been tested in *Escherichia coli*. Ajo-Franklin et al. have demonstrated that plasmid-based expression of the *S. oneidensis* MR-1 CymA/Mtr pathway and overexpression of *E. coli* heme maturation machinery (*ccm* operon) facilitates functional EET in engineered *E. coli* strains[277,298]. Similar to our approach taken with *S. oneidensis* in Chapter 5, they showed that synthetic

biology workflows can optimize pathway expression and EET performance[368]. The success of their efforts suggests that other gram-negative bacteria could also be transformed to exhibit functional EET activity.

E. coli Nissle 1917 is an attractive choice for engineering EET in human probiotics, as it is a well-precedented gut colonizer and clinically utilized for ameliorating gastrointestinal diseases[482–484]. Overlapping genetics and metabolism between the Ajo-Franklin strains (derivatives of BL21) and Nissle 1917 lends further credence to successful functioning of the Mtr pathway and presents the opportunity for adapting previously developed genetic tools[485,486]. Because of their broad-host range colonization of plants, *Pseudomonas* spp. are also well-positioned to act as EET-capable gram-negative hosts[487–489]. In addition to possessing a comparable membrane structure with *S. oneidensis* (which is likely required for functional localization/activity of the MtrCAB conduit), many *Pseudomonas* spp. exhibit electroactivity through secretion of soluble redox shuttles (i.e., phenazines) and can couple carbon metabolism with reduction of insoluble substrates[474,490]. Heterologous EET pathways may be able to tap into shared metabolite pools between these processes (e.g., anaerobic quinones)[82,92], and further augment reduction capabilities. With both these sets of organisms, we propose to express the Mtr and heme maturation proteins, and assay EET performance using the methods developed in Chapters 2-6. While optimizing multi-protein processes in heterologous organisms possesses many known challenges, recently developed genetic toolkits can decrease the timescale of the design-build-test cycle[206,229]. Nonetheless, the enhanced understanding of engineering EET activity that is developed by this dissertation should make it easier to expand the utility of EET as described in these proposals.

In conclusion, this dissertation represents significant advancements in the application and genetic regulation of EET by *S. oneidensis*. Novel methods and tools are developed that may be broadly applicable in catalysis, materials synthesis, bioremediation, bioelectronics, and synthetic biology. Given the ubiquity of redox interactions and tractability of *S. oneidensis* as a chassis organism, EET offers promise for enabling genetic

control over new processes and technical fields that are traditionally outside the realm of biotechnology.

Appendices

APPENDIX A: SUPPLEMENTARY DATA FOR CHAPTER 2

Supplementary Tables for Chapter 2

Reagent	Quantity in 1L of 200X Stock
EDTA	0.5 g (2.69 mL of 0.5 M stock)
$MgSO_4•7H_2O$	3.0 g
$MnSO_4•H_2O$	0.5 g
NaCl	1.0 g
$FeSO_4•7H_2O$	0.1 g
$Co(NO_3)_2•6H_2O$	0.1 g
$CaCl_2$	0.9 mL from 1 M stock
$ZnSO_4•7H_2O$	0.1 g
$CuSO_4•5H_2O$	10 mg
$AlK(SO_4)_2$	10 mg
H_3BO_3	10 mg
$Na_2MoO4•2H_2O$	10 mg
Na_2SeO_3	1 mg
$Na_2WO_4•2H_2O$	10 mg
$NiCl_2•6H_2O$	20 mg
ddH_2O	1 L

Table A.1: Metals present in *Shewanella* basal medium Wolfe's mineral solution. Adapted from ATCC recipe.

Entry	[Cat.]/μM	[M]/[I]	M_n (Theor.)	M_n (Exp.)	Đ
Cu(II/I)-EDTA	100	10/1	5.0×10^3	7.5×10^5	2.43
Cu(II/I)-EDTA	100	1000/1	5.0×10^5	2.8×10^6	2.49
Cu(II/I)-EDTA	10	10/1	5.0×10^3	8.0×10^6	1.26
Cu(II/I)-EDTA	10	1000/1	5.0×10^5	1.2×10^7*	1.05*
Cu(II/I)-TPMA	2	1000/1	5.0×10^5	1.4×10^6	1.09

Table A.2: MR-1 mediated controlled polymerization of $OEOMA_{500}$ in SBM buffer at 30 °C. (*exclusion limit)

Strain or plasmid	Description/Genotype	Reference or source
S. oneidensis Strains		
MR-1	MR-1 (ATCC700550), wild-type strain	American-Type Culture Collection
JG749	Lacks outer membrane cytochromes, MtrC and OmcA; Δ*mtrC*Δ*omcA*	[86]
JG1758	Lacks inner membrane flavin adenine dinucleotide exporter, Bfe; Δ*bfe*	[120]
Δ*hydA*Δ*hyaB*	Lacks periplasmic hydrogenases, HydA and HyaB; Δ*hydA*Δ*hyaB*	Jeffrey Gralnick, U. of Minnesota
BK2	MR-1 with empty pShew, Km^r	This study
BK13	JG749 (Δ*mtrC*Δ*omcA*) with empty pShew, Km^r	This study
BK14	JG749 (Δ*mtrC*Δ*omcA*) with pShew-mtrC, Km^r	This study
E. coli Strains		
MG1655	Wild-type strain	Lydia Contreras, U. of Texas at Austin
DH5α	Cloning strain; F^- Φ80*lac*ZΔM15 Δ(*lac*ZYA-*arg*F) U169 *rec*A1 *end*A1 *hsd*R17(r_k^-, m_k^+) *pho*A *sup*E44 *thi*-1 *gyr*A96 *rel*A1 λ^-	Life Technologies
WM3064	Conjugation strain; *thrB1004 pro thi rpsL hsdS lacZ* M15 RP4-1360 (*araBAD*)*567 dapA1341*::[*erm pir*(wt)]	[77]
Plasmids		
pZ8-T_dcas9	pZ8-1 plasmid carrying *dcas9*, driven by IPTG inducible Ptac promoter, expresses $LacI_q$ repressor, Km^r, p15A origin of replication	[279] (Addgene)
pShew	PZ8-T_dcas9 derived vector that lacks *dcas9* and has a ClaI site removed from Km^r gene	This study
pShew-mtrC	pShew plasmid carrying *mtrC*, driven by Ptac	This study

Table A.3: Bacterial strains and plasmids used in this study.

Primer	Sequence (5' → 3')	Restriction Sites
pShewFWD1	TCACACAGGAAACAGAATTCGGATCCGTCG ACCTGCAGCC	None
pShewREV1	GATAATGTCGGGCAATCAGGTGCGACAATC TATCGCTTGTATGGG	ClaI removal
pShewFWD2	ACAAGCGATAGATTGTCGCACCTGATTGCC CGACATTATC	ClaI removal
pShewREV2	GGCTGCAGGTCGACGGATCCGAATTCTGTT TCCTGTGTGA	None
Shew_genome_mtr C_fwd	GCTATTGAATTCATGATGAACGCACAAAAAT CAAAAATCGCAC	EcoRI
Shew_genome_mtr C_rev	ATTCGAGTCGACTTACATTTTCACTTTAGTGT GATCTGCAACTGTTG	SalI

Table A.4: Primers used in this study.

Entry	Strain/genotype	Carbon Source	[monomer]/[RX]/[Catalyst]	Catalyst	k (h^{-1})
1	MR-1	Lactate	1000/1/0.02	Cu/TPMA	2.20
2	MR-1	Pyruvate	1000/1/0.02	Cu/TPMA	1.57
3	MR-1	Acetate	1000/1/0.02	Cu/TPMA	1.16
4	MR-1	None (Starved)	1000/1/0.02	Cu/TPMA	1.30
5	Δ*hydA*Δ*hyaB*	Lactate	1000/1/0.02	Cu/TPMA	2.29
6	Δ*mtrC*Δ*omcA*	Lactate	1000/1/0.02	Cu/TPMA	0.29
7	Δ*bfe*	Lactate	1000/1/0.02	Cu/TPMA	2.60
8	MR-1+empty	Lactate	1000/1/0.02	Cu/TPMA	2.68
9	Δ*mtrC*Δ*omcA*+empty	Lactate	1000/1/0.02	Cu/TPMA	0.58
10	Δ*mtrC*Δ*omcA*+*mtrC*	Lactate	1000/1/0.02	Cu/TPMA	1.19
11	MR-1	Lactate	1000/1/0.002	Cu/EDTA	0.065
12	MR-1	Lactate	[monomer]/[RX] =1000/1	Wolfe's mineral solution (0.5%)	0.11
13[273]	N/A*	N/A*	200/1/1	Cu/TPMA	1.52

*electrochemical ATRP performed in water with E_{app} = –0.21 V, T = 25 °C

Table A.5: Comparison of first-order rate constants under different polymerization conditions.

Supplementary Figures for Chapter 2

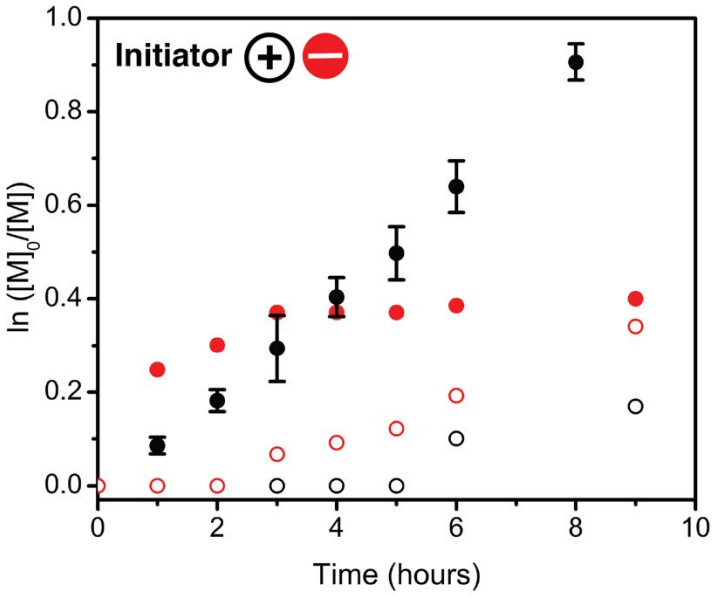

Figure A.1: Kinetics of monomer conversion using MR-1 in SBM with (solid points) and without (hollow points) added metal. Data show mean ± S.D. of three independent experiments.

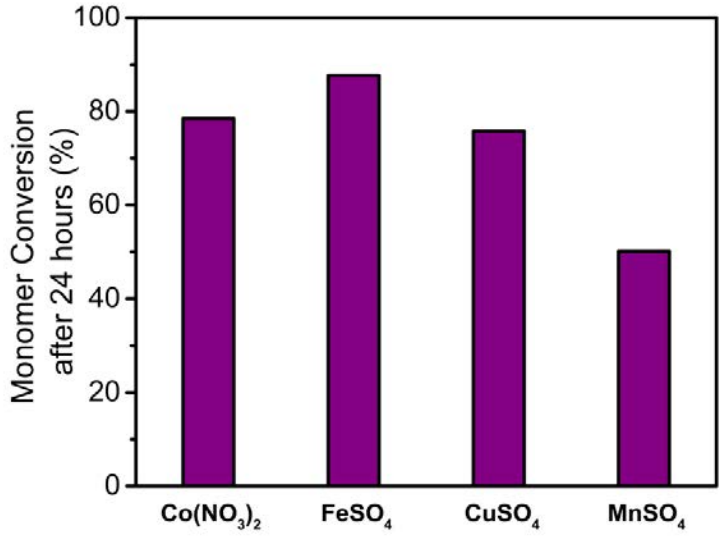

Figure A.2: Conversion of $(OEOMA)_{500}$ using other metals as catalysts and EDTA as ligand. Metals were evaluated at their concentrations listed in Table A.1.

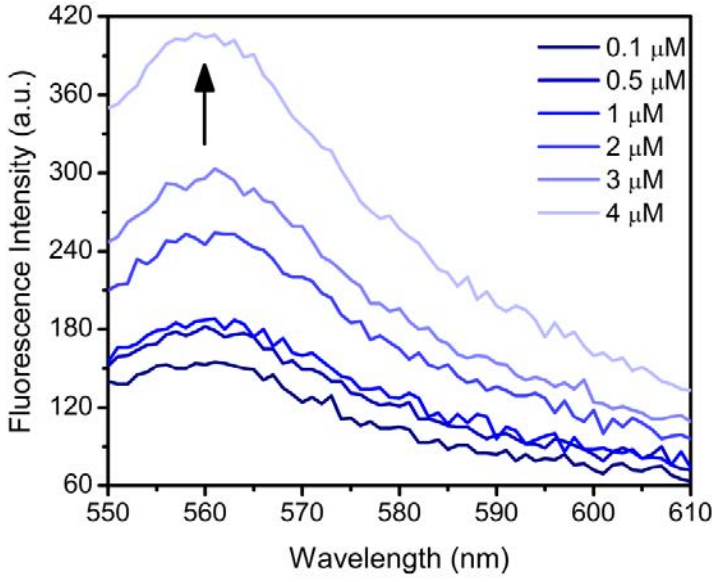

Figure A.3: Fluorescence intensity change of CF4 with increasing concentrations of $Cu^{I}(CH_3CN)_4BF_4$.

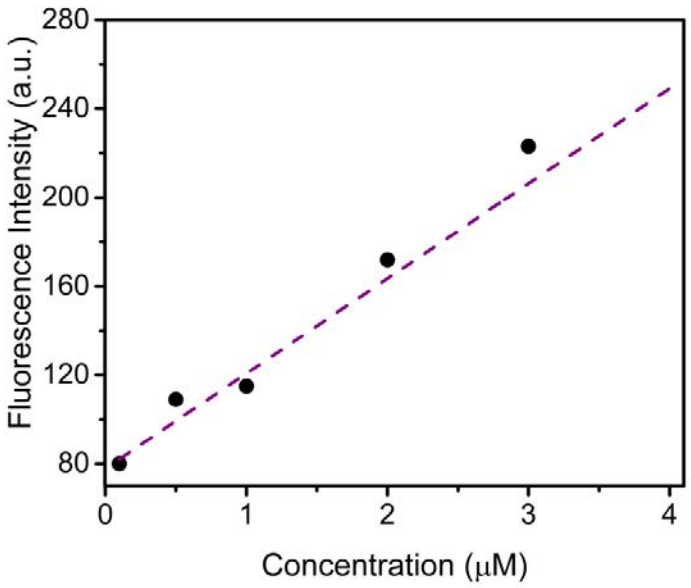

Figure A.4: Calibration curve for CF4 fluorescence intensity as a function of increasing concentrations of $Cu^{I}(CH_3CN)_4BF_4$. Line of best fit: $y = 77.8 + 42.8X$, $R^2 = 0.929$.

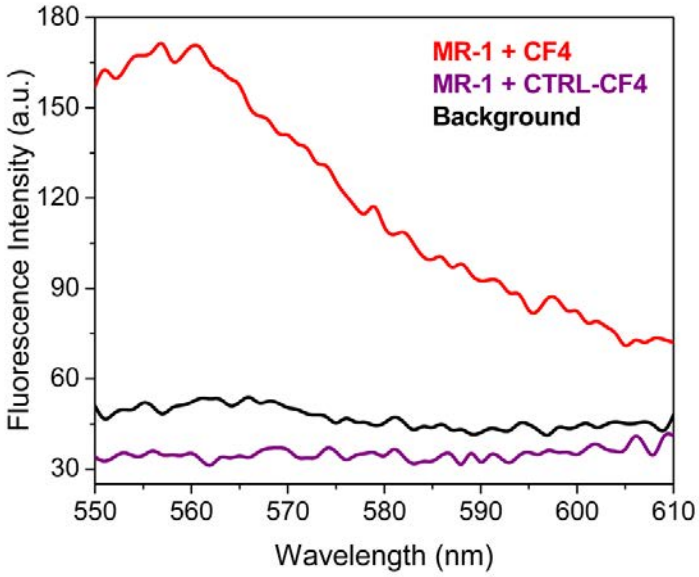

Figure A.5: Fluorescence intensity change in MR-1 supernatant following incubation with $CuSO_4 \cdot 5H_2O$ (2 μM) and CF4 or CTRL-CF4.

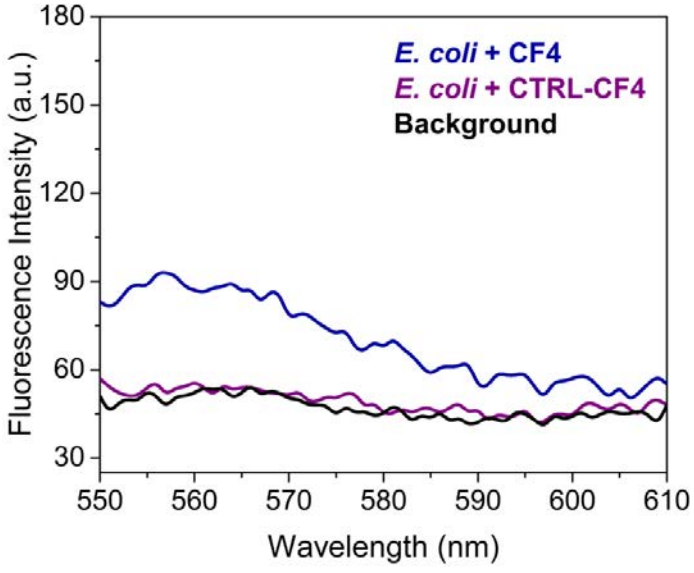

Figure A.6: Fluorescence intensity change in *E. coli* (MG1655) supernatant following incubation with $CuSO_4 \cdot 5H_2O$ (2 μM) and CF4 or CTRL-CF4.

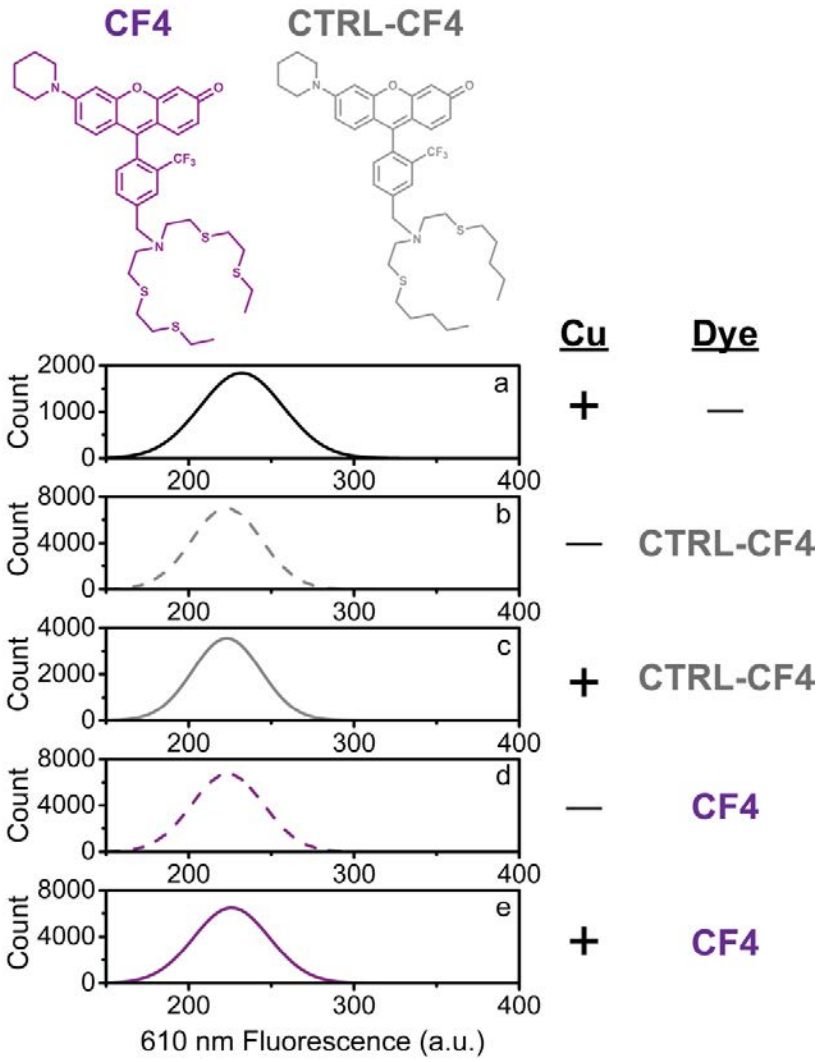

Figure A.7. No detectable increase in cytoplasmic Cu(I) following incubation with exogeneous Cu(II).

Flow cytometry data for *S. oneidensis* MR-1 incubated with $CuSO_4 \cdot 5H_2O$ (2 μM) for 2 hours, followed by either CF4 or CTRL-CF4 incubation. (a) Background with no fluorescent dye added. (b,c) Incubation with non-binding CTRL-CF4 dye without and with exogenous Cu(II). (d,e) Incubation with Cu(I)-binding probe CF4 without and with exogenous Cu(II).

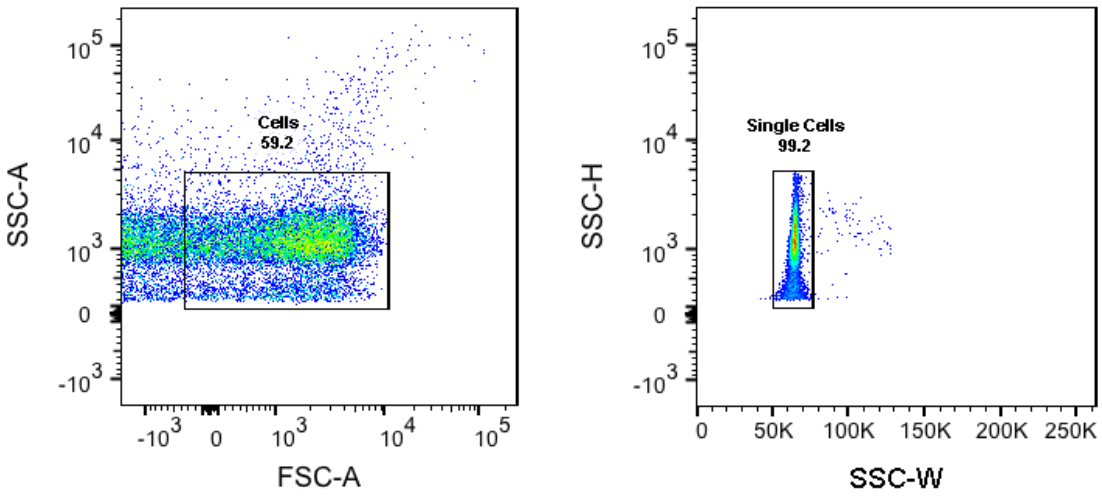

Figure A.8: Representative gating scheme for flow cytometric analyses on a BD LSRII Fortessa SOPR Flow Cytometer.

Cells were gated based on forward and side scatter, and singlet events isolated by side scatter. The singlet populations were used to create histograms for each sample of 610/20 nm fluorescence using a 561 nm laser.

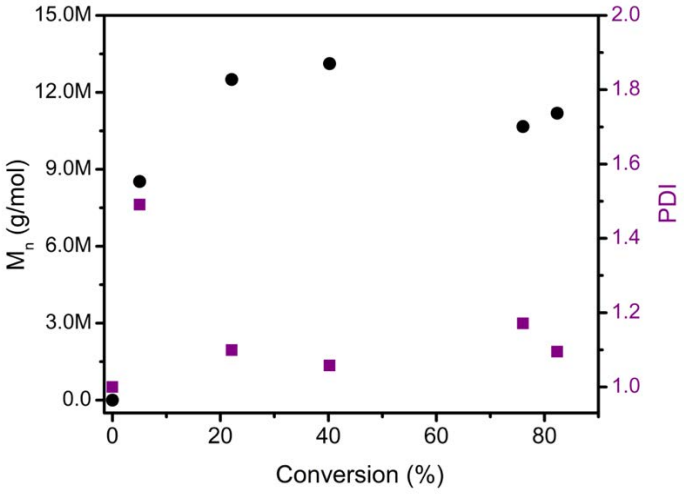

Figure A.9: Number average molecular weight and PDI versus conversion using MR-1, Cu(II/I)-EDTA as catalyst, and $OEOMA_{500}$ as monomer. Data points were collected over a 24-hour time period.

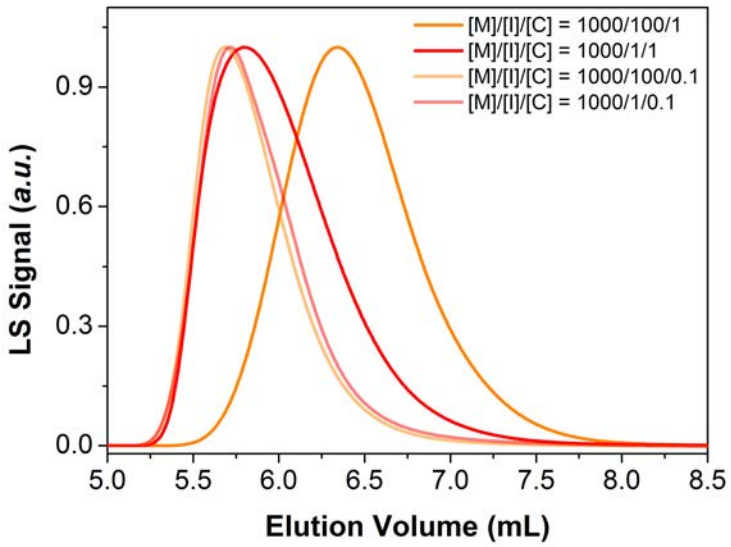

Figure A.10: Gel permeation chromatographs of poly($OEOMA_{500}$) synthesized via MR-1, Cu(II/I)-EDTA as catalyst and $OEOMA_{500}$ as monomer after 24 hours. GPC mobile phase was DMF. (Note: [M] = $OEOMA_{500}$, [I] = HEBIB, [C] = Cu(II/I)-EDTA, molar concentration.)

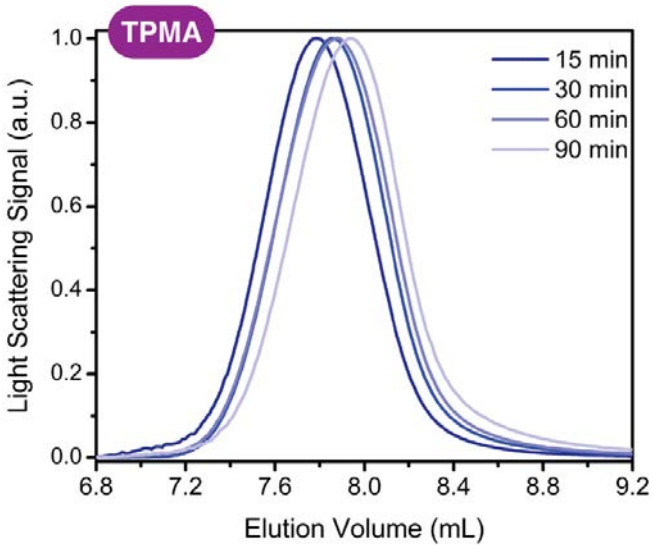

Figure A.11: Gel permeation chromatographs of poly($OEOMA_{500}$) synthesized via MR-1, Cu(II/I)-TPMA as catalyst and $OEOMA_{500}$ as monomer at different time points. GPC mobile phase was PBS buffer.

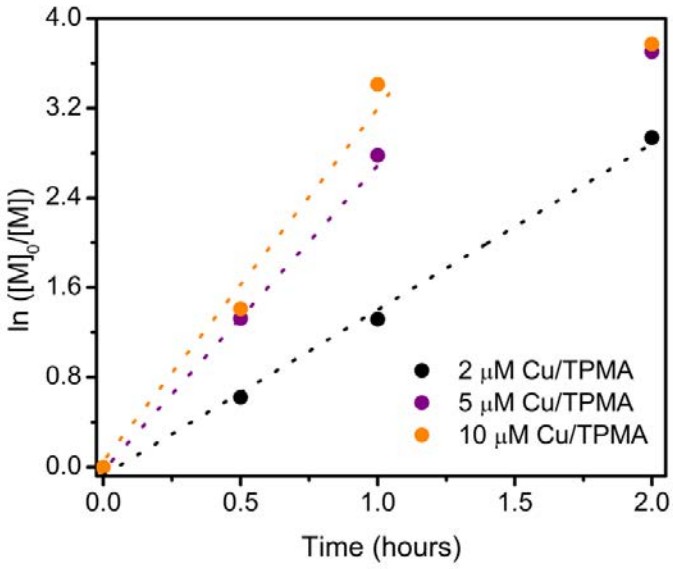

Figure A.12: Effect of different Cu(II/I)-TPMA concentrations on polymerization kinetics.

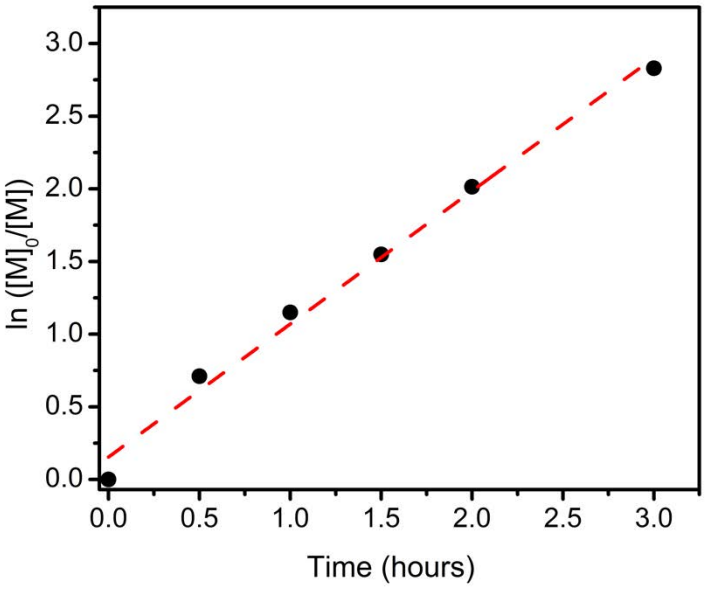

Figure A.13: Linear polymerization kinetics using MR-1, Cu(II/I)-TPMA, and $OEOMA_{900}$ as monomer. Line of best fit: $y = 0.15 + 0.92X$, $R^2 = 0.988$.

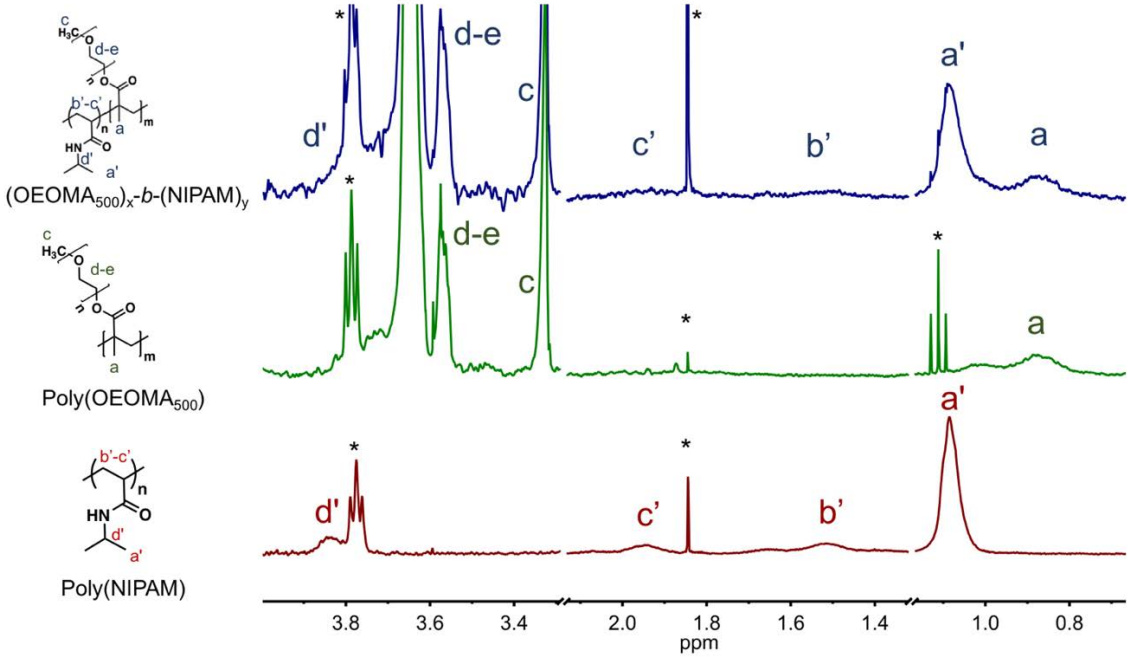

Figure A.14: ^{1}H NMR spectra for the polymerization of Poly(OEOMA$_{500}$)$_m$-*b*-(NIPAM)$_n$ (blue) and its respective homo-polymers, poly(OEOMA$_{500}$)$_m$ (green) and poly(NIPAM)$_n$ (Red).

(Note: * proton peaks due to the impurities from cell culture medium. Proton peaks d' is not apparent for block polymer due to the interference of the long oligo ethylene oxide side chain of OEOMA$_{500}$.)

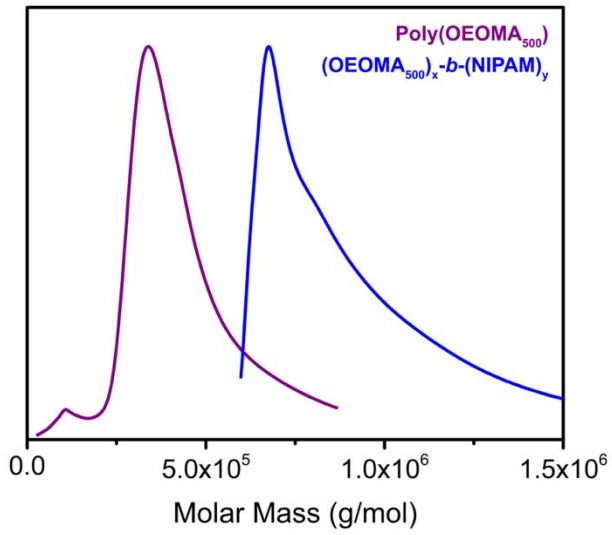

Figure A.15: Molecular weight distribution of poly($OEOMA_{500}$) and block copolymer $(OEOMA_{500})_x$-*b*-$(NIPAM)_y$.

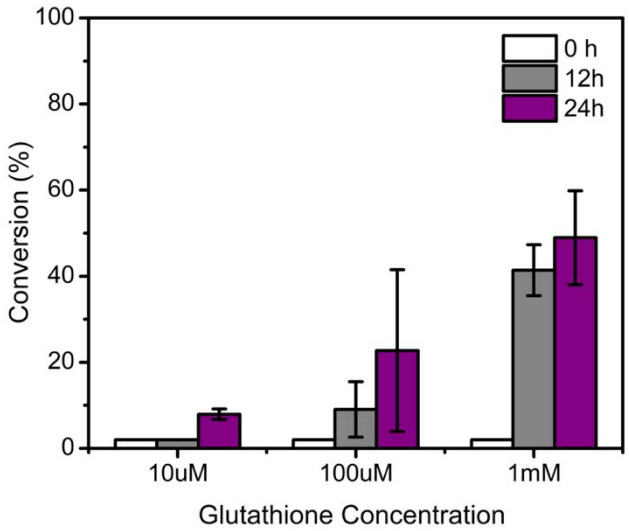

Figure A.16: Reducing factors such as glutathione contribute to polymerization in a dose-dependent manner.

Conversion of $OEOMA_{500}$ to polymer with Cu(II/I)-TPMA and varying concentrations of glutathione as reductant. Data show mean ± S.D. of three independent experiments.

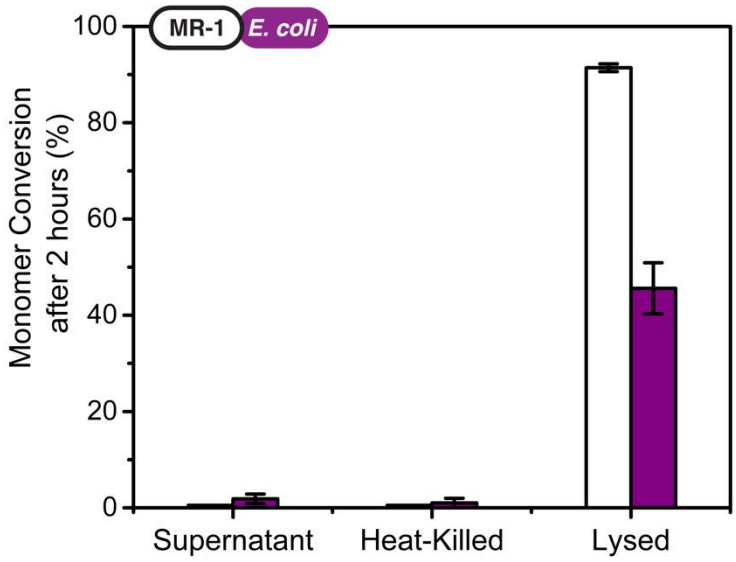

Figure A.17: Monomer conversion is dependent on cell metabolism and membrane integrity.

MR-1 (white) and *E. coli* (purple) supernatant and heat-killed cells exhibited negligible conversion of $OEOMA_{500}$. Both lysed MR-1 and *E. coli* showed significant conversion of $OEOMA_{500}$ using Cu(II/I)-TPMA as catalyst. Data show mean ± S.D. of three independent experiments.

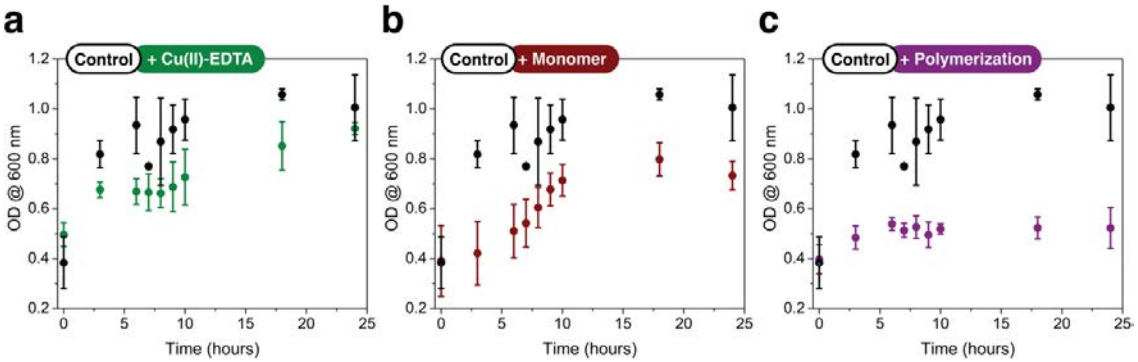

Figure A.18: Growth curves for MR-1 under aerobic conditions when incubated with **a**, $CuBr_2$-EDTA (5 μM). **b**, $OEOMA_{500}$ (100 mM). **c**, anaerobic polymerization conditions including Cu-EDTA (2 μM), $OEOMA_{500}$ (100 mM), and HEBIB (100 μM). Data show mean ± S.D. of three independent experiments.

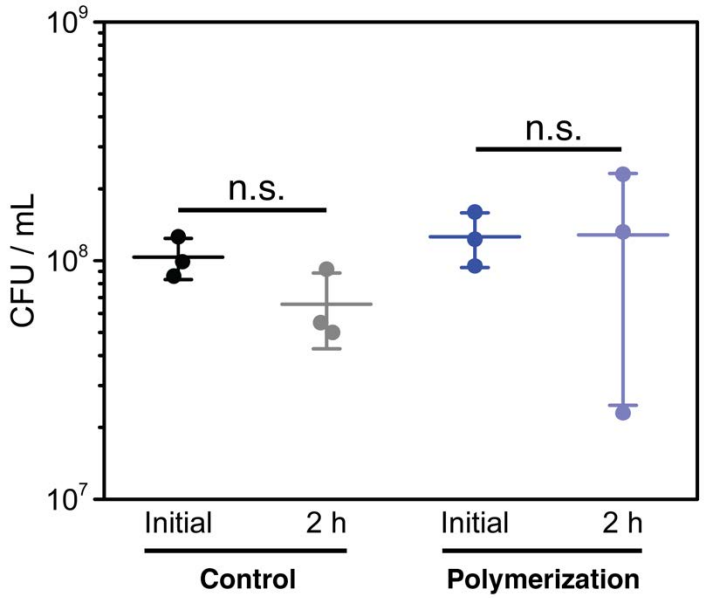

Figure A.19: MR-1 is viable following polymerization.

CFU counts of MR-1 following standard polymerization conditions using Cu(II/I)-TPMA as catalyst. Percent conversion for the polymerization sample after 2 h was 90 ± 5.8 %. Data show mean ± S.D. of three independent experiments. n.s., not significant.

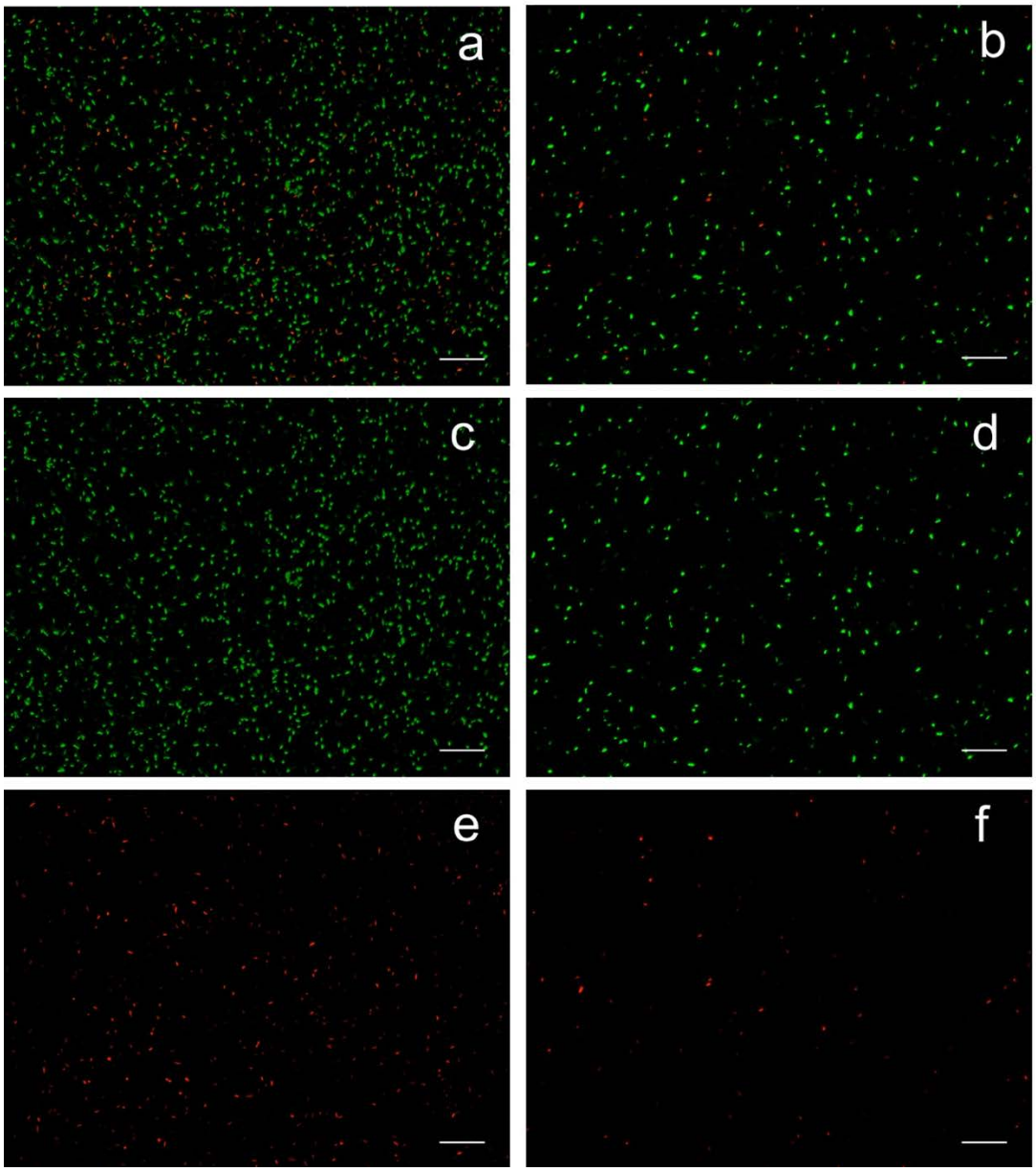

Figure A.20: Bacterial viability assessment post-polymerization shows mostly live cells for both MR-1 and *E. coli*.

a, b, Representative composite images of green (c, d) and red (e, f) fluorescence channels for MR-1 (left) and *E. coli* MG1655 (right). MR-1 was quantified by thresholding each channel from triplicate samples to be 74 ± 2.5% viable, and *E. coli* was quantified to be 86 ± 1.5% viable. Scale bars are 20 μm.

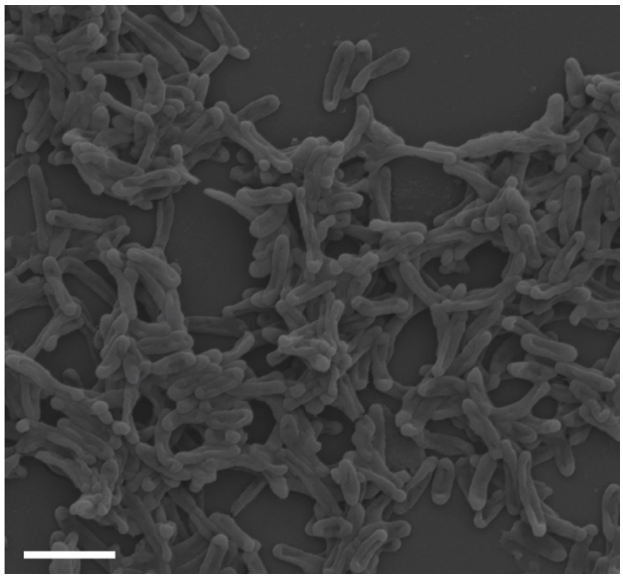

Figure A.21: Scanning electron micrograph (SEM) of MR-1 before polymerization, scale bar = 2 μm.

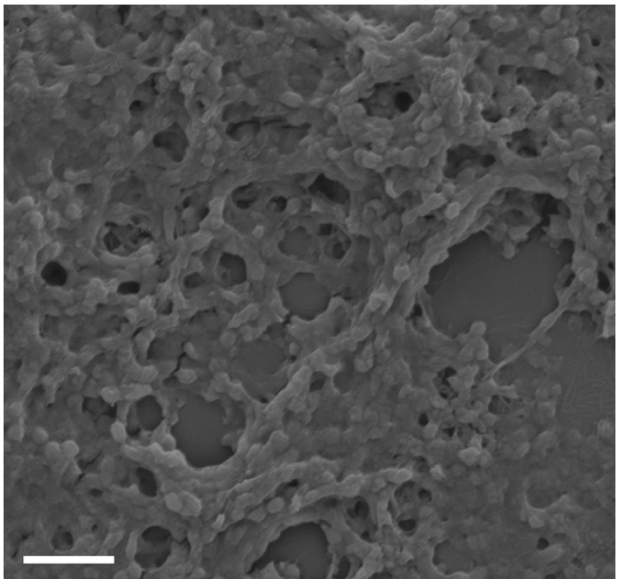

Figure A.22: Scanning electron micrograph (SEM) of MR-1 after polymerization, scale bar = 2 μm.

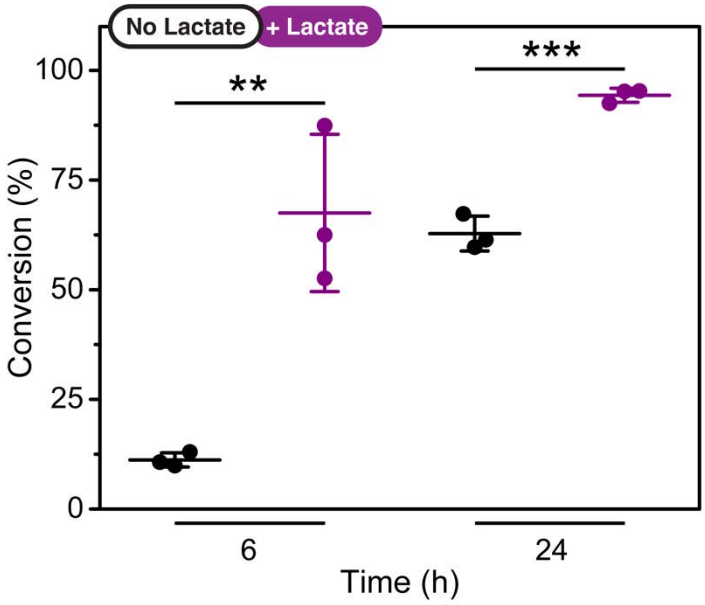

Figure A.23: Metabolic activity is required for monomer conversion.

Conversion of $OEOMA_{500}$ using Cu(II/I)-EDTA as catalyst with starved (black) or lactate supplemented (20 mM, purple) MR-1. Data show mean ± S.D. of three independent experiments. **, $P < 0.01$; ***, $P < 0.001$.

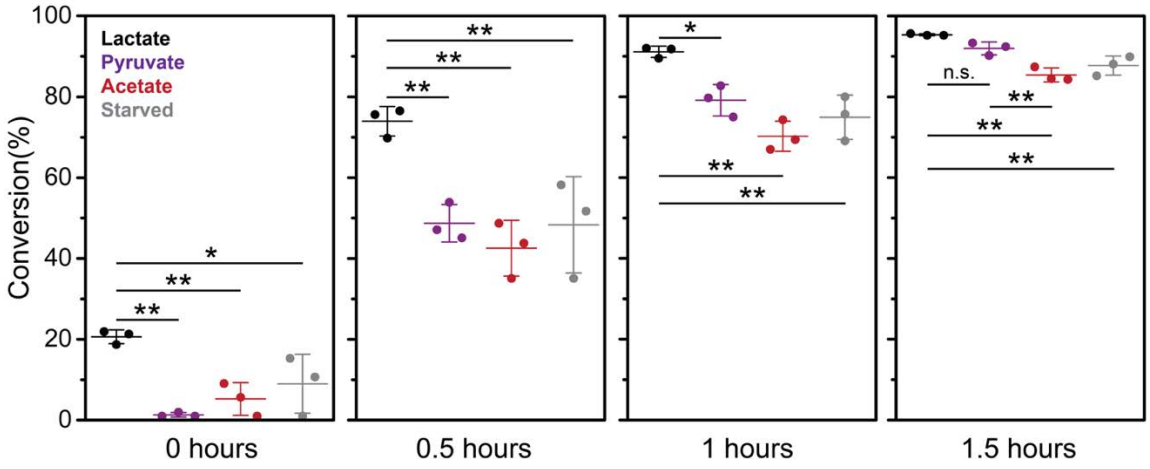

Figure A.24: Accompanying for Figure 2.3b.

Conversion of $OEOMA_{500}$ using Cu(II/I)-TPMA as catalyst with different carbon sources. Data show mean ± S.D. of three independent experiments. **, $P < 0.01$; ***, $P < 0.001$; n.s., not significant using a one way ANOVA test.

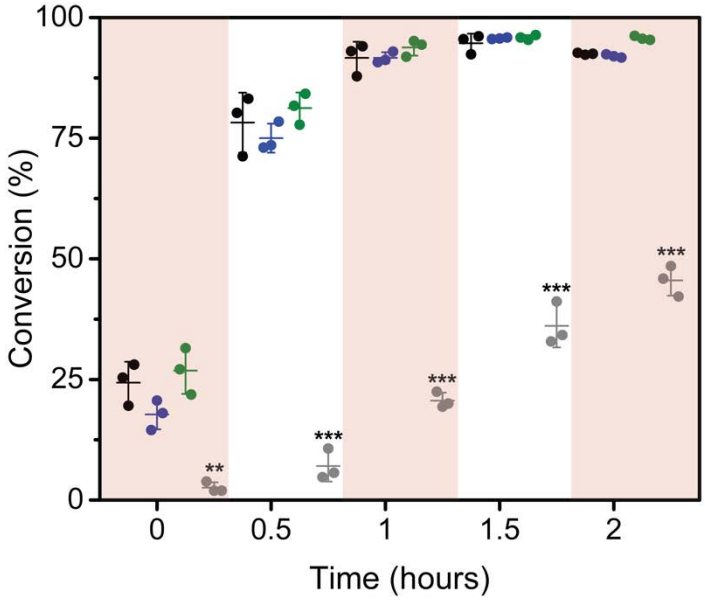

Figure A.25: Accompanying for Figure 2.4b.

Conversion of $OEOMA_{500}$ using Cu(II/I)-TPMA as catalyst with MR-1 (black), Δ*hyd*Δ*hyaB* (blue), Δ*bfe* (green), Δ*mtrC*Δ*omcA* (grey). Data show mean ± S.D. of three independent experiments. **, $P < 0.01$; ***, $P < 0.001$; n.s., not significant using two-tailed Student t-test comparison to MR-1 (black).

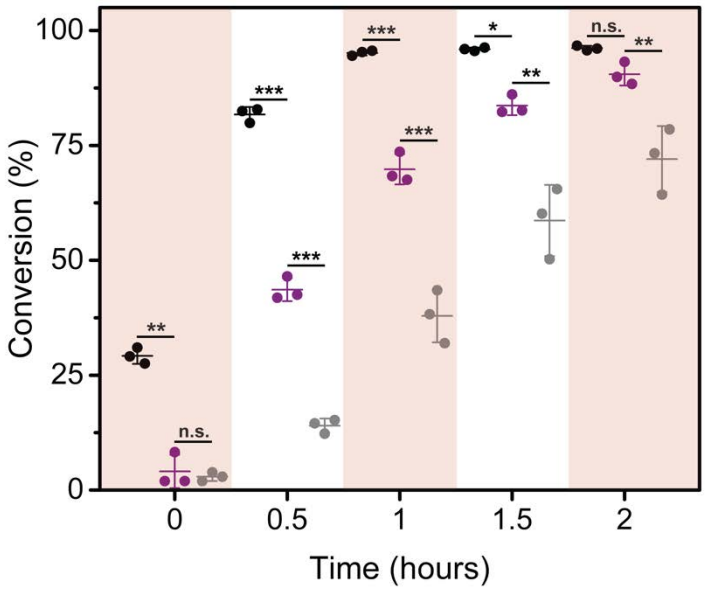

Figure A.26: Accompanying for Figure 2.4c.

Conversion of $OEOMA_{500}$ using Cu(II/I)-TPMA as catalyst with MR-1+empty (black), Δ*mtrC*Δ*omcA*+*mtrC* (purple), Δ*mtrC*Δ*omcA*+empty (grey). Data show mean ± S.D. of three independent experiments. *, $P < 0.05$; **, $P < 0.01$; ***, $P < 0.001$; n.s., not significant using a one way ANOVA test.

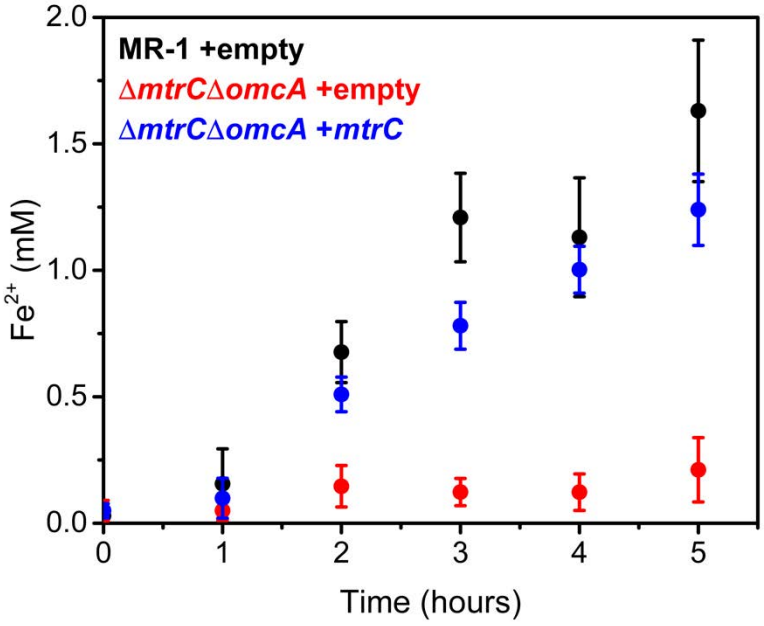

Figure A.27: Iron reduction of different *S. oneidensis* strains.

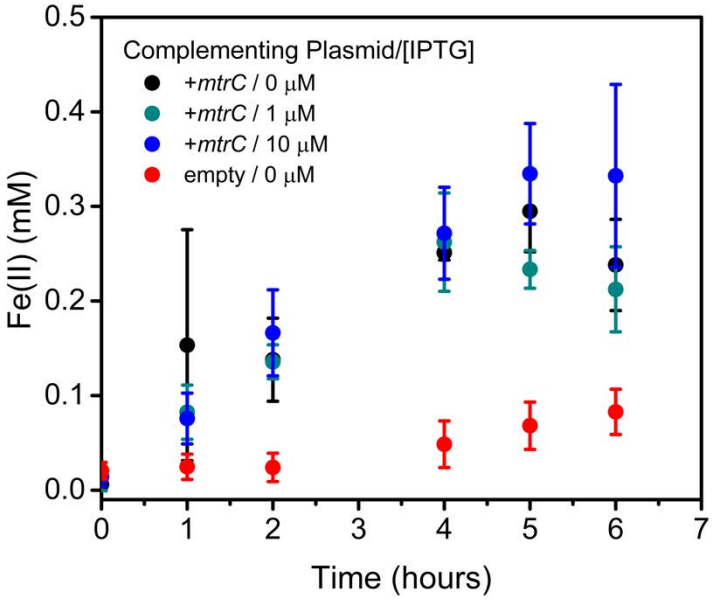

Figure A.28: IPTG inducibility of MtrC and iron reduction in Δ*mtrC*Δ*omcA* strains.

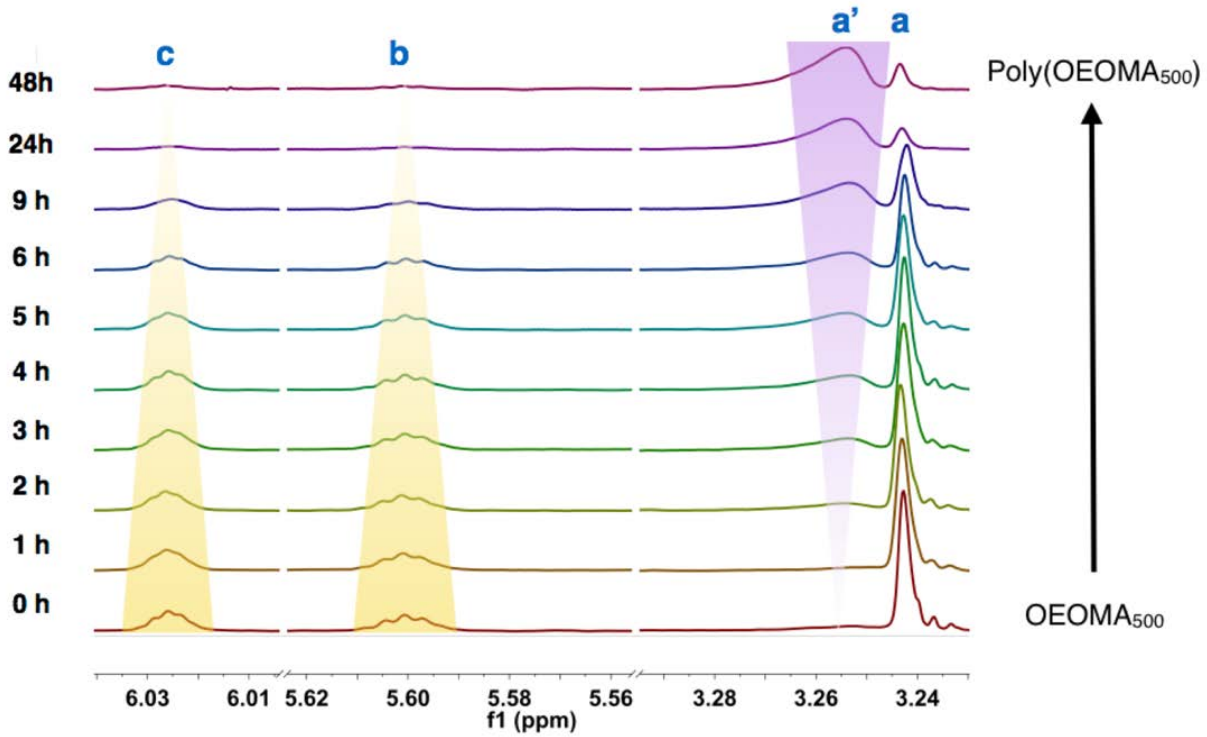

Figure A.29: Example of ^{1}H NMR spectra for determination of monomer conversion during the polymerization of $OEOMA_{500}$ ([M]/[I]=1000/1, HEBIB, *Shewanella* basal medium with Wolfe's mineral solution). Residual water peak has been removed for clarity.

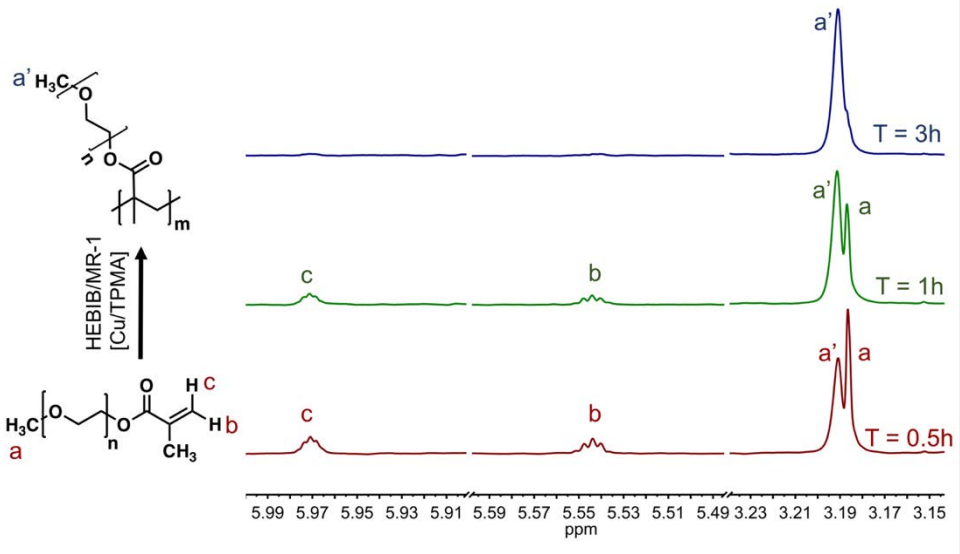

Figure A.30: ^{1}H NMR spectra for the polymerization of $OEOMA_{900}$. Residual water peak has been removed for clarity. (Note: T indicates different reaction time.)

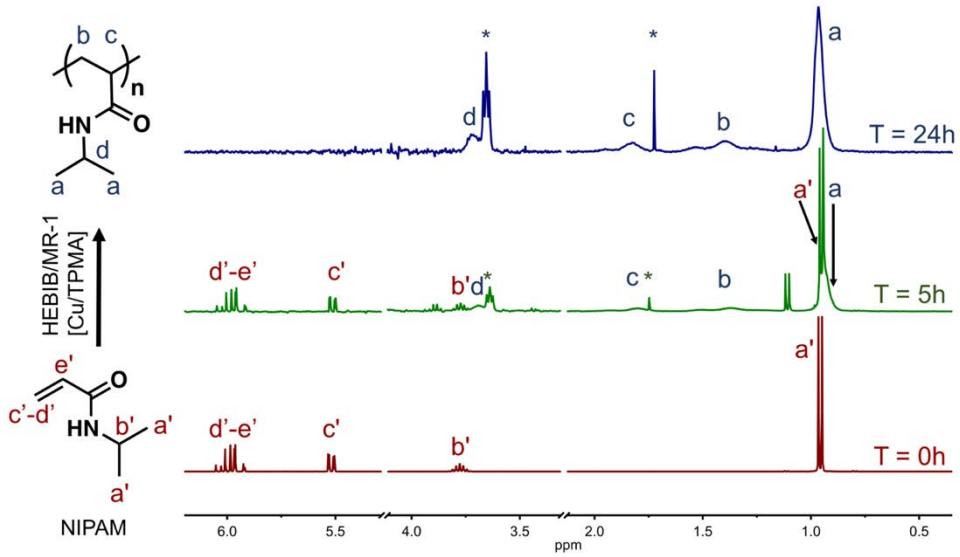

Figure A.31: ^{1}H NMR spectra for the polymerization of NIPAM ([M]/[I]/[Cu/TPMA]=1000/1/0.02, MR-1 initial OD = 0.02, SBM lacking trace mineral mix and supplemented with casamino acids). Residual water peak has been removed for clarity. (Note: T indicates different reaction time. * proton peaks due to the impurities from cell culture medium.)

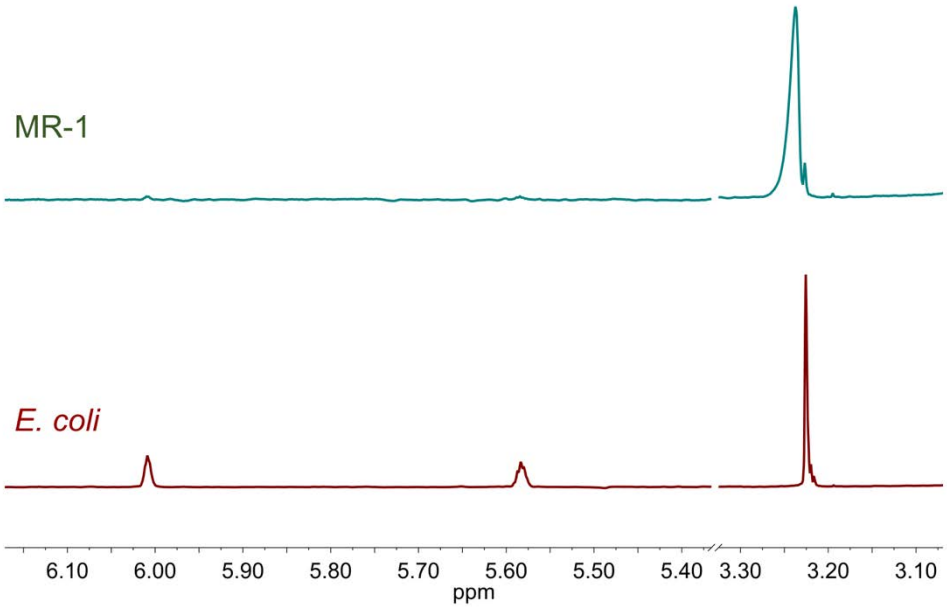

Figure A.32: ^{1}H NMR spectra for the polymerization of OEOMA500 using MR-1 and E. coli, respectively ([M]/[I]/[Cu/TPMA]=1000/1/0.02, Initial OD600 = 0.02, SBM lacking trace mineral mix and supplemented with casamino acids, 2 hours). Residual water peak has been removed for clarity.

APPENDIX B: SUPPLEMENTARY DATA FOR CHAPTER 3

Supplementary Tables for Chapter 3

Strain or plasmid	Description/Genotype	Reference or source
S. oneidensis Strains		
MR-1	MR-1 (ATCC700550), wild-type strain	American-Type Culture Collection
JG749	Lacks outer membrane cytochromes, MtrC and OmcA; Δ*mtrC*Δ*omcA*	86
Δ*hydA*Δ*hyaB*	Lacks periplasmic hydrogenases, HydA and HyaB; Δ*hydA*Δ*hyaB*	Jeffrey Gralnick, U. of Minnesota
BK2	MR-1 with empty pShew, Km^r	293
BK13	JG749 (Δ*mtrC*Δ*omcA*) with empty pShew, Km^r	293
BK14	JG749 (Δ*mtrC*Δ*omcA*) with pShew-mtrC, Km^r	293
BK15	JG749 (Δ*mtrC*Δ*omcA*) with pShew-omcA, Km^r	This Study
E. coli Strains		
MG1655	Wild-type strain	Lydia Contreras, U. of Texas at Austin
Plasmids		
pShew	Empty expression vector carrying *lacI*	293
pShew-mtrC	pShew plasmid carrying *mtrC*, driven by Ptac	293
pShew-omcA	pShew plasmid carrying *omcA*, driven by Ptac	This Study

Table B.1: Bacterial Strains and Plasmids Used in this Study.

Supplementary Figures for Chapter 3

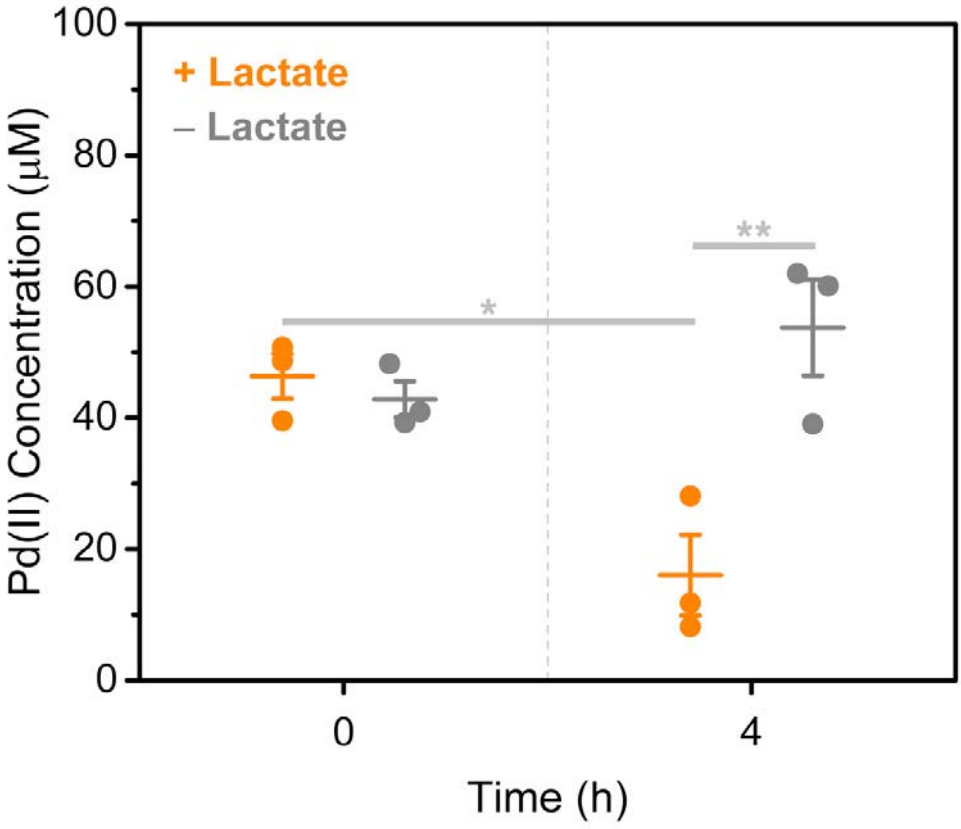

Figure B.1: Effect of lactate on Pd(II) reduction by *S. oneidensis*.

Pd(II) reduction kinetics for *S. oneidensis* MR-1 with and without 20 mM sodium lactate in a 100 μM Pd(II) reaction mixture. Raw data is overlaid on bars representing mean ± S.D. * $p < 0.05$, ** $p < 0.01$, $n = 3$.

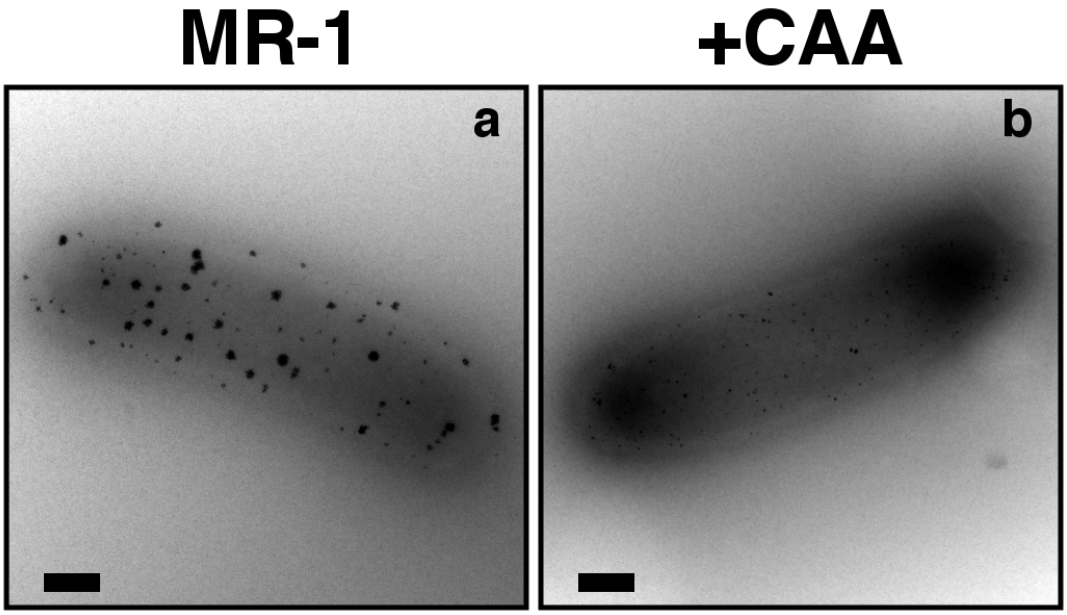

Figure B.2: Effect of casamino acids on Pd nanoparticle formation by *S. oneidensis*.

Whole-mount transmission electron micrographs of *S. oneidensis* (a) MR-1 and (b) MR-1 in the presence of 0.05% casamino acids after 24 hours with 1000 μM Pd(II). Scale bar represent 200 nm.

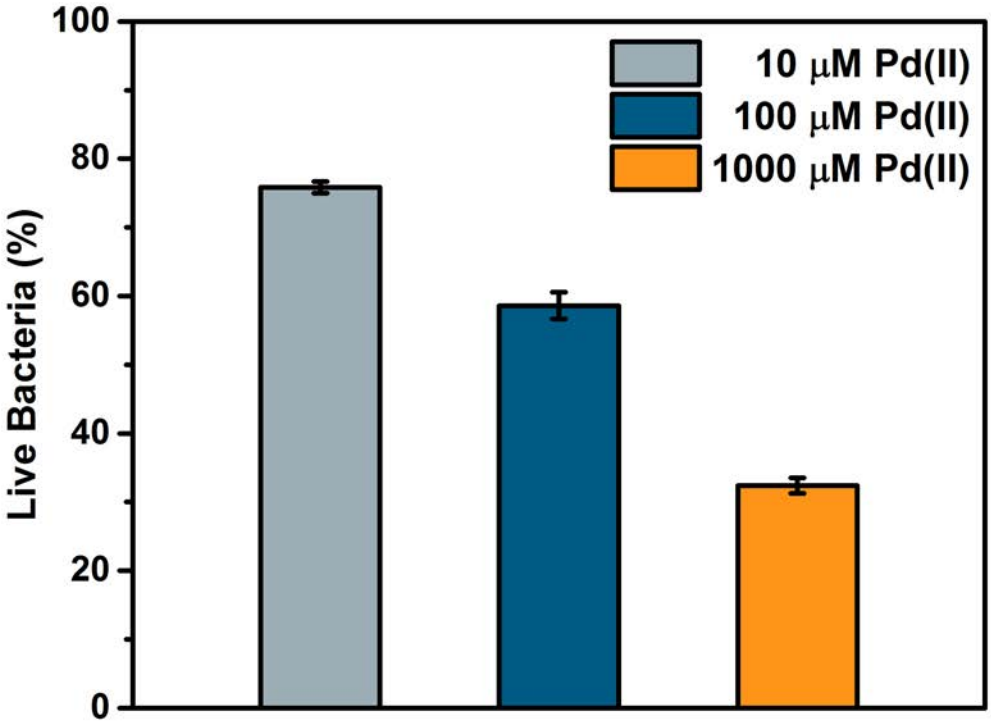

Figure B.3: Effect of Pd(II) concentration on *S. oneidensis* MR-1 viability.

Viability was assessed after 2 hours of Pd(II) reduction. Error bars represent mean ± S.D., n = 3.

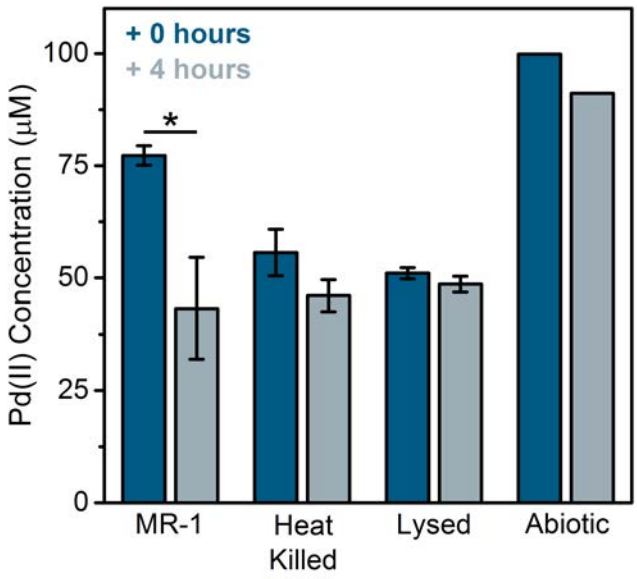

Figure B.4: Bacterial viability affects reduction of 100 μM Pd(II).

Pd(II) levels were quantified for reaction mixtures containing viable MR-1, heat-killed MR-1, sonically lysed MR-1, or no cells. Histogram bars represent the mean ± S.D. * $p < 0.05$, $n = 3$.

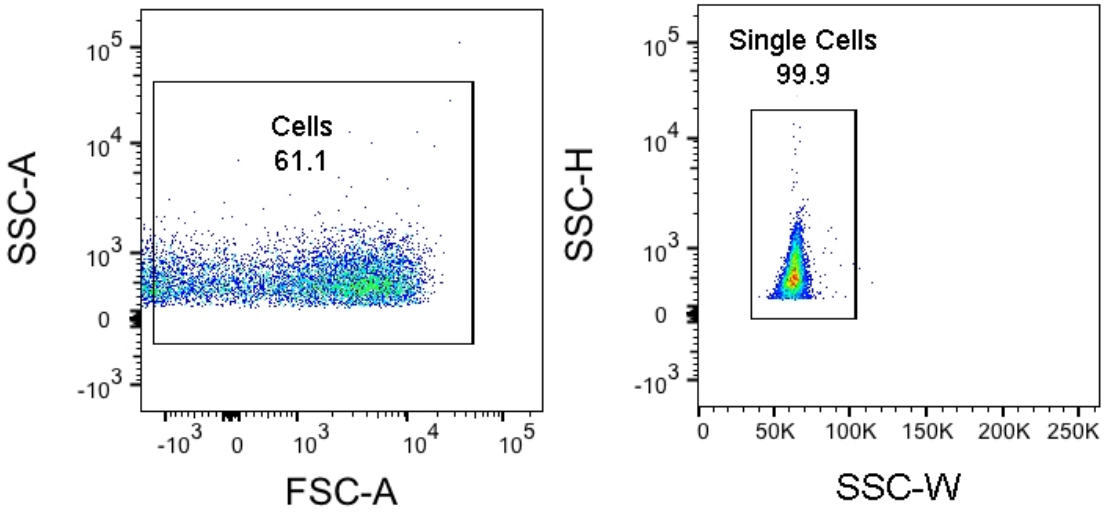

Figure B.5: Representative gating scheme for flow cytometric analyses of *S. oneidensis*.

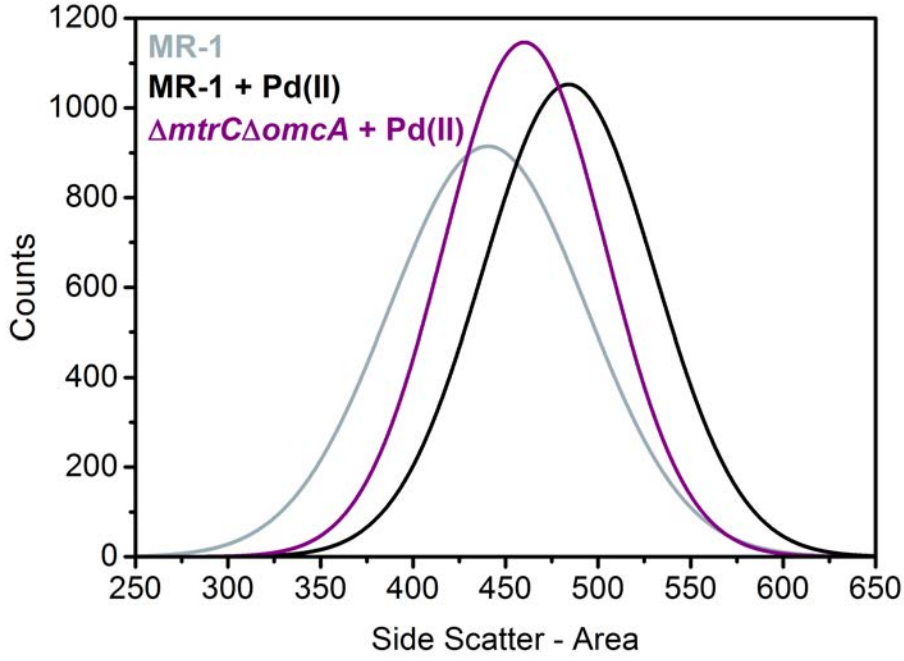

Figure B.6: Flow cytometry side scatter signal for Pd-free MR-1 and MR-1/Δ*mtrC*Δ*omcA* after 2 hours of reaction with 100 μM Pd(II).

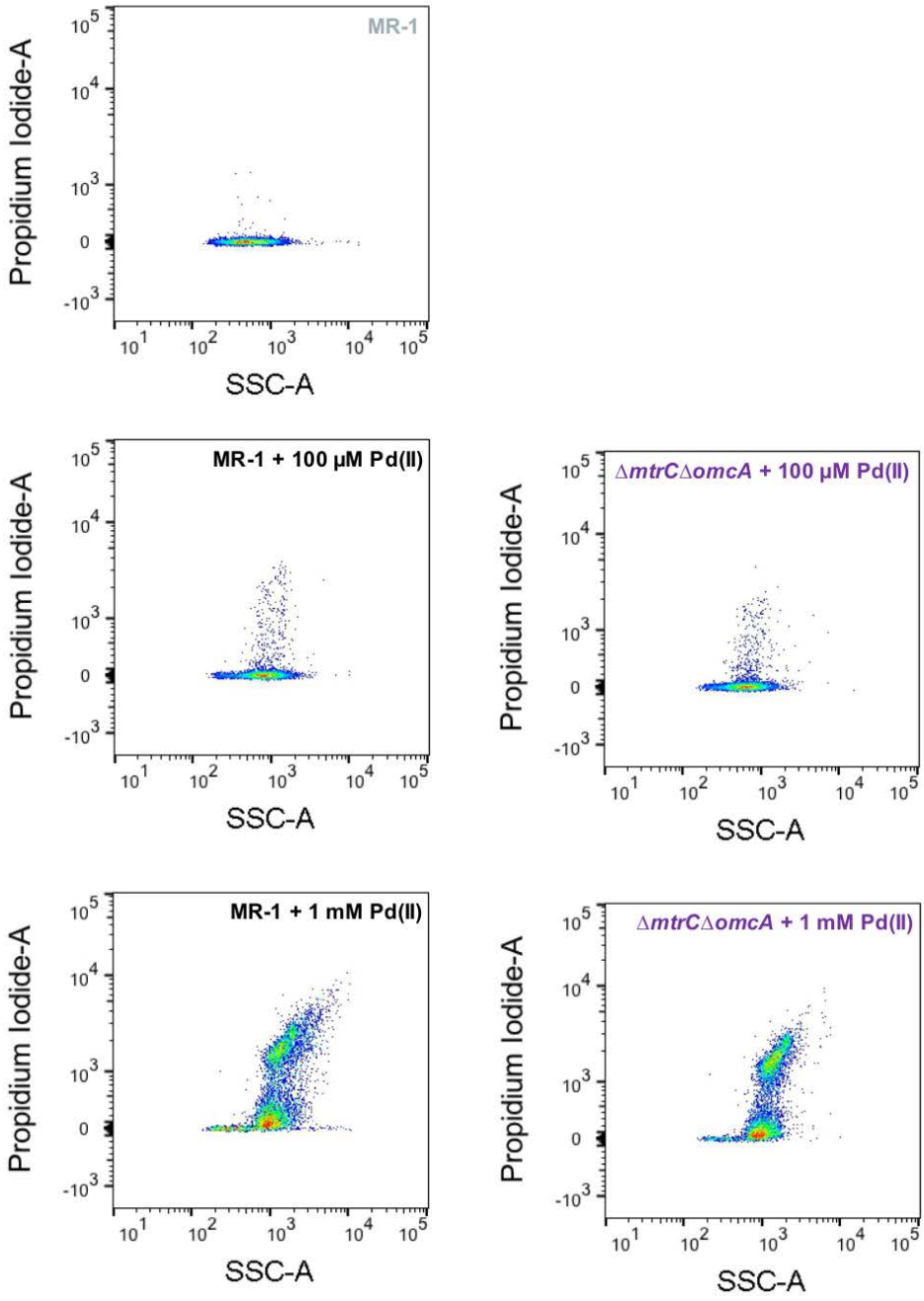

Figure B.7: Simultaneous quantification of palladization and cell death for *S. oneidensis* MR-1 and Δ*mtrC*Δ*omcA* using flow cytometry.

Increased side scatter (SSC-A), relative to Pd-free samples, was used to detect bacterial palladizaton. Dead cells with compromised membranes fluoresced upon staining with the membrane impermeable dye, propidium iodide.

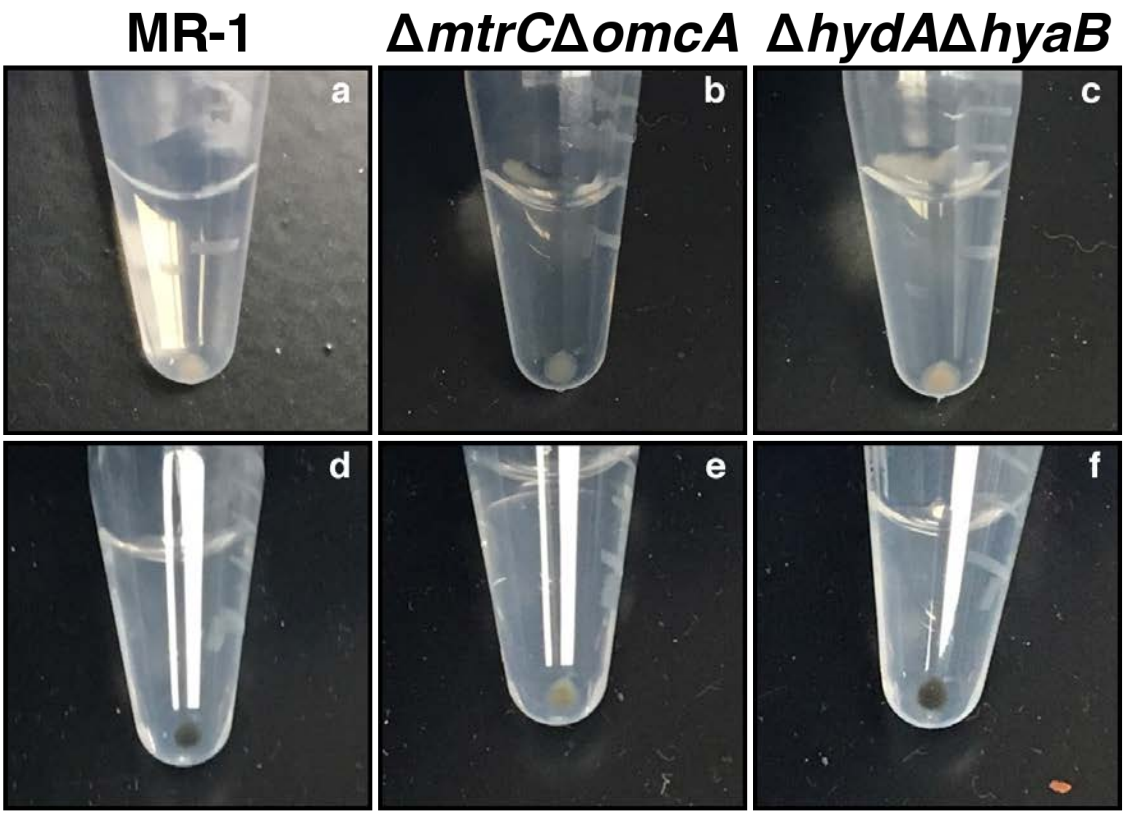

Figure B.8: Color change of *S. oneidensis* cell pellet after Pd(II) reduction.

Cell pellet of (a) MR-1, (b) Δ*mtrC*Δ*omcA*, and (c) Δ*hydA*Δ*hyaB* from spun-down aliquots taken immediately after inoculation of each reaction mixture. Cell pellets of (d) MR-1, (e) Δ*mtrC*Δ*omcA*, and (f) Δ*hydA*Δ*hyaB* of spun-down aliquots taken 4 hours after inoculation. Reactions occurred with 100 μM Pd(II).

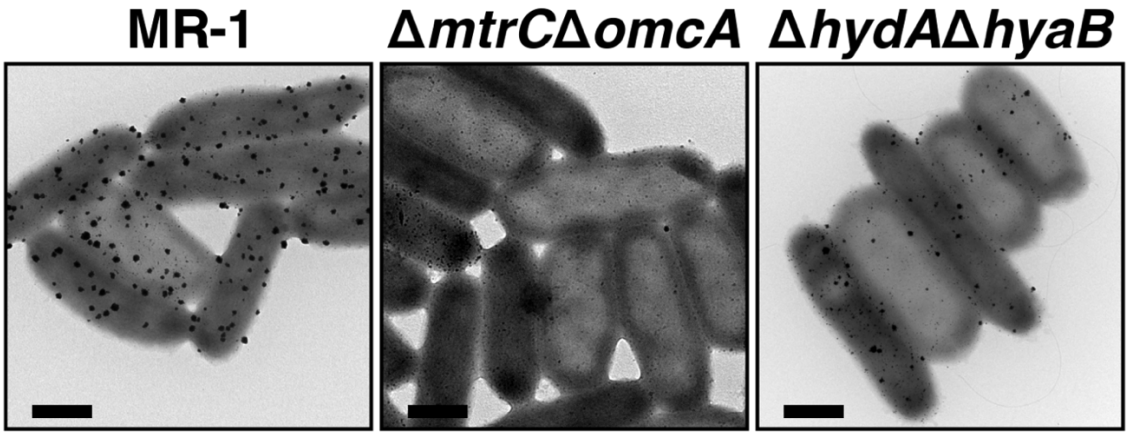

Figure B.9: Effect of *S. oneidensis* genotype on Pd nanoparticle formation.

Whole-mount transmission electron micrographs of *S. oneidensis* MR-1, Δ*mtrC*Δ*omcA*, and Δ*hydA*Δ*hyaB* after 2 hours with 100 μM Pd(II). Scale bars represent 500 nm.

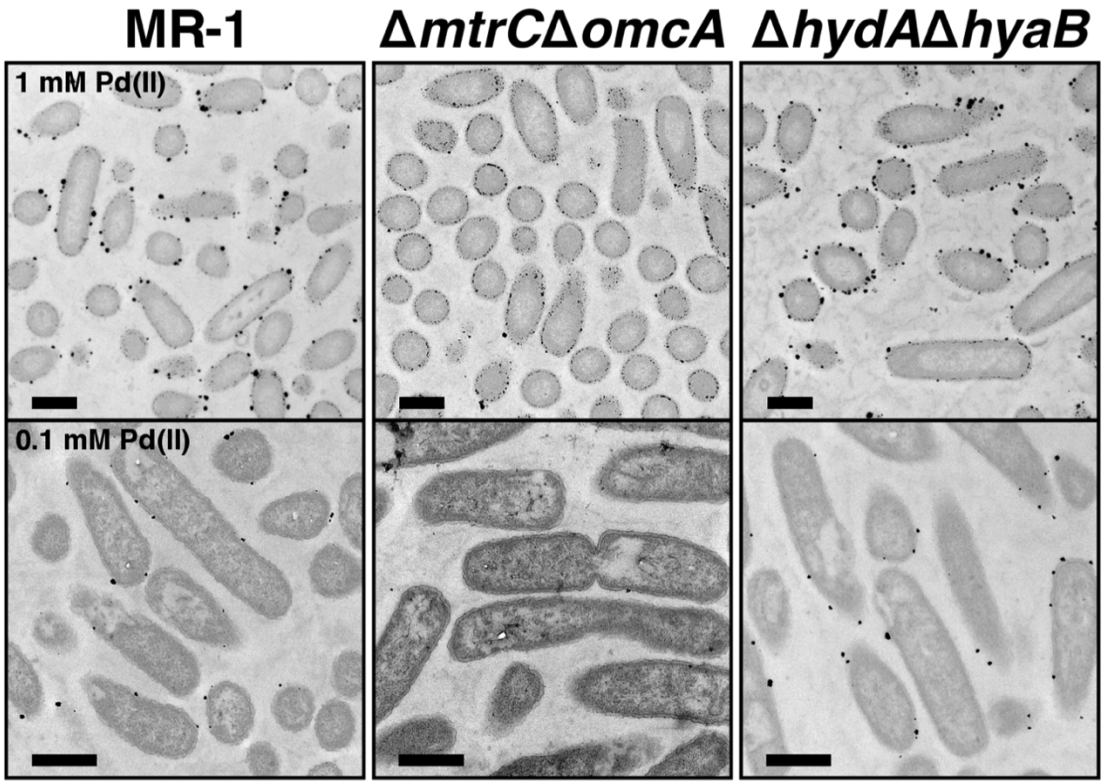

Figure B.10: Effect of *S. oneidensis* genotype on Pd nanoparticle localization.

Wide-view thin section transmission electron micrographs of *S. oneidensis* strains. Top panel images are *S. oneidensis* strains after 24 hours with 1000 μM Pd(II). Bottom panel images are *S. oneidensis* strains after 2 hours with 100 μM Pd(II). Scale bars represent 500 nm.

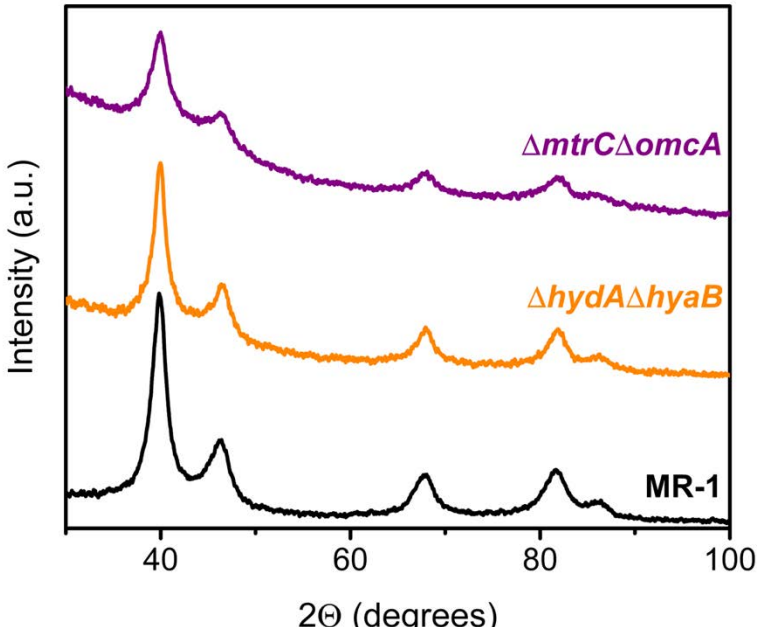

Figure B.11: Effect of *S. oneidensis* genotype on Pd nanoparticle powder x-Ray diffraction patterns. Data was normalized to the most intense peak height.

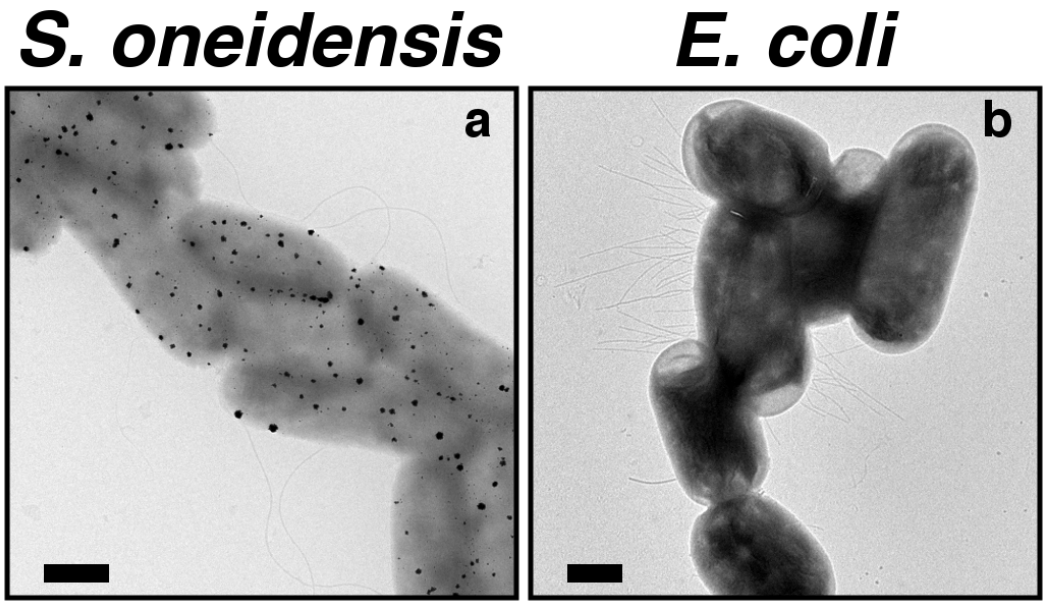

Figure B.12: Effect of 100 μM Pd(II) on (a) *S. oneidensis* MR-1 and (b) *E. coli* MG1655 after 4 hours. Scale bars represent 500 nm.

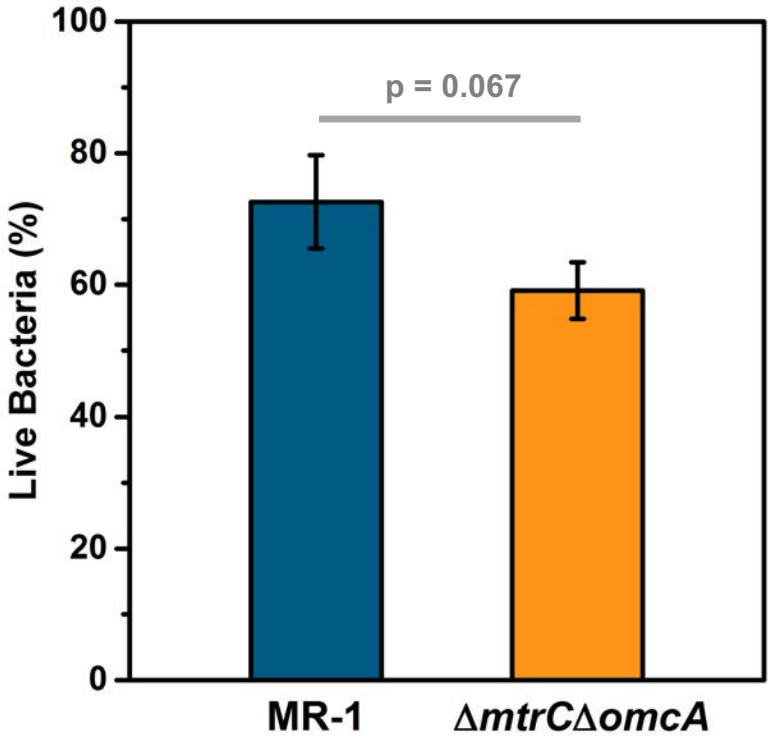

Figure B.13: Effect of *S. oneidensis* genotype on viability during Pd(II) reduction.

Viability was assessed after 2 hours with 100 μM Pd(II). Error bars represent mean ± S.D, n = 3.

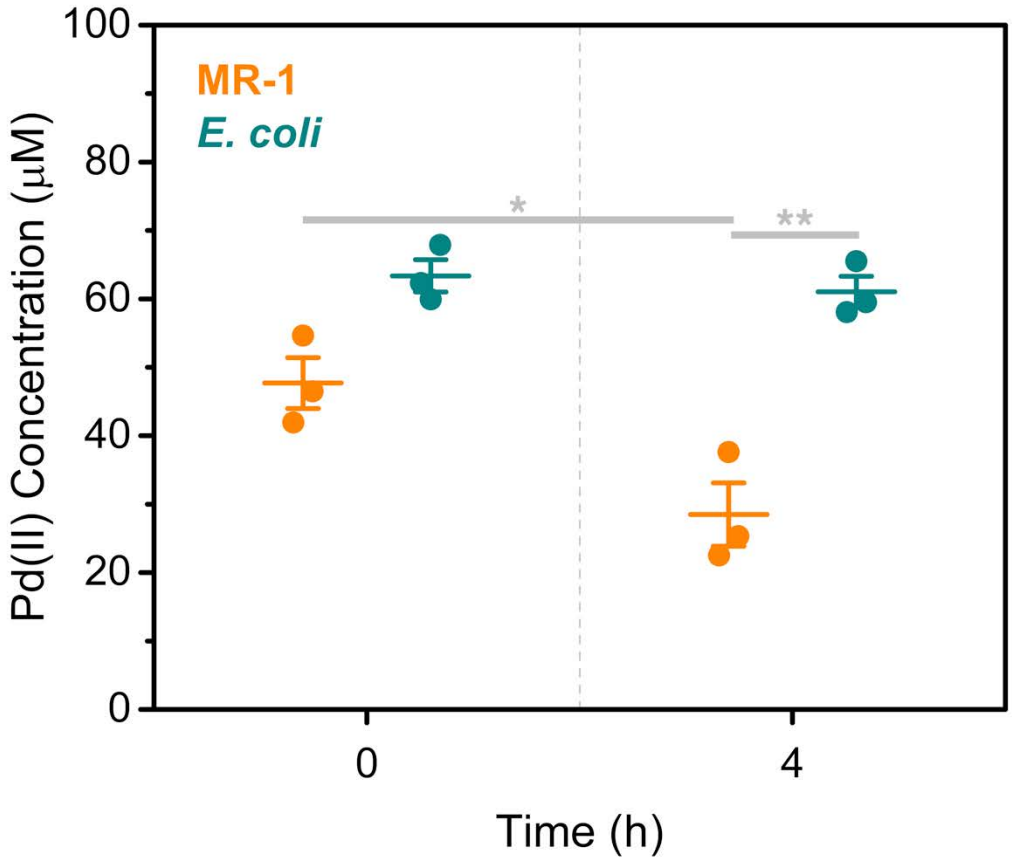

Figure B.14: Pd(II) reduction by *S. oneidensis* MR-1 and *E. coli* MG1655 after 4 hours. Raw data is overlaid on bars representing mean ± S.D. * $p < 0.05$, ** $p < 0.01$, $n = 3$.

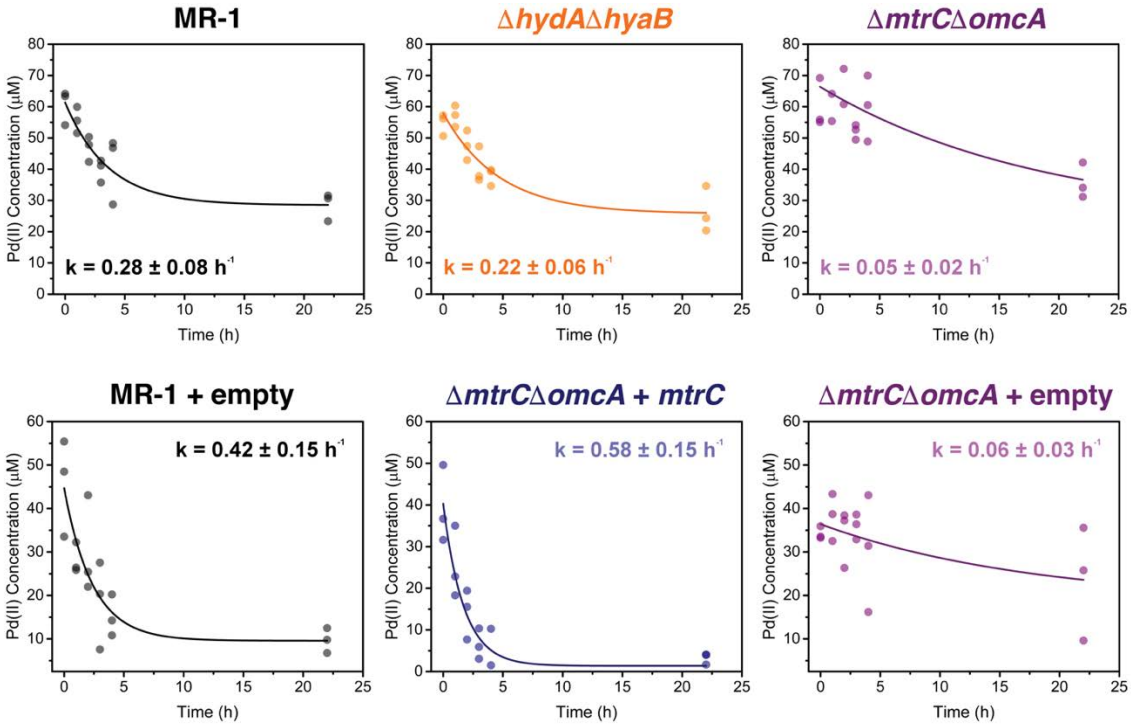

Figure B.15: Pd(II) reduction kinetics fitting for knockout and complemented knockout *S. oneidensis* strains.

Data was concatenated from 3 kinetic runs and fit to $[Pd(II)]_{time = t} = Ae^{-kt} + B$. Rate constants are reported as the best fit value ± fitting error.

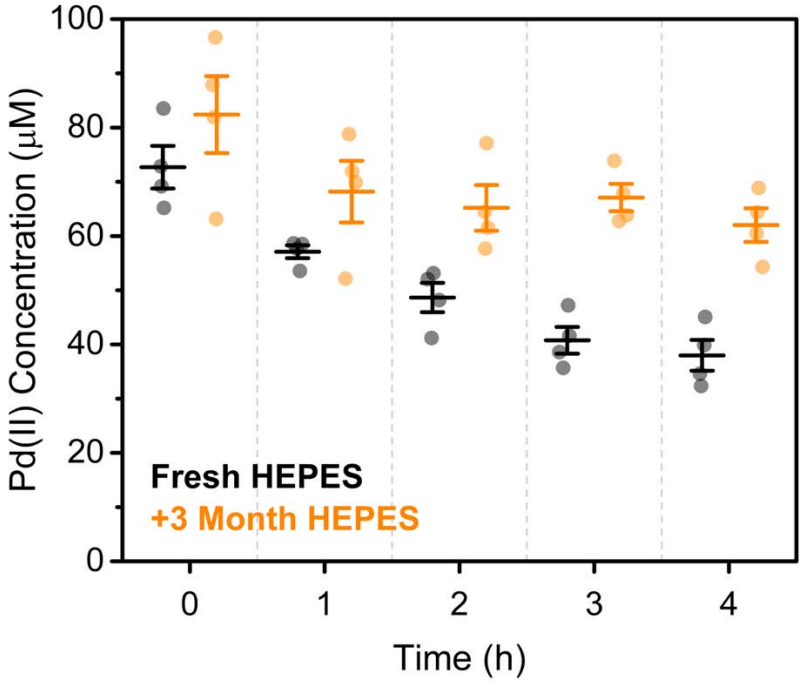

Figure B.16: HEPES buffer age affects Pd(II) reduction rate by *S. oneidensis* MR-1. Raw data is overlaid on bars representing mean ± S.D., n = 4.

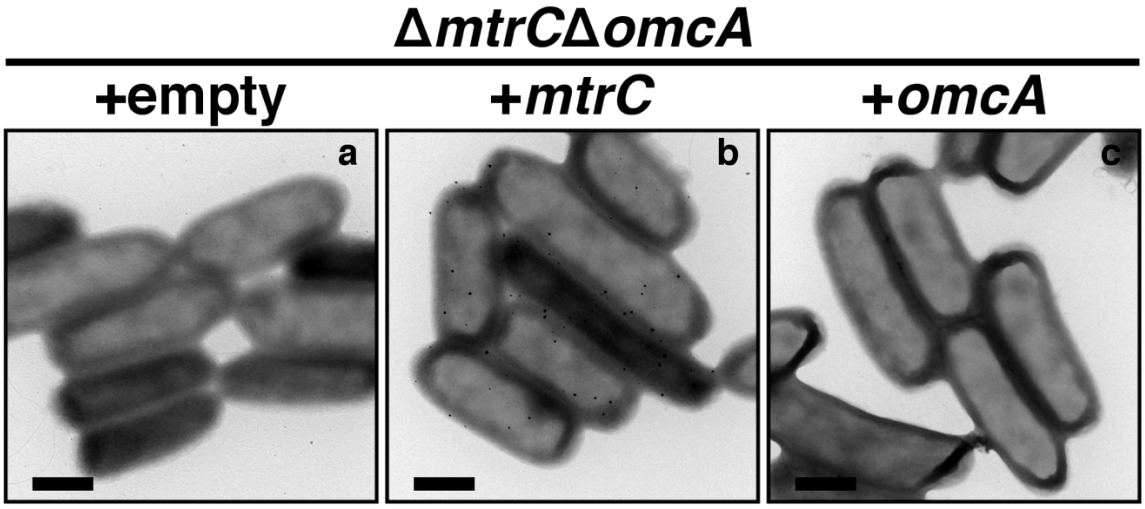

Figure B.17: Effect of outer membrane cytochrome complementation on Pd nanoparticle formation.

Whole mount transmission electron micrographs of *S. oneidensis* Δ*mtrC*Δ*omcA* complemented with an (a) empty, (b) *mtrC,* or (c) *omcA* expression vector. Scale bars represent 500 nm.

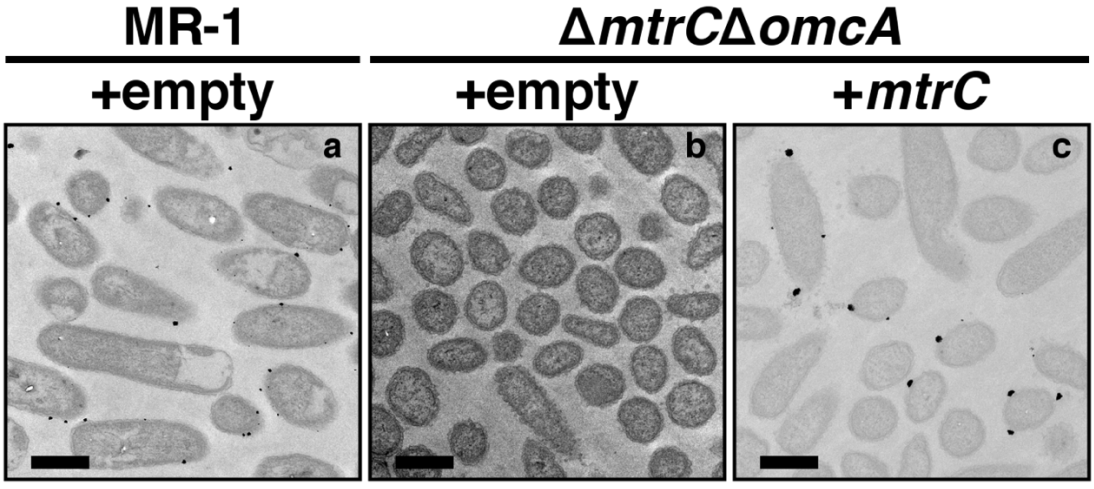

Figure B.18: Effect of MtrC expression on Pd nanoparticle localization by *S. oneidensis*.

Wide-view thin-section transmission electron micrographs of (a) MR-1 with an empty vector and Δ*mtrC*Δ*omcA* with an (b) empty vector or (c) *mtrC* vector after 2 hours with 100 μM Pd(II). Scale bars represent 100 nm.

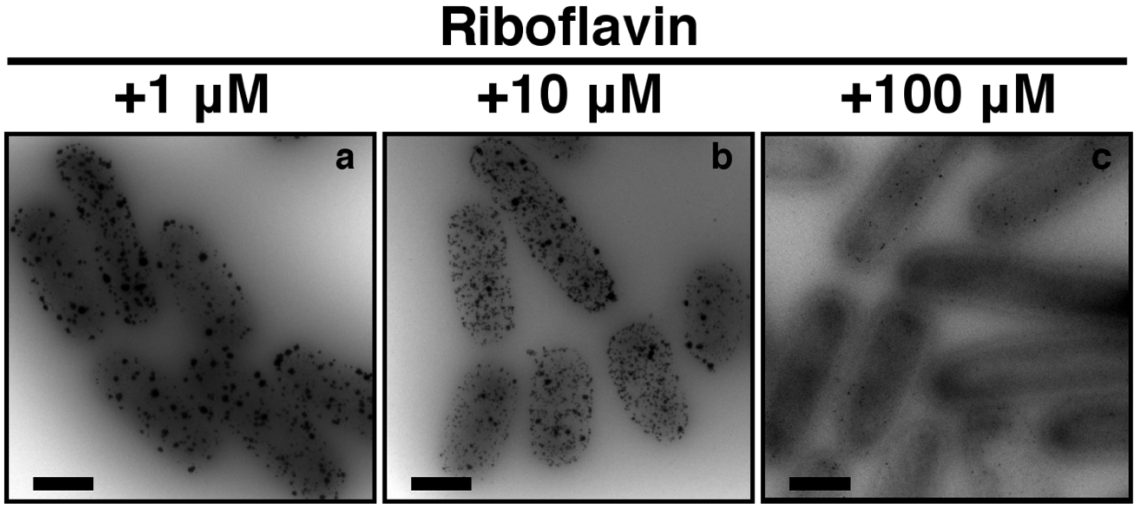

Figure B.19: Effect of increasing riboflavin concentration on Pd nanoparticle formation by *S. oneidensis* MR-1.

Whole mount transmission electron micrographs of *S. oneidensis* MR-1 supplemented with (a) 1 µM, (b) 10 µM, and (c) 100 µM riboflavin after 24 hours with 1000 µM Pd(II). Scale bars represent 500 nm.

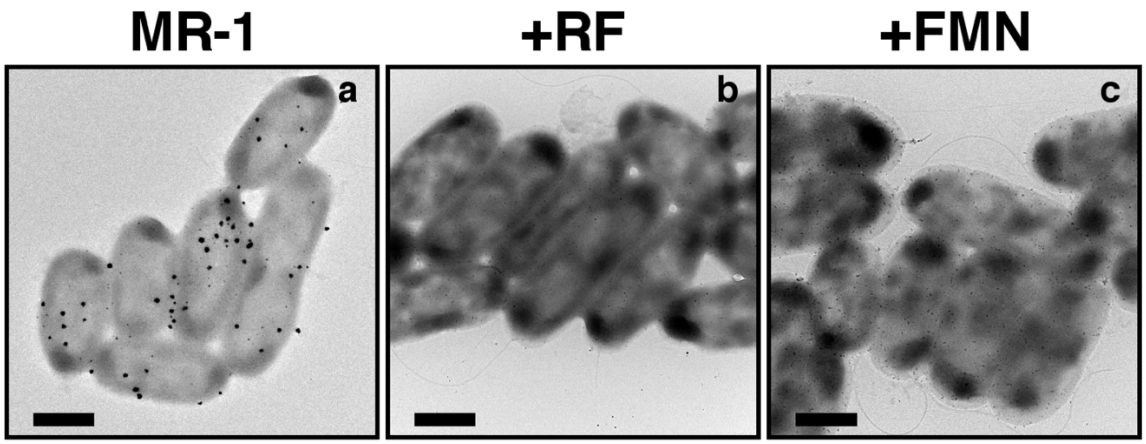

Figure B.20: Effect of supplemented riboflavin and flavin mononucleotide on Pd nanoparticle formation by *S. oneidensis* MR-1.

Whole mount transmission electron micrographs of (a) unsupplemented MR-1 and MR-1 supplemented with (b) 100 µM riboflavin (RF) or (c) 100 µM flavin mononucleotide after 2 hours with 100 µM Pd(II). Scale bars represent 500 nm.

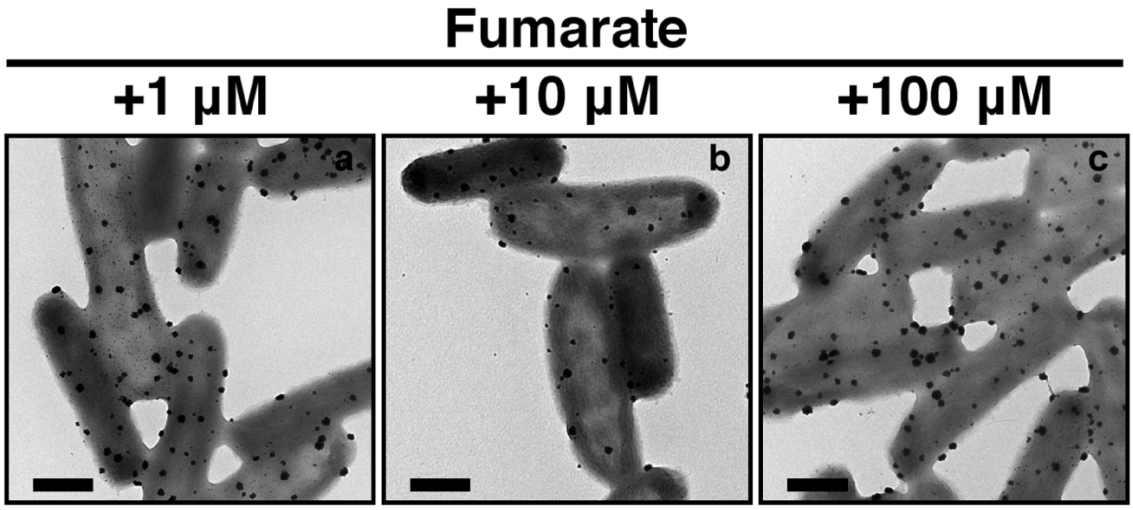

Figure B.21: Effect of increasing sodium fumarate concentration on Pd nanoparticle formation by *S. oneidensis* MR-1.

Whole mount transmission electron micrographs of *S. oneidensis* MR-1 supplemented with (a) 1 µM, (b) 10 µM, and (c) 100 µM sodium fumarate after 24 hours with 1000 µM Pd(II). Scale bars represent 500 nm.

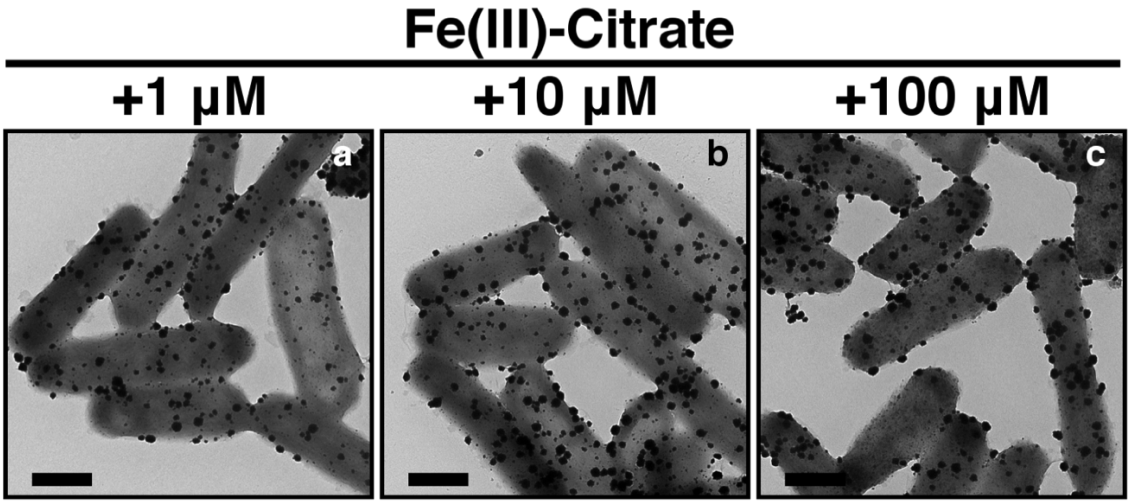

Figure B.22: Effect of Increasing Fe(III)-Citrate Concentration on Pd Nanoparticle Formation by *S. oneidensis* MR-1.

Whole mount transmission electron micrographs of *S. oneidensis* MR-1 supplemented with (a) 1 µM, (b) 10 µM, and (c) 100 µM Fe(III)-citrate after 24 hours with 1000 µM Pd(II). Scale bars represent 500 nm.

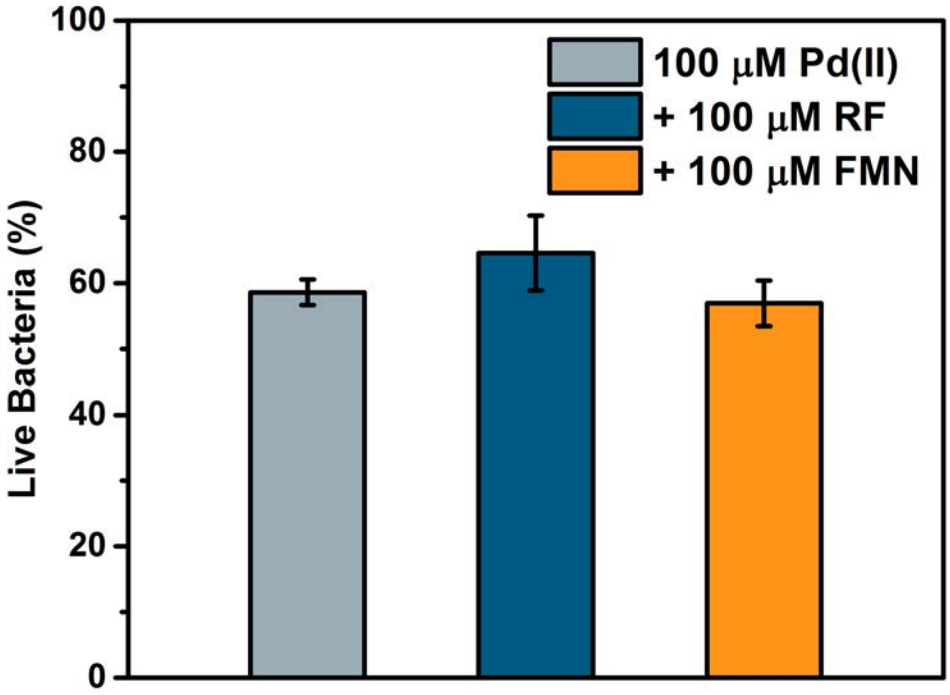

Figure B.23: Effect of flavin supplementation on *S. oneidenis* viability during Pd(II) reduction.

Viability was assessed after 2 hours of Pd(II) reduction without flavins or in the presence of 100 μM riboflavin (RF) or 100 μM flavin mononucleotide (FMN). Error bars represent mean ± S.D, n = 3.

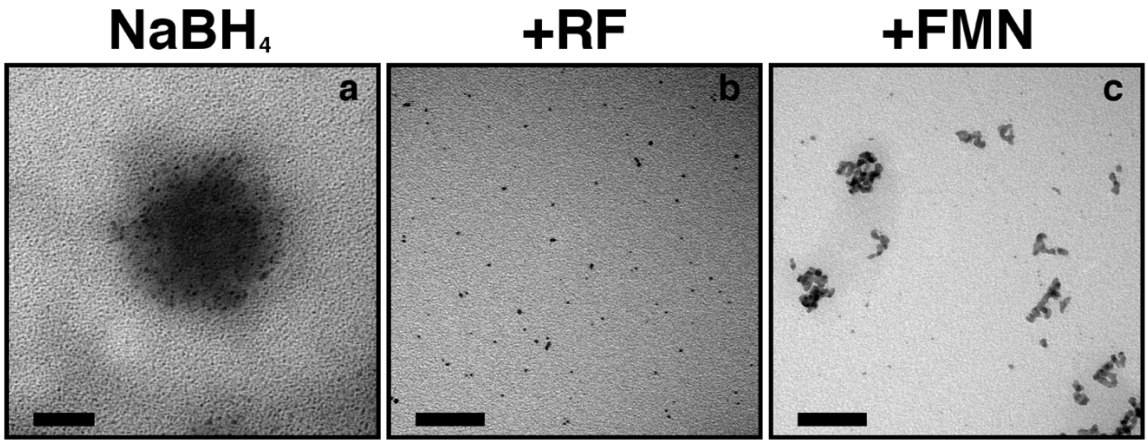

Figure B.24: Effect of flavins on abiotic Pd nanoparticle formation.

(a) Abiotic Pd nanoparticle synthesis with 100 μM Pd(II) and 2 mM $NaBH_4$ in water. Flavin-supplemented reactions also contained (b) 100 μM riboflavin (RF) or (c) 100 μM flavin mononucleotide (FMN). Scale bars represent 50 nm.

APPENDIX C: SUPPLEMENTARY DATA FOR CHAPTER 4

Supplementary Tables for Chapter 4

Cycle Number	Culture Volume (µL)	Volume of 500 mM Cr(VI) Added (µL)	Cr(VI) Removed (mg g^{-1}) Biotic MIL-100	Cr(VI) Removed (mg g^{-1}) Biotic Ferrihydrite
1	1960	1.96	7.61 ± 0.09	3.28 ± 1.07
2	1842	1.84	15.49 ± 0.09	5.96 ± 1.25
3	1724	1.72	23.52 ± 0.09	4.59 ± 2.20
4	1606	1.61	31.40 ± 0.09	5.00 ± 1.48
5	1487	1.49	39.23 ± 0.09	4.25 ± 1.34
6	1369	1.37	47.26 ± 0.00	1.37 ± 2.08
7	1250	1.25	55.09 ± 0.09	5.55 ± 0.62
8	1131	1.13	62.97 ± 0.09	2.74 ± 2.25
9	1012	1.01	70.85 ± 0.09	5.21 ± 3.29
10	893	0.89	78.67 ± 0.09	5.14 ± 2.56

Table C.1: Cr(VI) cycles.

Material	Cr(VI) Capacity ($mg\ g^{-1}$)	Process	Reference
Humic Acid Coated Magnetite Nanoparticles	3.37	Fe Oxidation	[491]
Bio amended Fe^0	6.2	Fe Oxidation	[492]
Ferrihydrite	12.97	Fe Oxidation	[493]
FIR-53	17.8	Anion Exchange	[331]
UV Modified Corn Straw	20.04	-OH, $-CO_3$, -COOH Complexation	[494]
***Geobacter sulfurreducens*-Reduced Chlorite (+AQDS)**	20.8	Fe Oxidation	[328]
Sulfamate-Bacterial Cellulose	22.73	$-NH_3$ and $–OH_2$ Reactions	[495]
Living *Bacillus coagulans* Biomass	23.8	Biosorption	[496]
Wheat Straw Biochar	24.6	Surface Reduction	[497]
FIR-54	24.7	Anion Exchange	[331]
Aluminum Substituted Ferrihydrite	39.79	Fe Oxidation	[493]
Dead *B. coagulans* Biomass	39.9	Biosorption	[496]
ABT·$2ClO_4$	65	Anion Exchange	[329]
MONT-1	55.2	Anion Exchange	[329]
HCl Modified Willow Residue+Fe(III)	113.64	Adsorption	[498]
Wheat Straw +FeS	150	Adsorption/Fe Oxidation	[499]
HCl Modified Willow Residue	217.39	Adsorption	[498]
Zn-MOF-74	750	Fe(II) Surface Enhancement	[332]
UTSA-74	796	Fe(II) Surface Enhancement	[332]

Table C.2: Cr(VI) removal by both biotic and abiotic agents.

Material	Measured Langmuir Surface Area (m^2g^{-1})	Reported BET Surface Area (m^2g^{-1})	Reference
MIL-100	2188 ± 25	1974	[316]
Fe-BTC	1512 ± 92	1092	[317]
MIL-88A	130 ± 3	25	[318]

Table C.3: Metal-organic framework surface areas.

Supplementary Figures for Chapter 4

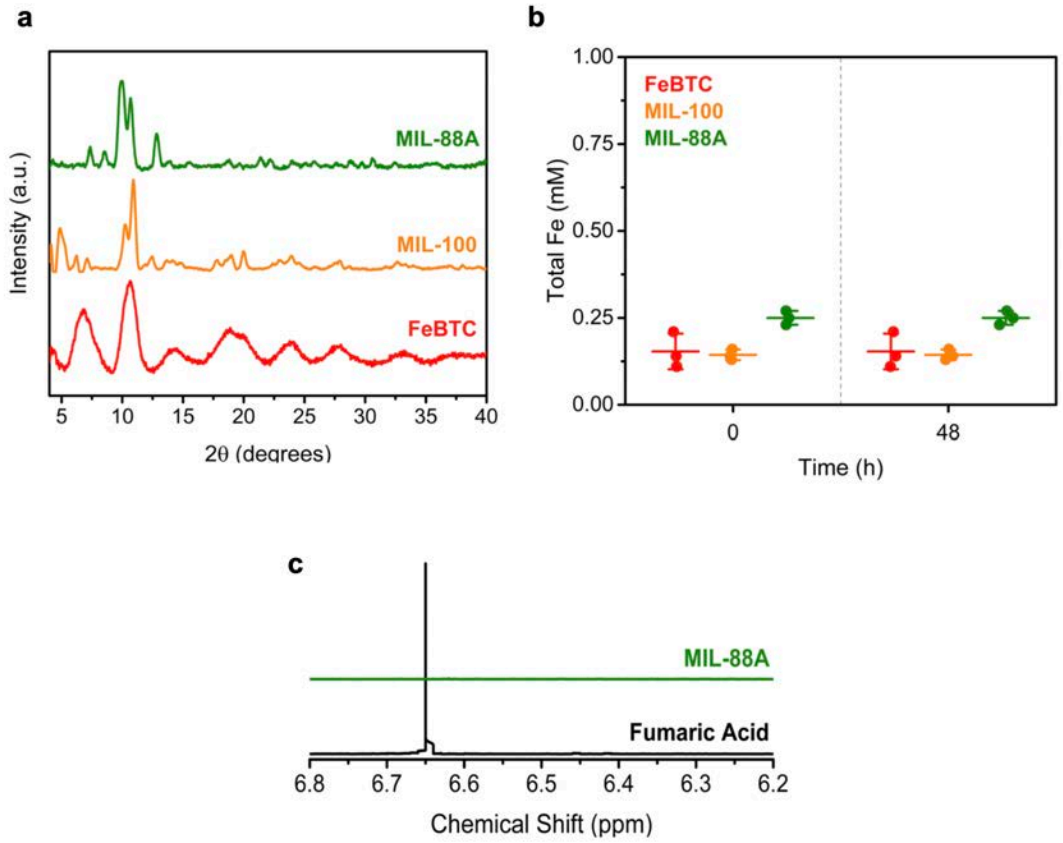

Figure C.1: Stability of metal-organic frameworks.

(a) PXRD spectra of Fe-BTC, MIL-100, and MIL-88A after exposure to standard culture conditions for 48 h (SBM, 20 mM lactate 30 ºC). (b) [Fe(III)] in the supernatant of Fe-BTC, MIL-100, and MIL-88A after 48 h. (c) ^{1}H NMR of the MIL-88A supernatant after 48 h and a 1 mg/mL fumaric acid standard (limit of detection: 18.6 μM).

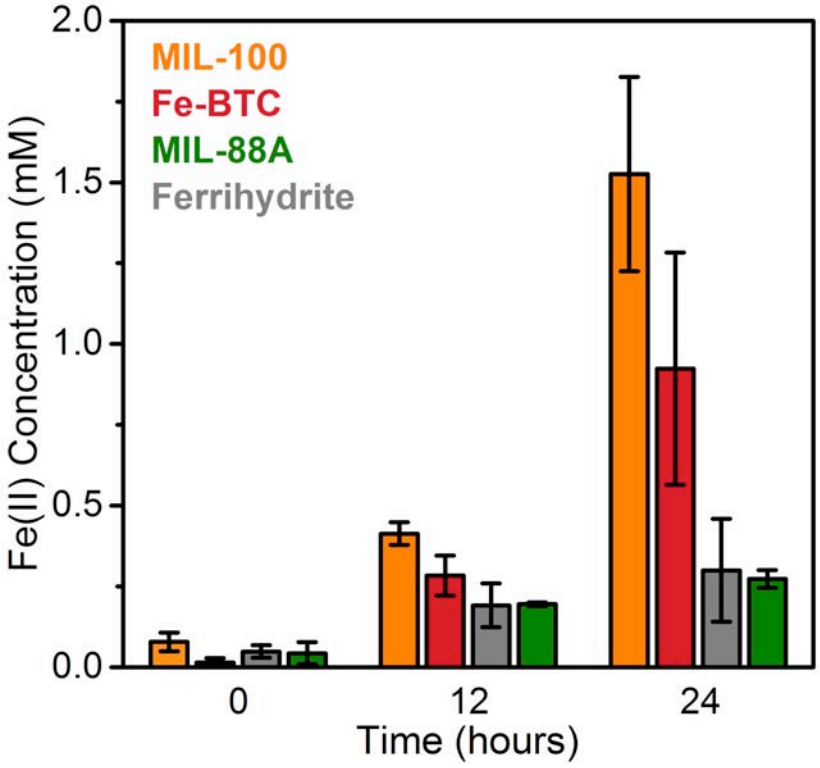

Figure C.2: Concomitant Fe(III) reduction with CFU counts.

Fe(II) concentrations of cultures of *S. oneidensis* MR-1 (inoculating OD_{600}=0.002) in SBM with 20 mM lactate and either MIL-100, Fe-BTC, MIL-88A, or ferrihydrite. Data show mean ± S.D. for three independent biological replicates. These data were collected concomitantly with growth (as measured by CFU) shown in Figure 4.2a.

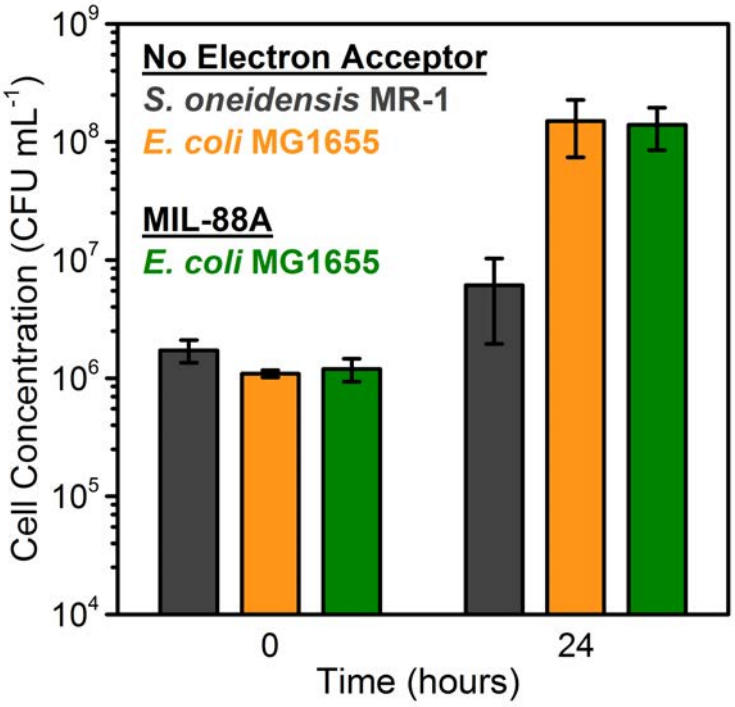

Figure C.3: Growth on MIL-88A.

CFU counts of *S. oneidensis* MR-1 and *E. coli* MG1655 with no electron acceptor present (only SBM and lactate), as well as MG1655 with MIL-88A as an electron acceptor. The initial inoculating OD_{600}=0.002. Data show mean ± S.E. for three independent biological replicates.

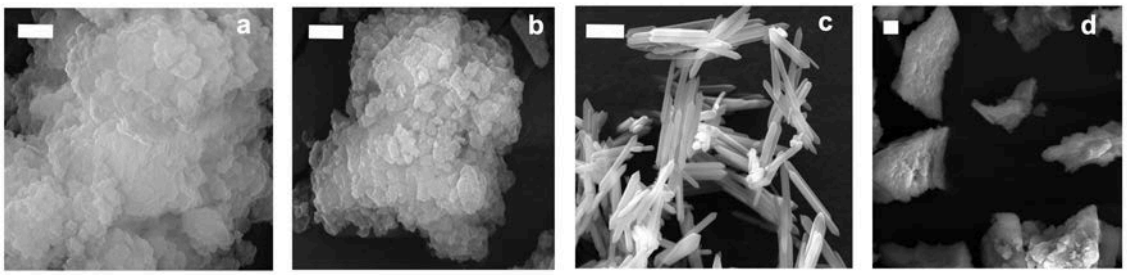

Figure C.4: Morphology of metal-organic frameworks and ferrihydrite.

SEM images of (a) MIL-100, (b) Fe-BTC, (c) MIL-88A, and (d) ferrihydrite, as synthesized. Scale bars are 2 μm.

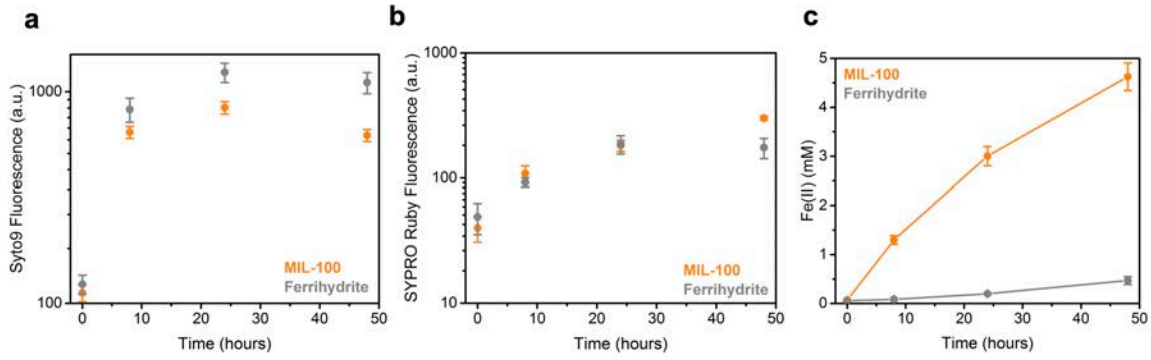

Figure C.5: Nucleic acid and biofilm matrix protein quantification.

(a) Measure of nucleic acids (Syto™ 9) for *S. oneidensis* MR-1 (inoculating OD_{600}=0.02) grown on MIL-100 and ferrihydrite over 48 h. Data show mean ± S.E. for four independent biological replicates. (b) Measure of biofilm matrix proteins (SYPRO™ Ruby) for *S. oneidensis* MR-1 (inoculated OD_{600}=0.02) grown on MIL-100 and ferrihydrite over 48 h. (c) Fe(III) reduction by MR-1 grown on MIL-100 and ferrihydrite over 48 h, measured in parallel with Syto™ 9 and SYPRO™ Ruby. The initial inoculating OD_{600}=0.02. Data show mean ± S.D. for four independent biological replicates.

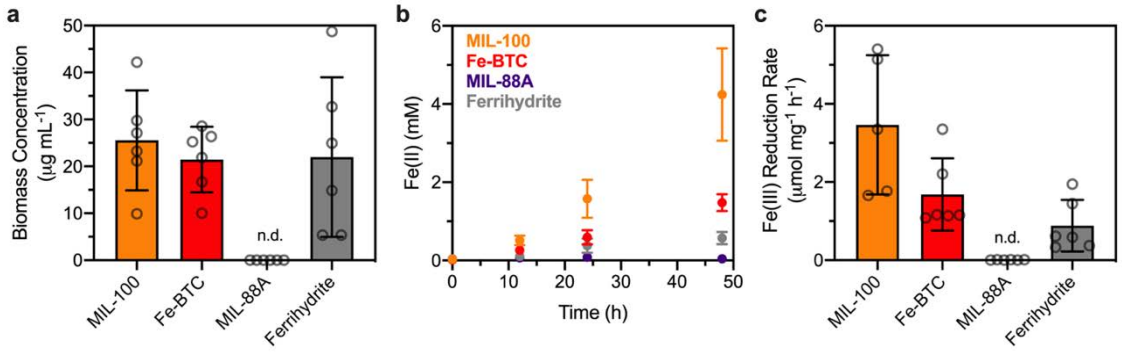

Figure C.6: Normalized Fe(III) reduction rates after 48 h.

(a) Total protein concentrations of *S. oneidensis* MR-1 (inoculating OD_{600}=0.002) grown on MIL-100, Fe-BTC, MIL-88A, and ferrihydrite after 48 h. Data shown are mean ± S.D. for six independent replicates. (b) Total Fe(II) concentrations in suspensions containing *S. oneidensis* MR-1 (inoculating OD_{600}=0.002) and either MIL-100, Fe-BTC, MIL-88A, or ferrihydrite over 48 h. Data shown are mean ± S.D. for six independent replicates. (c) Total protein normalized Fe(III) reduction rates for *S. oneidensis* MR-1 grown on MIL-100, Fe-BTC, MIL-88A, and ferrihydrite at 48 h. "n.d." indicates the rate could not be determined due to lack of detectable biomass. Data shown are mean ± S.D. for at least 5 independent replicates.

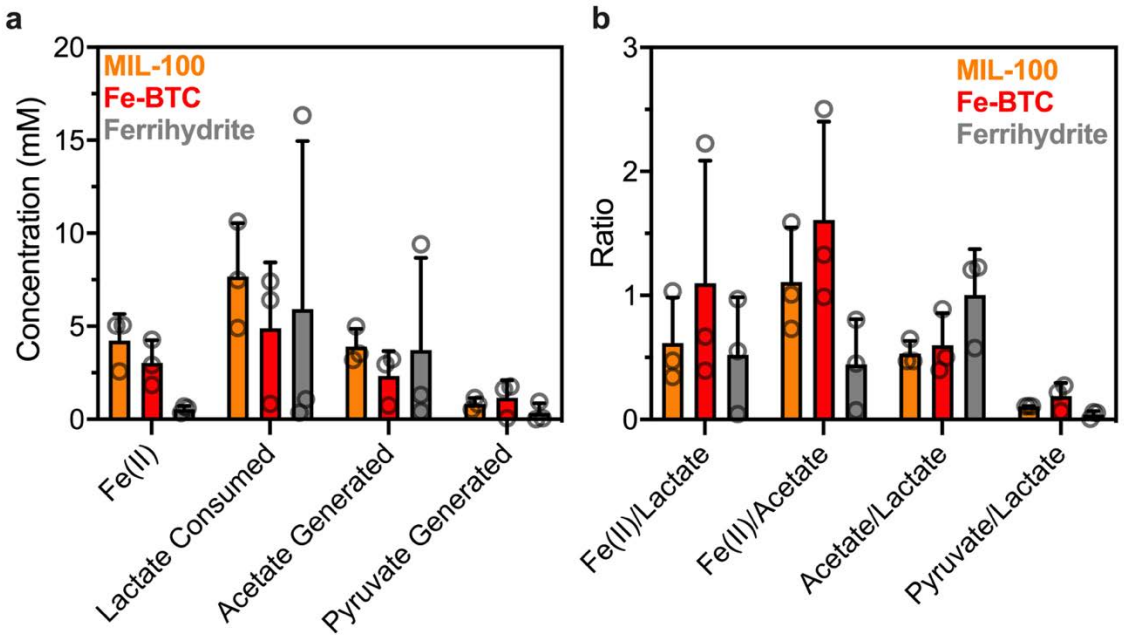

Figure C.7: Metabolite quantification.

(a) Concentrations of Fe(II), lactate consumed, acetate generated and pyruvate generated in *S. oneidensis* MR-1 cultures after 48 hours (inoculating OD_{600}=0.002) and MIL-100, Fe-BTC, or ferrihydrite. Data shown are mean + S.D. for three independent replicates. (b) The ratios of utilized and generated metabolites within replicates. Data shown are mean + S.D. for three independent replicates.

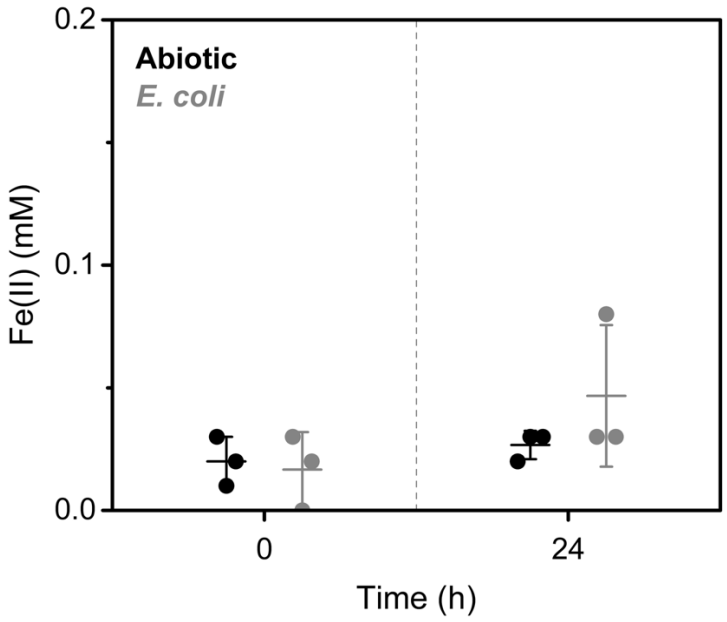

Figure C.8: *E. coli* reduction of MIL-100.

Reduction of Fe(III) by *E. coli* (inoculating OD_{600}=0.002) when cultured with MIL-100 ($[Fe(III)]_0$=15 mM) and 20 mM lactate in SBM.

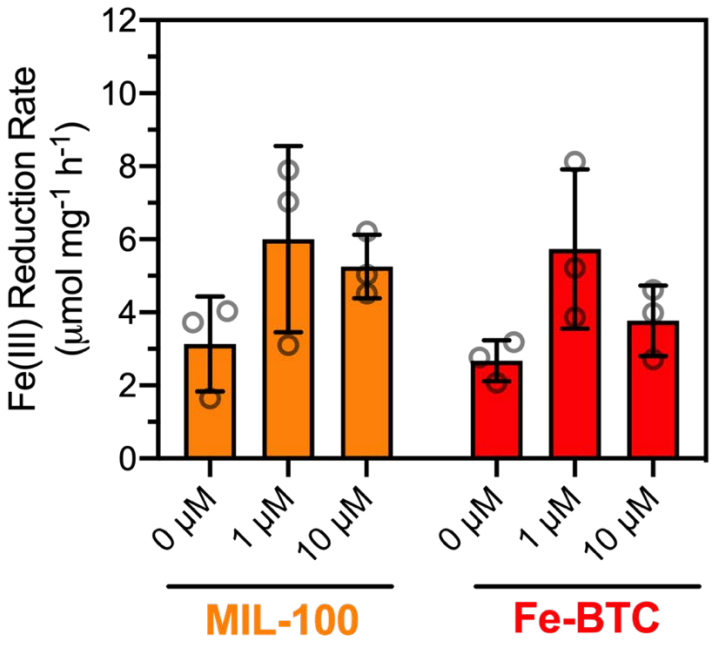

Figure C.9: Normalized Fe(III) reduction rate with exogenous riboflavin.

Total protein normalized Fe(III) reduction of MIL-100 and Fe-BTC by *S. oneidensis* MR-1 with 0 μM, 1 μM, and 10 μM exogenous riboflavin. Data show mean ± S.D. for three independent experiments.

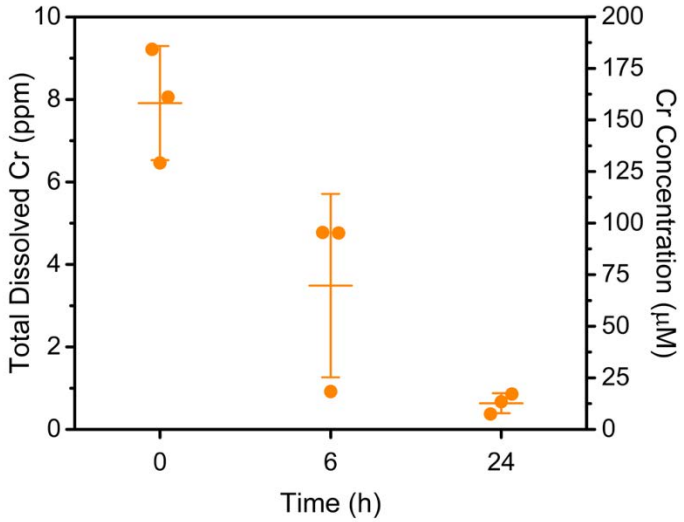

Figure C.10: Total Cr removal.

Total Cr, as measured by ICP-MS, in the supernatant of MR-1 reduced MIL-100 after a challenge with 0.5 mM Cr(VI).

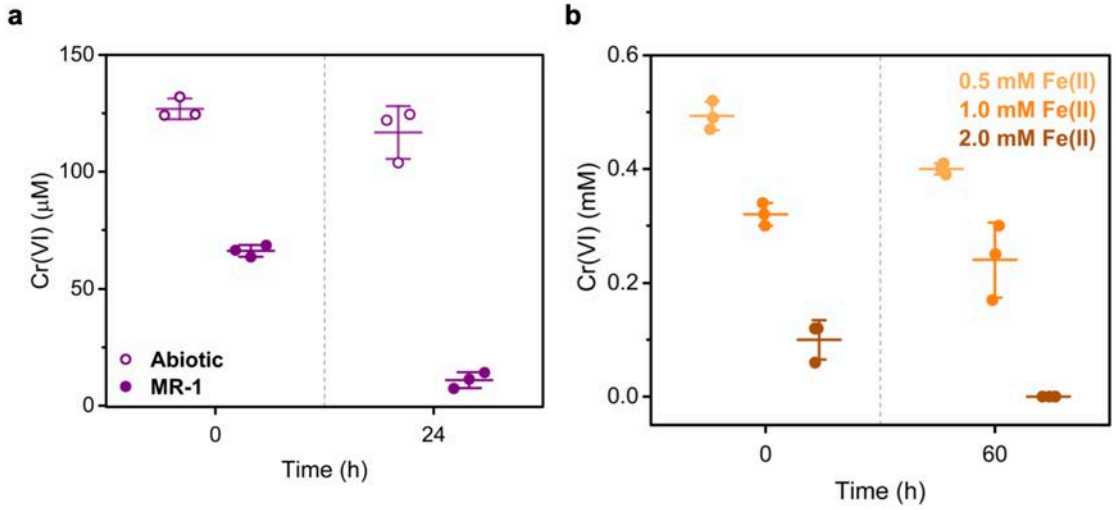

Figure C.11: Cr(VI) reduction by *S. oneidensis* and Fe(II).

(a) Reduction of 100 μM Cr(VI) by *S. oneidensis* MR-1 and (b) reduction of 0.5 mM Cr(VI) by $FeCl_2 \cdot 4H_2O$ (either 0.5 mM, 1.0 mM, or 2.0 mM).

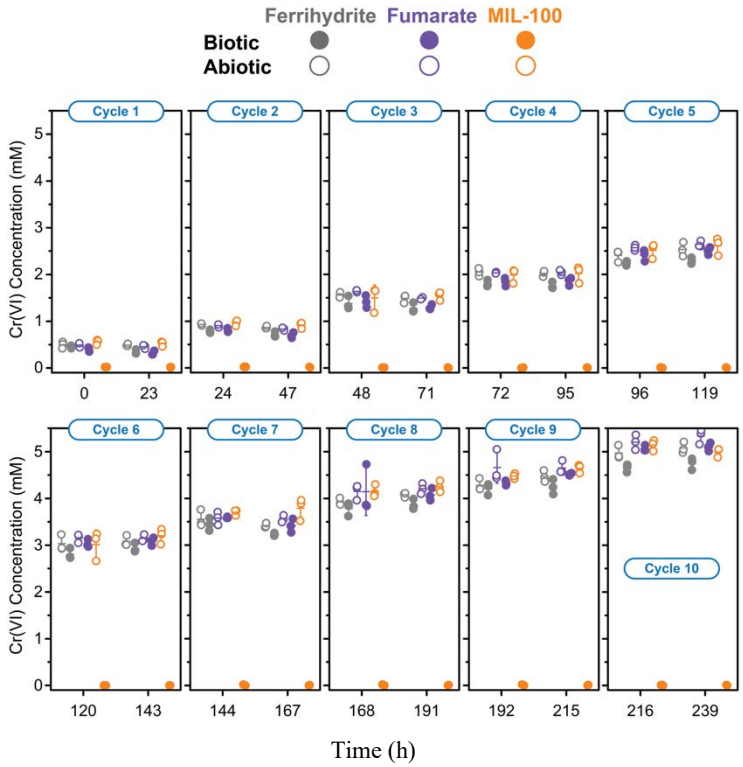

Figure C.12: Cr(VI) cycling.

Cr(VI) concentrations in the supernatant for each Cr(VI) challenge (1-10) for MIL-100 (*orange*), ferrihydrite (*grey*), and fumarate (*purple*).

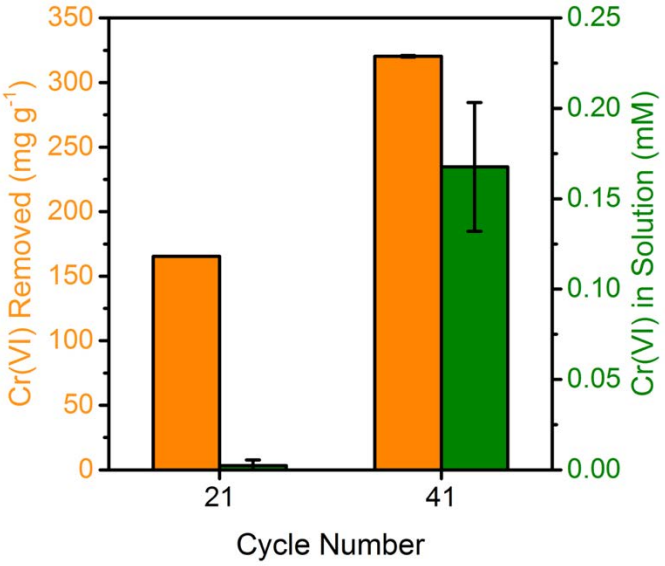

Figure C.13: Cr(VI) removal for long-term cycling.

Cr(VI) remaining in the supernatant and total Cr(VI) removed for biotic MIL-100 samples after 21 and 41 additions of 0.5 mM Cr(VI).

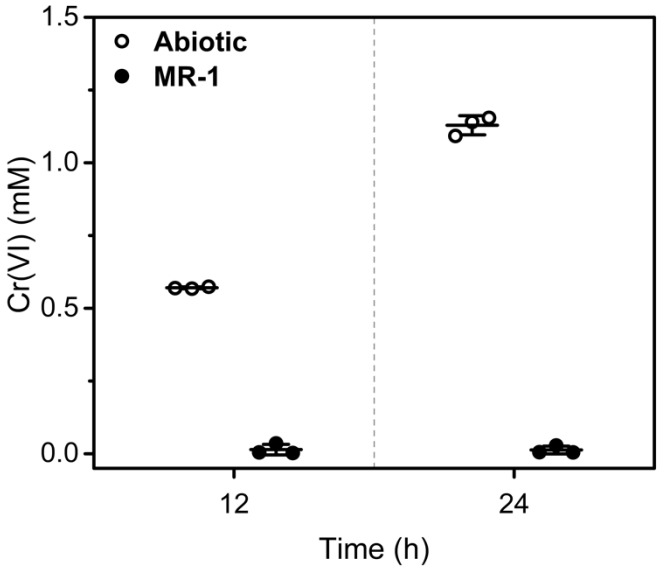

Figure C.14: Fe(II) reduction of Cr(VI).

Reduction of 0.5 mM Cr(VI) by *S. oneidensis* MR-1 reduced Fe(III)-citrate (2 cycles). *S. oneidensis* MR-1 was grown on Fe(III)-citrate for ca. 12 h prior to initial Cr(VI) addition. A second dose of Cr(VI) was added at 24 h.

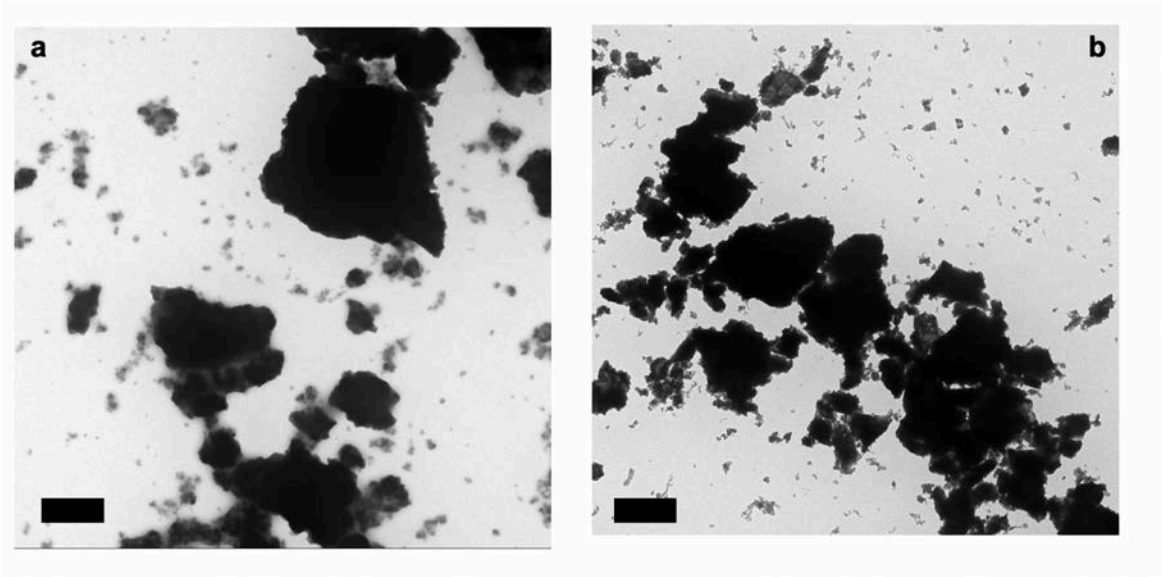

Figure C.15: Cycled metal-organic framework morphology.

TEM images of (a) abiotic MIL-100 and (b) biotic MIL-100 after 10 Cr(VI) challenges. Scale bars are 1 μm.

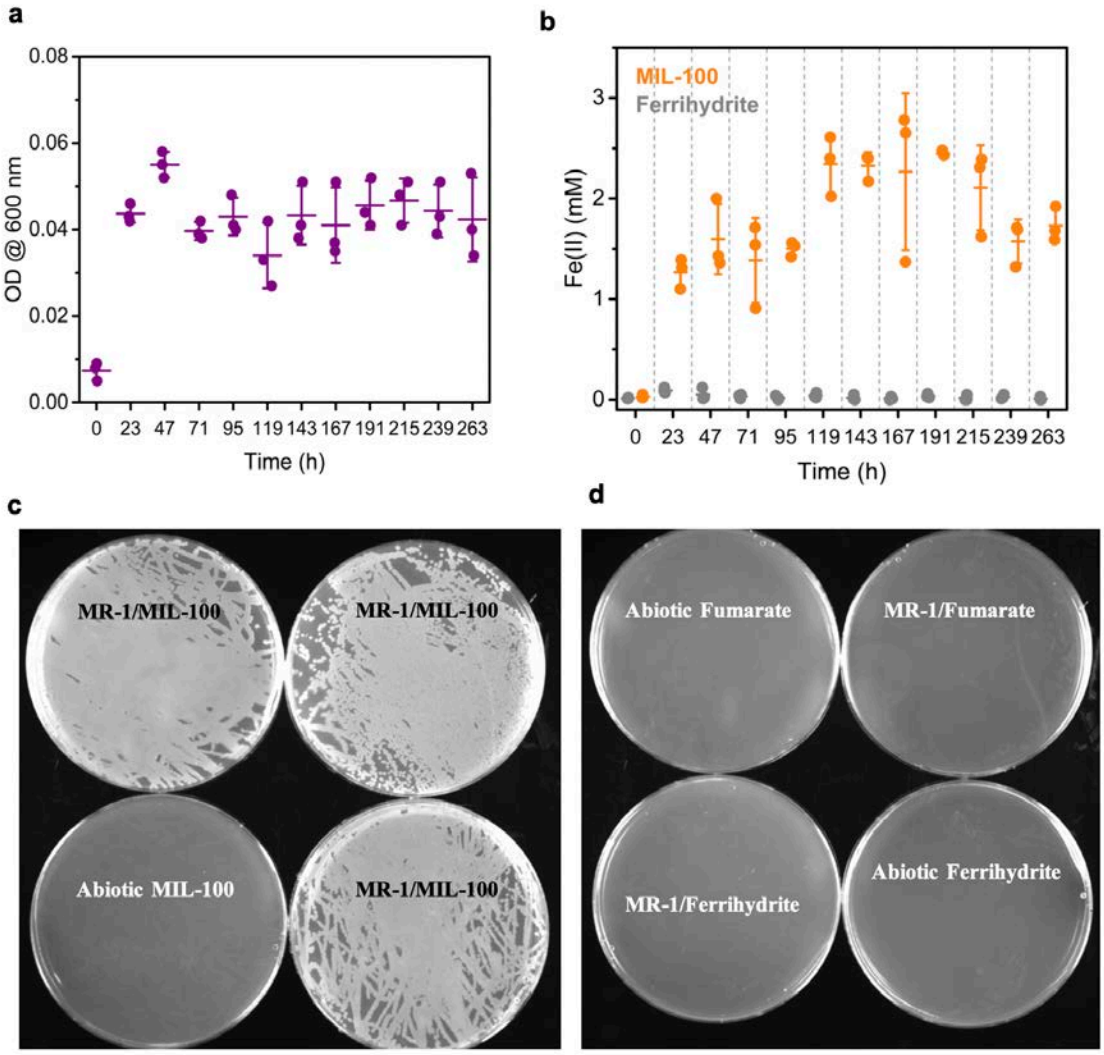

Figure C.16: Bacterial viability post-cycling.

(a) Growth of MR-1 when grown on soluble fumarate (40 mM) over the course of the 10 Cr(VI) cycles. (b) Fe(III) reduction of ferrihydrite (*grey*) and MIL-100 (*orange*) over the course of 10 Cr(VI) challenges. (c-d) Bacterial viability assessed by plating on LB agar plates 23 h after the tenth 0.5 mM Cr(VI) challenge in MR-1/MIL-100, MR-1/Ferrihydrite, MR-1/Fumarate, and the abiotic samples. MIL-100 biotic samples are shown in triplicate, while only a single plate is shown for the others. Only MR-1/ MIL-100 samples exhibited growth.

APPENDIX D: SUPPLEMENTARY DATA FOR CHAPTER 5

Supplementary Tables for Chapter 5

Strain or plasmid	Description/Genotype	Reference or source
***S. oneidensis* Strains (+plasmid)**		
MR-1	MR-1 (ATCC700550), wild-type strain	American-Type Culture Collection
JG596	Lacks outer membrane cytochromes MtrC, OmcA, and MtrF; Δ*mtrC*Δ*omcA*Δ*mtrF*	86
Δ*cymA*	Lacks inner membrane cytochrome CymA	Jeffrey Gralnick, U. of Minnesota
Δ*mtrA*	Lacks periplasmic cytochrome, MtrA	This work
MR-1+pCD7sfGFP	Wild-type with *sfgfp* Buffer gate	This work
MR-1+pCD8	Wild-type with empty Buffer gate	This work
MR-1+pCDd4	Wild-type with empty NOT gate	This work
Δ*cymA*+pCD8	Δ*cymA* with empty Buffer gate	This work
Δ*cymA*+pCD26r1	Δ*cymA* with *cymA* Buffer gate ($sRBS1_{cymA}$)	This work
Δ*cymA*+pCD26r2	Δ*cymA* with *cymA* Buffer gate ($sRBS2_{cymA}$)	This work
Δ*cymA*+pCD26r3	Δ*cymA* with *cymA* Buffer gate ($sRBS3_{cymA}$)	This work
Δ*cymA*+pCD26r4	Δ*cymA* with *cymA* Buffer gate ($sRBS4_{cymA}$)	This work
Δ*cymA*+pCD26r5	Δ*cymA* with *cymA* Buffer gate ($sRBS5_{cymA}$)	This work
Δ*cymA*+pCD26r6	Δ*cymA* with *cymA* Buffer gate ($sRBS6_{cymA}$)	This work
Δ*cymA*+pCDd4	Δ*cymA* with empty NOT gate	This work
Δ*cymA*+pCDd3r4	Δ*cymA* with *cymA* NOT gate ($sRBS4_{cymA}$)	This work
Δ*mtrA*+pCD8	Δ*mtrA* with empty Buffer gate	This work
Δ*mtrA*+pCD25r0	Δ*mtrA* with *mtrA* Buffer gate ($sRBS0_{mtrA}$)	This work
Δ*mtrA*+pCD25r0.5	Δ*mtrA* with *mtrA* Buffer gate ($sRBS0.5_{mtrA}$)	This work
Δ*mtrA*+pCD25r1	Δ*mtrA* with *mtrA* Buffer gate ($sRBS1_{mtrA}$)	This work
Δ*mtrA*+pCD25r2	Δ*mtrA* with *mtrA* Buffer gate ($sRBS2_{mtrA}$)	This work

Δ*mtrA*+pCD25r3	Δ*mtrA* with *mtrA* Buffer gate ($sRBS3_{mtrA}$)	This work
JG596+pCD8	JG596 with empty Buffer gate	This work
JG596+pCD24r1	JG596 with *mtrC* Buffer gate ($sRBS1_{mtrC}$)	This work
JG596+pCD24r2	JG596 with *mtrC* Buffer gate ($sRBS2_{mtrC}$)	This work
JG596+pCD24r3	JG596 with *mtrC* Buffer gate ($sRBS3_{mtrC}$)	This work
JG596+pCD24r6	JG596 with *mtrC* Buffer gate ($sRBS6_{mtrC}$)	This work
JG596+pCD24	JG596 with *mtrC* Buffer gate (B0032)	This work
JG596+pCDd4	JG596 with empty NOT gate	This work
JG596+pCDd1	JG596 with *mtrC* NOT gate ($sRBS1_{mtrC}$)	This work
Plasmids		
pCD7sfGFP	*sfgfp* Buffer gate	This work
pCD8	Empty Buffer gate	This work
pCD24r1	*mtrC* Buffer gate ($sRBS1_{mtrC}$)	This work
pCD24r2	*mtrC* Buffer gate ($sRBS2_{mtrC}$)	This work
pCD24r3	*mtrC* Buffer gate ($sRBS3_{mtrC}$)	This work
pCD24r6	*mtrC* Buffer gate ($sRBS6_{mtrC}$)	This work
pCD24	*mtrC* Buffer gate (B0032)	This work
pCD25r0	*mtrA* Buffer gate ($sRBS0_{mtrA}$)	This work
pCD25r0.5	*mtrA* Buffer gate ($sRBS0.5_{mtrA}$)	This work
pCD25r1	*mtrA* Buffer gate ($sRBS1_{mtrA}$)	This work
pCD25r2	*mtrA* Buffer gate ($sRBS2_{mtrA}$)	This work
pCD25r3	*mtrA* Buffer gate ($sRBS3_{mtrA}$)	This work
pCD26r1	*cymA* Buffer gate ($sRBS1_{cymA}$)	This work
pCD26r2	*cymA* Buffer gate ($sRBS2_{cymA}$)	This work
pCD26r3	*cymA* Buffer gate ($sRBS3_{cymA}$)	This work
pCD26r4	*cymA* Buffer gate ($sRBS4_{cymA}$)	This work
pCD26r5	*cymA* Buffer gate ($sRBS5_{cymA}$)	This work
pCD26r6	*cymA* Buffer gate ($sRBS6_{cymA}$)	This work
pCDd4	Empty NOT gate	This work
pCDd1	*mtC* NOT gate ($sRBS1_{mtrC}$)	This work
pCDd3r4	*cymA* NOT gate ($sRBS4_{cymA}$)	This work

Table D.1: Bacterial strains and plasmids used in this study.

Strains	Plasmid	EET Gene RBS	Predicted RBS Strength (kcal mol^{-1})
JG596	pCD24r1	$sRBS1_{mtrC}$	18.6
JG596	pCD24r2	$sRBS2_{mtrC}$	16.0
JG596	pCD24r3	$sRBS3_{mtrC}$	10.6
JG596	pCD24r6	$sRBS6_{mtrC}$	3.55
JG596	pCD24	B0032	-5.34
Δ*mtrA*	pCD25r0	$sRBS0_{mtrA}$	16.4
Δ*mtrA*	pCD25r0.5	$sRBS0.5_{mtrA}$	13.4
Δ*mtrA*	pCD25r1	$sRBS1_{mtrA}$	9.15
Δ*mtrA*	pCD25r2	$sRBS2_{mtrA}$	4.00
Δ*mtrA*	pCD25r3	$sRBS3_{mtrA}$	-1.11
Δ*cymA*	pCD26r1	$sRBS1_{cymA}$	23.1
Δ*cymA*	pCD26r2	$sRBS2_{cymA}$	18.2
Δ*cymA*	pCD26r3	$sRBS3_{cymA}$	13.3
Δ*cymA*	pCD26r4	$sRBS4_{cymA}$	8.19
Δ*cymA*	pCD26r5	$sRBS5_{cymA}$	3.06
Δ*cymA*	pCD26r6	$sRBS6_{cymA}$	-1.89

Table D.2: Strain/Plasmid Information for RBS Library.

Genetic Part	DNA Sequence (5' to 3')
Promoters	
$P_{tacsymO}$[361]	TGTTGACAATTAATCATCGGCTCGTATAATGTGTGGAATTGTGAG CGCTCACAATTCTATGGACTATGTTT
P_{lacI}	GCGGCGCGCCATCGAATGGCGCAAAACCTTTCGCGGTATGGCA TGATAGCGCCCGGAAGAGAGTCAATTCAGGGTGGTGAAT
P_{tet}[21]	TACTCCACCGTTGGCTTTTTTCCCTATCAGTGATAGAGATTGACA TCCCTATCAGTGATAGAGATAATGAGCAC
Ribosome Binding Sites	
B0032	TCACACAGGAAAGTACTAG
$sRBS1_{mtrC}$	GGGGAAAAACAGCAGTGCGAT
$sRBS2_{mtrC}$	GGAGAAAAACAGCAGTGCGAT
$sRBS3_{mtrC}$	CGGCAAAAACAGCAGTACGAA
$sRBS6_{mtrC}$	CGGGAAAAACAGGAGTGCGAA
$sRBS0_{mtrA}$	ATAGGCGGCTTCATTGACGGTCCCA
$sRBS0.5_{mtrA}$	ATAGGCGGCTTCACTGACGGTCCCA
$sRBS1_{mtrA}$	TTACCCTAAGCTTCAGTAGGCGTTC
$sRBS2_{mtrA}$	ATAGGCTGCTTCGCTGAGGGTCCCA
$sRBS3_{mtrA}$	ATAGACTGCTTCGCTGAGGGTCCCA
$sRBS1_{cymA}$	TTCGCTTTGGGTTTTTATGTAGCACGCA
$sRBS2_{cymA}$	TTCGCTTTGGGTTTTTATGTAGGACGCA
$sRBS3_{cymA}$	TTCCCTTTGGGTTTTTAAGTAGCACGCA
$sRBS4_{cymA}$	TTCGCTTTGGGTTTTTAAGGAGGACGCA
$sRBS5_{cymA}$	TTCCCTTTTGGTTTTTACGGAGCACGGA
$sRBS6_{cymA}$	TTCCCTTTTGGTTTTTACGGAGGACGGA
tetR RBS[373]	CTATGGACTATGTTTTCACACAGGAAAGGCCTCG
Terminators	
ECK120029600[500]	TTCAGCCAAAAAACTTAAGACCGCCGGTCTTGTCCACTACCTTG CAGTAATGCGGTGGACAGGATCGGCGGTTTTCTTTTCTCTTCTC AA
L3S2P21[500]	TCGGTACCAAATTCCAGAAAAGAGGCCTCCCGAAAGGGGGGCC TTTTTTCGTTTTGGTCC
B0015	TAATCTAGACCAGGCATCAAATAAAACGAAAGGCTCAGTCGAAA GACTGGGCCTTTCGTTTTATCTGTTGTTTGTCGGTGAACGCTCTC TACTAGAGTCACACTGGCTCACCTTCGGGTGGGCCTTTCTGCGT TTATA
ECK120033737[500]	GGAAACACAGAAAAAAGCCCGCACCTGACAGTGCGGGCTTTTTT TTTCGACCAAAGG
L3S2P55[500]	CTCGGTACCAAAGACGAACAATAAGACGCTGAAAAGCGTCTTTT TTCGTTTTGGTCC
ECK120033736[500]	AACGCATGAGAAAGCCCCCGGAAGATCACCTTCCGGGGGCTTT TTTATTGCGC
Ribozymes	
RiboJ[367]	AGCTGTCACCGGATGTGCTTTCCGGTCTGATGAGTCCGTGAGGA CGAAACAGCCTCTACAAATAATTTTGTTTAA
ElvJ[367]	AGCCCCATAGGGTGGTGTGTACCACCCCTGATGAGTCCAAAAG GACGAAATGGGGCCTCTACAAATAATTTTGTTTAA

PlmJ[367]	AGTCATAAGTCTGGGCTAAGCCCACTGATGAGTCGCTGAAATGC GACGAAACTTATGACCTCTACAAATAATTTTGTTTAA
RiboJ64[367]	AGGAGTCAATTAATGTGCTTTTAATTCTGATGAGACGGTGACGTC GAAACTCCCTCTACAAATAATTTTGTTTAA
Genes	
tetR (codon optimized for MR-1)	ATGTCTCGTTTAGATAAATCTAAAGTTATCAACTCTGCTTTAGAAT TATTAAACGAAGTTGGTATCGAAGGTTTAACTACTCGTAAATTAG CTCAAAAATTAGGTGTTGAACAGCCCACATTATACTGGCACGTTA AAAACAAGAGGGCGTTATTAGATGCTCTCGCTATCGAAATGTTA GATCGTCACCACACTCACTTCTGTCCATTAGAAGGTGAATCTTG GCAAGATTTCTTACGTAACAACGCTAAATCGTTCCGTTGTGCGTT ATTATCGCACCGTGATGGTGCTAAAGTTCACTTAGGTACTCGTC CAACTGAAAAACAATACGAAACTTTAGAAAACCAATTAGCTTTCT TATGTCAACAAGGTTTCTCGCTCGAAAACGCGCTCTATGCGTTAT CGGCTGTTGGCCACTTCACTTTAGGTTGTGTTTTAGAAGATCAAG AACACCAAGTTGCTAAAGAAGAACGTGAAACTCCAACTACTGATT CTATGCCACCATTATTACGTCAAGCTATCGAATTATTCGATCACC AAGGTGCCGAGCCAGCGTTCCTCTTCGGTTTAGAATTAATCATC TGTGGTTTAGAAAAACAATTAAAATGTGAATCTGGTTCTTAA
lacI	GTGAAACCAGTAACGTTATACGATGTCGCAGAGTATGCCGGTGT CTCTTATCAGACCGTTTCCCGCGTGGTGAACCAGGCCAGCCAC GTTTCTGCGAAAACGCGGGAAAAAGTGGAAGCGGCGATGGCGG AGCTGAATTACATTCCCAACCGCGTGGCACAACAACTGGCGGG CAAACAGTCGTTGCTGATTGGCGTTGCCACCTCCAGTCTGGCCC TGCACGCGCCGTCGCAAATTGTCGCGGCGATTAAATCTCGCGC CGATCAACTGGGTGCCAGCGTGGTGGTGTCGATGGTAGAACGA AGCGGCGTCGAAGCCTGTAAAGCGGCGGTGCACAATCTTCTCG CGCAACGCGTCAGTGGGCTGATCATTAACTATCCGCTGGATGAC CAGGATGCCATTGCTGTGGAAGCTGCCTGCACTAATGTTCCGGC GTTATTTCTTGATGTCTCTGACCAGACACCCATCAACAGTATTAT TTTCTCCCATGAAGACGGTACGCGACTGGGCGTGGAGCATCTG GTCGCATTGGGTCACCAGCAAATCGCGCTGTTAGCGGGCCCAT TAAGTTCTGTCTCGGCGCGTCTGCGTCTGGCTGGCTGGCATAAA TATCTCACTCGCAATCAAATTCAGCCGATAGCGGAACGGGAAGG CGACTGGAGTGCCATGTCCGGTTTTCAACAAACCATGCAAATGC TGAATGAGGGTATCGTTCCCACTGCGATGCTGGTTGCCAACGAT CAGATGGCGCTGGGCGCAATGCGCGCCATTACCGAGTCCGGGC TGCGCGTTGGTGCGGATATCTCGGTAGTGGGATACGACGATAC CGAAGACAGCTCATGTTATATCCCGCCGTTAACCACCATCAAAC AGGATTTTCGCCTGCTGGGGCAAACCAGCGTGGACCGCTTGCT GCAACTCTCTCAGGGCCAGGCGGTGAAGGGCAATCAGCTGTTG CCCGTGTCACTGGTGAAAAGAAAAACCACCCTGGCGCCCAATAC GCAAACCGCCTCTCCCCGCGCGTTGGCCGATTCATTAATGCAGC TGGCACGACAGGTTTCCCGACTGGAAAGCGGGCAGTGA
sfgfp	ATGCGTAAAGGCGAAGAGCTGTTCACTGGTGTCGTCCCTATTCT GGTGGAACTGGATGGTGATGTCAACGGTCATAAGTTTTCCGTGC GTGGCGAGGGTGAAGGTGACGCAACTAATGGTAAACTGACGCT GAAGTTCATCTGTACTACTGGTAAACTGCCGGTACCTTGGCCGA CTCTGGTAACGACGCTGACTTATGGTGTTCAGTGCTTTGCTCGT

	TATCCGGACCATATGAAGCAGCATGACTTCTTCAAGTCCGCCAT GCCGGAAGGCTATGTGCAGGAACGCACGATTTCCTTTAAGGATG ACGGCACGTACAAAACGCGTGCGGAAGTGAAATTTGAAGGCGA TACCCTGGTAAACCGCATTGAGCTGAAAGGCATTGACTTTAAAG AAGACGGCAATATCCTGGGCCATAAGCTGGAATACAATTTTAAC AGCCACAATGTTTACATCACCGCCGATAAACAAAAAAATGGCATT AAAGCGAATTTTAAAATTCGCCACAACGTGGAGGATGGCAGCGT GCAGCTGGCTGATCACTACCAGCAAAACACTCCAATCGGTGATG GTCCTGTTCTGCTGCCAGACAATCACTATCTGAGCACGCAAAGC GTTCTGTCTAAAGATCCGAACGAGAAACGCGATCATATGGTTCT GCTGGAGTTCGTAACCGCAGCGGGCATCACGCATGGTATGGAT GAACTGTACAAATGATGA
mtrC	ATGATGAACGCACAAAAATCAAAAATCGCACTGCTGCTCGCAGC AAGTGCCGTCACAATGGCCTTAACCGGCTGTGGTGGAAGCGAT GGTAATAACGGCAATGATGGTAGTGATGGTGGTGAGCCAGCAG GTAGCATCCAGACGTTAAACCTAGATATCACTAAAGTAAGCTATG AAAATGGTGCACCTATGGTCACTGTTTTCGCCACTAACGAAGCC GACATGCCAGTGATTGGTCTCGCAAATTTAGAAATCAAAAAAGCA CTGCAATTAATACCGGAAGGGGCGACAGGCCCAGGTAATAGCG CTAACTGGCAAGGCTTAGGCTCATCAAAGAGCTATGTCGATAAT AAAAACGGTAGCTATACCTTTAAATTCGACGCCTTCGATAGTAAT AAGGTCTTTAATGCTCAATTAACGCAACGCTTTAACGTTGTTTCT GCTGCGGGTAAATTAGCAGACGGAACGACCGTTCCCGTTGCCG AAATGGTTGAAGATTTCGACGGCCAAGGTAATGCGCCGCAATAT ACAAAAAATATCGTTAGCCACGAAGTATGTGCTTCTTGCCACGTA GAAGGTGAAAAGATTTATCACCAAGCTACTGAAGTCGAAACTTGT ATTTCTTGCCACACTCAAGAGTTTGCGGATGGTCGCGGCAAACC CCATGTCGCCTTTAGTCACTTAATTCACAATGTGCATAATGCCAA CAAAGCTTGGGGCAAAGACAATAAAATCCCTACAGTTGCACAAA ATATTGTCCAAGATAATTGCCAAGTTTGTCACGTTGAATCCGACA TGCTCACCGAGGCAAAAAACTGGTCACGTATTCCAACAATGGAA GTCTGTTCTAGCTGTCACGTAGACATCGATTTTGCTGCGGGTAA AGGCCACTCTCAACAACTCGATAACTCCAACTGTATCGCCTGCC ATAACAGCGACTGGACTGCTGAGTTACACACAGCCAAAACCACC GCAACTAAGAACTTGATTAATCAATACGGTATCGAGACTACCTCG ACAATTAATACCGAAACTAAAGCAGCCACAATTAGTGTTCAAGTT GTAGATGCGAACGGTACTGCTGTTGATCTCAAGACCATCCTGCC TAAAGTGCAACGCTTAGAGATCATCACCAACGTTGGTCCTAATAA TGCAACCTTAGGTTATAGTGGCAAAGATTCAATATTTGCAATCAA AAATGGAGCTCTTGATCCAAAAGCTACTATCAATGATGCTGGCAA ACTGGTTTATACCACTACTAAAGACCTCAAACTTGGCCAAAACGG CGCAGACAGCGACACAGCATTTAGCTTTGTAGGTTGGTCAATGT GTTCTAGCGAAGGTAAGTTTGTAGACTGTGCAGACCCTGCATTT GATGGTGTTGATGTAACTAAGTATACCGGCATGAAAGCGGATTT AGCCTTTGCTACTTTGTCAGGTAAAGCACCAAGTACTCGCCACG TTGATTCTGTTAACATGACAGCCTGTGCCAATTGCCACACTGCTG AGTTCGAAATTCACAAAGGCAAACAACATGCAGGCTTTGTGATG ACAGAGCAACTATCACACACCCAAGATGCTAACGGTAAAGCGAT TGTAGGCCTTGACGCATGTGTGACTTGTCATACTCCTGATGGCA

	CCTATAGCTTTGCCAACCGTGGTGCGCTAGAGCTAAAACTACAC AAAAAACACGTTGAAGATGCCTACGGCCTCATTGGTGGCAATTG TGCCTCTTGTCACTCAGACTTCAACCTTGAGTCTTTCAAGAAGAA AGGCGCATTGAATACTGCCGCTGCAGCAGATAAAACAGGTCTAT ATTCTACGCCGATCACTGCAACTTGTACTACCTGTCACACAGTTG GCAGCCAGTACATGGTCCATACGAAAGAAACCCTGGAGTCTTTC GGTGCAGTTGTTGATGGCACAAAAGATGATGCTACCAGTGCGGC ACAGTCAGAAACCTGTTTCTACTGCCATACCCCAACAGTTGCAG ATCACACTAAAGTGAAAATGTAA
mtrA	ATGAAGAACTGCCTAAAAATGAAAAACCTACTGCCGGCACTTAC CATCACAATGGCAATGTCTGCAGTTATGGCATTAGTCGTCACAC CAAACGCTTATGCGTCGAAGTGGGATGAGAAAATGACGCCAGA GCAAGTCGAAGCCACCTTAGATAAGAAGTTTGCCGAAGGCAACT ACTCCCCTAAAGGCGCCGATTCTTGCTTGATGTGCCATAAGAAA TCCGAAAAAGTCATGGACCTTTTCAAAGGTGTCCACGGTGCGAT TGACTCCTCTAAGAGTCCAATGGCTGGCCTGCAATGTGAGGCAT GCCACGGCCCACTGGGTCAGCACAACAAAGGCGGCAACGAGCC GATGATCACTTTTGGTAAGCAATCAACCTTAAGTGCCGACAAGC AAAACAGCGTATGTATGAGCTGTCACCAAGACGATAAGCGTATG TCTTGGAATGGCGGTCACCATGACAATGCCGATGTTGCTTGTGC TTCTTGTCACCAAGTACACGTCGCAAAAGATCCTGTGTTATCTAA AAACACGGAAATGGAAGTCTGTACTAGCTGCCATACAAAGCAAA AAGCGGATATGAATAAACGCTCAAGTCACCCACTCAAATGGGCA CAAATGACCTGTAGCGACTGTCACAATCCCCATGGGAGCATGAC AGATTCCGATCTTAACAAGCCTAGCGTGAATGATACCTGTTATTC CTGTCACGCCGAAAAACGCGGCCCAAAACTTTGGGAGCATGCA CCCGTCACTGAGAATTGTGTCACTTGCCACAATCCTCACGGTAG TGTGAATGACGGTATGCTGAAAACCCGTGCGCCACAGCTATGTC AGCAATGTCACGCCAGCGATGGCCACGCCAGCAACGCCTACTT AGGTAACACTGGATTAGGTTCAAATGTCGGTGACAATGCCTTTA CTGGTGGAAGAAGCTGCTTAAATTGCCATAGTCAGGTTCATGGT TCTAACCATCCATCTGGCAAGCTATTACAGCGCTAA
cymA	ATGAACTGGCGTGCACTATTTAAACCCAGCGCGAAATATTCCAT CCTAGCGCTACTGGTTGTTGGTATCGTGATTGGTGTTGTGGGCT ATTTTGCAACTCAGCAGACTTTACATGCGACAAGTACAGATGCGT TCTGTATGTCTTGCCATAGCAATCATTCCTTGAAGAATGAAGTGC TGGCATCTGCCCACGGTGGCGGCAAAGCCGGGGTTACTGTTCA GTGTCAAGACTGTCACTTACCCCATGGCCCTGTTGATTATTTAAT TAAGAAAATCATCGTATCTAAAGATTTATATGGTTTCTTAACTATT GATGGCTTTAACACTCAAGCTTGGTTAGACGAAAACCGCAAAGA GCAAGCCGACAAAGCATTGGCTTACTTCCGTGGTAACGACTCAG CAAACTGTCAACACTGCCATACTCGCATTTATGAAAACCAGCCA GAAACCATGAAGCCAATGGCTGTGAGAATGCACACCAACAACTT CAAGAAAGATCCTGAAACGAGAAAGACCTGTGTGGATTGCCACA AAGGTGTCGCTCACCCCTATCCAAAAGGATAA

Table D.3: Genetic parts/sequences used to construct the plasmids in this study. Underline indicates added insulator sequence.

Figure	Fitted Values				95% Confidence Interval				R^2 (weighted)
	MIN	n	MAX	$K_{1/2}$	MIN	n	MAX	$K_{1/2}$	
Figure 5.4b	6124	1.699	29301	97.83	5698 to 6715	1.317 to 2.118	27860 to 32435	82.29 to 124.2	0.9559
Figure 5.4c	0.6299	1.296	2.578	14.2	0.5184 to 0.8713	0.7638 to 2.463	2.445 to 3.150	9.113 to 30.58	0.8232
Figure 5.4d	= 0.2767	0.653	= 1.318	221.4	n.d.	0.4771 to 1.365	n.d.	37.05 to 282.2	0.5958
Figure 5.4e	0.2731	1.75	1.368	15.53	0.2087 to 0.4044	0.8473 to 3.638	1.295 to 1.731	10.29 to 28.25	0.8385
Figure 5.5b	15.83	1.176	113.2	79.54	10.38 to 20.84	0.9112 to 1.521	107.6 to 121.0	64.82 to 98.42	0.9676
Figure 5.5c	0.8899	1.199	37.6	279.4	0.8290 to 1.394	1.046 to 1.519	31.24 to 46.20	187.7 to 428.5	0.9499
Figure 5.5d	0.7018	0.6978	35.63	188.1	0.4938 to 1.515	0.4875 to 0.9073	30.18 to 235.1	90.48 to 25541	0.8319
Figure 5.6b	= 0.6370	2.419	= 3.075	50.44	n.d.	1.246 to n.d.	n.d.	45.34 to 248.2	0.7014
Figure 5.6c	0.4392	1.93	2.27	17.46	0.3645 to 1.439	0.3533 to 3.380	1.666 to 3.560	5.951 to 68.18	0.5635

Table D.4: Nonlinear fit parameters for main text Figures 5.4-5.6.

Supplementary Figures for Chapter 5

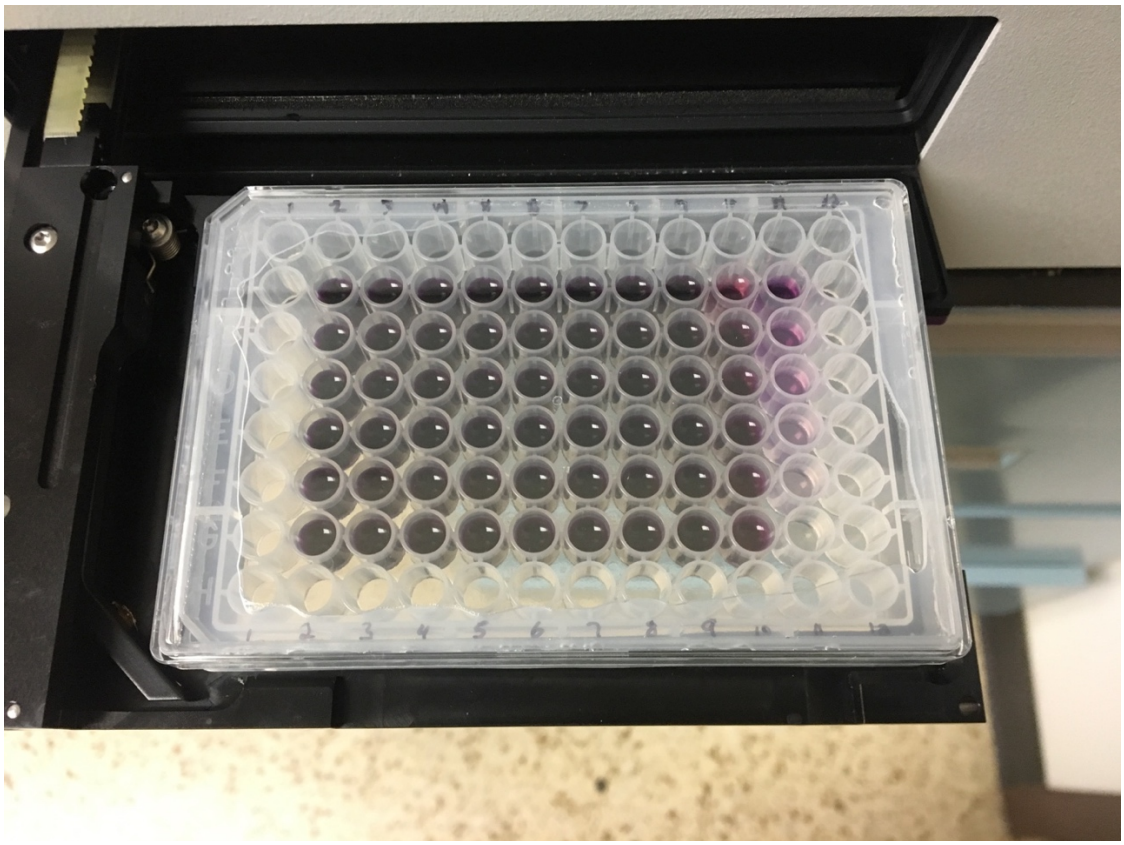

Figure D.1: Anaerobically sealed 96-well plate within a plate reader after an 18-hour microbial Fe(III) reduction experiment.

The dark purple color is a result of ferrozine in the growth medium complexing *S. oneidensis*-generated Fe(II). Labeled column 11 shows that the abiotic Fe(II) standards exhibit a range of purple hues after 18 hours, which suggests that the sealed plate maintains anaerobicity on the timescale of experiments.

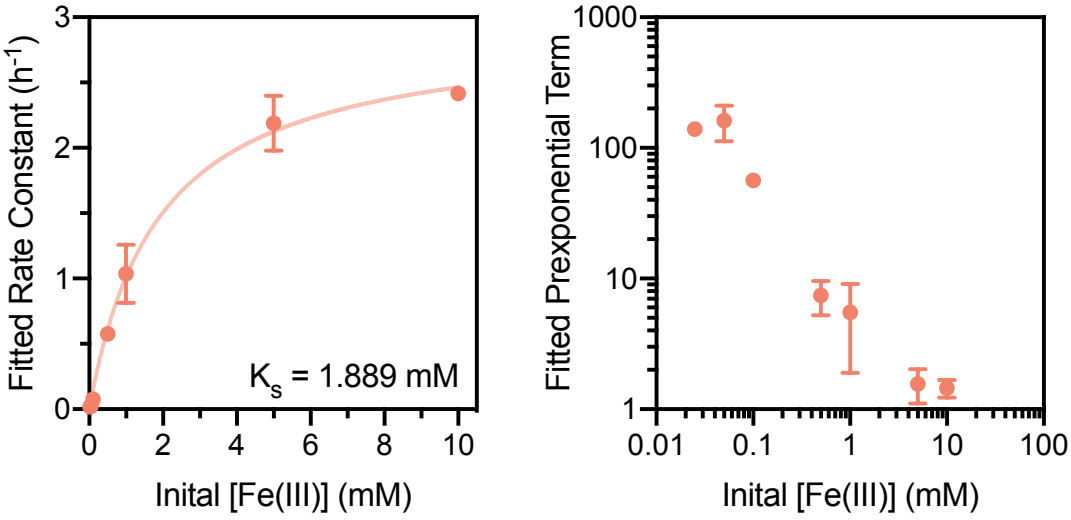

Figure D.2: Inducible *mtrC* construct exhibits Monod-type behavior for fitted rate constant with varying initial Fe(III) concentration.

A range of initial Fe(III) citrate concentrations were tested with the RBS-optimized *mtrC* construct (*S. oneidensis* Δ*mtrC*Δ*omcA*Δ*mtrF* +pCD24r1), which was induced with 1 mM IPTG. The solid line represents fitting of the exponential model rate constants from each tested Fe(III) concentration to equation (2), and K_S was determined to be 1.889 mM (left). This value is comparable to previously measured values for *S. oneidensis* soluble Fe(III) Monod constants (0.028-6 mM)[360,501]. The prexponential term from equation (10) was also determined as a function of initial Fe(III) citrate concentration (right), and was generally invariant near the initial Fe(III) concentration used for most experiments (5 mM).

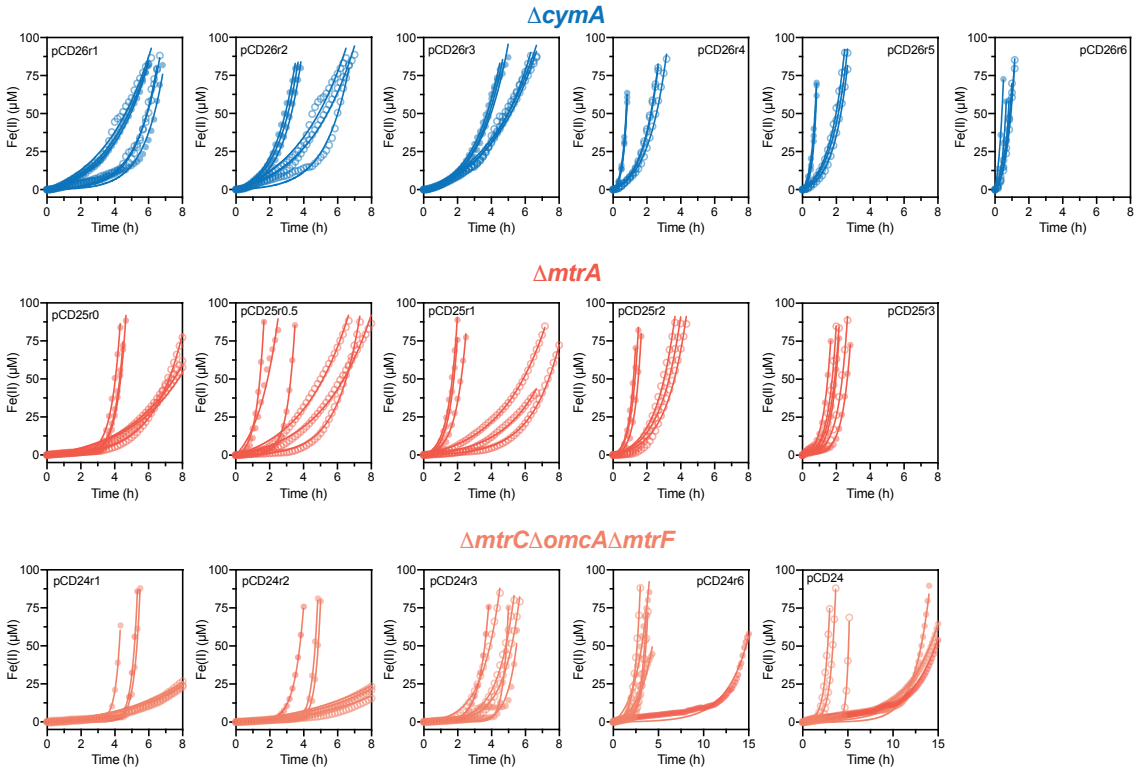

Figure D.3: Raw kinetic data for RBS libraries.

The fitted constants from this data are shown in main text Figure 5.3. Here, each graph shows induced (filled circles) and uninduced (open circles) replicates overlaid with respective exponential model fitted curves (solid lines). Induced samples were supplemented with 1500 μM IPTG and uninduced samples with 0 μM IPTG. Each row is a single RBS library (increasing translation strength from left to right), with the respective plasmid stated near the top of each graph. Above each row is the *S. oneidensis* knockout strain transformed by each RBS library member plasmid.

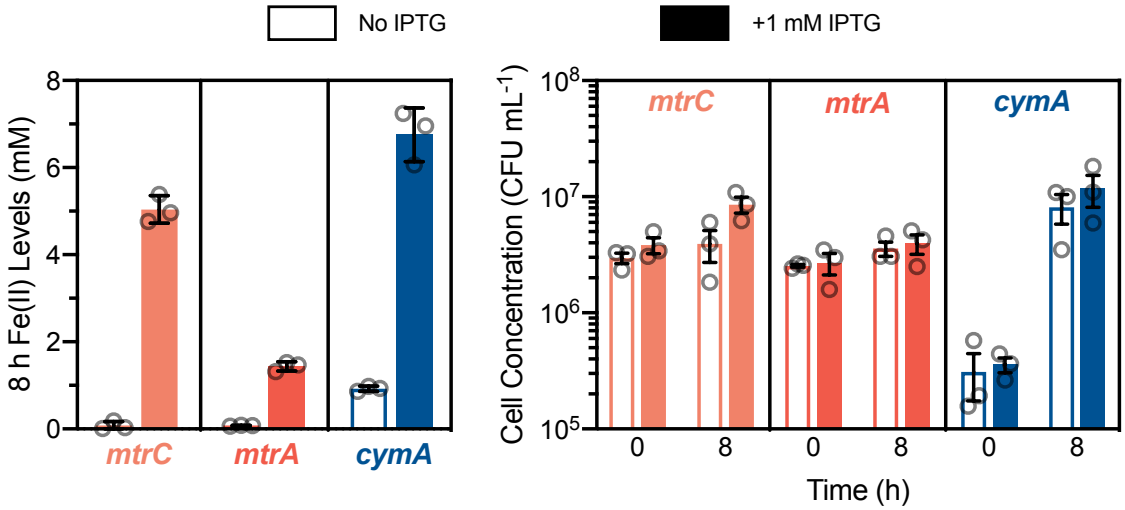

Figure D.4: Concomitant Fe(III) reduction (left) and CFU counts (right) for RBS-optimized *mtrC* (*S. oneidensis* Δ*mtrC*Δ*omcA*Δ*mtrF*+pCD24r1), *mtrA* (*S. oneidensis* Δ*mtrA*+pCD25r0), and *cymA* (*S. oneidensis* Δ*cymA*+pCD26r4) constructs.

The *mtrC* and *mtrA* constructs were pregrown anaerobically and the *cymA* construct was pregrown aerobically. Using the same Fe(III) reduction reaction conditions as in the main text experiments, 1 mL cultures were set up that omitted ferrozine in the Fe(III) reduction medium. Aliquots were acidified with equal volume 1 N HCl to quantify Fe(II) or serially diluted with SBM containing kanamycin for colony counting on LB agar plates. For Fe(III) reduction (left), data represent the mean ± s.d. for n = 3 biological replicates. For cell growth (right), data represent the mean ± s.e.m for n = 3 biological replicates.

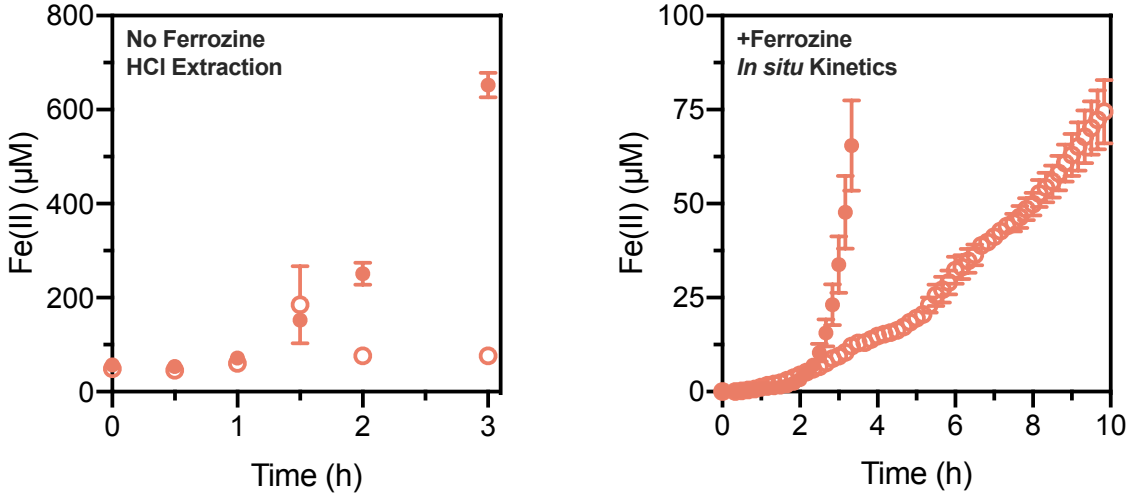

Figure D.5: Early timescale Fe(III) reduction by the *mtrC* construct (*S. oneidensis* Δ*mtrC*Δ*omcA*Δ*mtrF*+pCD24r1).

Experiments were performed either in the absence of ferrozine (left) or with ferrozine (right) in the growth medium. Other than the presence of ferrozine, Fe(III) reduction medium of both experiments was identical to typical reaction conditions detailed in the Materials and Methods (100-fold dilution from stationary-phase anaerobic pregrowth, 20 mM sodium lactate, 5 mM Fe(III) citrate). For the left graph, experiments were performed within an anaerobic chamber at 30 °C, and aliquots were acidified with equal volume 1 N HCl for Fe(II) quantification. For the right graph, experiments were initially set up inside an anaerobic chamber and then moved to a BMG ClarioStar plate reader with temperature control set to 30 °C. Data for the right graph was obtained from Figure D.3 and is included for comparison. Note that absolute Fe(II) levels are higher for HCl acidified samples, which likely is due to a combination of increased Fe(II) extraction[379] and quantification of intracellular Fe(II) from HCl-lysed cells. In both graphs, filled circles represent cultures supplemented with 1500 μM IPTG and open circles represent cultures with 0 μM IPTG. Data for both graphs represent the mean ± s.e.m. for n = 3 biological replicates.

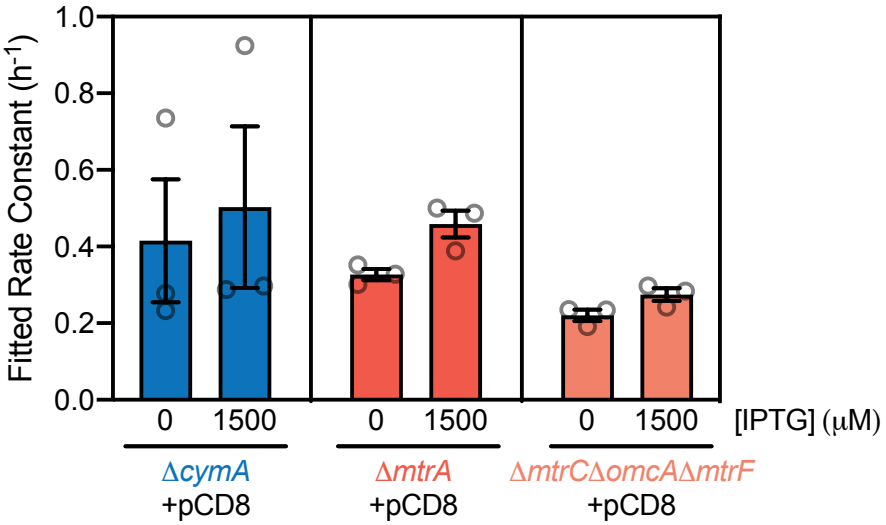

Figure D.6: Fe(III) reduction by each Buffer gate strain background carrying the empty Buffer gate plasmid (pCD8).

Each empty Buffer gate strain was tested in parallel with the respective Buffer gate shown in main text Figure 5.3. Induced samples were supplemented with 1500 μM IPTG and uninduced samples with 0 μM IPTG. Rate constants were determined using the exponential model. Data represent the mean ± s.e.m for n = 3 biological replicates.

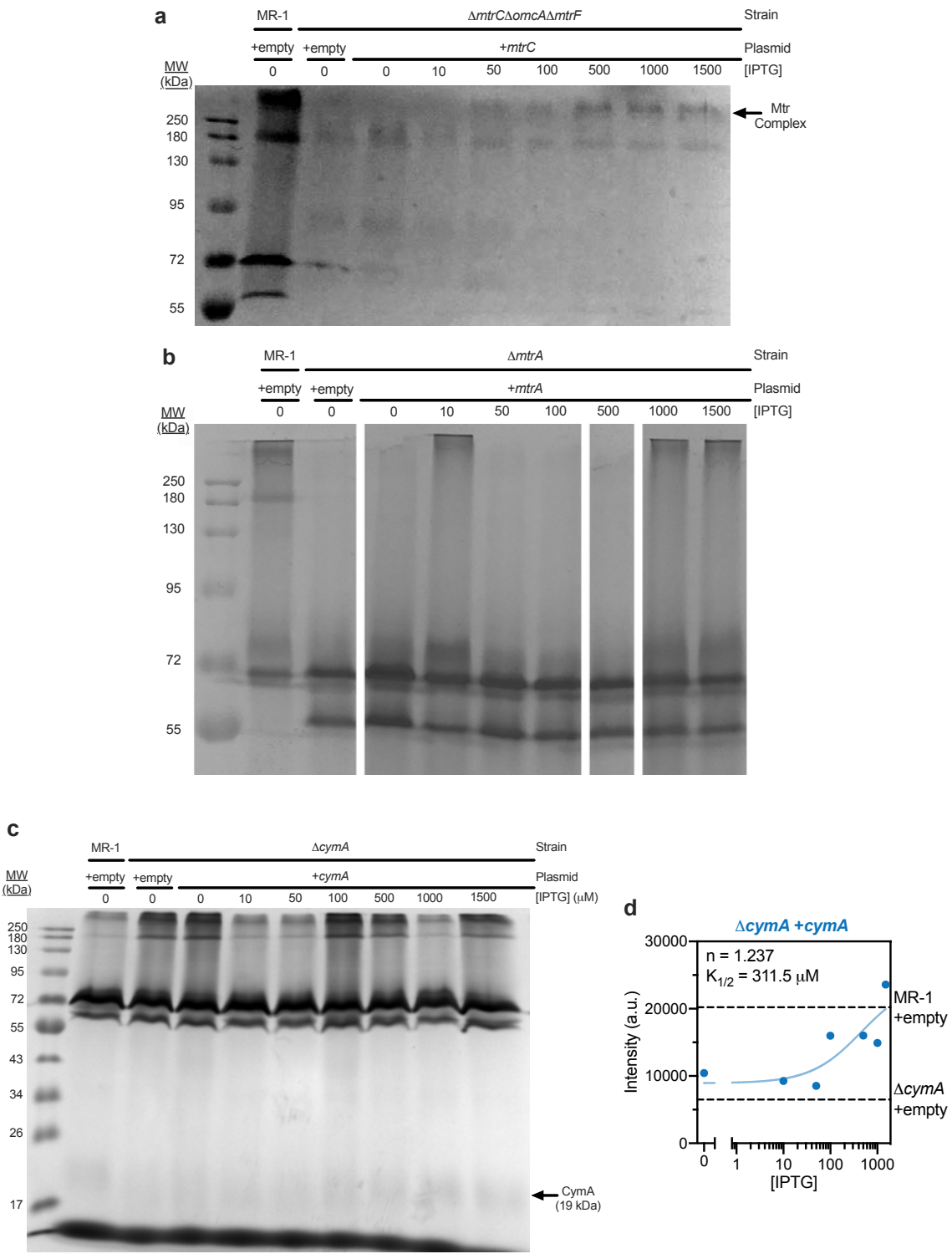

Figure D.7: Heme staining of IPTG-induced EET gene expression constructs.

Figure D.7: Heme staining of IPTG-induced EET gene expression constructs.

(a) 10 μg of protein was loaded into each lane for either the *mtrC* construct (*S. oneidensis* Δ*mtrC*Δ*omcA*Δ*mtrF* +pCD24r1) or positive (*S. oneidensis* MR-1 +pCD8) and negative (*S. oneidensis* Δ*mtrC*Δ*omcA*Δ*mtrF*+pCD8) empty vector controls. (b) 25 μg of protein was loaded into each lane for either the *mtrA* construct (*S. oneidensis* Δ*mtrA*+pCD25r0) or positive (*S. oneidensis* MR-1+pCD8) and negative (*S. oneidensis* Δ*mtrA*+pCD8) empty vector controls. (c) 50 μg of protein was loaded into each lane for either the *cymA* construct (*S. oneidensis* Δ*cymA*+pCD26r4) or positive (*S. oneidensis* MR-1 +pCD8) and negative (*S. oneidensis* Δ*cymA*+pCD8) empty vector controls. (d) Densitometry of the CymA band in (c) denoted by the arrows was performed using the ImageJ gel analysis feature. The data was fit to an activating Hill function with the MIN and MAX values constrained by the intensities at 0 μM and 1500 μM IPTG, respectively. The general cell lysis/heme staining procedure was performed as follows. Briefly, 5 mL of cells that were induced for 18-24 hours with IPTG either aerobically (*cymA*) or anaerobically (*mtrC* and *mtrA*) were harvested by centrifugation at 3400 rcf for 30 minutes. The cells were washed once with 1 mL 1x Phosphate Buffered Saline (PBS) and the cell pellet was frozen at -80 °C. Prior to lysis, cells were thawed in 150 μL 1x PBS + 0.1% Triton, and the suspension was bath sonicated for 1 hour. Unlysed cell debris was spun down at 6000 rcf for 5 minutes, and the supernatant was separated, and protein content analyzed via Bradford assay. Heme staining was performed according to previous methods.

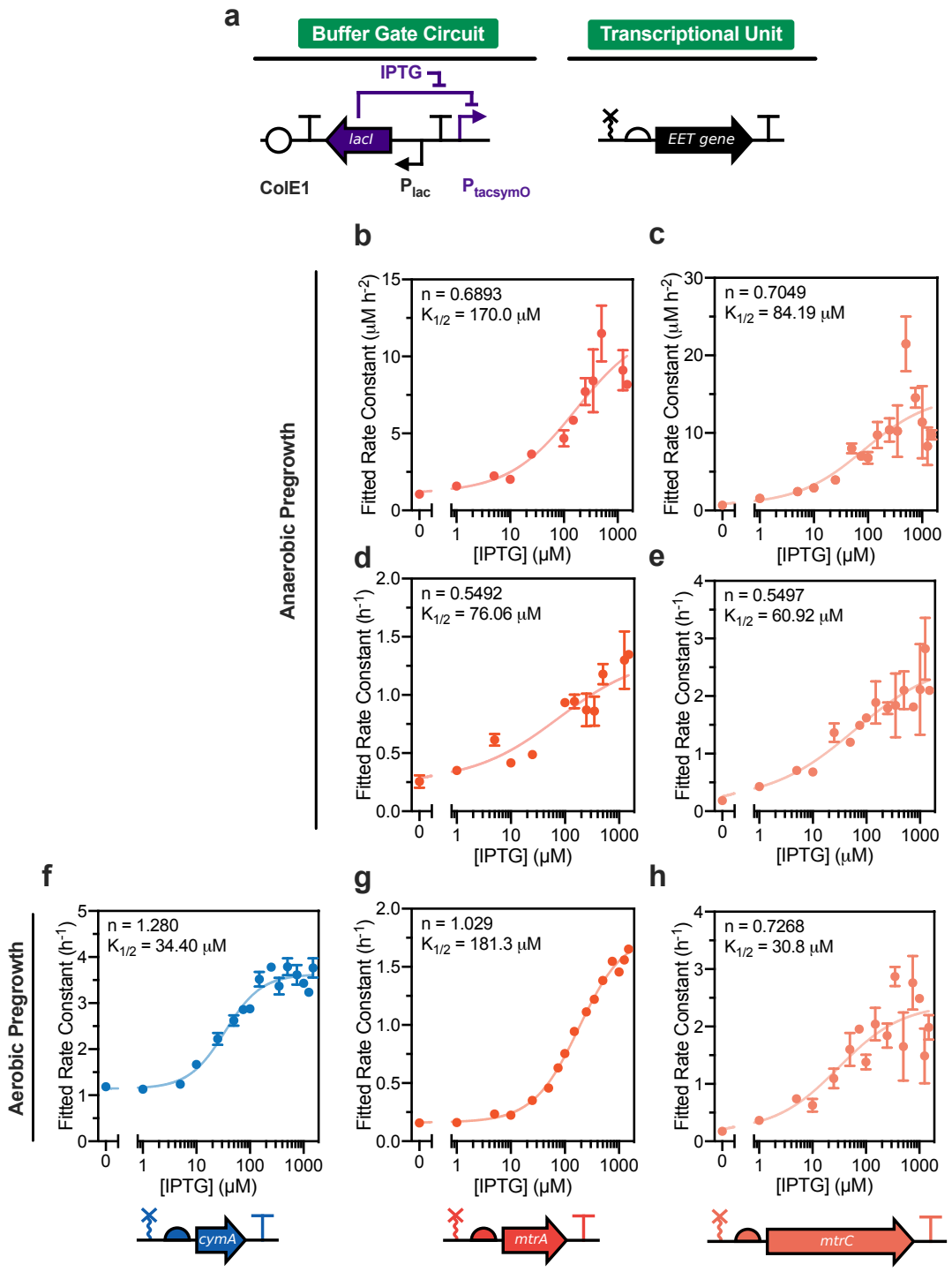

Figure D.8: Buffer gate response functions under dynamic expression for *cymA*, *mtrA*, and *mtrC* constructs using Monod and polynomial parameters.

Figure D.8: Buffer gate response functions under dynamic expression for *cymA*, *mtrA*, and *mtrC* constructs using Monod and polynomial parameters.

(a) Diagram of Buffer gate circuit used to control each EET gene transcriptional output. (b) and (d) Fe(III) reduction response functions generated by anaerobically pregrown *S. oneidensis* Δ*mtrA* expressing the *mtrA* Buffer gate circuit (pCD25r0). Kinetics were fit using the (b) polynomial model or (d) exponential model. (c) and (e) Fe(III) reduction response function generated by anaerobically pregrown *S. oneidensis* Δ*mtrC*Δ*omcA*Δ*mtrF* expressing the *mtrC* Buffer gate circuit (pCD24r1). Kinetics were fit using the (c) polynomial model or (e) exponential model. Aerobic pregrowth Fe(III) reduction response function generated by the (f) *cymA*, (g) *mtrA*, and (h) *mtrC* constructs. Kinetics for (f)-(h) were fit using the exponential model. In these experiments, IPTG was supplemented immediately prior to measuring Fe(III) reduction kinetics. The solid line and Hill parameters shown in each graph were obtained by fitting individual replicates to a four-parameter activating Hill function with weighted error. To improve Hill function fitting for (d), the minimum and maximum Hill function values were constrained by the mean fitted rate constants at 0 and 1500 μM IPTG, respectively. All data represent the mean ± s.e.m. of fitted rate constants for n = 3 biological replicates.

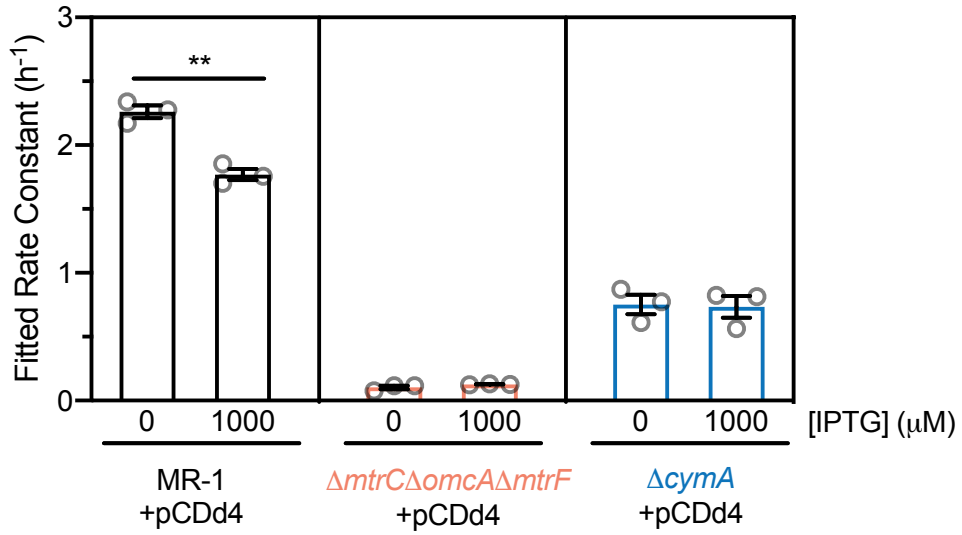

Figure D.9: NOT gate empty vector controls with MR-1 and knockout strains.

The NOT gate circuit lacking any transcriptional output gene (pCDd4) was used to transform *S. oneidensis* strains MR-1, Δ*mtrC*Δ*omcA*Δ*mtrF*, and Δ*cymA*. MR-1 and the Δ*mtrC*Δ*omcA*Δ*mtrF* strains were pregrown anaerobically. The Δ*cymA* strain was pregregrown aerobically. All strains were preinduced for 24 hours with IPTG prior to analyzing Fe(III) reduction kinetics. Kinetics were fit to the exponential model to obtain fitted rate constants. Data represent mean mean ± s.e.m. for n = 3 biological replicates. **p = 0.0018.

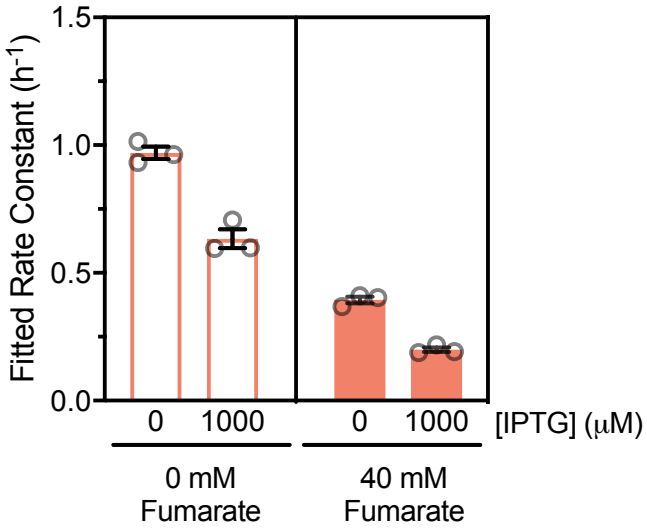

Figure D.10: Dynamic NOT gate activity for *mtrC* construct with 0 and 40 mM sodium fumarate.

S. oneidensis Δ*mtrC*Δ*omcA*Δ*mtrF* was pregrown anaerobically in the absence of IPTG. 0 or 1000 μM IPTG was added to microbially Fe(III) reduction reactions immediately prior to kinetic measurements. Additionally, experiments were supplemented with either 0 or 40 mM sodium fumarate during the Fe(III) reduction. Kinetics were fit to the exponential model to obtain fitted rate constants. Data represent mean ± s.e.m. for n = 3 biological replicates.

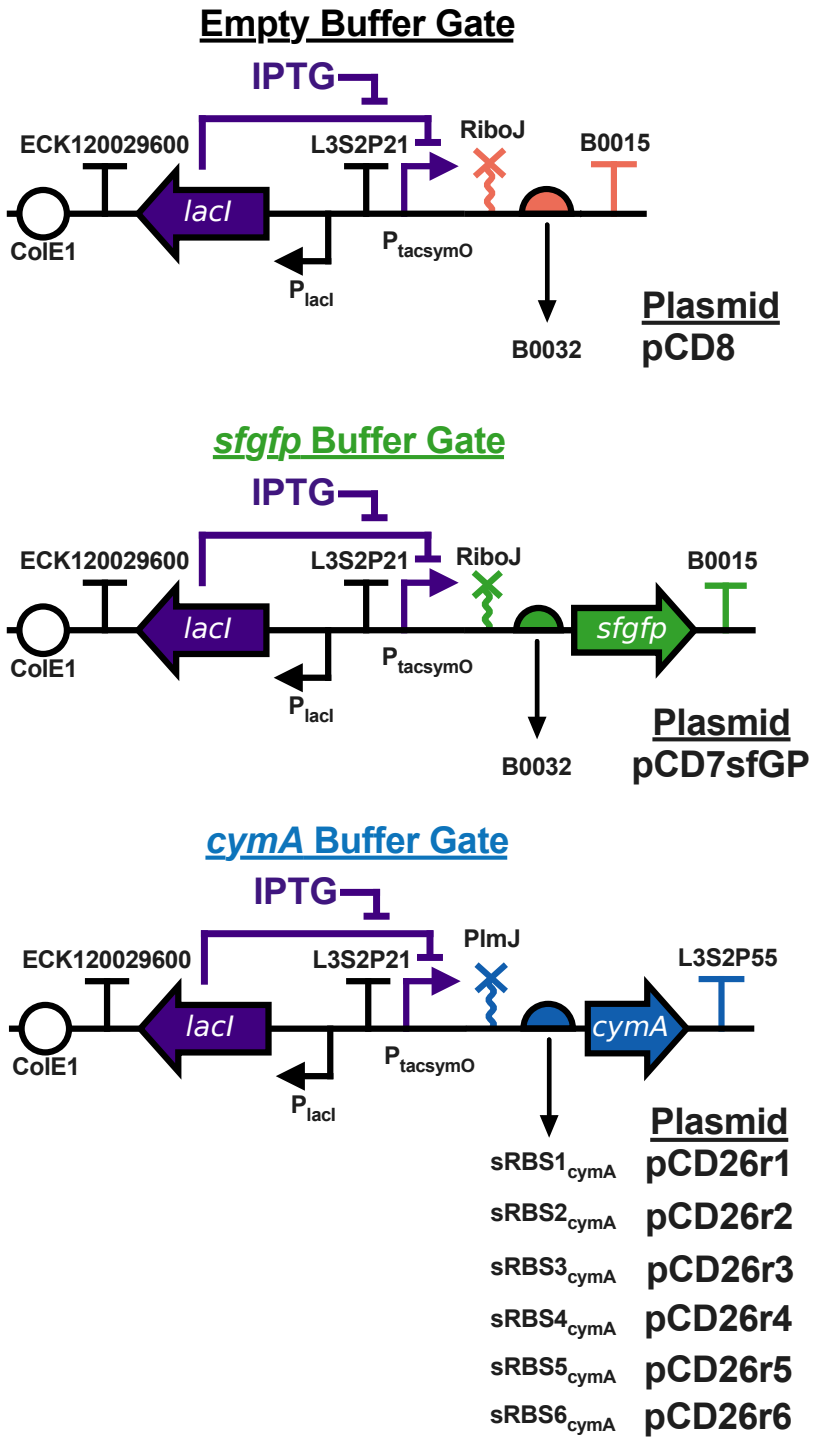

Figure D.11: Gene circuit maps for the empty, *sfgfp*, *cymA*, *mtrA*, and *mtrC* Buffer gate plasmids.

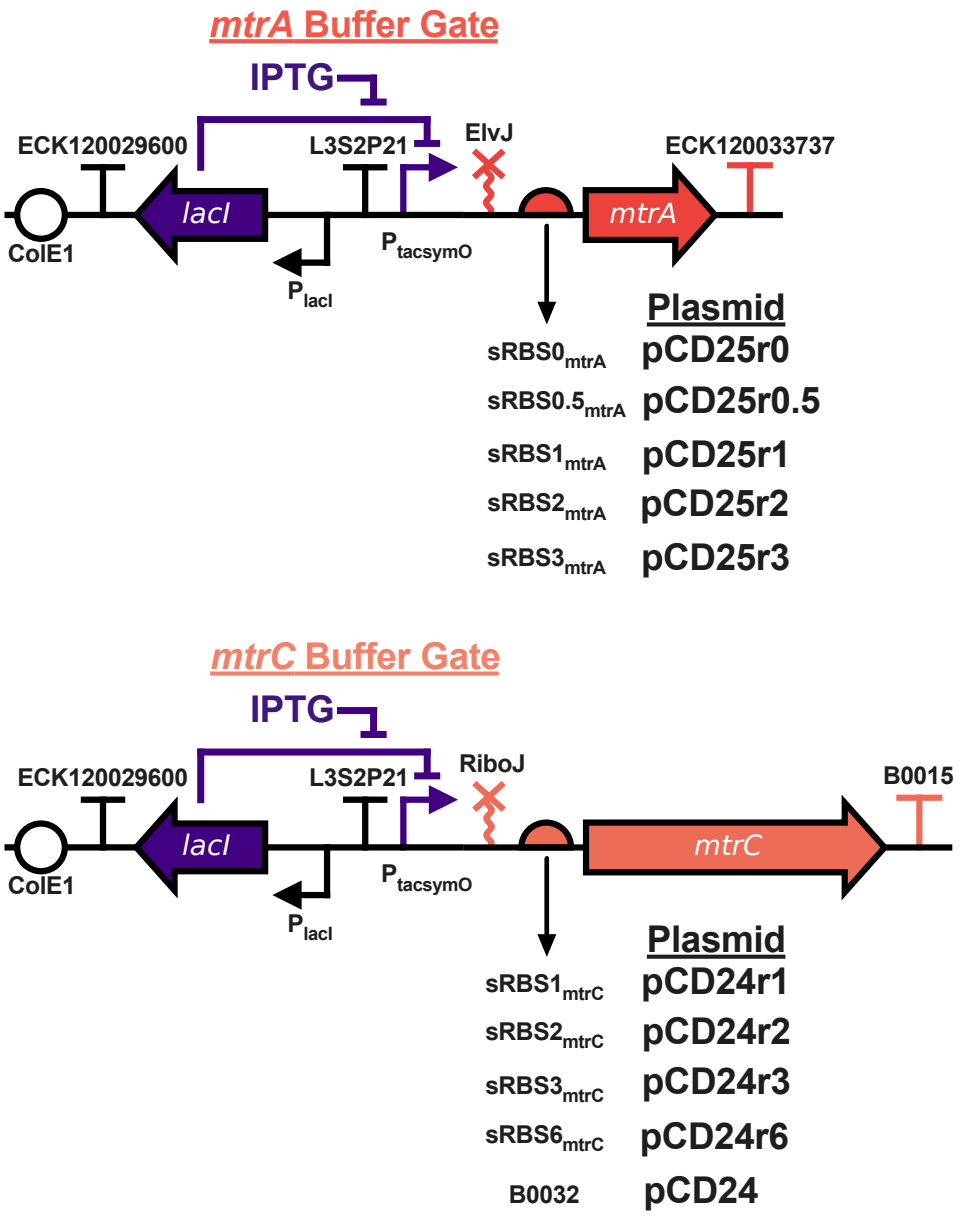

Figure D.11: Gene circuit maps for the empty, *sfgfp*, *cymA*, *mtrA*, and *mtrC* Buffer gate plasmids.

Outside of the flanking terminators, all vectors are identical and contain the ColE1 origin of replication and a kanamycin resistance marker.

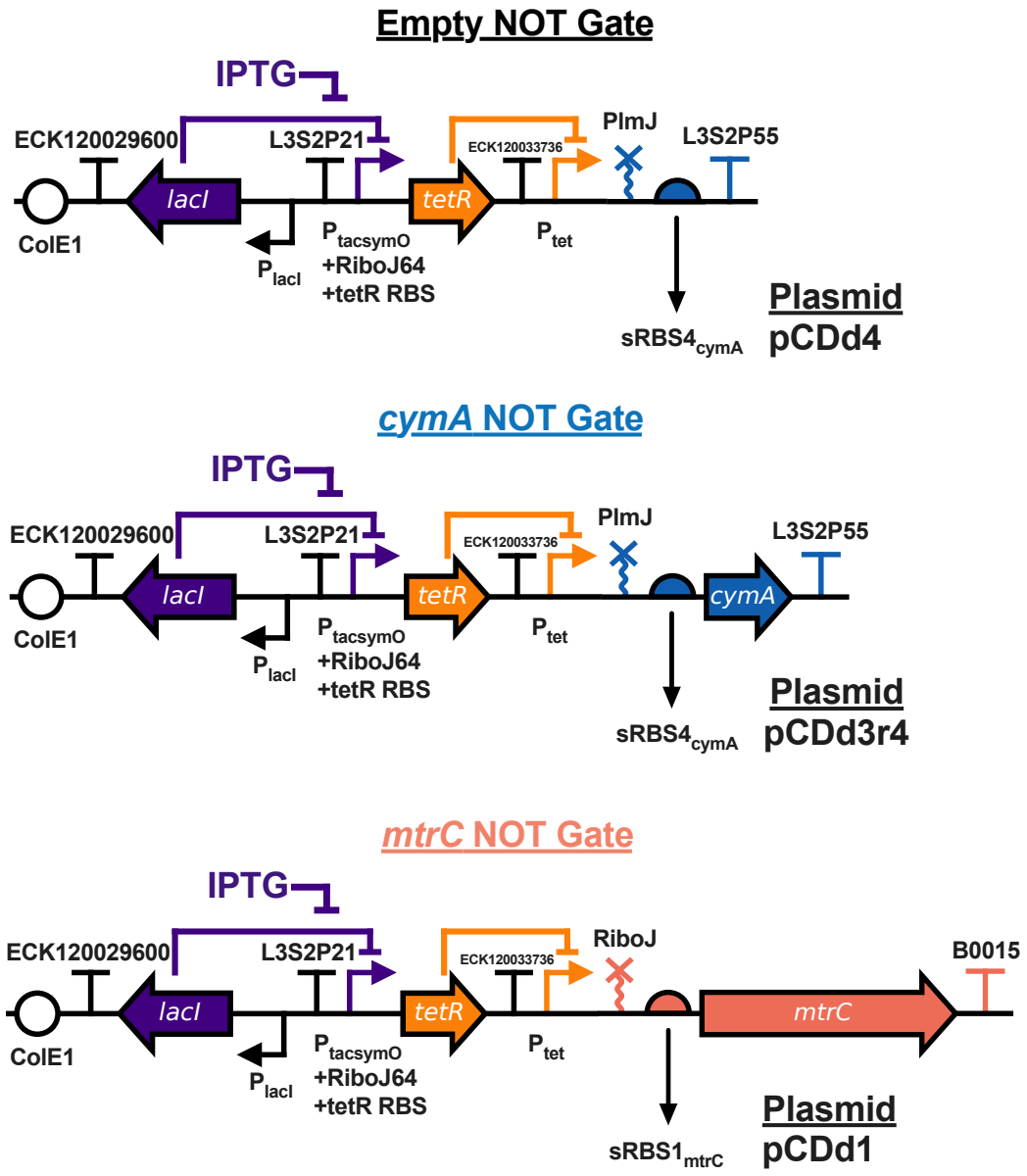

Figure D.12: Gene circuit maps for the empty, *cymA*, and *mtrC* NOT gate plasmids.

Outside of the flanking terminators, all vectors are identical and contain the ColE1 origin of replication and a kanamycin resistance marker.

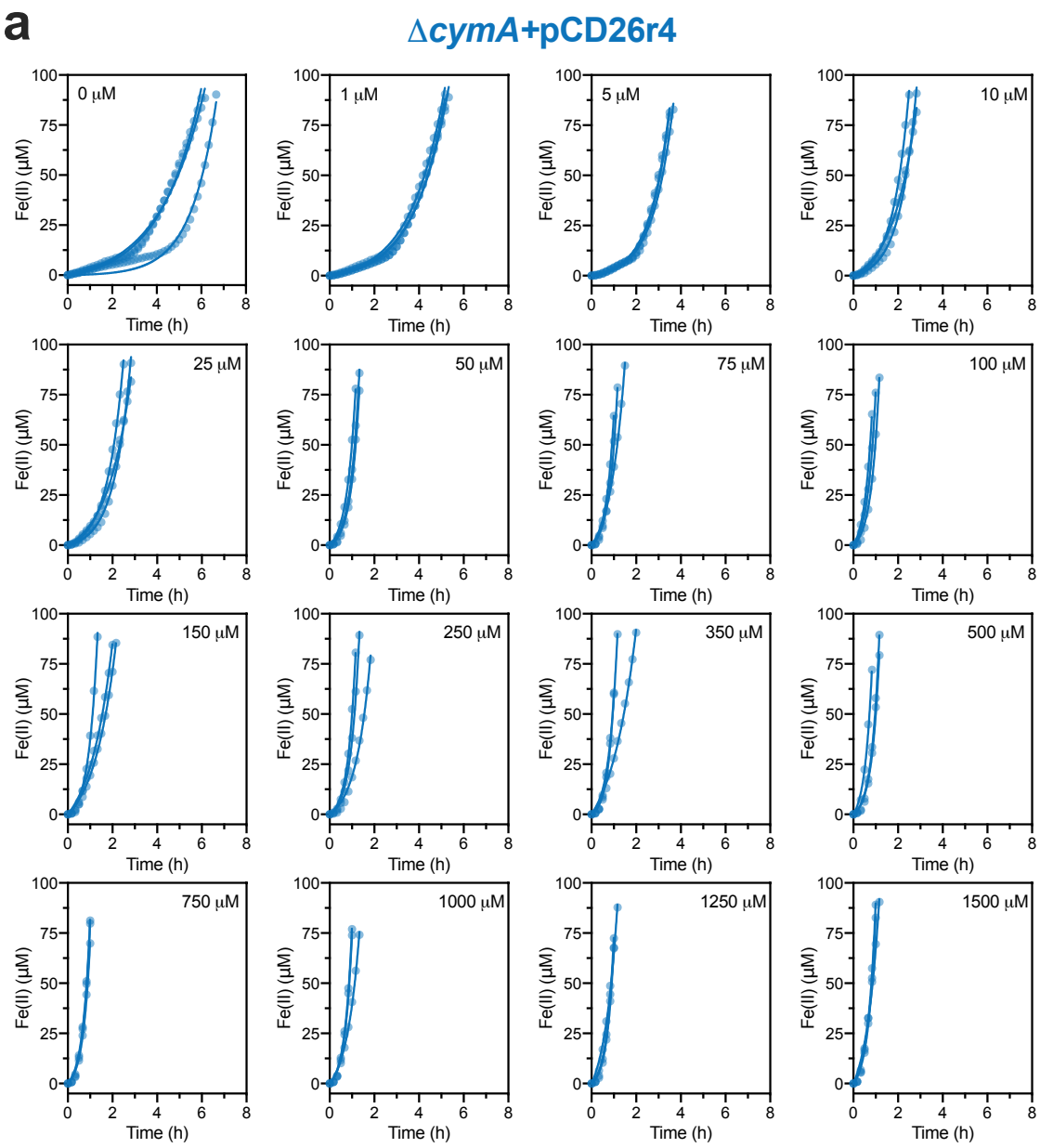

Figure D.13: Raw kinetic data and replicates for main text Figure 5.4.

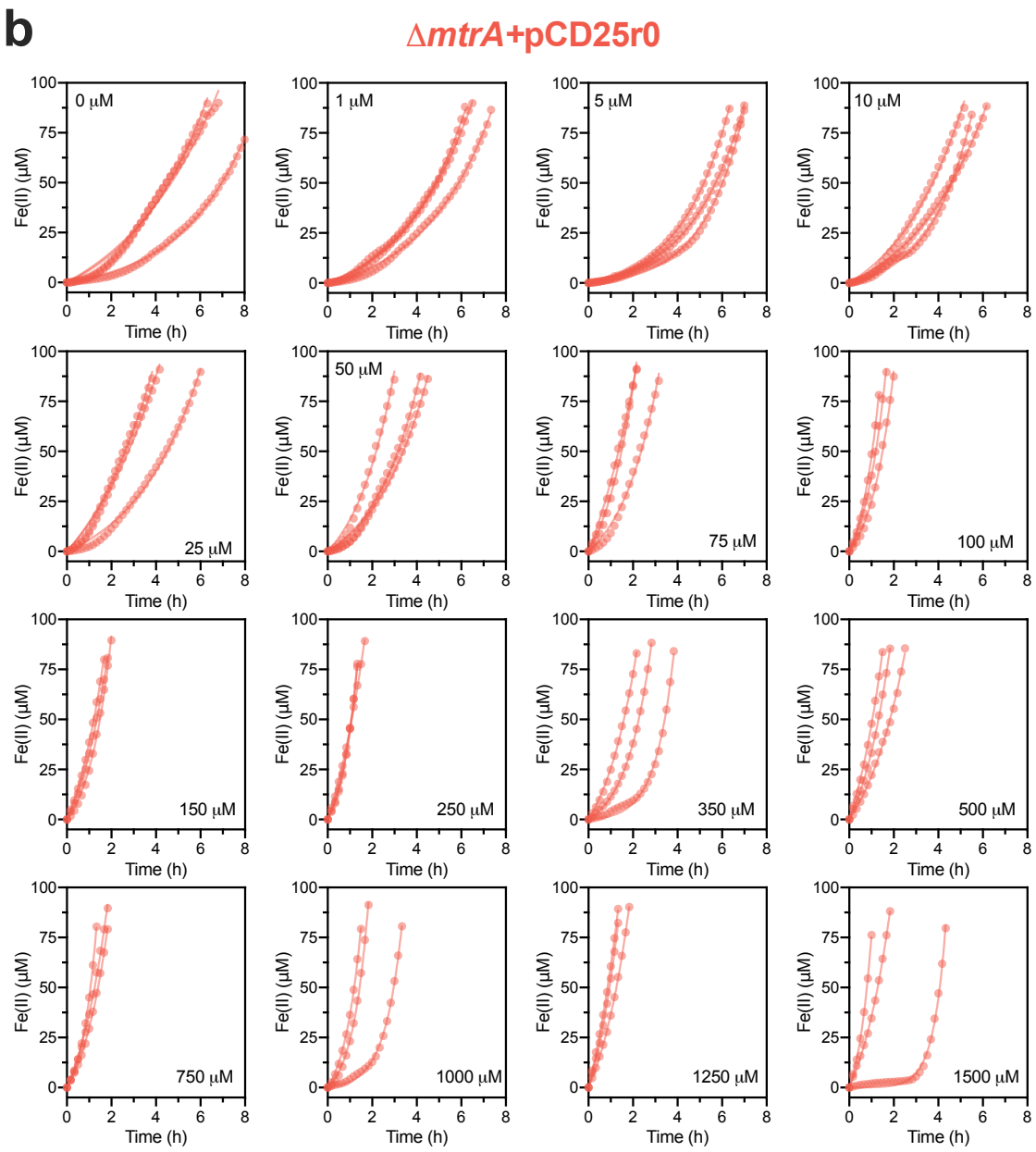

Figure D.13: Raw kinetic data and replicates for main text Figure 5.4.

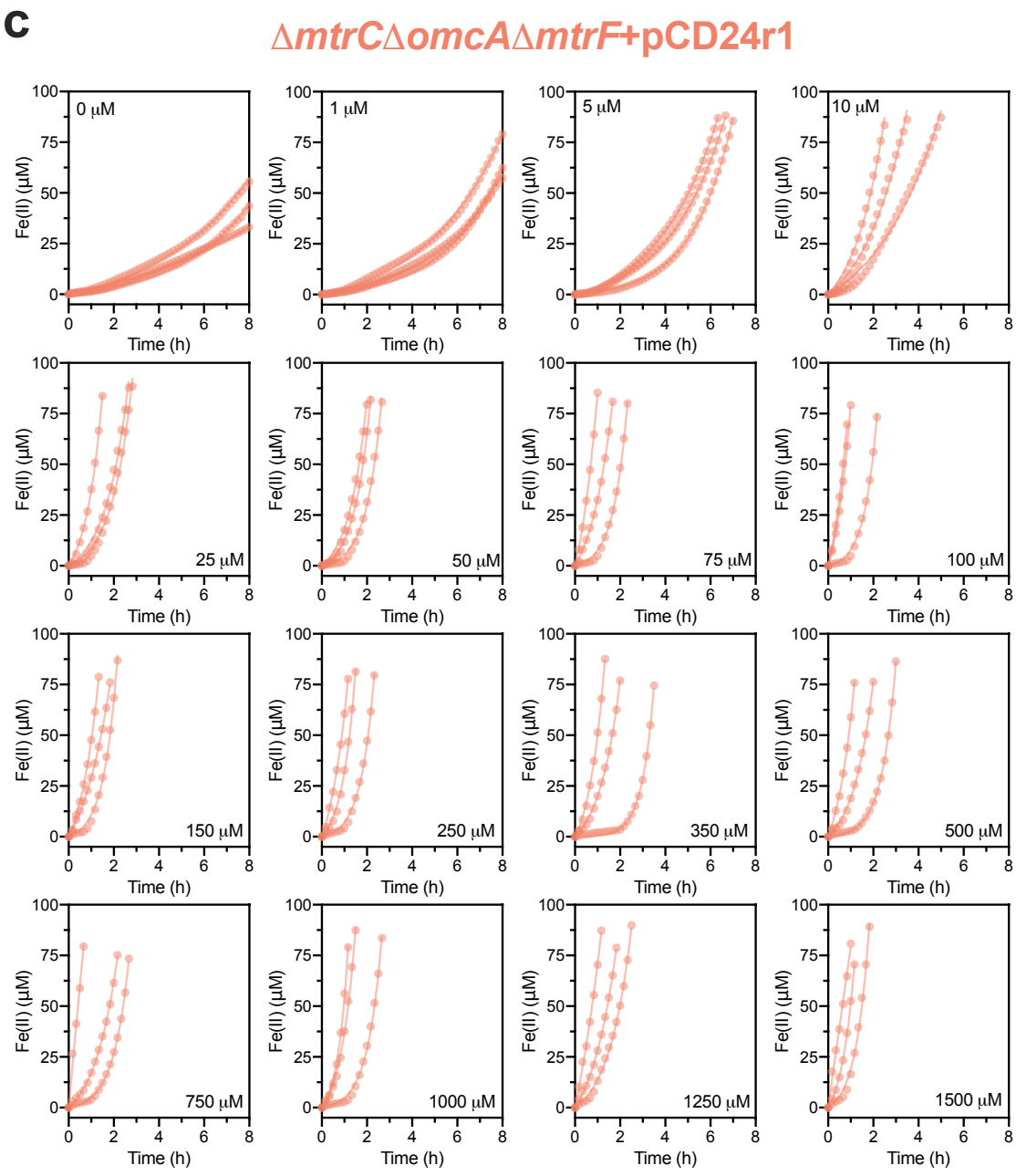

Figure D.13: Raw kinetic data and replicates for main text Figure 5.4.

Figure D.13: Raw kinetic data and replicates for main text Figure 5.4.

(a) Raw kinetic data and overlaid fitted curves for Figure 5.4c. (b) Raw kinetic data and overlaid fitted curves for Figure 5.4d. (c) Raw kinetic data and overlaid fitted curves for Figure 5.4e. IPTG concentrations are stated in the corner of each graph.

APPENDIX E: SUPPLEMENTARY DATA FOR CHAPTER 6

Supplementary Tables for Chapter 6

Strain or plasmid	Description/Genotype	Reference or source
***S. oneidensis* Strains**		
MR-1	MR-1 (ATCC700550), wild-type strain	American-Type Culture Collection
JG749	Lacks outer membrane cytochromes, MtrC and OmcA; Δ*mtrC*Δ*omcA*	86
JG596	Lacks out membrane cytochromes MtrC, OmcA, and MtrF; Δ*mtrC*Δ*omcA*Δ*mtrF*	86
JG1194	Lacks numerous proteins responsible for EET, including outer membrane cytochromes, β-barrel cytochromes, and periplasmic electron carriers; ΔMtr	111
MR-1 + pCD7sfGFP	Wild-type with a LacI repressed *sfGFP* circuit (Fig. S16-17)	This work
JG596 + pCD7sfGFP	JG596 with a LacI repressed *sfGFP* circuit (Fig. E.16-17)	This work
MR-1 + pCD8	Wild-type with an empty vector on the LacI repressed circuit	This work
JG596 + pCD8	JG596 with an empty vector on the LacI repressed circuit (Fig. E.17)	This work
JG596 + pCD24r1	JG596 with a LacI repressed *mtrC* circuit (Fig. E.16-17)	This work
***E. coli* Strains**		
MG1655	Wild-type strain	Lydia Contreras, U. of Texas at Austin
Plasmids		
pCD7sfGFP	See Fig. E.16-17	This work
pCD8	See Fig. E.17	This work
pCD24r1	See Fig. E.16-17	This work

Table E.1: Bacterial strains and plasmids used in this study.

Ingredient	Quantity for 1L of 1x SBM
K_2HPO_4	225 mg
KH_2PO_4	225 mg
NaCl	460 mg
$(NH_4)_2SO_4$	1.703 mL of 1 M stock
$MgSO_4 \cdot 7H_2O$	0.475 mL of 1 M stock

HEPES	100 mL of 1 M stock
Casamino acids	5 mL of 10% stock
Wolfe's mineral solution	5 mL of 200x stock
ddH_2O	Up to 1 L, adjust to pH = 7.2

Table E.2: Ingredients in *Shewanella* Basal Medium. Growth media was supplemented with casamino acids and Wolfe's mineral solution, whereas crosslinking media was only supplemented with casamino acids.

Reagent	Quantity in 1L of 200X Stock
EDTA	0.5 g (2.69 mL of 0.5 M stock)
$MgSO_4•7H_2O$	3.0 g
$MnSO_4•H_2O$	0.5 g
NaCl	1.0 g
$FeSO_4•7H_2O$	0.1 g
$Co(NO_3)_2•6H_2O$	0.1 g
$CaCl_2$	0.9 mL from 1 M stock
$ZnSO_4•7H_2O$	0.1 g
$CuSO_4•5H_2O$	10 mg
$AlK(SO_4)_2$	10 mg
H_3BO_3	10 mg
$Na_2MoO4•2H_2O$	10 mg
Na_2SeO_3	1 mg
$Na_2WO_4•2H_2O$	10 mg
$NiCl_2•6H_2O$	20 mg
ddH_2O	1 L

Table E.3: Ingredients in Wolfe's mineral solution, adapted from ATCC recipe.

Genetic Part	DNA Sequence (5' to 3')
Promoters	
$P_{tacsymO}$	TGTTGACAATTAATCATCGGCTCGTATAATGTGTGGAATTGTGAGCGC TCACAATTCTATGGACTATGTTT
P_{lacI}	GCGGCGCGCCATCGAATGGCGCAAAACCTTTCGCGGTATGGCATGAT AGCGCCCGGAAGAGAGTCAATTCAGGGTGGTGAAT
Ribosome Binding Sites	

B0032	TCACACAGGAAAGTACTAG
$sRBS1_{mtrC}$	GGGGAAAAACAGCAGTGCGAT
Terminators	
ECK120029600	TTCAGCCAAAAAACTTAAGACCGCCGGTCTTGTCCACTACCTTGCAGT AATGCGGTGGACAGGATCGGCGGTTTTCTTTTCTCTTCTCAA
L3S2P2111	TCGGTACCAAATTCCAGAAAAGAGGCCTCCCGAAAGGGGGGCCTTTT TTCGTTTTGGTCC
B0015	TAATCTAGACCAGGCATCAAATAAAACGAAAGGCTCAGTCGAAAGACT GGGCCTTTCGTTTTATCTGTTGTTTGTCGGTGAACGCTCTCTACTAGA GTCACACTGGCTCACCTTCGGGTGGGCCTTTCTGCGTTTATA
Ribozymes	
RiboJ	AGCTGTCACCGGATGTGCTTTCCGGTCTGATGAGTCCGTGAGGACGA AACAGCCTCTACAAATAATTTTGTTTAA
Genes	
lacI	GTGAAACCAGTAACGTTATACGATGTCGCAGAGTATGCCGGTGTCTCT TATCAGACCGTTTCCCGCGTGGTGAACCAGGCCAGCCACGTTTCTGC GAAAACGCGGGAAAAAGTGGAAGCGGCGATGGCGGAGCTGAATTAC ATTCCCAACCGCGTGGCACAACAACTGGCGGGCAAACAGTCGTTGCT GATTGGCGTTGCCACCTCCAGTCTGGCCCTGCACGCGCCGTCGCAAA TTGTCGCGGCGATTAAATCTCGCGCCGATCAACTGGGTGCCAGCGTG GTGGTGTCGATGGTAGAACGAAGCGGCGTCGAAGCCTGTAAAGCGG CGGTGCACAATCTTCTCGCGCAACGCGTCAGTGGGCTGATCATTAAC TATCCGCTGGATGACCAGGATGCCATTGCTGTGGAAGCTGCCTGCAC TAATGTTCCGGCGTTATTTCTTGATGTCTCTGACCAGACACCCATCAA CAGTATTATTTTCTCCCATGAAGACGGTACGCGACTGGGCGTGGAGC ATCTGGTCGCATTGGGTCACCAGCAAATCGCGCTGTTAGCGGGCCCA TTAAGTTCTGTCTCGGCGCGTCTGCGTCTGGCTGGCTGGCATAAATAT CTCACTCGCAATCAAATTCAGCCGATAGCGGAACGGGAAGGCGACTG GAGTGCCATGTCCGGTTTTCAACAAACCATGCAAATGCTGAATGAGG GTATCGTTCCCACTGCGATGCTGGTTGCCAACGATCAGATGGCGCTG GGCGCAATGCGCGCCATTACCGAGTCCGGGCTGCGCGTTGGTGCGG ATATCTCGGTAGTGGGATACGACGATACCGAAGACAGCTCATGTTATA TCCCGCCGTTAACCACCATCAAACAGGATTTTCGCCTGCTGGGGCAA ACCAGCGTGGACCGCTTGCTGCAACTCTCTCAGGGCCAGGCGGTGA AGGGCAATCAGCTGTTGCCCGTGTCACTGGTGAAAAGAAAAACCACC CTGGCGCCCAATACGCAAACCGCCTCTCCCCGCGCGTTGGCCGATTC ATTAATGCAGCTGGCACGACAGGTTTCCCGACTGGAAAGCGGGCAGT GA
sfgfp	ATGCGTAAAGGCGAAGAGCTGTTCACTGGTGTCGTCCCTATTCTGGT GGAACTGGATGGTGATGTCAACGGTCATAAGTTTTCCGTGCGTGGCG AGGGTGAAGGTGACGCAACTAATGGTAAACTGACGCTGAAGTTCATC TGTACTACTGGTAAACTGCCGGTACCTTGGCCGACTCTGGTAACGAC GCTGACTTATGGTGTTCAGTGCTTTGCTCGTTATCCGGACCATATGAA GCAGCATGACTTCTTCAAGTCCGCCATGCCGGAAGGCTATGTGCAGG AACGCACGATTTCCTTTAAGGATGACGGCACGTACAAAACGCGTGCG GAAGTGAAATTTGAAGGCGATACCCTGGTAAACCGCATTGAGCTGAAA GGCATTGACTTTAAAGAAGACGGCAATATCCTGGGCCATAAGCTGGA ATACAATTTTAACAGCCACAATGTTTACATCACCGCCGATAAACAAAAA AATGGCATTAAAGCGAATTTTAAAATTCGCCACAACGTGGAGGATGGC AGCGTGCAGCTGGCTGATCACTACCAGCAAAACACTCCAATCGGTGA TGGTCCTGTTCTGCTGCCAGACAATCACTATCTGAGCACGCAAAGCGT

	TCTGTCTAAAGATCCGAACGAGAAACGCGATCATATGGTTCTGCTGGA GTTCGTAACCGCAGCGGGCATCACGCATGGTATGGATGAACTGTACA AATGATGA
mtrC	ATGATGAACGCACAAAAATCAAAAATCGCACTGCTGCTCGCAGCAAGT GCCGTCACAATGGCCTTAACCGGCTGTGGTGGAAGCGATGGTAATAA CGGCAATGATGGTAGTGATGGTGGTGAGCCAGCAGGTAGCATCCAGA CGTTAAACCTAGATATCACTAAAGTAAGCTATGAAAATGGTGCACCTAT GGTCACTGTTTTCGCCACTAACGAAGCCGACATGCCAGTGATTGGTCT CGCAAATTTAGAAATCAAAAAAGCACTGCAATTAATACCGGAAGGGGC GACAGGCCCAGGTAATAGCGCTAACTGGCAAGGCTTAGGCTCATCAA AGAGCTATGTCGATAATAAAAACGGTAGCTATACCTTTAAATTCGACG CCTTCGATAGTAATAAGGTCTTTAATGCTCAATTAACGCAACGCTTTAA CGTTGTTTCTGCTGCGGGTAAATTAGCAGACGGAACGACCGTTCCCG TTGCCGAAATGGTTGAAGATTTCGACGGCCAAGGTAATGCGCCGCAA TATACAAAAAATATCGTTAGCCACGAAGTATGTGCTTCTTGCCACGTA GAAGGTGAAAAGATTTATCACCAAGCTACTGAAGTCGAAACTTGTATT TCTTGCCACACTCAAGAGTTTGCGGATGGTCGCGGCAAACCCCATGT CGCCTTTAGTCACTTAATTCACAATGTGCATAATGCCAACAAAGCTTG GGGCAAAGACAATAAAATCCCTACAGTTGCACAAAATATTGTCCAAGA TAATTGCCAAGTTTGTCACGTTGAATCCGACATGCTCACCGAGGCAAA AAACTGGTCACGTATTCCAACAATGGAAGTCTGTTCTAGCTGTCACGT AGACATCGATTTTGCTGCGGGTAAAGGCCACTCTCAACAACTCGATAA CTCCAACTGTATCGCCTGCCATAACAGCGACTGGACTGCTGAGTTACA CACAGCCAAAACCACCGCAACTAAGAACTTGATTAATCAATACGGTAT CGAGACTACCTCGACAATTAATACCGAAACTAAAGCAGCCACAATTAG TGTTCAAGTTGTAGATGCGAACGGTACTGCTGTTGATCTCAAGACCAT CCTGCCTAAAGTGCAACGCTTAGAGATCATCACCAACGTTGGTCCTAA TAATGCAACCTTAGGTTATAGTGGCAAAGATTCAATATTTGCAATCAAA AATGGAGCTCTTGATCCAAAAGCTACTATCAATGATGCTGGCAAACTG GTTTATACCACTACTAAAGACCTCAAACTTGGCCAAAACGGCGCAGAC AGCGACACAGCATTTAGCTTTGTAGGTTGGTCAATGTGTTCTAGCGAA GGTAAGTTTGTAGACTGTGCAGACCCTGCATTTGATGGTGTTGATGTA ACTAAGTATACCGGCATGAAAGCGGATTTAGCCTTTGCTACTTTGTCA GGTAAAGCACCAAGTACTCGCCACGTTGATTCTGTTAACATGACAGCC TGTGCCAATTGCCACACTGCTGAGTTCGAAATTCACAAAGGCAAACAA CATGCAGGCTTTGTGATGACAGAGCAACTATCACACACCCAAGATGCT AACGGTAAAGCGATTGTAGGCCTTGACGCATGTGTGACTTGTCATACT CCTGATGGCACCTATAGCTTTGCCAACCGTGGTGCGCTAGAGCTAAA ACTACACAAAAAACACGTTGAAGATGCCTACGGCCTCATTGGTGGCAA TTGTGCCTCTTGTCACTCAGACTTCAACCTTGAGTCTTTCAAGAAGAAA GGCGCATTGAATACTGCCGCTGCAGCAGATAAAACAGGTCTATATTCT ACGCCGATCACTGCAACTTGTACTACCTGTCACACAGTTGGCAGCCA GTACATGGTCCATACGAAAGAAACCCTGGAGTCTTTCGGTGCAGTTGT TGATGGCACAAAAGATGATGCTACCAGTGCGGCACAGTCAGAAACCT GTTTCTACTGCCATACCCCAACAGTTGCAGATCACACTAAAGTGAAAA TGTAA

Table E.4: Genetic parts/sequences used to construct the plasmids in this study.

Parameter	*sfgfp* Nonlinear Fit Value (units)	*mtrC* Nonlinear Fit Value (units)
Best-fit Values		
Hillslope	1.569	1.402
EC_{50}	98.58 (μM)	96.38 (μM)
Max	1.032 (REU)	3360 (Pa); 1.08 (Relative Hydrogel Modulus)
Min	0.2086 (REU)	158.4 (Pa); 0.05 (Relative Hydrogel Modulus)
95% Confidence Interval		
Hillslope	1.028 to 2.505	0.3979 to 4.671
EC_{50}	78.01 to 132.5 (μM)	50.92 to 3650 (μM)
Max	0.9654 to 1.137 (REU)	2730 to 9795 (Pa)
Min	0.1475 to 0.2644 (REU)	-401.7 to 568.6 (Pa)
Goodness of Fit		
R^2	0.9314	0.8632

Table E.5: Nonlinear fit parameters for products of *sfgfp* expression (fluorescence) and *mtrC* expression (storage modulus)

Supplementary Figures for Chapter 6

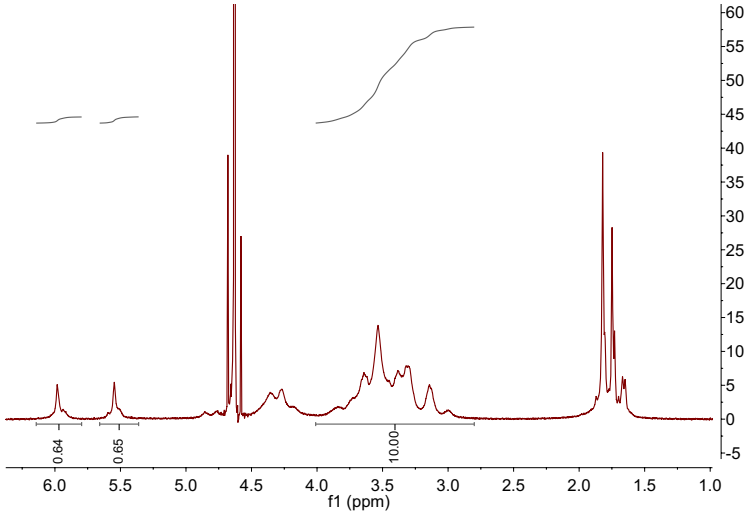

Figure E.1: ^{1}H-NMR spectrum of 65% methacrylated hyaluronic acid macromer dissolved in D_2O after synthesis, dialysis, and lyophilization.

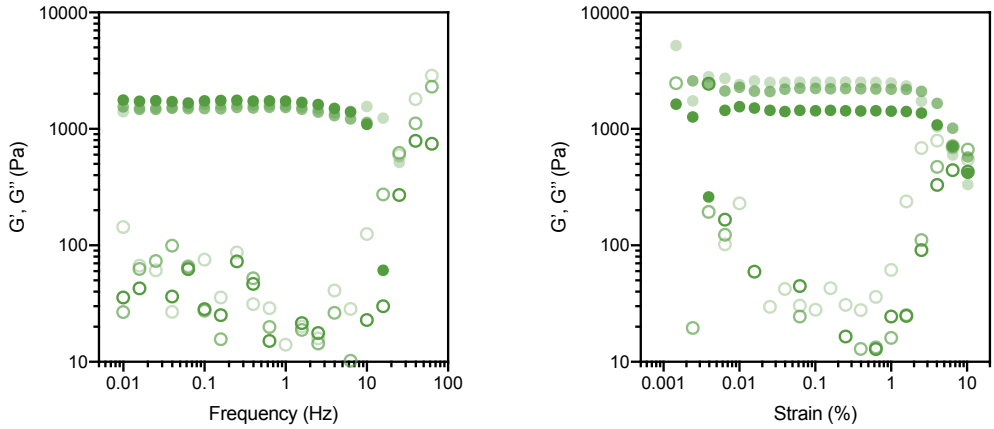

Figure E.2: Strain and frequency sweeps of MeHA hydrogels crosslinked by *S. oneidensis* MR-1 at standard conditions (OD_{600} = 0.2 cells, 3 wt.% MeHA65, 10 µM Cu-TPMA, 500 µM HEBIB, 20 mM lactate, 40 mM fumarate) to determine storage modulus (G', closed circles) and loss modulus (G'', open circles) for n = 3 biological replicates.

Storage modulus calculations for all subsequent gels were made using frequency sweeps at 0.1% strain, which is within the linear viscoelastic regime.

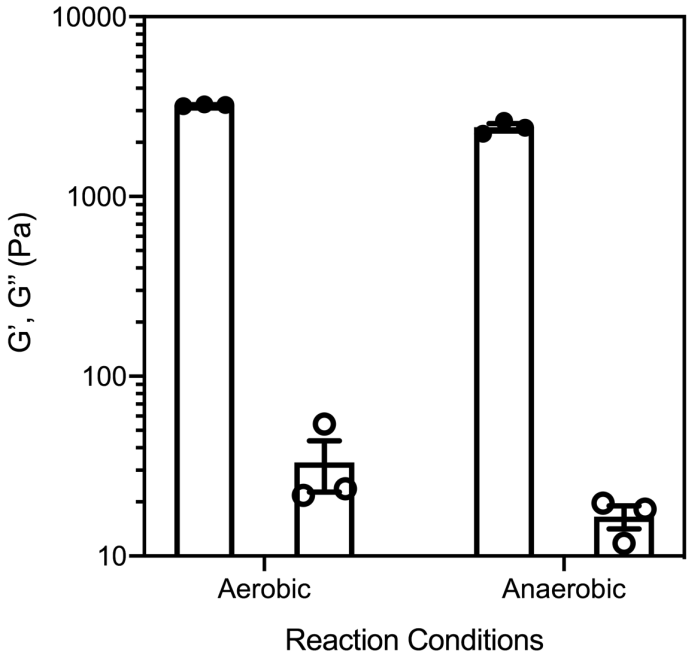

Figure E.3: Storage modulus (G', filled circles) and loss modulus (G'', open circles) of hydrogels crosslinked by *S. oneidensis* MR-1 at standard conditions in either aerobic or anaerobic environments.

Data shown are mean ± SEM for n = 3 biological replicates. MeHA65 networks are predominately elastic in nature, as demonstrated by significantly larger G' than G''.

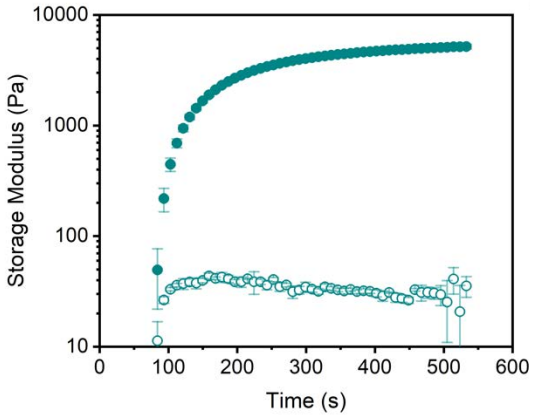

Figure E.4: *In situ* rheology showing G' (filled circles) and G'' (open circles) of MeHA65 gels synthesized using 500 µM lithium phenyl-2,4,6-trimethylbenzoylphosphinate (LAP) as a photoinitiator with 365 nm light at 10 mW/cm^2 laser intensity.

Data are reported as the mean ± SD of n = 3 gels.

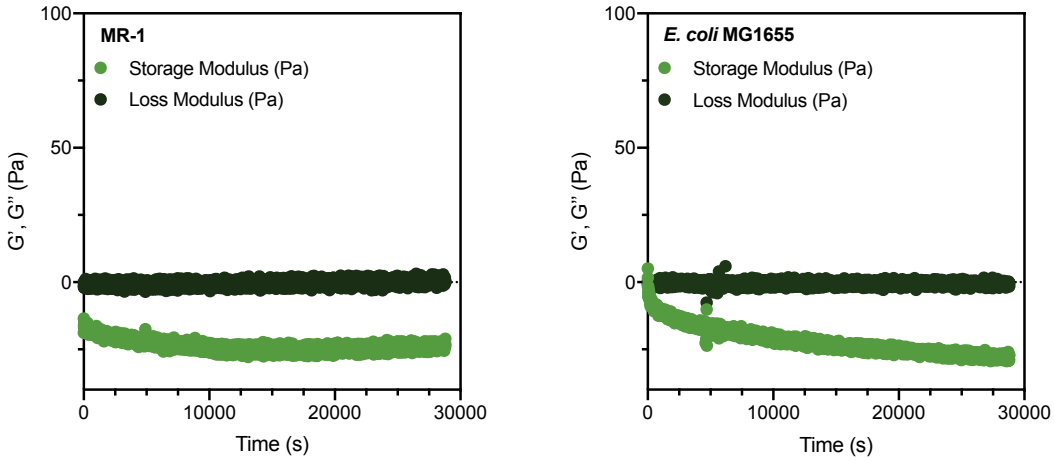

Figure E.5: *In situ* rheology showing G' and G'' of non-functionalized HA solutions containing all crosslinking components and either MR-1 (left) or *E. coli* MG1655 (right).

Gels did not form; negative G' is attributed to dominant inertial forces and small plate geometry (weak elastic component)[502].

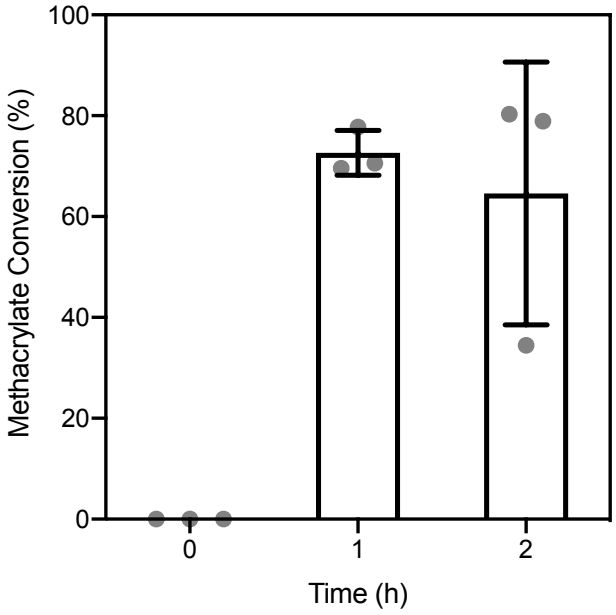

Figure E.6: Methacrylate functional group conversion as determined by ^{1}H-NMR spectroscopy after enzymatically degrading MeHA hydrogels with hyaluronidase.

Samples were diluted in D_2O and the integration values of the methacrylate peaks were normalized against the average value at $t = 0$ h to determine conversion. Gels were formed at standard conditions using *S. oneidensis* MR-1. Data reported are the mean ± SD of $n = 3$ gels.

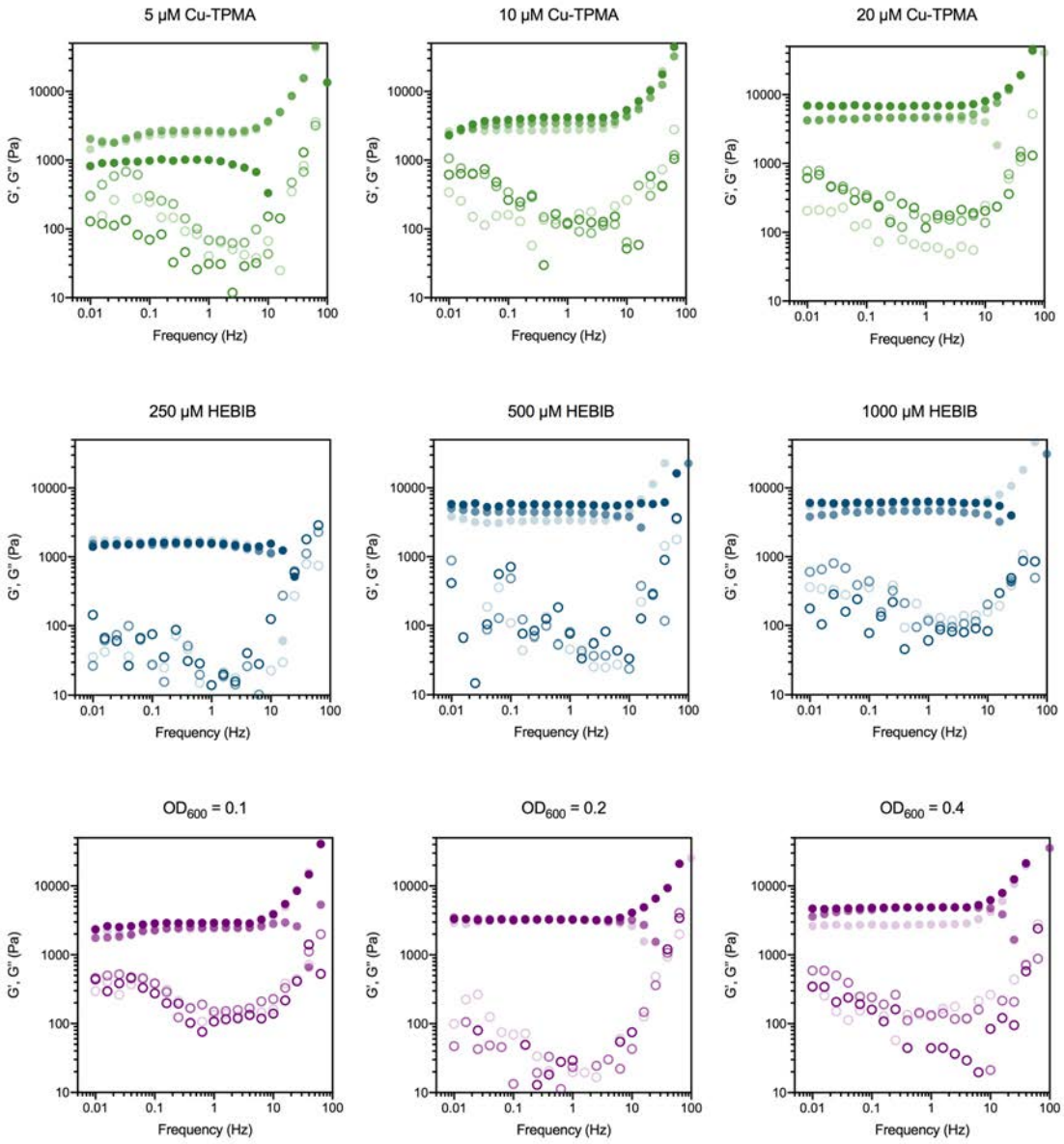

Figure E.7: Rheological frequency sweeps for end-point measurements in Fig. 6.2. G' (filled circles) and G'' (open circles) for n = 3 biological replicates.

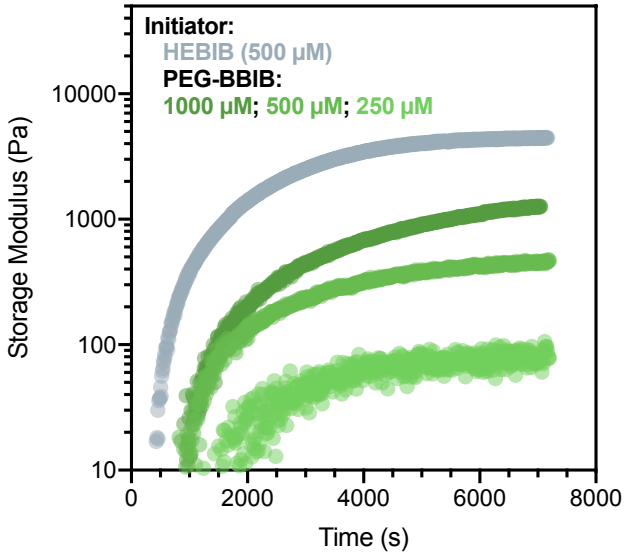

Figure E.8: *In situ* G' measurement of MeHA65 gels synthesized using varying concentrations of poly(ethylene glycol) bis(2-bromoisobutyrate) ($M_{n,avg}$ = 700 g/mol, PEGBBiB). HEBiB, the initiator for standard gelation conditions, is included for comparison.

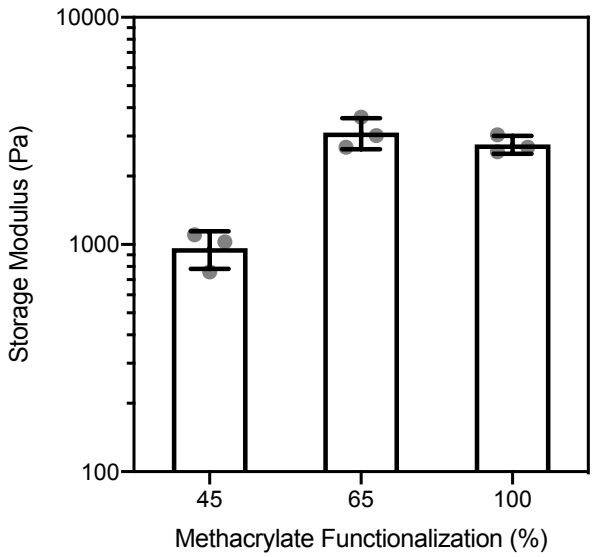

Figure E.9: Storage modulus for MeHA hydrogels crosslinked at standard conditions for 2 hours with varying degrees of methacrylate functionalization of the HA backbone.

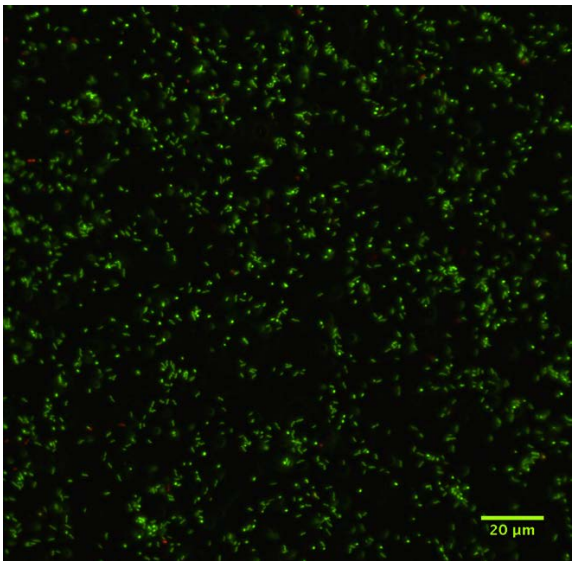

Figure E.10: Viability analysis 5 days after crosslinking as determined by the BacLight Live/Dead stain. Cells are almost completely viable (green) as opposed to non-viable (red).

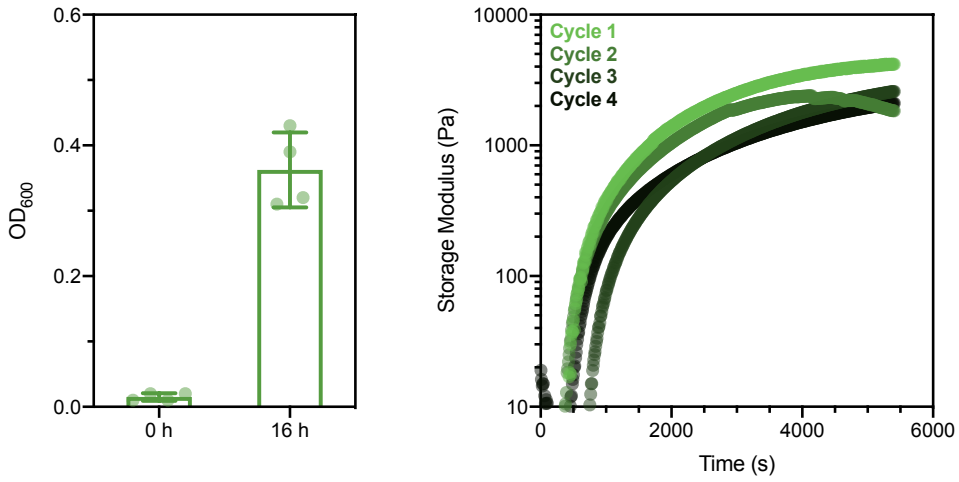

Figure E.11: Cells can be recovered after crosslinking to synthesize new gels.

Left, OD_{600} measurements of cultures after inoculating from swelling mixture into growth media, data are shown as mean ± SEM of $n = 4$ measurements. Right, *in situ* storage modulus measurements (right) of gels crosslinked by recovered bacteria cultures (inoculated from hydrogel swelling media and grown overnight).

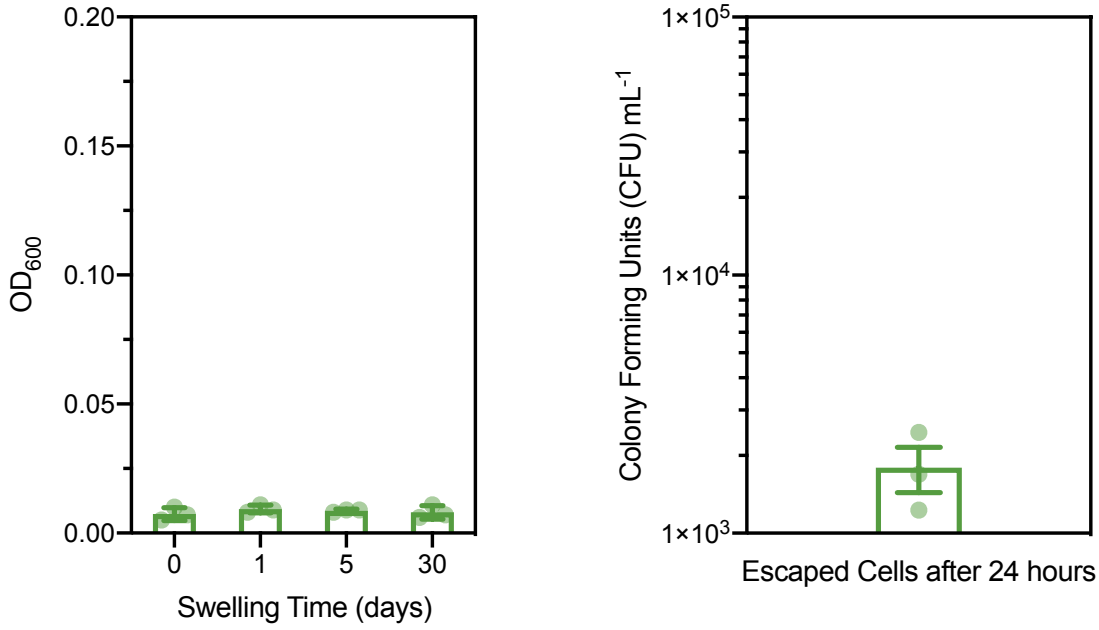

Figure E.12: Bacteria do not appreciably escape the gels after synthesis. OD_{600} measurements of swelling media (left) after washing gels 3x in PBS and allowing to swell in 1 mL PBS for varying lengths of time.

Colony counting (right) confirms that escaped cells account for < 0.005% of inoculating density (~4 x 10^7 CFU/mL or OD_{600} = 0.2) after 3x washing in PBS. Data are shown as mean ± SEM for n = 3 biological replicates.

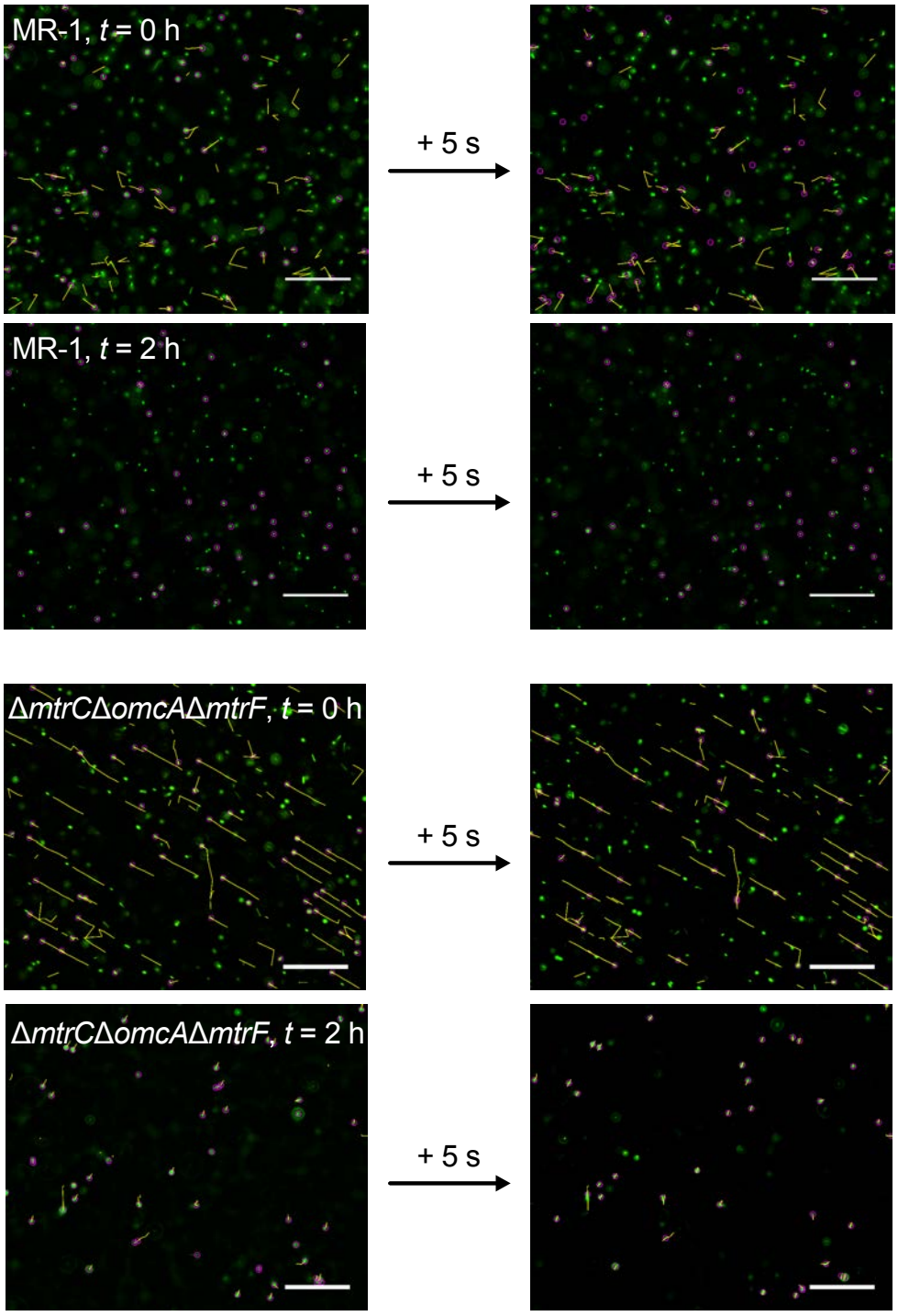

Figure E.13: Fluorescence microscopy images of 1000 μM IPTG induced MR-1 and Δ*mtrC*Δ*omcA*Δ*mtrF* strains show swimming and convective movement over 5 seconds.

Figure E.13: Fluorescence microscopy images of 1000 µM IPTG induced MR-1 and Δ*mtrC*Δ*omcA*Δ*mtrF* strains show swimming and convective movement over 5 seconds.

Cells (purple circles) were tracked over 5 s (yellow lines) using TrackMate in Fiji 1.0. The average displacement of highest quality tracks (as determined by the software, $n = 33$) was then calculated for each strain at 0 and 2 hours. Scale bars are 40 µm.

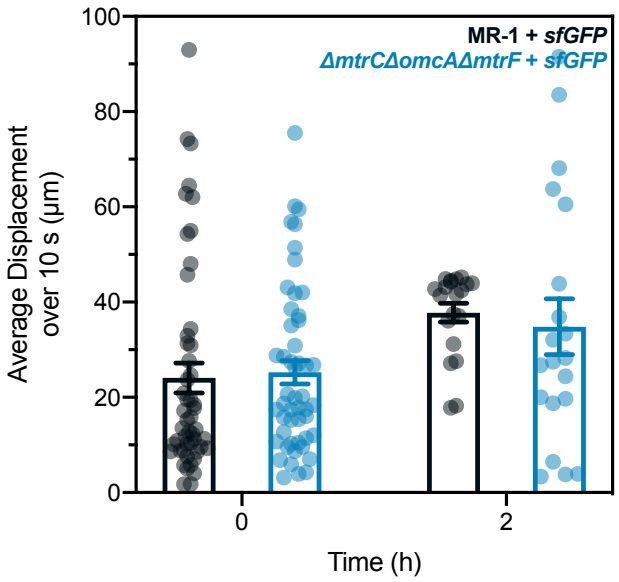

Figure E.14: Average cell displacement within a non-functionalized 3 wt.% HA solution as measured by microscopy over 10 s time-lapses at 0 and 2 hours.

Displacement was quantified using TrackMate in Fiji 1.0. Student t-test shows no statistical difference ($p = 0.95$ at 0 hours, $n = 50$; $p = 0.76$ at 2 hours, $n = 20$), indicating that differences in the functionalized MeHA is due to crosslinking. Data are shown as mean ± SEM.

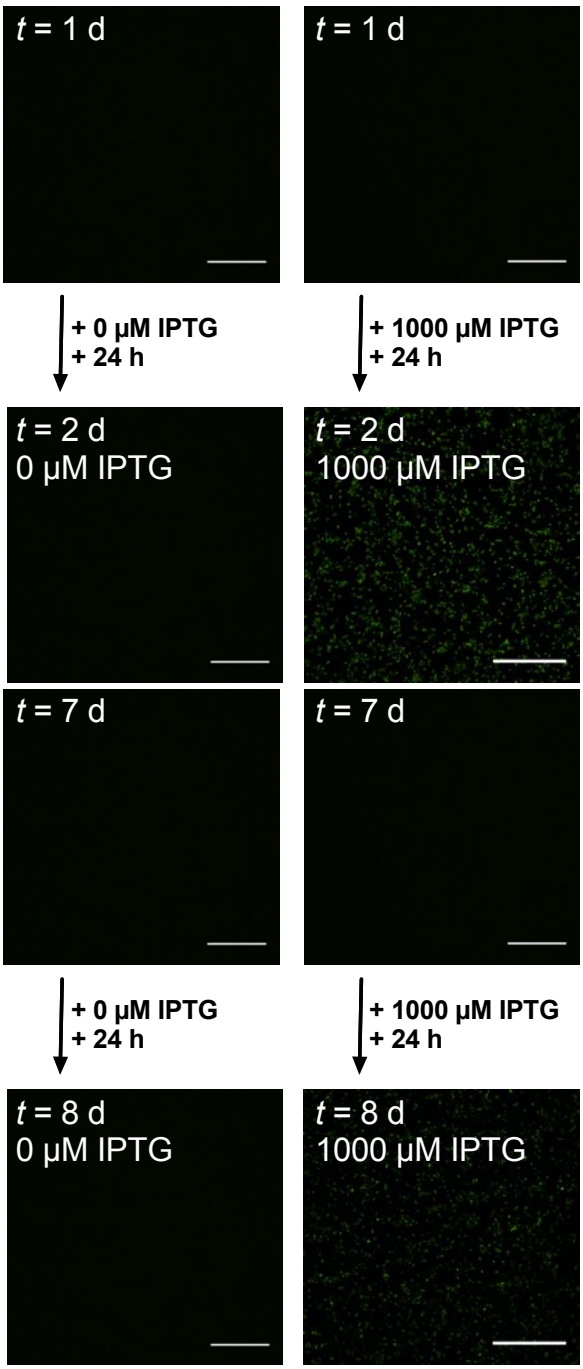

Figure E.15: sfGFP fluorescence demonstrates metabolic activity for extended time periods after crosslinking.

Figure E.15: sfGFP fluorescence demonstrates metabolic activity for extended time periods after crosslinking.

Crosslinked gels were swollen in 1x PBS for 1 and 7 days after crosslinking, then moved into 0 or 1000 μM IPTG-containing PBS for 24 h and imaged by microscopy. Gels imaged before overnight induction with IPTG did not fluoresce. All images taken with equivalent exposure times to allow comparison of protein expression and circuit maintenance. Scale bars are 40 μm.

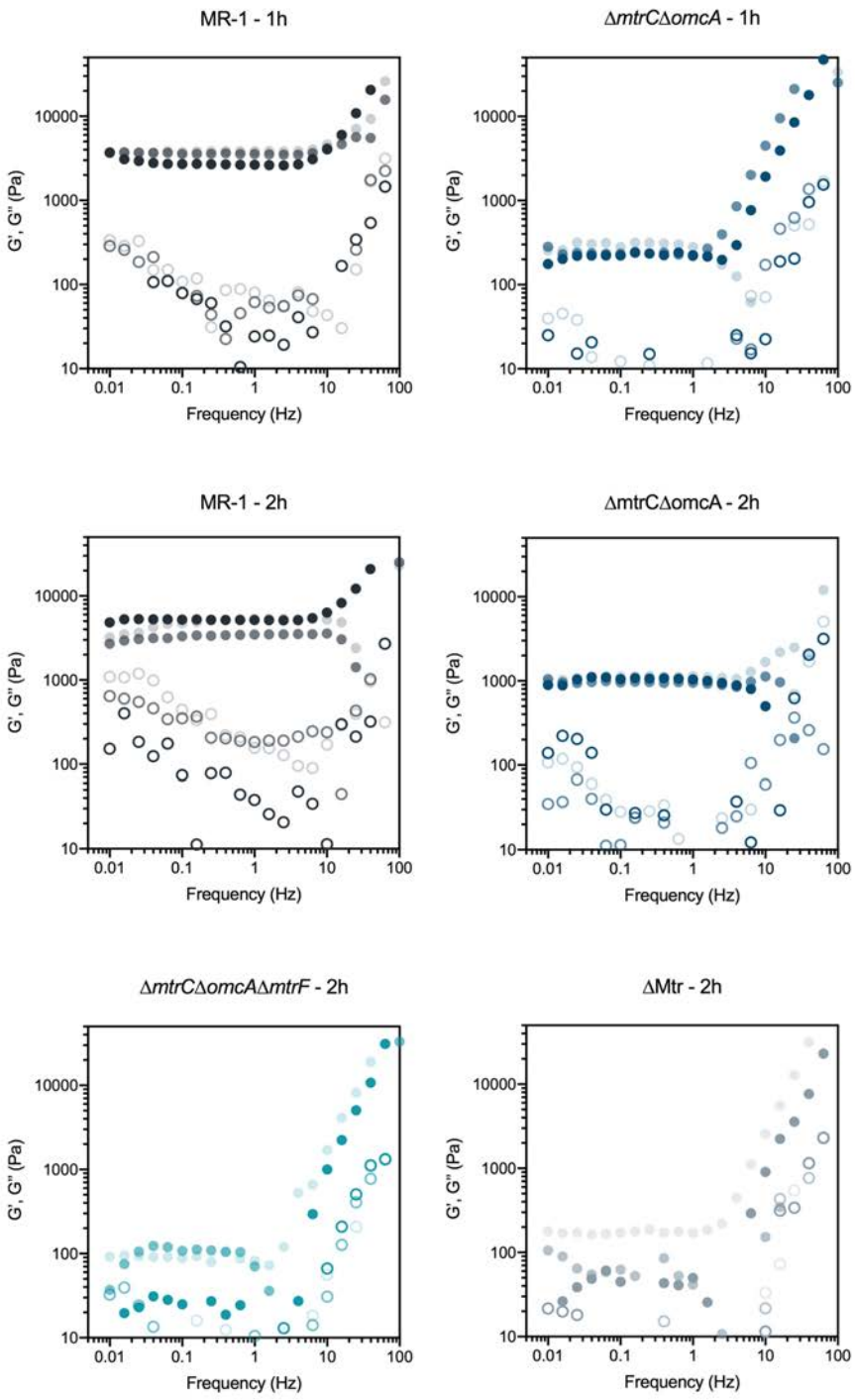

Figure E.16: Rheological frequency sweeps for end-point measurements in Fig. 6.3. G' (filled circles) and G'' (open circles) for individual replicates.

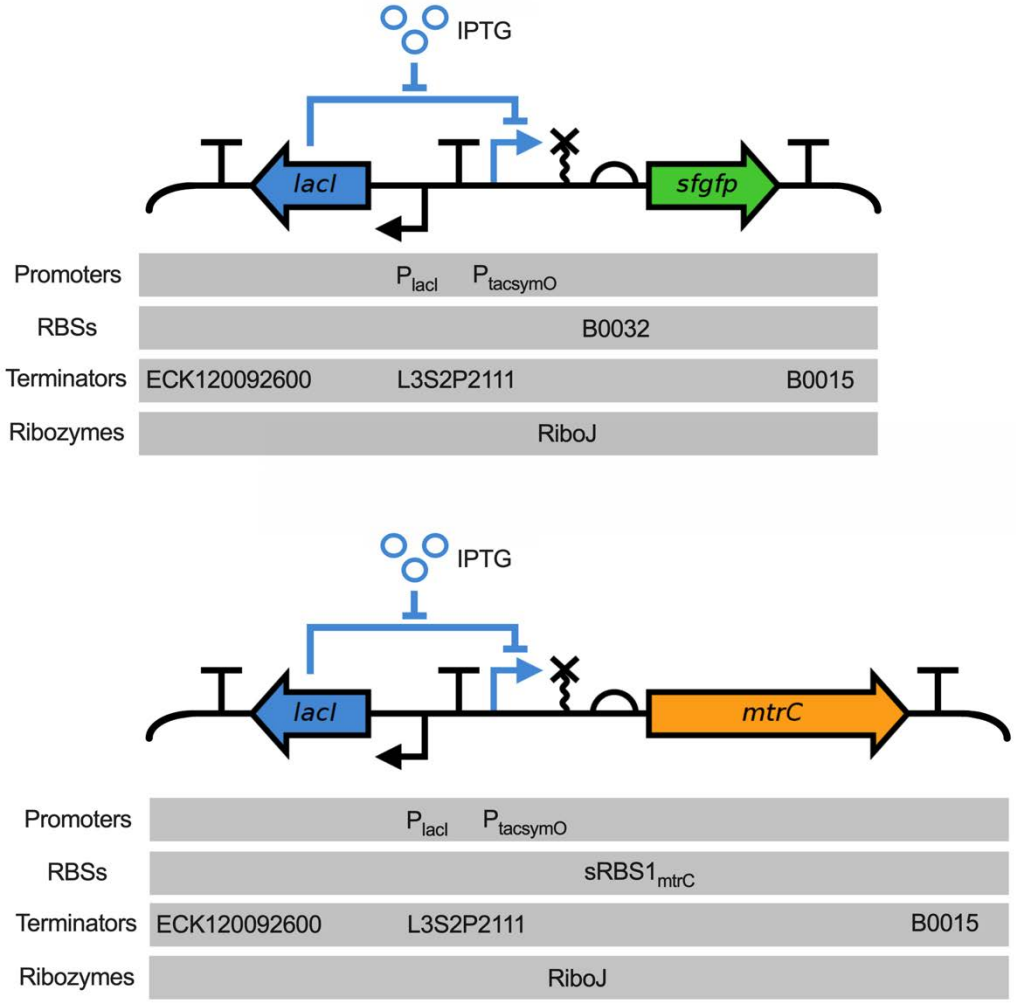

Figure E.17: Gene circuit maps for both the *sfgfp* (top, pCD7sfGFP) and *mtrC* (bottom, pCD24r1) expression vectors.

Outside of the flanking terminators, both vectors are identical and contain the ColE1 origin of replication and a kanamycin resistance marker. The empty vector (pCD8) is identical to pCD7sfGFP, but lacks *sfgfp*.

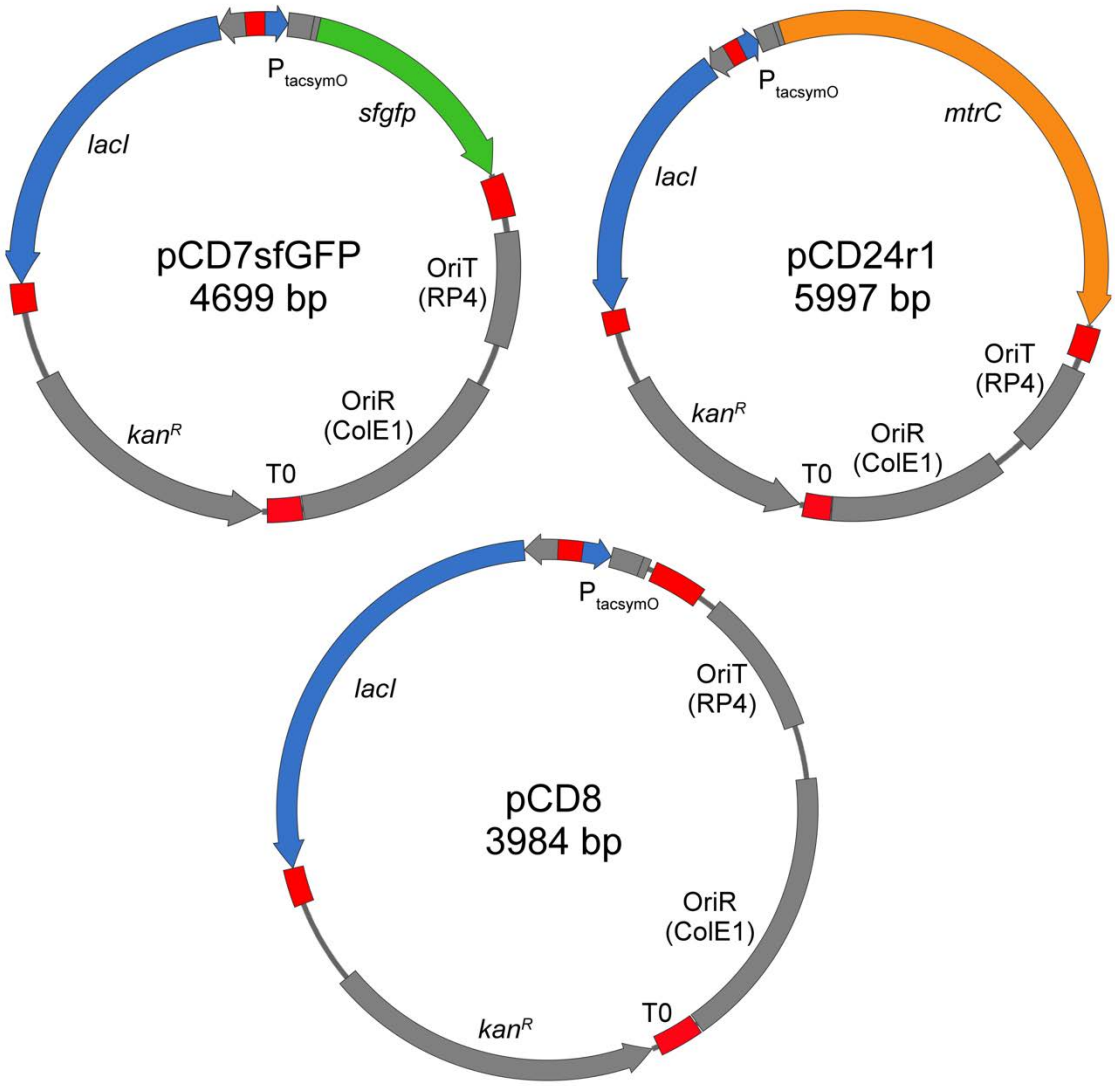

Figure E.18: Plasmid maps for all plasmids used in this study. Terminator sequences are depicted as red, *lacI* and $P_{tacsymO}$ as blue, *sfgfp* as green, and *mtrC* as orange.

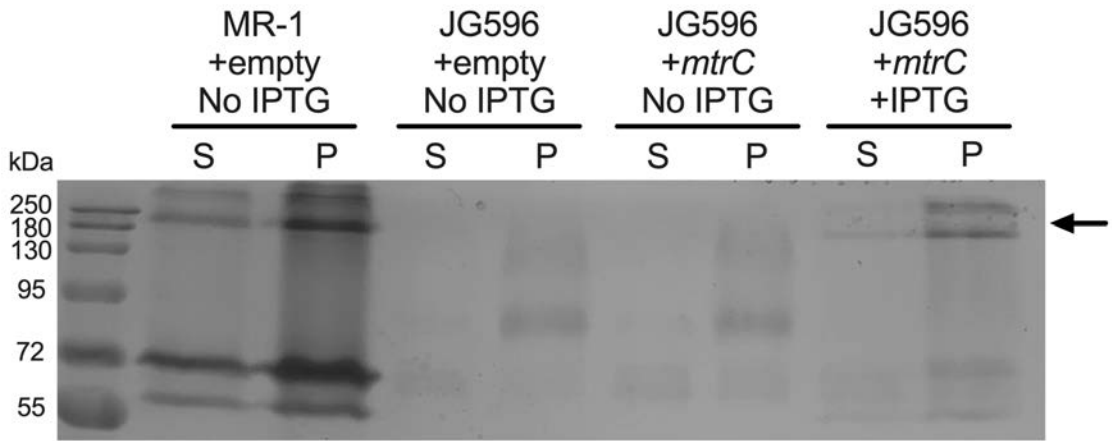

Figure E.19: Heme-stained SDS-PAGE gel of uninduced (0 μM IPTG) and induced (1000 μM IPTG) *S. oneidensis* strains.

10 μg of protein (as determined by Bradford assay) was loaded into each lane. +empty indicates strains harboring the empty expression vector (pCD8) and +*mtrC* indicates strains harboring the IPTG-inducible *mtrC* vector (pCD24r1). After sonication, cell lysate was pelleted at 10,000 rcf for 5 minutes and the soluble fraction (S) and pellet (P) were separated for analysis. The arrow indicates the bands that appear in the JG596 +*mtrC* +IPTG lanes, which correspond to the apparent size of the MtrCAB complex (~210 kDa)[103].

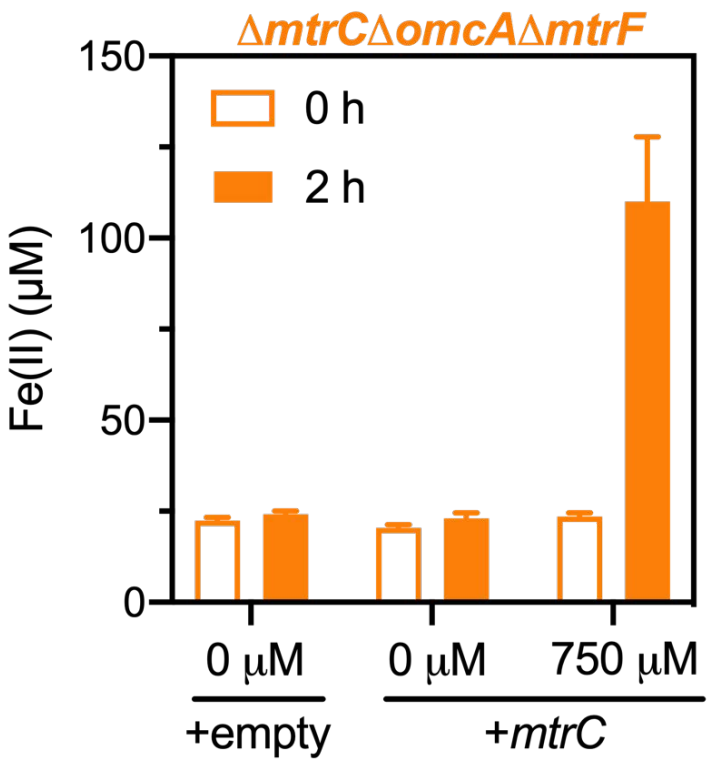

Figure E.20: Reduction of Fe(III)-citrate over 2 hours by *S. oneidensis* Δ*mtrC*Δ*omcA*Δ*mtrF* carrying either pCD24r1 (+*mtrC*) or pCD8 (+empty).

Cells were either uninduced (0 μM) or induced (750 μM) with IPTG at 0 h. Data shown are mean ± SD for $n = 3$ biological replicates.

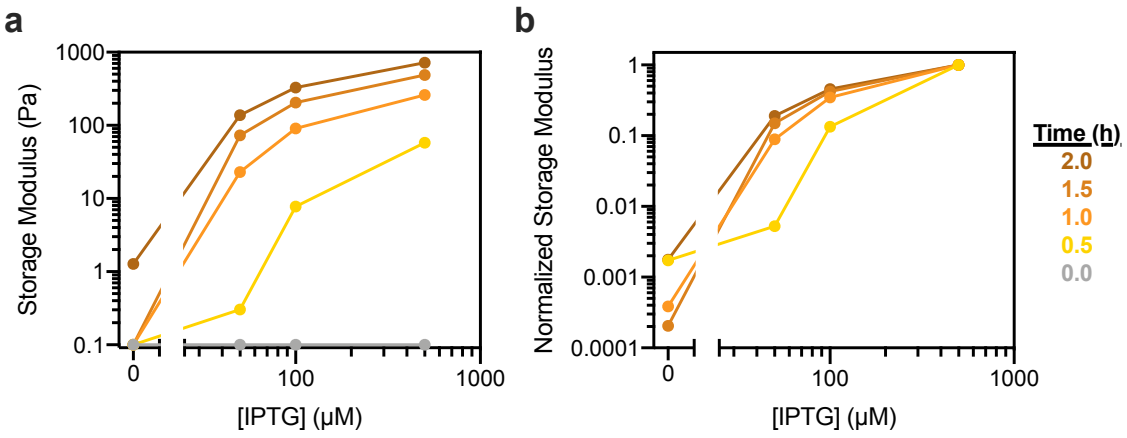

Figure E.21: Dynamic range of storage modulus response function changes with time.

(a) Storage moduli of hydrogels crosslinked by *S. oneidensis* Δ*mtrC*Δ*omcA*Δ*mtrF* carrying pCD24r1 (+*mtrC*) and (un)induced at various IPTG levels. Storage modulus was arbitrarily set at 0.1 Pa when stiffness was below the limit of detection. (b) Storage moduli from each timepoint when normalized to the highest IPTG concentration (500 μM). Past 1.0 h, all response curves collapse to similar functions. Each curve represents data from a single timepoint. Data shown are values from individual *in situ* rheology experiments (n = 1 biological replicate) that are also depicted in Figure 6.4b.

References

1. Pfeifer, B. A., Admiraal, S. J., Gramajo, H., Cane, D. E. & Khosla, C. Biosynthesis of Complex Polyketides in a Metabolically Engineered Strain of E. coli. *Science* **291**, 1790–1792 (2001).

2. Ro, D.-K. *et al.* Production of the antimalarial drug precursor artemisinic acid in engineered yeast. *Nature* **440**, 940–943 (2006).

3. Ajikumar, P. K. *et al.* Isoprenoid Pathway Optimization for Taxol Precursor Overproduction in Escherichia coli. *Science* **330**, 70–74 (2010).

4. Galanie, S., Thodey, K., Trenchard, I. J., Interrante, M. F. & Smolke, C. D. Complete biosynthesis of opioids in yeast. *Science* **349**, 1095–1100 (2015).

5. Fischer, C. R., Klein-Marcuschamer, D. & Stephanopoulos, G. Selection and optimization of microbial hosts for biofuels production. *Metab Eng* **10**, 295–304 (2008).

6. Atsumi, S., Hanai, T. & Liao, J. C. Non-fermentative pathways for synthesis of branched-chain higher alcohols as biofuels. *Nature* **451**, 86–89 (2008).

7. Peralta-Yahya, P. P. *et al.* Identification and microbial production of a terpene-based advanced biofuel. *Nat Commun* **2**, 483 (2011).

8. Blazeck, J. *et al.* Harnessing Yarrowia lipolytica lipogenesis to create a platform for lipid and biofuel production. *Nat Commun* **5**, 3131 (2014).

9. Yim, H. *et al.* Metabolic engineering of Escherichia coli for direct production of 1,4-butanediol. *Nat Chem Biol* **7**, 445–452 (2011).

10. McKenna, R. & Nielsen, D. R. Styrene biosynthesis from glucose by engineered E. coli. *Metab Eng* **13**, 544–554 (2011).

11. Leonard, E. *et al.* Combining metabolic and protein engineering of a terpenoid biosynthetic pathway for overproduction and selectivity control. *Proc Natl Acad Sci USA* **107**, 13654–13659 (2010).

12. Riglar, D. T. *et al.* Engineered bacteria can function in the mammalian gut long-term as live diagnostics of inflammation. *Nat Biotechnol* **35**, 653–658 (2017).

13. Mimee, M. *et al.* An ingestible bacterial-electronic system to monitor gastrointestinal health. *Science* **360**, 915–918 (2018).

14. Oliva, R. *et al.* Broad-spectrum resistance to bacterial blight in rice using genome editing. *Nat Biotechnol* **37**, 1344–1350 (2019).

15. Mitiouchkina, T. *et al.* Plants with genetically encoded autoluminescence. *Nat Biotechnol* 1–3 (2020) doi:10.1038/s41587-020-0500-9.

16. Jinek, M. *et al.* A Programmable Dual-RNA-Guided DNA Endonuclease in Adaptive Bacterial Immunity. *Science* **337**, 816–821 (2012).

17. Cong, L. *et al.* Multiplex Genome Engineering Using CRISPR/Cas Systems. *Science* **339**, 819–823 (2013).

18. Woo, J. W. *et al.* DNA-free genome editing in plants with preassembled CRISPR-Cas9 ribonucleoproteins. *Nat Biotechnol* **33**, 1162 (2015).

19. Moon, T. S., Lou, C., Tamsir, A., Stanton, B. C. & Voigt, C. A. Genetic programs constructed from layered logic gates in single cells. *Nature* **491**, 249–253 (2012).

20. Bonnet, J., Yin, P., Ortiz, M. E., Subsoontorn, P. & Endy, D. Amplifying Genetic Logic Gates. *Science* **340**, 599–603 (2013).

21. Nielsen, A. A. K. *et al.* Genetic circuit design automation. *Science* **352**, aac7341–aac7341 (2016).

22. Zakeri, B. *et al.* Peptide tag forming a rapid covalent bond to a protein, through engineering a bacterial adhesin. *Proc Natl Acad Sci USA* **109**, E690–E697 (2012).

23. Martell, J. D. *et al.* Engineered ascorbate peroxidase as a genetically encoded reporter for electron microscopy. *Nat Biotechnol* **30**, 1143–8 (2012).

24. Kan, S. B. J., Lewis, R. D., Chen, K. & Arnold, F. H. Directed evolution of cytochrome c for carbon–silicon bond formation: Bringing silicon to life. *Science* **354**, 1048–1051 (2016).

25. Kan, S. B. J., Huang, X., Gumulya, Y., Chen, K. & Arnold, F. H. Genetically programmed chiral organoborane synthesis. *Nature* **54**, 3351–65 (2017).

26. Endy, D. Foundations for engineering biology. *Nature* **438**, 449–453 (2005).

27. Keasling, J. D. Manufacturing Molecules Through Metabolic Engineering. *Science* **330**, 1355–1358 (2010).

28. Yadav, V. G., Mey, M. D., Lim, C. G., Ajikumar, P. K. & Stephanopoulos, G. The future of metabolic engineering and synthetic biology: towards a systematic practice. *Metab Eng* **14**, 233–241 (2012).

29. Reed, K. B. & Alper, H. S. Expanding beyond canonical metabolism: Interfacing alternative elements, synthetic biology, and metabolic engineering. *Synth Syst Biotechnol* **3**, 20–33 (2018).

30. Nieto-Domínguez, M. & Nikel, P. I. Intersecting Xenobiology and Neometabolism To Bring Novel Chemistries to Life. *ChemBioChem* (2020) doi:10.1002/cbic.202000091.

31. Lovley, D. R. e-Biologics: Fabrication of Sustainable Electronics with "Green" Biological Materials. *mBio* **8**, e00695-17–7 (2017).

32. Nguyen, P. Q., Courchesne, N.-M. D., Duraj-Thatte, A., Praveschotinunt, P. & Joshi, N. S. Engineered Living Materials: Prospects and Challenges for Using Biological Systems to Direct the Assembly of Smart Materials. *Adv Mater* **30**, 1704847 (2018).

33. Meldrum, F. C. & Cölfen, H. Controlling Mineral Morphologies and Structures in Biological and Synthetic Systems. *Chem Rev* **108**, 4332–4432 (2008).

34. Keasling, J. D. Synthetic Biology for Synthetic Chemistry. *ACS Chem Biol* **3**, 64–76 (2008).

35. Menezes, A. A., Montague, M. G., Cumbers, J., Hogan, J. A. & Arkin, A. P. Grand challenges in space synthetic biology. *J Roy Soc Interface* **12**, 20150803 (2015).

36. Nangle, S. N. *et al.* The case for biotech on Mars. *Nat Biotechnol* **38**, 401–407 (2020).

37. Schuergers, N., Werlang, C., Ajo-Franklin, C. M. & Boghossian, A. A. A synthetic biology approach to engineering living photovoltaics. *Energy Environ Sci* **10**, 1102–1115 (2017).

38. Salimijazi, F., Parra, E. & Barstow, B. Electrical energy storage with engineered biological systems. *J Biol Eng* **13**, 38 (2019).

39. Edmundson, M. C., Capeness, M. & Horsfall, L. Exploring the potential of metallic nanoparticles within synthetic biology. *New Biotechnol* **31**, 572 (2014).

40. Chen, A. Y., Zhong, C. & Lu, T. K. Engineering Living Functional Materials. *ACS Synth Biol* **4**, 8–11 (2015).

41. Gilbert, C. & Ellis, T. Biological Engineered Living Materials: Growing Functional Materials with Genetically Programmable Properties. *ACS Synth Biol* **8**, 1–15 (2018).

42. Choi, Y., Park, T. J., Lee, D. C. & Lee, S. Y. Recombinant Escherichia coli as a biofactory for various single- and multi-element nanomaterials. *Proc Natl Acad Sci USA* **115**, 5944–5949 (2018).

43. Brown, S., Sarikaya, M. & Johnson, E. A genetic analysis of crystal growth. *J Mol Biol* **299**, 725–735 (2000).

44. Lee, S.-W., Mao, C., Flynn, C. E. & Belcher, A. M. Ordering of Quantum Dots Using Genetically Engineered Viruses. *Science* **292**, 892–895 (2002).

45. Scott, M., Gunderson, C. W., Mateescu, E. M., Zhang, Z. & Hwa, T. Interdependence of cell growth and gene expression: origins and consequences. *Science* **330**, 1099–102 (2010).

46. Thiele, I. & Palsson, B. Ø. A protocol for generating a high-quality genome-scale metabolic reconstruction. *Nat Protoc* **5**, 93–121 (2010).

47. Solomon, K. V., Sanders, T. M. & Prather, K. L. J. A dynamic metabolite valve for the control of central carbon metabolism. *Metab Eng* **14**, 661–671 (2012).

48. Hildebrand, M. Diatoms, Biomineralization Processes, and Genomics. *Chem Rev* **108**, 4855–4874 (2008).

49. Faivre, D. & Godec, T. U. From Bacteria to Mollusks: The Principles Underlying the Biomineralization of Iron Oxide Materials. *Angew Chem* **127**, 4810–4829 (2015).

50. Ehrlich, H., Newman, D. & Kappler, A. Ehrlich's Geomicrobiology, Sixth Edition. 1–5 (2015) doi:10.1201/b19121-2.

51. Yan, Q. & Fong, S. S. Challenges and Advances for Genetic Engineering of Non-model Bacteria and Uses in Consolidated Bioprocessing. *Front Microbiol* **8**, 2060 (2017).

52. Fatma, Z., Schultz, J. C. & Zhao, H. Recent advances in domesticating non-model microorganisms. *Biotechnol Prog* e3008 (2020) doi:10.1002/btpr.3008.

53. Schäfer, G., Purschke, W. & Schmidt, C. L. On the origin of respiration: electron transport proteins from archaea to man. *FEMS Microbiol Rev* **18**, 173–188 (1996).

54. Hsia, C. C. W., Schmitz, A., Lambertz, M., Perry, S. F. & Maina, J. N. Evolution of air breathing: oxygen homeostasis and the transitions from water to land and sky. *Compr Physiol* **3**, 849–915 (2013).

55. Kracke, F., Vassilev, I. & Krömer, J. O. Microbial electron transport and energy conservation - the foundation for optimizing bioelectrochemical systems. *Front Microbiol* **6**, 575 (2015).

56. Lovley, D. R. & Coates, J. D. Novel forms of anaerobic respiration of environmental relevance. *Curr Opin Microbiol* **3**, 252–256 (2000).

57. Gralnick, J. A. & Newman, D. K. Extracellular respiration. *Mol Microbiol* **65**, 1–11 (2007).

58. Logan, B. E. Exoelectrogenic bacteria that power microbial fuel cells. *Nat Rev Microbiol* **7**, 375–381 (2009).

59. Kumar, A. *et al.* The ins and outs of microorganism–electrode electron transfer reactions. *Nat Rev Chem* **1**, 0024 (2017).

60. Nealson, K. H. & Scott, J. Ecophysiology of the Genus Shewanella. in vol. 51 1133–1151 (2006).

61. Hau, H. H. & Gralnick, J. A. Ecology and Biotechnology of the Genus Shewanella. *Annu Rev Microbiol* **61**, 237–258 (2007).

62. Myers, C. R. & Nealson, K. H. Bacterial Manganese Reduction and Growth with Manganese Oxide as the Sole Electron Acceptor. *Science* 1319–1321 (1988).

63. Lovley, D. R. & Phillips, E. J. Novel mode of microbial energy metabolism: organic carbon oxidation coupled to dissimilatory reduction of iron or manganese. *Appl Environ Microbiol* **54**, 1472–80 (1988).

64. Shi, L. *et al.* Extracellular electron transfer mechanisms between microorganisms and minerals. *Nat Rev Microbiol* **14**, 651–662 (2016).

65. Jeuken, L. J. C., Hards, K. & Nakatani, Y. Extracellular Electron Transfer: Respiratory or Nutrient Homeostasis? *J Bacteriol* **202**, (2020).

66. Ciemniecki, J. A. & Newman, D. K. The Potential for Redox-Active Metabolites To Enhance or Unlock Anaerobic Survival Metabolisms in Aerobes. *J Bacteriol* **202**, (2020).

67. Bond, D. R., Holmes, D. E., Tender, L. M. & Lovley, D. R. Electrode-Reducing Microorganisms That Harvest Energy from Marine Sediments. *Science* **295**, 483–485 (2002).

68. Weiss, J. V., Emerson, D., Backer, S. M. & Megonigal, J. P. Enumeration of Fe(II)-oxidizing and Fe(III)-reducing bacteria in the root zone of wetland plants: Implications for a rhizosphere iron cycle. *Biogeochem* **64**, 77–96 (2003).

69. Valencia-Cantero, E. *et al.* Role of dissimilatory fermentative iron-reducing bacteria in Fe uptake by common bean (Phaseolus vulgaris L.) plants grown in alkaline soil. *Plant Soil* **291**, 263–273 (2007).

70. Light, S. H. *et al.* A flavin-based extracellular electron transfer mechanism in diverse Gram-positive bacteria. *Nature* **562**, 140–144 (2018).

71. Naradasu, D., Miran, W., Sakamoto, M. & Okamoto, A. Isolation and Characterization of Human Gut Bacteria Capable of Extracellular Electron Transport by Electrochemical Techniques. *Front Microbiol* **9**, 3267 (2019).

72. Beal, E. J., House, C. H. & Orphan, V. J. Manganese- and iron-dependent marine methane oxidation. *Science* **325**, 184–7 (2009).

73. Roden, E. E. Microbial iron-redox cycling in subsurface environments. *Biochem Soc Trans* **40**, 1249–1256 (2012).

74. Melton, E. D., Swanner, E. D., Behrens, S., Schmidt, C. & Kappler, A. The interplay of microbially mediated and abiotic reactions in the biogeochemical Fe cycle. *Nat Rev Microbiol* **12**, 797–809 (2014).

75. Fredrickson, J. K. *et al.* Towards environmental systems biology of Shewanella. *Nat Rev Microbiol* **6**, 592–603 (2008).

76. Abboud, R. *et al.* Low-Temperature Growth of Shewanella oneidensis MR-1. *Appl Environ Microbiol* **71**, 811–816 (2005).

77. Saltikov, C. W. & Newman, D. K. Genetic identification of a respiratory arsenate reductase. *Proc Natl Acad Sci USA* **100**, 10983–10988 (2003).

78. Corts, A. D., Thomason, L. C., Gill, R. T. & Gralnick, J. A. A new recombineering system for precise genome-editing in Shewanella oneidensis strain MR-1 using single-stranded oligonucleotides. *Sci Rep* **9**, 1–10 (2018).

79. Corts, A. D., Thomason, L. C., Gill, R. T. & Gralnick, J. A. Efficient and Precise Genome Editing in Shewanella with Recombineering and CRISPR/Cas9-Mediated Counter-Selection. *ACS Synth Biol* **8**, 1877–1889 (2019).

80. Cao, Y. *et al.* A Synthetic Plasmid Toolkit for Shewanella oneidensis MR-1. *Front Microbiol* **10**, 410 (2019).

81. Beliaev, A. S. & Saffarini, D. Shewanella putrefaciens mtrB Encodes an Outer Membrane Protein Required for Fe(III) and Mn(IV) Reduction. *J Bacteriol* **180**, 6292-6297 (1998).

82. Myers, J. M. & Myers, C. R. Role of the Tetraheme Cytochrome CymA in Anaerobic Electron Transport in Cells of Shewanella putrefaciens MR-1 with Normal Levels of Menaquinone. *J Bacteriol* **182**, 67–75 (2000).

83. Beliaev, A. S., Saffarini, D. A., McLaughlin, J. L. & Hunnicutt, D. MtrC, an outer membrane decahaem c cytochrome required for metal reduction in Shewanella putrefaciens MR-1. *Mol Microbiol* **39**, 722–730 (2001).

84. Myers, C. R. & Myers, J. M. MtrB Is Required for Proper Incorporation of the Cytochromes OmcA and OmcB into the Outer Membrane of Shewanella putrefaciens MR-1. *Appl Environ Microbiol* **68**, 5585–5594 (2002).

85. Coursolle, D., Baron, D. B., Bond, D. R. & Gralnick, J. A. The Mtr Respiratory Pathway Is Essential for Reducing Flavins and Electrodes in Shewanella oneidensis. *J Bacteriol* **192**, 467–474 (2010).

86. Coursolle, D. & Gralnick, J. A. Modularity of the Mtr respiratory pathway of Shewanella oneidensis strain MR-1. *Mol Microbiol* **55**, 995–1008 (2010).

87. Sturm, G. *et al.* A dynamic periplasmic electron transfer network enables respiratory flexibility beyond a thermodynamic regulatory regime. *ISME J* **9**, 1802–1811 (2015).

88. Edwards, M. J., White, G. F., Butt, J. N., Richardson, D. J. & Clarke, T. A. The Crystal Structure of a Biological Insulated Transmembrane Molecular Wire. *Cell* **181**, 665-673.e10 (2020).

89. Shi, L. *et al.* Molecular underpinnings of Fe(III) oxide reduction by Shewanella oneidensis MR-1. *Front Microbiol* **3**, (2012).

90. TerAvest, M. A. & Ajo-Franklin, C. M. Transforming exoelectrogens for biotechnology using synthetic biology. *Biotechnol Bioeng* **113**, 687–697 (2015).

91. Glaven, S. M. Bioelectrochemical systems and synthetic biology: more power, more products. *Microb Biotechnol* **12**, 819–823 (2019).

92. Myers, C. R. & Myers, J. M. Role of menaquinone in the reduction of fumarate, nitrate, iron(III) and manganese(IV) by Shewanella putrefaciens MR-1. *FEMS Microbiol Lett* **114**, 215–222 (1993).

93. Serres, M. H. & Riley, M. Genomic Analysis of Carbon Source Metabolism of Shewanella oneidensis MR-1: Predictions versus Experiments. *J Bacteriol* **188**, 4601–4609 (2006).

94. Hunt, K. A., Flynn, J. M., Naranjo, B., Shikhare, I. D. & Gralnick, J. A. Substrate-Level Phosphorylation Is the Primary Source of Energy Conservation during Anaerobic Respiration of Shewanella oneidensis Strain MR-1. *J Bacteriol* **192**, 3345–3351 (2010).

95. Kane, A. L. *et al.* Formate Metabolism in Shewanella oneidensis Generates Proton Motive Force and Prevents Growth without an Electron Acceptor. *J Bacteriol* **198**, 1337–1346 (2016).

96. Kasai, T., Suzuki, Y., Kouzuma, A. & Watanabe, K. Roles of D-Lactate Dehydrogenases in the Anaerobic Growth of Shewanella oneidensis MR-1 on Sugars. *Appl Environ Microbiol* **85**, (2018).

97. Madsen, C. S. & TerAvest, M. A. NADH dehydrogenases Nuo and Nqr1 contribute to extracellular electron transfer by Shewanella oneidensis MR-1 in bioelectrochemical systems. *Sci Rep* **9**, 14959 (2019).

98. Rodionov, D. A. *et al.* Genomic encyclopedia of sugar utilization pathways in the Shewanella genus. *BMC Genomics* **11**, 494 (2010).

99. Myers, C. R. & Myers, J. M. Cloning and sequence of cymA, a gene encoding a tetraheme cytochrome c required for reduction of iron(III), fumarate, and nitrate by Shewanella putrefaciens MR-1. *J Bacteriol* **179**, 1143–1152 (1997).

100. Murphy, J. N. & Saltikov, C. W. The cymA gene, encoding a tetraheme c-type cytochrome, is required for arsenate respiration in Shewanella species. *J Bacteriol* **189**, 2283–2290 (2007).

101. Ing, N. L., El-Naggar, M. Y. & Hochbaum, A. I. Going the Distance: Long-Range Conductivity in Protein and Peptide Bioelectronic Materials. *J Phys Chem B* **122**, 10403–10423 (2018).

102. Barrozo, A., El-Naggar, M. Y. & Krylov, A. I. Distinct Electron Conductance Regimes in Bacterial Decaheme Cytochromes. *Angew Chem* **57**, 6805–6809 (2018).

103. Hartshorne, R. S. *et al.* Characterization of an electron conduit between bacteria and the extracellular environment. *Proc Natl Acad Sci USA* **106**, 22169–22174 (2009).

104. Schwalb, C., Chapman, S. K. & Reid, G. A. The Tetraheme Cytochrome CymA Is Required for Anaerobic Respiration with Dimethyl Sulfoxide and Nitrite in Shewanella oneidensis. *Biochem* **42**, 9491–9497 (2003).

105. Schwalb, C., Chapman, S. K. & Reid, G. A. The membrane-bound tetrahaem c-type cytochrome CymA interacts directly with the soluble fumarate reductase in Shewanella. *Biochem Soc Trans* **30**, 658–662 (2002).

106. Fonseca, B. M. *et al.* Mind the gap: cytochrome interactions reveal electron pathways across the periplasm of Shewanella oneidensis MR-1. *Biochem J* **449**, 101–108 (2012).

107. Schuetz, B., Schicklberger, M., Kuermann, J., Spormann, A. M. & Gescher, J. Periplasmic Electron Transfer via the c-Type Cytochromes MtrA and FccA of Shewanella oneidensis MR-1. *Appl Environ Microbiol* **75**, 7789 (2009).

108. Ross, D. E. *et al.* Characterization of protein-protein interactions involved in iron reduction by Shewanella oneidensis MR-1. *Appl Environ Microbiol* **73**, 5797–5808 (2007).

109. Myers, J. M. & Myers, C. R. Role for Outer Membrane Cytochromes OmcA and OmcB of Shewanella putrefaciens MR-1 in Reduction of Manganese Dioxide. *Appl Environ Microbiol* **67**, 260–269 (2001).

110. Edwards, M. J. *et al.* Redox Linked Flavin Sites in Extracellular Decaheme Proteins Involved in Microbe-Mineral Electron Transfer. *Sci Rep* 1–11 (2015) doi:10.1038/srep11677.

111. Coursolle, D. & Gralnick, J. A. Reconstruction of extracellular respiratory pathways for iron(III) reduction in Shewanella oneidensis strain MR-1. *Front Microbiol* **3**, 1–11 (2012).

112. Xiong, Y. *et al.* High-Affinity Binding and Direct Electron Transfer to Solid Metals by the Shewanella oneidensis MR-1 Outer Membrane c -type Cytochrome OmcA. *J Am Chem Soc* **128**, 13978 (2006).

113. Ross, D. E., Brantley, S. L. & Tien, M. Kinetic Characterization of OmcA and MtrC, Terminal Reductases Involved in Respiratory Electron Transfer for Dissimilatory Iron

Reduction in Shewanella oneidensis MR-1. *Appl Environ Microbiol* **75**, 5218–5226 (2009).

114. Brutinel, E. D. & Gralnick, J. A. Shuttling happens: soluble flavin mediators of extracellular electron transfer in Shewanella. *Appl Microbiol Biotechnol* **93**, 41–8 (2011).

115. Wigginton, N. S., Rosso, K. M., Lower, B. H., Shi, L. & Hochella, M. F. Electron tunneling properties of outer-membrane decaheme cytochromes from Shewanella oneidensis. *Geochim Cosmochim Acta* **71**, 543–555 (2007).

116. Firer-Sherwood, M., Pulcu, G. S. & Elliott, S. J. Electrochemical interrogations of the Mtr cytochromes from Shewanella: opening a potential window. *J Biol Inorg Chem* **13**, 849–854 (2008).

117. Marsili, E. *et al.* Shewanella secretes flavins that mediate extracellular electron transfer. *Proc Natl Acad Sci USA* **105**, 3968–3973 (2008).

118. Okamoto, A., Hashimoto, K., Nealson, K. H. & Nakamura, R. Rate enhancement of bacterial extracellular electron transport involves bound flavin semiquinones. *Proc Natl Acad Sci USA* **110**, 7856–7861 (2013).

119. Okamoto, A., Hashimoto, K. & Nealson, K. H. Flavin Redox Bifurcation as a Mechanism for Controlling the Direction of Electron Flow during Extracellular Electron Transfer. *Angew Chem* **53**, 10988–10991 (2014).

120. Kotloski, N. J. & Gralnick, J. A. Flavin Electron Shuttles Dominate Extracellular Electron Transfer by Shewanella oneidensis. *mBio* **4**, 1–4 (2013).

121. Sydow, A., Krieg, T., Mayer, F., Schrader, J. & Holtmann, D. Electroactive bacteria—molecular mechanisms and genetic tools. *Appl Microbiol Biotechnol* **98**, 8481–8495 (2014).

122. Kim, B. H. *et al.* Electrochemical activity of an Fe(III)-reducing bacterium, Shewanella putrefaciens IR-1, in the presence of alternative electron acceptors. *Biotechnol Tech* **13**, 475–478 (1999).

123. Kim, B. H., Kim, H. J., Hyun, M. S. & Park, D. H. Direct electrode reaction of Fe(III)-reducing bacterium, Shewanella putrefaciens. *J Microbiol Biotechnol* **1**, 127–131 (1999).

124. Kim, H. J. *et al.* A mediator-less microbial fuel cell using a metal reducing bacterium, Shewanella putrefaciens. *Enzyme Microb Technol* **30**, 145–152 (2002).

125. Bretschger, O. *et al.* Current Production and Metal Oxide Reduction by Shewanella oneidensis MR-1 Wild Type and Mutants. *Appl Environ Microbiol* **73**, 7003–7012 (2007).

126. Tender, L. M. *et al.* Harnessing microbially generated power on the seafloor. *Nat Biotechnol* **20**, 821–825 (2002).

127. Zhou, A. Y., Zajdel, T. J., TerAvest, M. A. & Maharbiz, M. M. A miniaturized monitoring system for electrochemical biosensing using Shewanella oneidensis in environmental applications. *Proc Annu Int Conf IEEE Eng Med Biol Soc EMBS* **2015**, 7518–7521 (2015).

128. Zhou, A. Y., Baruch, M., Ajo-Franklin, C. M. & Maharbiz, M. M. A portable bioelectronic sensing system (BESSY) for environmental deployment incorporating differential microbial sensing in miniaturized reactors. *PLOS One* **12**, e0184994 (2017).

129. Golitsch, F., Bücking, C. & Gescher, J. Proof of principle for an engineered microbial biosensor based on Shewanella oneidensis outer membrane protein complexes. *Biosens Bioelectron* **47**, 285–291 (2013).

130. Yang, Y. *et al.* Enhancing Bidirectional Electron Transfer of Shewanella oneidensis by a Synthetic Flavin Pathway. *ACS Synth Biol* **4**, 815–823 (2015).

131. Li, F. *et al.* Modular engineering to increase intracellular NAD(H/+) promotes rate of extracellular electron transfer of Shewanella oneidensis. *Nat Commun* **9**, 3637 (2018).

132. Choi, D. *et al.* Metabolically engineered glucose-utilizing Shewanella strains under anaerobic conditions. *Bioresour Technol* **154**, 59–66 (2014).

133. Li, F. *et al.* Engineering Shewanella oneidensis enables xylose-fed microbial fuel cell. *Biotechnol Biofuels* **10**, 1–10 (2017).

134. Hu, Y., Yang, Y., Katz, E. & Song, H. Programming the quorum sensing-based AND gate in Shewanella oneidensis for logic gated-microbial fuel cells. *Chem Commun* **51**, 4184–4187 (2015).

135. Hu, Y., Wu, Y., Mukherjee, M. & Cao, B. A near-infrared light responsive c-di-GMP module-based AND logic gate in Shewanella oneidensis. *Chem Commun* **53**, 1646–1648 (2017).

136. West, E. A., Jain, A. & Gralnick, J. A. Engineering a native inducible expression system in Shewanella oneidensis to control extracellular electron transfer. *ACS Synth Biol* (2017) doi:10.1021/acssynbio.6b00349.

137. Marsili, E., Rollefson, J. B., Baron, D. B., Hozalski, R. M. & Bond, D. R. Microbial Biofilm Voltammetry: Direct Electrochemical Characterization of Catalytic Electrode-Attached Biofilms. *Appl Environ Microb* **74**, 7329–7337 (2008).

138. Baron, D., LaBelle, E., Coursolle, D., Gralnick, J. A. & Bond, D. R. Electrochemical Measurement of Electron Transfer Kinetics by Shewanella oneidensis MR-1. *J Biol Chem* (2009) doi:10.1074/jbc.m109.043455.

139. Kane, A. L., Bond, D. R. & Gralnick, J. A. Electrochemical Analysis of Shewanella oneidensis Engineered To Bind Gold Electrodes. *ACS Synth Biol* **2**, 93 (2013).

140. Liu, T. *et al.* Enhanced Shewanella biofilm promotes bioelectricity generation. *Biotechnol Bioeng* **112**, 2051–2059 (2015).

141. Vellingiri, A. *et al.* Overexpression of c-type cytochrome, CymA in Shewanella oneidensis MR-1 for enhanced bioelectricity generation and cell growth in a microbial fuel cell: Overexpression of c-type cytochrome, CymA in Shewanella oneidensis MR-1. *J Chem Technol Biotechnol* **94**, 2115–2122 (2018).

142. Kipf, E. *et al.* Systematic screening of carbon-based anode materials for microbial fuel cells with Shewanella oneidensis MR-1. *Bioresour Technol* **146**, 386–392 (2013).

143. D, P. & J, Z. Impact of electrode composition on electricity generation in a single-compartment fuel cell using Shewanella putrefaciens. *Appl Microbiol Biotechnol* **59**, 58–61 (2002).

144. Sun, M. *et al.* A gold-sputtered carbon paper as an anode for improved electricity generation from a microbial fuel cell inoculated with Shewanella oneidensis MR-1. *Biosens Bioelectron* **26**, 338–343 (2010).

145. Qiao, Y., Wu, X.-S. & Li, C. M. Interfacial electron transfer of Shewanella putrefaciens enhanced by nanoflaky nickel oxide array in microbial fuel cells. *J Power Sources* **266**, 226–231 (2014).

146. Artyushkova, K. *et al.* Relationship between surface chemistry, biofilm structure, and electron transfer in Shewanella anodes. *Biointerphases* **10**, 019013–13 (2015).

147. Zhang, H. Ultrathin Two-Dimensional Nanomaterials. *ACS Nano* **9**, 9451–9469 (2015).

148. Chen, A. Y. *et al.* Synthesis and patterning of tunable multiscale materials with engineered cells. *Nat Mater* **13**, 515–523 (2014).

149. Lee, S.-W., Mao, C., Flynn, C. E. & Belcher, A. M. Ordering of Quantum Dots Using Genetically Engineered Viruses. *Science* **296**, 892–895 (2002).

150. Nam, K. T. *et al.* Virus-Enabled Synthesis and Assembly of Nanowires for Lithium Ion Battery Electrodes. *Science* **312**, 885–888 (2006).

151. Kolinko, I. *et al.* Biosynthesis of magnetic nanostructures in a foreign organism by transfer of bacterial magnetosome gene clusters. *Nat Nanotechnol* **9**, 193–197 (2014).

152. Sakimoto, K. K., Wong, A. B. & Yang, P. Self-photosensitization of nonphotosynthetic bacteria for solar-to-chemical production. *Science* **351**, 74–77 (2015).

153. Corte, S. D. *et al.* Gold nanoparticle formation using Shewanella oneidensis: a fast biosorption and slow reduction process. *J Chem Technol Biotechnol* **86**, 547–553 (2010).

154. Suresh, A. K. *et al.* Biofabrication of discrete spherical gold nanoparticles using the metal-reducing bacterium Shewanella oneidensis. *Acta Biomater* **7**, 2148–2152 (2011).

155. Wang, H. *et al.* Impact of Silver(I) on the Metabolism of Shewanella oneidensis. *J Bacteriol* **192**, 1143–1150 (2010).

156. Windt, W. D., Aelterman, P. & Verstraete, W. Bioreductive deposition of palladium (0) nanoparticles on Shewanella oneidensis with catalytic activity towards reductive dechlorination of polychlorinated biphenyls. *Environ Microbiol* **7**, 314–325 (2005).

157. Windt, W. D. *et al.* Biological control of the size and reactivity of catalytic Pd(0) produced by Shewanella oneidensis. *Antonie van Leeuwenhoek* **90**, 377–389 (2006).

158. Maes, S. *et al.* Biological Recovery of Platinum Complexes from Diluted Aqueous Streams by Axenic Cultures. *Plos One* **12**, e0169093 (2017).

159. Kimber, R. L. *et al.* Biosynthesis and Characterization of Copper Nanoparticles Using Shewanella oneidensis: Application for Click Chemistry. *Small* **116**, 1703145–8 (2018).

160. Djakovitch, L., Kohler, K. & Vries, J. G. de. The Role of Palladium Nanoparticles as Catalysts for Carbon-Carbon Coupling Reactions. in Nanoparticles and Catalysis 303–348 (2008).

161. Corte, S. D. *et al.* Influence of physicochemical parameters on stability and performance of biosupported Pd nanocatalysts. *Nanomater Environ* **1**, (2013).

162. Yin, Y. & Alivisatos, A. P. Colloidal nanocrystal synthesis and the organic–inorganic interface. *Nature* **437**, 664–670 (2005).

163. Cheong, S., Watt, J. D. & Tilley, R. D. Shape control of platinum and palladium nanoparticles for catalysis. *Nanoscale* **2**, 2045–53 (2010).

164. Guo, S., Zhang, S. & Sun, S. Tuning Nanoparticle Catalysis for the Oxygen Reduction Reaction. *Angew Chem* **52**, 8526–8544 (2013).

165. Marshall, M. J. *et al.* c -Type Cytochrome-Dependent Formation of U(IV) Nanoparticles by Shewanella oneidensis. *PLOS Biol* **4**, e268 (2006).

166. Tian, L.-J. *et al.* Directed Biofabrication of Nanoparticles through Regulating Extracellular Electron Transfer. *J Am Chem Soc* **139**, 12149–12152 (2017).

167. Li, D.-B. *et al.* Selenite reduction by Shewanella oneidensis MR-1 is mediated by fumarate reductase in periplasm. *Sci Rep* **4**, (2014).

168. Ng, C. K., Tan, T. K. C., Song, H. & Cao, B. Reductive formation of palladium nanoparticles by Shewanella oneidensis: role of outer membrane cytochromes and hydrogenases. *RSC Adv* **3**, 22498–6 (2013).

169. Mikheenko, I. P., Rousset, M., Dementin, S. & Macaskie, L. E. Bioaccumulation of Palladium by Desulfovibrio fructosivorans Wild-Type and Hydrogenase-Deficient Strains. *Appl Environ Microbiol* **74**, 6144–6146 (2008).

170. Deplanche, K., Caldelari, I., Mikheenko, I. P., Sargent, F. & Macaskie, L. E. Involvement of hydrogenases in the formation of highly catalytic Pd(0) nanoparticles by bioreduction of Pd(II) using Escherichia coli mutant strains. *Microbiol* **156**, 2630–2640 (2010).

171. Rajeshwar, K., Ibanez, J. G. & Swain, G. M. Electrochemistry and the environment. *J Appl Electrochem* **24**, 1077–1091 (1994).

172. Liu, G. *et al.* Decolorization of azo dyes by Shewanella oneidensis MR-1 in the presence of humic acids. *Appl Microbiol Biotechnol* **91**, 417–24 (2011).

173. Cai, P.-J. *et al.* Anaerobic biodecolorization mechanism of methyl orange by Shewanella oneidensis MR-1. *Appl Microbiol Biotechnol* **93**, 1769–1776 (2011).

174. Ji, Q. *et al.* Removal of water-insoluble Sudan dyes by Shewanella oneidensis MR-1. *Bioresour Technol* **114**, 144–8 (2012).

175. Liu, W. *et al.* Methylene blue enhances the anaerobic decolorization and detoxication of azo dye by Shewanella onediensis MR-1. *Biochem Eng J* **110**, 115–124 (2016).

176. Wang, J., Wu, M., Lu, G. & Si, Y. Biotransformation and biomethylation of arsenic by Shewanella oneidensis MR-1. *Chemosphere* **145**, 329–335 (2016).

177. Middleton, S. S. *et al.* Cometabolism of Cr(VI) by Shewanella oneidensis MR-1 produces cell-associated reduced chromium and inhibits growth. *Biotechnol Bioeng* **83**, 627–637 (2003).

178. Belchik, S. M. *et al.* Extracellular Reduction of Hexavalent Chromium by Cytochromes MtrC and OmcA of Shewanella oneidensis MR-1. *Appl Environ Microbiol* **77**, 4035–4041 (2011).

179. Petrovskis, E. A., Vogel, T. M. & Adriaens, P. Effects of electron acceptors and donors on transformation of tetrachloromethane by Shewanella putrefaciens MR-1. *FEMS Microbiol Lett* **121**, 357–363 (1994).

180. Hennebel, T. *et al.* Biocatalytic dechlorination of trichloroethylene with bio-palladium in a pilot-scale membrane reactor. *Biotechnol Bioeng* **102**, 995–1002 (2009).

181. Xiao, X. *et al.* Biodecolorization of Naphthol Green B dye by Shewanella oneidensis MR-1 under anaerobic conditions. *Bioresour Technol* **110**, 86–90 (2012).

182. Li, Q. *et al.* Anaerobic decolorization and detoxification of cationic red X-GRL by Shewanella oneidensis MR-1. *Environ Technol* **39**, 2382–2389 (2017).

183. Huang, J.-H. *et al.* Influence of Arsenate Adsorption to Ferrihydrite, Goethite, and Boehmite on the Kinetics of Arsenate Reduction by Shewanella putrefaciensstrain CN-32. *Environ Sci Tech* **45**, 7701–7709 (2011).

184. Yan, F.-F. *et al.* Carbon nanotubes promote Cr(VI) reduction by alginate-immobilized Shewanella oneidensis MR-1. *Biochem Eng J* **77**, 183–189 (2013).

185. Shen, C. R. *et al.* Driving Forces Enable High-Titer Anaerobic 1-Butanol Synthesis in Escherichia coli. *Appl Environ Microb* **77**, 2905–2915 (2011).

186. Berrıos-Rivera, S. J., Bennett, G. N. & San, K.-Y. Metabolic Engineering of Escherichia coli: Increase of NADH Availability by Overexpressing an NAD+-Dependent Formate Dehydrogenase. *Metab Eng* **4**, 217–229 (2002).

187. Hong, S. & Lee, S. Importance of redox balance on the production of succinic acid by metabolically engineered Escherichia coli. *Appl Microbiol Biotechnol* **58**, 286–290 (2002).

188. Karthikeyan, R., Singh, R. & Bose, A. Microbial electron uptake in microbial electrosynthesis: a mini-review. *J Ind Microbiol Biotechnol* **46**, 1419–1426 (2019).

189. Ross, D. E., Flynn, J. M., Baron, D. B., Gralnick, J. A. & Bond, D. R. Towards Electrosynthesis in Shewanella: Energetics of Reversing the Mtr Pathway for Reductive Metabolism. *PLOS One* **6**, e16649 (2011).

190. Rowe, A. R. *et al.* Tracking Electron Uptake from a Cathode into Shewanella Cells: Implications for Energy Acquisition from Solid-Substrate Electron Donors. *mBio* **9**, 9–19 (2018).

191. Tefft, N. M. & TerAvest, M. A. Reversing an Extracellular Electron Transfer Pathway for Electrode-Driven Acetoin Reduction. *ACS Synth Biol* **8**, 1590–1600 (2019).

192. Cao, Y. *et al.* Programmable assembly of pressure sensors using pattern-forming bacteria. *Nat Biotechnol* **35**, 1087–1093 (2017).

193. Din, M. O., Martin, A., Razinkov, I., Csicsery, N. & Hasty, J. Interfacing gene circuits with microelectronics through engineered population dynamics. *Sci Adv* **6**, eaaz8344 (2020).

194. Orth, J. D., Thiele, I. & Palsson, B. Ø. What is flux balance analysis? *Nat Biotechnol* **28**, 245–248 (2010).

195. Feist, A. M. *et al.* A genome-scale metabolic reconstruction for Escherichia coli K-12 MG1655 that accounts for 1260 ORFs and thermodynamic information. *Mol Syst Biol* **3**, 121 (2007).

196. Niebel, B., Leupold, S. & Heinemann, M. An upper limit on Gibbs energy dissipation governs cellular metabolism. *Nat Metabol* **1**, 125–132 (2019).

197. Gardner, T. S., Cantor, C. R. & Collins, J. J. Construction of a genetic toggle switch in Escherichia coli. *Nature* **403**, 339–342 (2000).

198. Elowitz, M. B. & Leibler, S. A synthetic oscillatory network of transcriptional regulators. *Nature* **403**, 335–338 (2000).

199. Knight, T. Idempotent vector design for standard assembly of biobricks. (2003).

200. Bônnet, J., Subsoontorn, P. & Endy, D. Rewritable digital data storage in live cells via engineered control of recombination directionality. *Proc Natl Acad Sci USA* **109**, 8884–8889 (2012).

201. Tabor, J. J. *et al.* A Synthetic Genetic Edge Detection Program. *Cell* **137**, 1272–1281 (2009).

202. Olson, E. J., Hartsough, L. A., Landry, B. P., Shroff, R. & Tabor, J. J. Characterizing bacterial gene circuit dynamics with optically programmed gene expression signals. *Nat Methods* **11**, 449–455 (2014).

203. Landry, B. P., Palanki, R., Dyulgyarov, N., Hartsough, L. A. & Tabor, J. J. Phosphatase activity tunes two-component system sensor detection threshold. *Nat Commun* **9**, 1–10 (2018).

204. Andrews, L. B., Nielsen, A. A. K. & Voigt, C. A. Cellular checkpoint control using programmable sequential logic. *Science* **361**, eaap8987 (2018).

205. Bourdeau, R. W. *et al.* Acoustic reporter genes for noninvasive imaging of microorganisms in mammalian hosts. *Nature* **553**, 86–90 (2018).

206. Ryu, M.-H. *et al.* Control of nitrogen fixation in bacteria that associate with cereals. *Nat Microbiol* **5**, 314–330 (2019).

207. Stricker, J. *et al.* A fast, robust and tunable synthetic gene oscillator. *Nature* **456**, 516–519 (2008).

208. Danino, T., Mondragón-Palomino, O., Tsimring, L. & Hasty, J. A synchronized quorum of genetic clocks. *Nature* **463**, 326–330 (2010).

209. Moser, F. *et al.* Dynamic control of endogenous metabolism with combinatorial logic circuits. *Mol Syst Biol* **14**, e8605-18 (2018).

210. Hirose, A., Kouzuma, A. & Watanabe, K. Towards development of electrogenetics using electrochemically active bacteria. *Biotechnol Adv* **37**, 107351 (2019).

211. Brophy, J. A. N. & Voigt, C. A. Principles of genetic circuit design. *Nat Methods* **11**, 508–520 (2014).

212. Kasai, T., Kouzuma, A., Nojiri, H. & Watanabe, K. Transcriptional mechanisms for differential expression of outer membrane cytochrome genes omcA and mtrC in Shewanella oneidensis MR-1. *BMC Microbiol* **15**, (2015).

213. Yi, Y.-C. & Ng, I.-S. Establishment of toolkit and T7RNA polymerase/promoter system in Shewanella oneidensis MR-1. *J Taiwan Inst Chem E* (2020) doi:10.1016/j.jtice.2020.02.003.

214. Webster, D. P. *et al.* An arsenic-specific biosensor with genetically engineered Shewanella oneidensis in a bioelectrochemical system. *Biosens Bioelectron* **62**, 320–324 (2014).

215. Cao, Y., Li, X., Li, F. & Song, H. CRISPRi–sRNA: Transcriptional–Translational Regulation of Extracellular Electron Transfer in Shewanella oneidensis. *ACS Synth Biol* **6**, 1679–1690 (2017).

216. Li, J. *et al.* Rediverting Electron Flux with an Engineered CRISPR-ddAsCpf1 System to Enhance the Pollutant Degradation Capacity of Shewanella oneidensis. *Environ Sci Technol* **54**, 3599–3608 (2020).

217. Gescher, J. S., Cordova, C. D. & Spormann, A. M. Dissimilatory iron reduction in Escherichia coli: identification of CymA of Shewanella oneidensis and NapC of E. coli as ferric reductases. *Mol Microbiol* **68**, 706–719 (2008).

218. Sekar, R., Shin, H. D. & DiChristina, T. J. Activation of an Otherwise Silent Xylose Metabolic Pathway in Shewanella oneidensis. *Appl Environ Microbiol* **82**, 3996–4005 (2016).

219. Howard, E. C., Hamdan, L. J., Lizewski, S. E. & Ringeisen, B. R. High frequency of glucose-utilizing mutants in Shewanella oneidensis MR-1. *FEMS Microbiol Lett* **327**, 9–14 (2011).

220. Nakagawa, G. *et al.* Metabolic Characteristics of a Glucose-Utilizing Shewanella oneidensis Strain Grown under Electrode-Respiring Conditions. *PLOS One* **10**, e0138813 (2015).

221. Flynn, J. M., Ross, D. E., Hunt, K. A., Bond, D. R. & Gralnick, J. A. Enabling Unbalanced Fermentations by Using Engineered Electrode-Interfaced Bacteria. *mBio* **1**, e00190-10-e00190-17 (2010).

222. Wang, X. *et al.* Improving electron trans-inner membrane movements in microbial electrocatalysis. *Chem. Commun* 1–5 (2016) doi:10.1039/c6cc00976j.

223. Li, F. *et al.* Modular Engineering Intracellular NADH Regeneration Boosts Extracellular Electron Transfer of Shewanella oneidensis MR-1. *ACS Synth Biol* **7**, 885–895 (2018).

224. Joshi, K., Kane, A. L., Kotloski, N. J., Gralnick, J. A. & Bond, D. R. Preventing Hydrogen Disposal Increases Electrode Utilization Efficiency by Shewanella oneidensis. *Front Energy Res* **7**, 95 (2019).

225. Min, D. *et al.* Enhancing Extracellular Electron Transfer of Shewanella oneidensis MR-1 through Coupling Improved Flavin Synthesis and Metal-Reducing Conduit for Pollutant Degradation. *Environ Sci Technol* **51**, 5082–5089 (2017).

226. Logan, B. E., Rossi, R., Ragab, A. & Saikaly, P. E. Electroactive microorganisms in bioelectrochemical systems. *Nat Rev Microbiol* **17**, 307–319 (2019).

227. Ang, J., Harris, E., Hussey, B. J., Kil, R. & McMillen, D. R. Tuning Response Curves for Synthetic Biology. *ACS Synth Biol* **2**, 547–567 (2013).

228. Salis, H. M., Mirsky, E. A. & Voigt, C. A. Automated design of synthetic ribosome binding sites to control protein expression. *Nat Biotechnol* **27**, 946–950 (2009).

229. Meyer, A. J., Segall-Shapiro, T. H., Glassey, E., Zhang, J. & Voigt, C. A. Escherichia coli "Marionette" strains with 12 highly optimized small-molecule sensors. *Nat Chem Biol* **15**, 196–204 (2019).

230. Yuan, S.-J. *et al.* A plate-based electrochromic approach for the high-throughput detection of electrochemically active bacteria. *Nat Protoc* **9**, 112–119 (2014).

231. Kelly, J. R. *et al.* Measuring the activity of BioBrick promoters using an in vivo reference standard. *J Biol Eng* **3**, 4–13 (2009).

232. Liu, C., Gorby, Y. A., Zachara, J. M., Fredrickson, J. K. & Brown, C. F. Reduction kinetics of Fe(III), Co(III), U(VI), Cr(VI), and Tc(VII) in cultures of dissimilatory metal-reducing bacteria. *Biotechnol Bioeng* **80**, 637–649 (2002).

233. Canton, B., Labno, A. & Endy, D. Refinement and standardization of synthetic biological parts and devices. *Nat Biotechnol* **26**, 787–793 (2008).

234. Rosenfeld, N. & Alon, U. Response Delays and the Structure of Transcription Networks. *J Mol Biol* **329**, 645–654 (2003).

235. Florea, M. *et al.* Engineering control of bacterial cellulose production using a genetic toolkit and a new cellulose-producing strain. *Proc Natl Acad Sci USA* **113**, E3431–E3440 (2016).

236. Malvankar, N. S. & Lovley, D. R. Microbial nanowires for bioenergy applications. *Curr Opin Biotechnol* **27**, 88–95 (2014).

237. Rabaey, K. & Rozendal, R. A. Microbial electrosynthesis — revisiting the electrical route for microbial production. *Nat Rev Microbiol* **8**, 706–716 (2010).

238. Nichols, E. M. *et al.* Hybrid bioinorganic approach to solar-to-chemical conversion. *Proc Natl Acad Sci USA* **112**, 11461–11466 (2015).

239. Pirbadian, S. *et al.* Shewanella oneidensis MR-1 nanowires are outer membrane and periplasmic extensions of the extracellular electron transport components. *Proc Natl Acad Sci USA* **111**, 12883–12888 (2014).

240. White, G. F. *et al.* Rapid electron exchange between surface-exposed bacterial cytochromes and Fe(III) minerals. *Proc Natl Acad Sci USA* **110**, 6346–6351 (2013).

241. Zacharoff, L. A. & El-Naggar, M. Y. Redox conduction in biofilms: From respiration to living electronics. *Curr Opin Electrochem* **4**, 182–189 (2017).

242. Beliav, A. S. *et al.* Global Transcriptome Analysis of Shewanella oneidensis MR-1 Exposed to Different Terminal Electron Acceptors. *J Bacteriol* **187**, 7138–7145 (2005).

243. Flynn, T. M., O'Loughlin, E. J., Mishra, B., DiChristina, T. J. & Kemner, K. M. Sulfur-mediated electron shuttling during bacterial iron reduction. *Science* **344**, 1039–1042 (2014).

244. Sekar, R. & DiChristina, T. J. Microbially Driven Fenton Reaction for Degradation of the Widespread Environmental Contaminant 1,4-Dioxane. *Environ Sci Technol* **48**, 12858–12867 (2014).

245. Boyer, C. *et al.* Copper-Mediated Living Radical Polymerization (Atom Transfer Radical Polymerization and Copper(0) Mediated Polymerization): From Fundamentals to Bioapplications. *Chem Rev* **116**, 1803–1949 (2015).

246. Simakova, A., Averick, S. E., Konkolewicz, D. & Matyjaszewski, K. Aqueous ARGET ATRP. *Macromolecules* **45**, 6371–6379 (2012).

247. Magennis, E. P. *et al.* Bacteria-instructed synthesis of polymers for self-selective microbial binding and labelling. *Nat Mater* **13**, 748–755 (2014).

248. Niu, J. *et al.* Engineering live cell surfaces with functional polymers via cytocompatible controlled radical polymerization. *Nat Chem* **9**, 537–545 (2017).

249. Magenau, A. J. D., Strandwitz, N. C., Gennaro, A. & Matyjaszewski, K. Electrochemically Mediated Atom Transfer Radical Polymerization. *Science* **332**, 81–84 (2011).

250. Workman, D. J., Woods, S. L., Gorby, Y. A., Fredrickson, J. K. & Truex, M. J. Microbial Reduction of Vitamin B 12 by Shewanella alga Strain BrY with Subsequent Transformation of Carbon Tetrachloride. *Environ Sci Technol* **31**, 2292–2297 (1997).

251. Encinas, M. V., Rufs, A. M., Bertolotti, S. & Previtali, C. M. Free Radical Polymerization Photoinitiated by Riboflavin/Amines. Effect of the Amine Structure. *Macromolecules* **34**, 2845–2847 (2001).

252. Simakova, A., Mackenzie, M., Averick, S. E., Park, S. & Matyjaszewski, K. Bioinspired Iron-Based Catalyst for Atom Transfer Radical Polymerization. *Angew Chem* **52**, 12148–12151 (2013).

253. Peng, C.-H., Yang, T.-Y., Zhao, Y. & Fu, X. Reversible deactivation radical polymerization mediated by cobalt complexes: recent progress and perspectives. *Org Biomol Chem* **12**, 8580–8587 (2014).

254. Heffern, M. C. *et al.* In vivo bioluminescence imaging reveals copper deficiency in a murine model of nonalcoholic fatty liver disease. *Proc Natl Acad Sci USA* **113**, 14219–14224 (2016).

255. Cotruvo, Jr. J. A., Aron, A. T., Ramos-Torres, K. M. & Chang, C. J. Synthetic fluorescent probes for studying copper in biological systems. *Chem Soc Rev* **44**, 4400–4414 (2015).

256. Changela, A. *et al.* Molecular Basis of Metal-Ion Selectivity and Zeptomolar Sensitivity by CueR. *Science* **301**, 1383–1387 (2003).

257. Chandrangsu, P., Rensing, C. & Helmann, J. D. Metal homeostasis and resistance in bacteria. *Nat Rev Microbiol* **15**, 338–350 (2017).

258. Smirnova, G. V. & Oktyabrsky, O. N. Glutathione in Bacteria. *Biochem Mosc* **70**, 1199–1211 (2005).

259. Helbig, K., Bleuel, C., Krauss, G. J. & Nies, D. H. Glutathione and transition-metal homeostasis in Escherichia coli. *J Bacteriol* **190**, 5431–8 (2008).

260. Sporer, A. J., Kahl, L. J., Price-Whelan, A. & Dietrich, L. E. P. Redox-Based Regulation of Bacterial Development and Behavior. *Annu Rev Biochem* **86**, 777–797 (2017).

261. Braymer, J. J. & Giedroc, D. P. Recent developments in copper and zinc homeostasis in bacterial pathogens. *Curr Opin Chem Biol* **19**, 59–66 (2014).

262. Fung, D. K. C., Lau, W. Y., Chan, W. T. & Yan, A. Copper Efflux Is Induced during Anaerobic Amino Acid Limitation in Escherichia coli To Protect Iron-Sulfur Cluster Enzymes and Biogenesis. *J Bacteriol* **195**, 4556–4568 (2013).

263. Toes, A.-C. M., Daleke, M. H., Kuenen, J. G. & Muyzer, G. Expression of copA and cusA in Shewanella during copper stress. *Microbiol* **154**, 2709–18 (2008).

264. Pinchuk, G. E. *et al.* Pyruvate and Lactate Metabolism by Shewanella oneidensis MR-1 under Fermentation, Oxygen Limitation, and Fumarate Respiration Conditions. *Appl Environ Microbiol* **77**, 8234–8240 (2011).

265. Esteve-Núñez, A., Sosnik, J., Visconti, P. & Lovley, D. R. Fluorescent properties of c-type cytochromes reveal their potential role as an extracytoplasmic electron sink in Geobacter sulfurreducens. *Environ Microbiol* **10**, 497–505 (2008).

266. Breuer, M., Rosso, K. M. & Blumberger, J. Electron flow in multiheme bacterial cytochromes is a balancing act between heme electronic interaction and redox potentials. *Proc Natl Acad Sci USA* **111**, 611–616 (2014).

267. Glasser, N. R., Saunders, S. H. & Newman, D. K. The Colorful World of Extracellular Electron Shuttles. *Annu Rev Microbiol* **71**, annurev-micro-090816-093913-21 (2017).

268. Meshulam-Simon, G., Behrens, S., Choo, A. D. & Spormann, A. M. Hydrogen metabolism in Shewanella oneidensis MR-1. *Appl Environ Microbiol* **73**, 1153–1165 (2007).

269. Meyer, T. E. *et al.* Identification of 42 Possible Cytochrome C Genes in the Shewanella oneidensis Genome and Characterization of Six Soluble Cytochromes. *OMICS Journal Int Biol* **8**, 57–77 (2004).

270. Tonga, G. Y. *et al.* Supramolecular regulation of bioorthogonal catalysis in cells using nanoparticle-embedded transition metal catalysts. *Nat Chem* **7**, 597–603 (2015).

271. Wang, J. *et al.* Palladium-Triggered Chemical Rescue of Intracellular Proteins via Genetically Encoded Allene-Caged Tyrosine. *J Am Chem Soc* **138**, 15118–15121 (2016).

272. Sirasani, G., Tong, L. & Balskus, E. P. A Biocompatible Alkene Hydrogenation Merges Organic Synthesis with Microbial Metabolism. *Angew Chem* **53**, 7785–7788 (2014).

273. Bortolamei, N., Isse, A. A., Magenau, A. J. D., Gennaro, A. & Matyjaszewski, K. Controlled Aqueous Atom Transfer Radical Polymerization with Electrochemical Generation of the Active Catalyst. *Angew Chem* **123**, 11593–11596 (2011).

274. Canning, S. L., Smith, G. N. & Armes, S. P. A Critical Appraisal of RAFT-Mediated Polymerization-Induced Self-Assembly. *Macromolecules* **49**, 1985–2001 (2016).

275. Park, J. H., Hong, D., Lee, J. & Choi, I. S. Cell-in-Shell Hybrids: Chemical Nanoencapsulation of Individual Cells. *Acc Chem Res* **49**, 792–800 (2016).

276. Lui, L. T. *et al.* Bacteria clustering by polymers induces the expression of quorum-sensing-controlled phenotypes. *Nat Chem* **5**, 1058–1065 (2013).

277. Jensen, H. M., TerAvest, M. A., Kokish, M. G. & Ajo-Franklin, C. M. CymA and Exogenous Flavins Improve Extracellular Electron Transfer and Couple It to Cell Growth in Mtr-ExpressingEscherichia coli. *ACS Synth Biol* **5**, 679–688 (2016).

278. Hemp, S. T., Smith, A. E., Bunyard, W. C., Rubinstein, M. H. & Long, T. E. RAFT polymerization of temperature- and salt-responsive block copolymers as reversible hydrogels. *Polymer* **55**, 2325–2331 (2014).

279. Cleto, S., Jensen, J., Wendisch, V. & Lu, T. Corynebacterium glutamicum Metabolic Engineering with CRISPR Interference (CRISPRi). *ACS Synth Biol* **5**, 375–85 (2016).

280. Myers, C. R. & Myers, J. M. Replication of plasmids with the p15A origin in Shewanella putrefaciens MR-1. *Lett Appl Microbiol* **24**, 221–225 (1997).

281. Hajimorad, M. & Gralnick, J. A. Towards enabling engineered microbial-electronic systems: RK2-based conjugal transfer system for Shwanella synthetic biology. *Electron Lett* **52**, 426–428 (2016).

282. Rachkevych, N., Sybirna, K., Boyko, S., Boretsky, Y. & Sibirny, A. Improving the efficiency of plasmid transformation in Shewanella oneidensis MR-1 by removing ClaI restriction site. *J Microbiol Methods* **99**, 35–37 (2014).

283. Uebe, R. & Schüler, D. Magnetosome biogenesis in magnetotactic bacteria. *Nat Rev Microbiol* **14**, 621–637 (2016).

284. Cheng, H.-Y. *et al.* Activating electrochemical catalytic activity of bio-palladium by hybridizing with carbon nanotube as “e- Bridge”. *Sci Rep* **7**, 1–9 (2017).

285. Coppage, R. *et al.* Determining peptide sequence effects that control the size, structure, and function of nanoparticles. *ACS Nano* **6**, 1625–1636 (2012).

286. Zhou, C. *et al.* Palladium Recovery in a H2-Based Membrane Biofilm Reactor: Formation of Pd(0) Nanoparticles through Enzymatic and Autocatalytic Reductions. *Environ Sci Technol* **50**, 2546–2555 (2016).

287. Lee, S. Y., Royston, E., Culver, J. N. & Harris, M. T. Improved metal cluster deposition on a genetically engineered tobacco mosaic virus template. *Nanotechnol* **16**, S435–S441 (2005).

288. Ishiki, K., Shiigi, H. & Nagaoka, T. Optical Elemental Analysis of Metals Using Shewanella oneidensis. *Anal Sci* 1–3 (2017).

289. Omajali, J. B., Mikheenko, I. P., Overton, T. W., Merroun, M. L. & Macaskie, L. E. Probing the viability of palladium-challenged bacterial cells using flow cytometry. *J Chem Techno Biotechnol* **78**, 95–7 (2018).

290. Klug, H. P. & Alexander, L. E. X-ray diffraction procedures: for polycrystalline and amorphous materials. *X-Ray Diffraction Procedures: For Polycrystalline and Amorphous Materials, 2nd Edition, by Harold P. Klug, Leroy E. Alexander, pp. 992. ISBN 0-471-49369-4. Wiley-VCH, May 1974.* 992 (1974).

291. Niu, W., Zhang, L. & Xu, G. Shape-Controlled Synthesis of Single-Crystalline Palladium Nanocrystals. *ACS Nano* **4**, 1987–1996 (2010).

292. Leaphart, A. B. *et al.* Transcriptome Profiling of Shewanella oneidensis Gene Expression following Exposure to Acidic and Alkaline pH. *J Bacteriol* **188**, 1633–1642 (2006).

293. Fan, G., Dundas, C. M., Graham, A. J., Lynd, N. A. & Keitz, B. K. Shewanella oneidensis as a living electrode for controlled radical polymerization. *Proc Natl Acad Sci USA* **115**, 4559–4564 (2018).

294. Gorby, Y. *et al.* Redox-reactive membrane vesicles produced by Shewanella. *Geobiol* **6**, 232–241 (2008).

295. Subramanian, P., Pirbadian, S., El-Naggar, M. Y. & Jensen, G. J. Ultrastructure of Shewanella oneidensis MR-1 nanowires revealed by electron cryotomography. *Proc Natl Acad Sci USA* **115**, E3246–E3255 (2018).

296. Albert, A. The Metal-Binding Properties of Riboflavin. *Biochem J* **47**, xxvii (1950).

297. Nadagouda, M. N. & Varma, R. S. Green and controlled synthesis of gold and platinum nanomaterials using vitamin B2: density-assisted self-assembly of nanospheres, wires and rods. *Green Chem* **8**, 516–3 (2006).

298. Jensen, H. M. *et al.* Engineering of a synthetic electron conduit in living cells. *Proc Natl Acad Sci USA* **107**, 19213–19218 (2010).

299. Tuo, Y. *et al.* Microbial formation of palladium nanoparticles by Geobacter sulfurreducens for chromate reduction. *Bioresour Technol* **133**, 606–611 (2013).

300. Yates, M. D., Cusick, R. D. & Logan, B. E. Extracellular Palladium Nanoparticle Production using Geobacter sulfurreducens. *ACS Sustain Chem Eng* **1**, 1165–1171 (2013).

301. Hyster, T. K. & Ward, T. R. Genetic Optimization of Metalloenzymes: Enhancing Enzymes for Non-Natural Reactions. *Angew Chem* **128**, 7468–7482 (2016).

302. Fukushima, T. *et al.* The Molecular Basis for Binding of an Electron Transfer Protein to a Metal Oxide Surface. *J Am Chem Soc* **139**, 12647–12654 (2017).

303. Covington, E. D., Gelbmann, C. B., Kotloski, N. J. & Gralnick, J. A. An essential role for UshA in processing of extracellular flavin electron shuttles by Shewanella oneidensis. *Mol Microbiol* **78**, 519–532 (2010).

304. Hau, H. H., Gilbert, A., Coursolle, D. & Gralnick, J. A. Mechanism and Consequences of Anaerobic Respiration of Cobalt by Shewanella oneidensis Strain MR-1. *Appl Environ Microbiol* **74**, 6880 (2008).

305. Rotaru, A.-E., jiang, wei, Finster, K., Skrydstrup, T. & Meyer, R. L. Non-Enzymatic Palladium Recovery on Microbial and Synthetic Surfaces. *Biotechnol Bioeng* **109**, 1889–1897 (2012).

306. Vargas, M., Kashefi, K., Blunt-Harris, E. L. & Lovley, D. R. Microbiological evidence for Fe(III) reduction on early Earth. *Nature* **395**, 65–67 (1998).

307. Tagliabue, A. *et al.* The integral role of iron in ocean biogeochemistry. *Nature* **543**, 51–59 (2017).

308. Cornell, R. M. & Schwertmann, U. *The Iron Oxides: Structure, Properties, Reactions, Occurrences and Uses*. (2003). doi:10.1002/3527602097.ch1.

309. D'Alessandro, D. M. Exploiting redox activity in metal–organic frameworks: concepts, trends and perspectives. *Chem Commun* **52**, 8957–8971 (2016).

310. O'Keeffe, M. & Yaghi, O. M. Deconstructing the Crystal Structures of Metal–Organic Frameworks and Related Materials into Their Underlying Nets. *Chem Rev* **112**, 675–702 (2011).

311. McDonald, T. M. *et al.* Cooperative insertion of CO2 in diamine-appended metal-organic frameworks. *Nature* **519**, 303–308 (2015).

312. Ranocchiari, M. & Bokhoven, J. A. van. Catalysis by metal–organic frameworks: fundamentals and opportunities. *Phys Chem Chem Phys* **13**, 6388 (2011).

313. Horcajada, P. *et al.* Metal–Organic Frameworks in Biomedicine. *Chem Rev* **112**, 1232–1268 (2012).

314. Li, L.-L., Feng, X.-Q., Han, R.-P., Zang, S.-Q. & Yang, G. Cr(VI) removal via anion exchange on a silver-triazolate MOF. *J Hazard Mater* **321**, 622–628 (2017).

315. Huskic, I., Pekov, I. V., Krivovichev, S. V. & Friscic, T. Minerals with metal-organic framework structures. *Sci Adv* **2**, e1600621–e1600621 (2016).

316. Guesh, K. *et al.* Sustainable Preparation of MIL-100(Fe) and Its Photocatalytic Behavior in the Degradation of Methyl Orange in Water. *Cryst Growth Des* **17**, 1806–1813 (2017).

317. Sanchez-Sanchez, M., Asua, I. de, Ruano, D. & Diaz, K. Direct Synthesis, Structural Features, and Enhanced Catalytic Activity of the Basolite F300-like Semiamorphous Fe-BTC Framework. *Cryst Growth Des* **15**, 4498–4506 (2015).

318. Wang, J. *et al.* Metal–organic frameworks MIL-88A with suitable synthesis conditions and optimal dosage for effective catalytic degradation of Orange G through persulfate activation. *RSC Adv* **6**, 112502–112511 (2016).

319. García, M. V. *et al.* Laboratory synthesis of goethite and ferrihydrite of controlled particle sizes. *Bol Soc Geol Mex* **67**, 433–446 (2015).

320. Burtch, N. C., Jasuja, H. & Walton, K. S. Water Stability and Adsorption in Metal–Organic Frameworks. *Chem Rev* **114**, 10575–10612 (2014).

321. Wang, J.-M., Wan, J.-Q., Ma, Y.-W., Wang, Y. & Guan, Z.-Y. Influence of Preparation Conditions of MIL-88A on Catalytic Degradation of Orange G and Dibutyl Phthalate. *ICSD* (2017) doi:10.2991/icsd-17.2017.3.

322. Parker, D. L., Borer, P. & Bernier-Latmani, R. The Response of Shewanella oneidensis MR-1 to Cr(III) Toxicity Differs from that to Cr(VI). *Front Microbiol* **2**, 223 (2011).

323. Kostka, J. E., Dalton, D. D., Skelton, H., Dollhopf, S. & Stucki, J. W. Growth of Iron(III)-Reducing Bacteria on Clay Minerals as the Sole Electron Acceptor and Comparison of Growth Yields on a Variety of Oxidized Iron Forms. *Appl Environ Microbiol* **68**, 6256–6262 (2002).

324. Jiao, Y. *et al.* Deciphering the Electron Transport Pathway for Graphene Oxide Reduction by Shewanella oneidensis MR-1. *J Bacteriol* **193**, 3662–3665 (2011).

325. Roden, E. E. & Zachara, J. M. Microbial Reduction of Crystalline Iron(III) Oxides: Influence of Oxide Surface Area and Potential for Cell Growth. *Environ Sci Technol* **30**, 1618–1628 (1996).

326. Sun, D. T., Gasilova, N., Yang, S., Oveisi, E. & Queen, W. L. Rapid, Selective Extraction of Trace Amounts of Gold from Complex Water Mixtures with a Metal–Organic Framework (MOF)/Polymer Composite. *J Am Chem Soc* **140**, 16697–16703 (2018).

327. Heyden, B. P. von der & Roychoudhury, A. N. Application, Chemical Interaction and Fate of Iron Minerals in Polluted Sediment and Soils. *Curr Pollut Rep* **1**, 265–279 (2015).

328. Brookshaw, D. R., Coker, V. S., Lloyd, J. R., Vaughan, D. J. & Pattrick, R. A. D. Redox Interactions Between Cr(VI) and Fe(II) in Bioreduced Biotite and Chlorite. *Environ Sci Technol* **48**, 11337–11342 (2014).

329. Li, X., Xu, H., Kong, F. & Wang, R. A Cationic Metal-Organic Framework Consisting of Nanoscale Cages: Capture, Separation, and Luminescent Probing of Cr 2 O 7 2− through a Single-Crystal to Single-Crystal Process. *Angew Chem* **52**, 13769–13773 (2013).

330. Fei, H., Han, C. S., Robins, J. C. & Oliver, S. R. J. A Cationic Metal–Organic Solid Solution Based on Co(II) and Zn(II) for Chromate Trapping. *Chem Mater* **25**, 647–652 (2013).

331. Fu, H.-R., Xu, Z.-X. & Zhang, J. Water-Stable Metal–Organic Frameworks for Fast and High Dichromate Trapping via Single-Crystal-to-Single-Crystal Ion Exchange. *Chem Mater* **27**, 205–210 (2014).

332. Luo, M. B. *et al.* The MOF + Technique: A Significant Synergic Effect Enables High Performance Chromate Removal. *Angew Chem* **56**, 16376–16379 (2017).

333. Mohan, D. & Jr, C. U. P. Activated carbons and low cost adsorbents for remediation of tri- and hexavalent chromium from water. *J Hazard Mater* **137**, 762–811 (2006).

334. Lovley, D. R., Phillips, E. J. & Lonergan, D. J. Hydrogen and Formate Oxidation Coupled to Dissimilatory Reduction of Iron or Manganese by Alteromonas putrefaciens. *Appl Environ Microbiol* **55**, 700–6 (1989).

335. Burdige, D. J., Dhakar, S. P. & Nealson, K. H. Effects of manganese oxide mineralogy on microbial and chemical manganese reduction. *Geomicrobiol J* **10**, 27–48 (1992).

336. Yan, B., Wrenn, B. A., Basak, S., Biswas, P. & Giammar, D. E. Microbial Reduction of Fe(III) in Hematite Nanoparticles by Geobacter sulfurreducens. *Environ Sc Technol* **42**, 6526–6531 (2008).

337. Bose, S. *et al.* Bioreduction of hematite nanoparticles by the dissimilatory iron reducing bacterium Shewanella oneidensis MR-1. *Geochim Cosmochim Acta* **73**, 962–976 (2009).

338. Liu, J. *et al.* Particle size effect and the mechanism of hematite reduction by the outer membrane cytochrome OmcA of Shewanella oneidensis MR-1. *Geochim Cosmochim Acta* **193**, 160–175 (2016).

339. Li, X. *et al.* Reduction of structural Fe(III) in oxyhydroxides by Shewanella decolorationis S12 and characterization of the surface properties of iron minerals. *J Soils Sediments* **12**, 217–227 (2012).

340. Tan, H. *et al.* Biological Reduction of Nanoengineered Iron(III) Oxide Sculptured Thin Films. *Environ Sci Technol* **40**, 5490–5495 (2006).

341. Zou, X., Zhang, L., Wang, Z. & Luo, Y. Mechanisms of the Antimicrobial Activities of Graphene Materials. *J Am Chem Soc* **138**, 2064–2077 (2016).

342. Ma, W. *et al.* Bacillus subtilis biofilm development in the presence of soil clay minerals and iron oxides. *NPJ Biofilms Microbi* **3**, 4 (2017).

343. Glasauer, S., Weidler, P. G., Langley, S. & Beveridge, T. J. Controls on Fe reduction and mineral formation by a subsurface bacterium. *Geochim Cosmochim Acta* **67**, 1277–1288 (2003).

344. Lienemann, M. *et al.* Towards patterned bioelectronics: facilitated immobilization of exoelectrogenic Escherichia coli with heterologous pili. *Microb Biotechnol* **11**, 1184–1194 (2018).

345. Abednatanzi, S. *et al.* Mixed-metal metal–organic frameworks. *Chem Soc Rev* **48**, 2535–2565 (2019).

346. Kostka, J. E., Haefele, E., Viehweger, R. & Stucki, J. W. Respiration and Dissolution of Iron(III)-Containing Clay Minerals by Bacteria. *Environ Sci Technol* **33**, 3127–3133 (1999).

347. Pham, B. T. N., Lund, L. M. & Song, D. Novel Luminescent Metal-Organic Frameworks [Eu 2 L 3 (DMSO) 2 (MeOH) 2]·2DMSO·3H 2 O and [Zn 2 L 2 (DMSO) 2]·1.6H 2 O (L = 4,4′-Ethyne-1,2-diyldibenzoate). *Inorg Chem* **47**, 6329–6335 (2008).

348. Feng, D. *et al.* Zirconium-Metalloporphyrin PCN-222: Mesoporous Metal-Organic Frameworks with Ultrahigh Stability as Biomimetic Catalysts. *Angew Chem* **51**, 10307–10310 (2012).

349. Park, S. S. *et al.* Cation-Dependent Intrinsic Electrical Conductivity in Isostructural Tetrathiafulvalene-Based Microporous Metal–Organic Frameworks. *J Am Chem Soc* **137**, 1774–1777 (2015).

350. Fredrickson, J. K. *et al.* Influence of Mn oxides on the reduction of uranium(VI) by the metal-reducing bacterium Shewanella putrefaciens. *Geochim Cosmochim Acta* **66**, 3247–3262 (2002).

351. Kato, S., Hashimoto, K. & Watanabe, K. Methanogenesis facilitated by electric syntrophy via (semi)conductive iron-oxide minerals. *Environ Microbiol* **14**, 1646–1654 (2011).

352. Liu, F. *et al.* Magnetite compensates for the lack of a pilin-associated c -type cytochrome in extracellular electron exchange: Magnetite compensates for the lack of OmcS. *Environ Microbiol* **17**, 648–655 (2014).

353. Bradford, M. M. A rapid and sensitive method for the quantitation of microgram quantities of protein utilizing the principle of protein-dye binding. *Anal Biochem* **72**, 248–254 (1976).

354. Stookey, L. L. Ferrozine-A New Spectrophotometric Reagent for Iron. *Anal Chem* **42**, 779–781 (1970).

355. Coreno-Alonso, A., Cruz-Jimenez, G., López-Martinez, L., Reyna-López, G. E. & Acevedo-Aguilar, F. J. A rapid, eco-friendly, and reliable microplate method for determination of Cr(VI). *Turk J Chem* **41**, 420–425 (2017).

356. Shi, L., Squier, T. C., Zachara, J. M. & Fredrickson, J. K. Respiration of metal (hydr)oxides by Shewanella and Geobacter: a key role for multihaem c-type cytochromes. *Mol Microbiol* **65**, 12–20 (2007).

357. Tamsir, A., Tabor, J. J. & Voigt, C. A. Robust multicellular computing using genetically encoded NOR gates and chemical 'wires'. *Nature* **469**, 212–215 (2010).

358. Arnold, R. G., Hoffmann, M. R., Dichristina, T. J. & Picardal, F. W. Regulation of Dissimilatory Fe(III) Reduction Activity in Shewanella putrefaciens. *Appl Environ Microbiol* **56**, 2811–7 (1990).

359. Dobbin, P. S., Powell, A. K., McEwan, A. G. & Richardson, D. J. The influence of chelating agents upon the dissimilatory reduction of Fe(III) by Shewanella putrefaciens. *Biometals* **8**, 163–173 (1995).

360. Borloo, J. *et al.* A kinetic approach to the dependence of dissimilatory metal reduction by Shewanella oneidensis MR-1 on the outer membrane cytochromes OmcA and OmcB. *FEBS J* **274**, 3728–3738 (2007).

361. Segall-Shapiro, T. H., Sontag, E. D. & Voigt, C. A. Engineered promoters enable constant gene expression at any copy number in bacteria. *Nat Biotechnol* **36**, 352–358 (2018).

362. Lutz, R. & Bujard, H. Independent and tight regulation of transcriptional units in Escherichia coli via the LacR/O, the TetR/O and AraC/I1-I2 regulatory elements. *Nucleic Acids Res* **25**, 1203–1210 (1997).

363. Monod, J. The Growth of Bacterial Cultures. *Annu Rev Microbiol* **3**, 371–394 (1949).

364. Alon, U. *An Introduction to Systems Biology: Design Principles of Biological Circuits*. (2006). doi:10.1201/9781420011432.

365. Farasat, I. *et al.* Efficient search, mapping, and optimization of multi-protein genetic systems in diverse bacteria. *Mol Syst Biol* **10**, 731 (2014).

366. Ng, C. Y., Farasat, I., Maranas, C. D. & Salis, H. M. Rational design of a synthetic Entner-Doudoroff pathway for improved and controllable NADPH regeneration. *Metab Eng* **29**, 86–96 (2015).

367. Lou, C., Stanton, B., Chen, Y.-J., Munsky, B. & Voigt, C. A. Ribozyme-based insulator parts buffer synthetic circuits from genetic context. *Nat Biotechnol* **30**, 1137–1142 (2012).

368. Goldbeck, C. P. *et al.* Tuning Promoter Strengths for Improved Synthesis and Function of Electron Conduits in Escherichia coli. *ACS Synth Biol* **2**, 150–159 (2013).

369. Lower, B. H., Hochella, M. F. & Lower, S. K. Putative mineral-specific proteins synthesized by a metal reducing bacterium. *Am J Sci* **305**, 687–710 (2005).

370. Kovárová-Kovar, K. & Egli, T. Growth kinetics of suspended microbial cells: from single-substrate-controlled growth to mixed-substrate kinetics. *Microbiol Mol Biol Rev* **62**, 646–66 (1998).

371. Rosenbaum, M. A. *et al.* Transcriptional Analysis of Shewanella oneidensis MR-1 with an Electrode Compared to Fe(III)Citrate or Oxygen as Terminal Electron Acceptor. *PLOS One* **7**, e30827 (2012).

372. Yokobayashi, Y., Weiss, R. & Arnold, F. H. Directed evolution of a genetic circuit. *Proc Natl Acad Sci USA* **99**, 16587–16591 (2002).

373. Stanton, B. C. *et al.* Genomic mining of prokaryotic repressors for orthogonal logic gates. *Nat Chem Biol* **10**, 99–105 (2014).

374. Xiong, Y. *et al.* Targeted Protein Degradation of Outer Membrane Decaheme Cytochrome MtrC Metal Reductase in Shewanella oneidensisMR-1 Measured Using Biarsenical Probe CrAsH-EDT 2. *Biochem* **50**, 9738–9751 (2011).

375. Edwards, M. J. *et al.* Structural modeling of an outer membrane electron conduit from a metal-reducing bacterium suggests electron transfer via periplasmic redox partners. *J Biol Chem* **293**, 8103–8112 (2018).

376. Schicklberger, M., Bücking, C., Schuetz, B., Heide, H. & Gescher, J. Involvement of the Shewanella oneidensis Decaheme Cytochrome MtrA in the Periplasmic Stability of the β-Barrel Protein MtrB. *Appl Environ Microbiol* **77**, 1520–1523 (2011).

377. Atkinson, J. T. *et al.* Metalloprotein switches that display chemical- dependent electron transfer in cells. *Nat Chem Biol* **107**, 1–10 (2018).

378. Schmidl, S. R. *et al.* Rewiring bacterial two-component systems by modular DNA-binding domain swapping. *Nat Chem Biol* **15**, 690–698 (2019).

379. Myers, C. R. & Myers, J. M. Ferric iron reduction-linked growth yields of Shewanella putrefaciens MR-1. *J Appl Bacteriol* **76**, 253–258 (1994).

380. Daniel, R., Rubens, J. R., Sarpeshkar, R. & Lu, T. K. Synthetic analog computation in living cells. *Nature* **497**, 619–623 (2013).

381. Kotula, J. W. *et al.* Programmable bacteria detect and record an environmental signal in the mammalian gut. *Proc Natl Acad Sci USA* **111**, 4838–4843 (2014).

382. Engler, C., Kandzia, R. & Marillonnet, S. A one pot, one step, precision cloning method with high throughput capability. *PLOS One* **3**, e3647 (2008).

383. Huebsch, N. & Mooney, D. J. Inspiration and application in the evolution of biomaterials. *Nature* **462**, 426–432 (2009).

384. Appiah, C. *et al.* Living Materials Herald a New Era in Soft Robotics. *Adv Mater* **31**, 1807747 (2019).

385. Schaffner, M., Rühs, P. A., Coulter, F., Kilcher, S. & Studart, A. R. 3D printing of bacteria into functional complex materials. *Sci Adv* **3**, eaao6804 (2017).

386. Liu, X. *et al.* 3D Printing of Living Responsive Materials and Devices. *Adv Mater* **30**, 1704821 (2017).

387. Liu, X. *et al.* Stretchable living materials and devices with hydrogel–elastomer hybrids hosting programmed cells. *Proc Natl Acad Sci USA* **114**, 2200–2205 (2017).

388. Mangayil, R. *et al.* Engineering and Characterization of Bacterial Nanocellulose Films as Low Cost and Flexible Sensor Material. *ACS Appl Mater Inter* **9**, 19048–19056 (2017).

389. Nguyen, P. Q., Botyanszki, Z., Tay, P. K. R. & Joshi, N. S. Programmable biofilm-based materials from engineered curli nanofibres. *Nat Commun* **5**, 4945 (2014).

390. Kalyoncu, E., Ahan, R. E., Ozcelik, C. E. & Seker, U. O. S. Genetic Logic Gates Enable Patterning of Amyloid Nanofibers. *Adv Mater* **31**, 1902888 (2019).

391. Huang, J. *et al.* Programmable and printable Bacillus subtilis biofilms as engineered living materials. *Nat Chem Biol* **15**, 34–41 (2018).

392. Botyanszki, Z., Tay, P. K. R., Nguyen, P. Q., Nussbaumer, M. G. & Joshi, N. S. Engineered catalytic biofilms: Site-specific enzyme immobilization onto E. coli curli nanofibers: Catalytic Biofilms Using Engineered Curli Fibers. *Biotechnol Bioeng* **112**, 2016–2024 (2015).

393. Tay, P. K. R., Nguyen, P. Q. & Joshi, N. S. A Synthetic Circuit for Mercury Bioremediation Using Self-Assembling Functional Amyloids. *ACS Synth Biol* **6**, 1841–1850 (2017).

394. Courchesne, N.-M. D. *et al.* Biomimetic engineering of conductive curli protein films. *Nanotechnology* **29**, 454002 (2018).

395. Duraj-Thatte, A. M. *et al.* Genetically Programmable Self-Regenerating Bacterial Hydrogels. *Adv Mater* **31**, 1901826 (2019).

396. Thongsomboon, W. *et al.* Phosphoethanolamine cellulose: A naturally produced chemically modified cellulose. *Science* **359**, 334–338 (2018).

397. McEvoy, M. A. & Correll, N. Materials that couple sensing, actuation, computation, and communication. *Science* **347**, 1261689–1261689 (2015).

398. Clarke, T. A. *et al.* Structure of a bacterial cell surface decaheme electron conduit. *Proc Natl Acad Sci USA* **108**, 9384–9389 (2011).

399. Gao, H., Chan, N., Oh, J. K. & Matyjaszewski, K. Designing Hydrogels by ATRP. in 69–105 (2015). doi:10.1007/978-981-287-152-7_4.

400. Lee, K. Y., Kong, H. J., Larson, R. G. & Mooney, D. J. Hydrogel Formation via Cell Crosslinking. *Adv Mater* **15**, 1828–1832 (2003).

401. Pitzler, C. *et al.* A fluorescent hydrogel-based flow cytometry high-throughput screening platform for hydrolytic enzymes. *Chem Biol* **21**, 1733–42 (2014).

402. Lülsdorf, N. *et al.* A flow cytometer-based whole cell screening toolbox for directed hydrolase evolution through fluorescent hydrogels. *Chem Commun* **51**, 8679–82 (2015).

403. Nagahama, K., Kimura, Y. & Takemoto, A. Living functional hydrogels generated by bioorthogonal cross-linking reactions of azide-modified cells with alkyne-modified polymers. *Nat Commun* **9**, 2195 (2018).

404. Liu, Y., Sakai, S., Kawa, S. & Taya, M. Identification of Hydrogen Peroxide-Secreting Cells by Cytocompatible Coating with a Hydrogel Membrane. *Anal Chem* **86**, 11592–11598 (2014).

405. Huang, A. *et al.* BioBits™ Explorer: A modular synthetic biology education kit. *Sci Adv* **4**, eaat5105 (2018).

406. Dooling, L. J. & Tirrell, D. A. Engineering the Dynamic Properties of Protein Networks through Sequence Variation. *ACS Central Sci* **2**, 812–819 (2016).

407. Rodell, C. B. *et al.* Shear-Thinning Supramolecular Hydrogels with Secondary Autonomous Covalent Crosslinking to Modulate Viscoelastic Properties In Vivo. *Adv Funct Mater* **25**, 636–644 (2014).

408. Xu, X., Jha, A. K., Harrington, D. A., Farach-Carson, M. C. & Jia, X. Hyaluronic acid-based hydrogels: from a natural polysaccharide to complex networks. *Soft Matter* **8**, 3280 (2012).

409. Engler, A. J., Sen, S., Sweeney, H. L. & Discher, D. E. Matrix Elasticity Directs Stem Cell Lineage Specification. *Cell* **126**, 677–689 (2006).

410. Matyjaszewski, K. Atom Transfer Radical Polymerization (ATRP): Current Status and Future Perspectives. *Macromolecules* **45**, 4015–4039 (2012).

411. Böl, M., Ehret, A. E., Albero, A. B., Hellriegel, J. & Krull, R. Recent advances in mechanical characterisation of biofilm and their significance for material modelling. *Crit Rev Biotechnol* **33**, 145–71 (2012).

412. Carr, D. A. & Peppas, N. A. Molecular structure of physiologically-responsive hydrogels controls diffusive behavior. *Macromol Biosci* **9**, 497–505 (2009).

413. Bathe, M., Rutledge, G. C., Grodzinsky, A. J. & Tidor, B. A Coarse-Grained Molecular Model for Glycosaminoglycans: Application to Chondroitin, Chondroitin Sulfate, and Hyaluronic Acid. *Biophys J* **88**, 3870–3887 (2005).

414. Paulick, A. *et al.* Two different stator systems drive a single polar flagellum in Shewanella oneidensis MR-1. *Mol Microbiol* **71**, 836–850 (2009).

415. Tinevez, J.-Y. *et al.* TrackMate: An open and extensible platform for single-particle tracking. *Methods* **115**, 80–90 (2017).

416. Linehan, J. L. *et al.* Non-classical Immunity Controls Microbiota Impact on Skin Immunity and Tissue Repair. *Cell* **172**, 784-796.e18 (2018).

417. Sommer, F. & Bäckhed, F. Know your neighbor: Microbiota and host epithelial cells interact locally to control intestinal function and physiology. *Bioessays* **38**, 455–464 (2016).

418. Zhang, Y., Ng, C. K., Cohen, Y. & Cao, B. Cell growth and protein expression of Shewanella oneidensis in biofilms and hydrogel-entrapped cultures. *Mol Biosyst* **10**, 1035 (2014).

419. Lu, Y., Aimetti, A. A., Langer, R. & Gu, Z. Bioresponsive materials. *Nat Rev Mater* **2**, 16075 (2016).

420. Badeau, B. A., Comerford, M. P., Arakawa, C. K., Shadish, J. A. & DeForest, C. A. Engineered modular biomaterial logic gates for environmentally triggered therapeutic delivery. *Nat Chem* **10**, 251–258 (2018).

421. Wang, H. *et al.* Covalently Adaptable Elastin-Like Protein-Hyaluronic Acid (ELP-HA) Hybrid Hydrogels with Secondary Thermoresponsive Crosslinking for Injectable Stem Cell Delivery. *Adv Funct Mater* **27**, 1605609 (2017).

422. Ionov, L. Hydrogel-based actuators: possibilities and limitations. *Mater Today* **17**, 494–503 (2014).

423. Almeida, P. de *et al.* Cytoskeletal stiffening in synthetic hydrogels. *Nat Commun* **10**, 609 (2019).

424. Na, J.-H. *et al.* Programming Reversibly Self-Folding Origami with Micropatterned Photo-Crosslinkable Polymer Trilayers. *Adv Mater* **27**, 79–85 (2014).

425. Yosef, N. & Regev, A. Impulse Control: Temporal Dynamics in Gene Transcription. *Cell* **144**, 886–896 (2011).

426. Thomas, P. E., Ryan, D. & Levin, W. An improved staining procedure for the detection of the peroxidase activity of cytochrome P-450 on sodium dodecyl sulfate polyacrylamide gels. *Anal Biochem* **75**, 168–176 (1976).

427. Johnson, I. Human insulin from recombinant DNA technology. *Science* **219**, 632–637 (1983).

428. Wang, J.-S. & Matyjaszewski, K. Controlled/"living" radical polymerization. atom transfer radical polymerization in the presence of transition-metal complexes. *J Am Chem Soc* **117**, 5614–5615 (1995).

429. Potvin-Trottier, L., Lord, N. D., Vinnicombe, G. & Paulsson, J. Synchronous long-term oscillations in a synthetic gene circuit. *Nature* **538**, 514–517 (2016).

430. Shipp, D. A., Wang, J.-L. & Matyjaszewski, K. Synthesis of Acrylate and Methacrylate Block Copolymers Using Atom Transfer Radical Polymerization. *Macromolecules* **31**, 8005–8008 (1998).

431. Fan, G., Graham, A. J., Kolli, J., Lynd, N. A. & Keitz, B. K. Aerobic radical polymerization mediated by microbial metabolism. *Nat Chem* **12**, 638–646 (2020).

432. Subramanian, S. H., Babu, R. P. & Dhamodharan, R. Ambient Temperature Polymerization of Styrene by Single Electron Transfer Initiation, Followed by Reversible Addition Fragmentation Chain Transfer Control. *Macromolecules* **41**, 262–265 (2008).

433. Wang, Y. *et al.* Electrochemically Mediated Reversible Addition–Fragmentation Chain-Transfer Polymerization. *Macromolecules* **50**, 7872–7879 (2017).

434. Hong, V., Udit, A. K., Evans, R. A. & Finn, M. G. Electrochemically Protected Copper(I)-Catalyzed Azide-Alkyne Cycloaddition. *ChemBioChem* **9**, 1481–1486 (2008).

435. Hod, I. *et al.* Fe-Porphyrin-Based Metal–Organic Framework Films as High-Surface Concentration, Heterogeneous Catalysts for Electrochemical Reduction of CO 2. *ACS Catal* **5**, 6302–6309 (2015).

436. Scheffold, R. *et al.* Vitamin B12-mediated electrochemical reactions in the synthesis of natural products. *Pure Appl Chem* **59**, 363–372 (1987).

437. Mosleh, I., Benamara, M., Greenlee, L., Beyzavi, M. H. & Beitle, R. Recombinant peptide fusion proteins enable palladium nanoparticle growth. *Mater Lett* **252**, 68–71 (2019).

438. Melamed, S., Elad, T. & Belkin, S. Microbial sensor cell arrays. *Curr Opin Biotech* **23**, 2–8 (2012).

439. Chen, H., Lin, W. & Yuan, L. Construction of a near-infrared fluorescence turn-on and ratiometric probe for imaging palladium in living cells. *Org Biomol Chem* **11**, 1938 (2013).

440. Keum, D., Kim, S. & Kim, Y. A fluorescence turn-on sensor for the detection of palladium ions that operates through in situ generation of palladium nanoparticles. *Chem Commun* **50**, 1268–1270 (2014).

441. Spicer, C. D., Triemer, T. & Davis, B. G. Palladium-Mediated Cell-Surface Labeling. *J Am Chem Soc* **134**, 800–803 (2012).

442. Li, N., Ramil, C. P., Lim, R. K. V. & Lin, Q. A Genetically Encoded Alkyne Directs Palladium-Mediated Protein Labeling on Live Mammalian Cell Surface. *ACS Chem Biol* **10**, 379–384 (2014).

443. Sohka, T. *et al.* An externally tunable bacterial band-pass filter. *Proc Natl Acad Sci USA* **106**, 10135–10140 (2009).

444. Liu, C. *et al.* Sequential establishment of stripe patterns in an expanding cell population. *Science* **334**, 238–241 (2011).

445. Payne, S. *et al.* Temporal control of self-organized pattern formation without morphogen gradients in bacteria. *Mol Syst Biol* **9**, 697 (2013).

446. Karig, D. *et al.* Stochastic Turing patterns in a synthetic bacterial population. *Proc Natl Acad Sci USA* **115**, 6572–6577 (2018).

447. Lee, J. *et al.* Metal-organic framework materials as catalysts. *Chem Soc Rev* **38**, 1450–9 (2009).

448. Bjerg, J. T. *et al.* Long-distance electron transport in individual, living cable bacteria. *Proc Natl Acad Sci USA* **115**, 5786–5791 (2018).

449. Wegener, G., Krukenberg, V., Riedel, D., Tegetmeyer, H. E. & Boetius, A. Intercellular wiring enables electron transfer between methanotrophic archaea and bacteria. *Nature* **526**, 587 (2015).

450. Fox, A. R. *et al.* Major cereal crops benefit from biological nitrogen fixation when inoculated with the nitrogen-fixing bacterium Pseudomonas protegens Pf-5 X940. *Environ Microbiol* **18**, 3522–3534 (2016).

451. Lee, K. Y. & Mooney, D. J. Hydrogels for Tissue Engineering. *Chem Rev* **101**, 1869–1880 (2001).

452. Rich, S. I., Wood, R. J. & Majidi, C. Untethered soft robotics. *Nat Electron* **1**, 102–112 (2018).

453. Rosales, A. M. & Anseth, K. S. The design of reversible hydrogels to capture extracellular matrix dynamics. *Nat Rev Mater* **1**, 15012 (2016).

454. Courbet, A., Endy, D., Renard, E., Molina, F. & Bonnet, J. Detection of pathological biomarkers in human clinical samples via amplifying genetic switches and logic gates. *Sci Transl Med* **7**, 289ra83-289ra83 (2015).

455. González, L. M., Mukhitov, N. & Voigt, C. A. Resilient living materials built by printing bacterial spores. *Nat Chem Biol* **16**, 126–133 (2019).

456. Hahn, M. S., Miller, J. S. & West, J. L. Three-Dimensional Biochemical and Biomechanical Patterning of Hydrogels for Guiding Cell Behavior. *Adv Mater* **18**, 2679–2684 (2006).

457. Khetan, S. & Burdick, J. A. Patterning hydrogels in three dimensions towards controlling cellular interactions. *Soft Matter* **7**, 830–838 (2011).

458. Wylie, R. G. *et al.* Spatially controlled simultaneous patterning of multiple growth factors in three-dimensional hydrogels. *Nat Mater* **10**, 799–806 (2011).

459. Davies, J. Using synthetic biology to explore principles of development. *Development* **144**, 1146–1158 (2017).

460. Xiao, X. *et al.* Degradation of rhodamine B in a novel bio-photoelectric reductive system composed of Shewanella oneidensis MR-1 and Ag3PO4. *Environ Int* **126**, 560–567 (2019).

461. Higashi, A., Saitoh, N., Ogi, T. & Konishi, Y. Recovery of Indium by Biosorption and Its Application to Recycling of Waste Liquid Crystal Display Panel. *J Jpn I Met* **75**, 620–625 (2011).

462. Ogi, T., Tamaoki, K., Saitoh, N., Higashi, A. & Konishi, Y. Recovery of indium from aqueous solutions by the Gram-negative bacterium Shewanella algae. *Biochem Eng J* **63**, 129–133 (2012).

463. Wang, Z. *et al.* Kinetics of Reduction of Fe(III) Complexes by Outer Membrane Cytochromes MtrC and OmcA of Shewanella oneidensis MR-1. *Appl Environ Microbiol* **74**, 6746–6755 (2008).

464. Brookins, D. G. Eh-pH Diagrams for Geochemistry. 141–143 (1988) doi:10.1007/978-3-642-73093-1_51.

465. Cao, X., Chen, Y., Wang, X. & Deng, X. Effects of redox potential and pH value on the release of rare earth elements from soil. *Chemosphere* **44**, 655–661 (2001).

466. Milo, R. & Phillips, R. Cell Biology by the Numbers. (2015) doi:10.1201/9780429258770.

467. Hyster, T. K. & Ward, T. R. Genetic Optimization of Metalloenzymes: Enhancing Enzymes for Non-Natural Reactions. *Angew Chem* **55**, 7344–7357 (2016).

468. Simon, A. J., d'Oelsnitz, S. & Ellington, A. D. Synthetic evolution. *Nat Biotechnol* **37**, 730–743 (2019).

469. Reyes, C. *et al.* Characterization of Axial and Proximal Histidine Mutations of the Decaheme Cytochrome MtrA from Shewanella sp. Strain ANA-3 and Implications for the Electron Transport System. *J Bacteriol* **194**, 5840–5847 (2012).

470. Neto, S. E., Melo-Diogo, D. de, Correia, I. J., Paquete, C. M. & Louro, R. O. Characterization of OmcA Mutants from Shewanella oneidensis MR-1 to Investigate the Molecular Mechanisms Underpinning Electron Transfer Across the Microbe-Electrode Interface. *Fuel Cells* **17**, 601–611 (2017).

471. Coelho, P. S. *et al.* A serine-substituted P450 catalyzes highly efficient carbene transfer to olefins in vivo. *Nat Chem Biol* **9**, 485–7 (2013).

472. Robin, A. *et al.* Chapter 4 Iron Dynamics in the Rhizosphere. in vol. 99 183–225 (2008).

473. Rajniak, J. *et al.* Biosynthesis of redox-active metabolites in response to iron deficiency in plants. *Nat Chem Biol* **14**, 442–450 (2018).

474. Hernandez, M. E., Kappler, A. & Newman, D. K. Phenazines and Other Redox-Active Antibiotics Promote Microbial Mineral Reduction. *Appl Environ Microbiol* **70**, 921–928 (2004).

475. Maisch, M., Lueder, U., Kappler, A. & Schmidt, C. From Plant to Paddy—How Rice Root Iron Plaque Can Affect the Paddy Field Iron Cycling. *Soil Syst* **4**, 28 (2020).

476. Zimmermann, M. B. & Hurrell, R. F. Nutritional iron deficiency. *Lancet* **370**, 511–520 (2007).

477. Murgia, I., Arosio, P., Tarantino, D. & Soave, C. Biofortification for combating 'hidden hunger' for iron. *Trends Plant Sci* **17**, 47–55 (2012).

478. Hunter, R. C. *et al.* Ferrous Iron Is a Significant Component of Bioavailable Iron in Cystic Fibrosis Airways. *mbio* **4**, e00557-13 (2013).

479. Hederstedt, L., Gorton, L. & Pankratova, G. Two Routes for Extracellular Electron Transfer in Enterococcus faecalis. *J Bacteriol* **202**, (2020).

480. Daeffler, K. N. M. *et al.* Engineering bacterial thiosulfate and tetrathionate sensors for detecting gut inflammation. *Mol Sys Biol* **13**, 923–13 (2017).

481. Reisner, E., Arion, V. B., Keppler, B. K. & Pombeiro, A. J. L. Electron-transfer activated metal-based anticancer drugs. *Inorg Chim Acta* **361**, 1569–1583 (2008).

482. Nissle, A. Weiteres über grundlagen und praxis der mutaflorbehandlung. *Dtsch Med Wochenschr* **51**, 1809–1813 (1925).

483. Kruis, W. *et al.* Maintaining remission of ulcerative colitis with the probiotic Escherichia coli Nissle 1917 is as effective as with standard mesalazine. *Gut* **53**, 1617–1623 (2004).

484. Monteiro, C. *et al.* Characterization of cellulose production in Escherichia coli Nissle 1917 and its biological consequences. *Environ Microbiol* **11**, 1105–1116 (2009).

485. Ou, B. *et al.* Genetic engineering of probiotic Escherichia coli Nissle 1917 for clinical application. *Appl Microbiol Biotechnol* **100**, 8693–9 (2016).

486. Praveschotinunt, P. *et al.* Engineered E. coli Nissle 1917 for the delivery of matrix-tethered therapeutic domains to the gut. *Nat Commun* **10**, 5580 (2019).

487. Walsh, U. F., Morrissey, J. P. & O'Gara, F. Pseudomonas for biocontrol of phytopathogens: from functional genomics to commercial exploitation. *Curr Opin Biotech* **12**, 289–295 (2001).

488. Ganeshan, G. & Kumar, A. M. Pseudomonas fluorescens , a potential bacterial antagonist to control plant diseases. *J Plant Interact* **1**, 123–134 (2005).

489. Haney, C. H., Samuel, B. S., Bush, J. & Ausubel, F. M. Associations with rhizosphere bacteria can confer an adaptive advantage to plants. *Nat Plants* **1**, 15051 (2015).

490. Glasser, N. R., Kern, S. E. & Newman, D. K. Phenazine redox cycling enhances anaerobic survival in P seudomonas aeruginosa by facilitating generation of ATP and a proton-motive force. *Mol Microbiol* **92**, 399–412 (2014).

491. Jiang, W. *et al.* Cr(VI) Adsorption and Reduction by Humic Acid Coated on Magnetite. *Environ Sci Technol* **48**, 8078–8085 (2014).

492. Yin, W. *et al.* Enhanced Cr(VI) removal from groundwater by Fe 0 -H 2 O system with bio-amended iron corrosion. *J Hazard Mater* **332**, 42–50 (2017).

493. Ni, C. *et al.* Adsorption performance of Cr(vi) onto Al-free and Al-substituted ferrihydrites. *Rsc Adv* **6**, 66412–66419 (2016).

494. Peng, Z. *et al.* UV modification of biochar for enhanced hexavalent chromium removal from aqueous solution. *Environ Sci Pollut Res Int* **25**, 10808–10819 (2018).

495. Lu, M., Guan, X.-H., Xu, X.-H. & Wei, D.-Z. Characteristic and mechanism of Cr(VI) adsorption by ammonium sulfamate-bacterial cellulose in aqueous solutions. *Chin Chem Lett* **24**, 253–256 (2013).

496. Srinath, T., Verma, T., Ramteke, P. W. & Garg, S. K. Chromium (VI) biosorption and bioaccumulation by chromate resistant bacteria. *Chemosphere* **48**, 427–435 (2002).

497. Tytłak, A., Oleszczuk, P. & Dobrowolski, R. Sorption and desorption of Cr(VI) ions from water by biochars in different environmental conditions. *Environ Sci Pollut Res* **22**, 5985–5994 (2014).

498. Zhu, Y. *et al.* Removal of hexavalent chromium from aqueous solution by different surface-modified biochars: Acid washing, nanoscale zero-valent iron and ferric iron loading. *Bioresour Technol* **261**, 142–150 (2018).

499. Lyu, H. *et al.* Removal of hexavalent chromium from aqueous solutions by a novel biochar supported nanoscale iron sulfide composite. *Chem Eng J* **322**, 516–524 (2017).

500. Chen, Y.-J. *et al.* Characterization of 582 natural and synthetic terminators and quantification of their design constraints. *Nat Methods* **10**, 659–664 (2013).

501. Hartshorne, R. S. *et al.* Characterization of Shewanella oneidensis MtrC: a cell-surface decaheme cytochrome involved in respiratory electron transport to extracellular electron acceptors. *J Biol Inorg Chem* **12**, 1083–1094 (2007).

502. Wetzel, D. L. B. & Charalambous, G. Instrumental Methods in Food and Beverage Analysis. *Talanta* (1998) doi:10.1016/s0039-9140(99)00355-0.